The Production of Point Defects in Solids by Radiation

P. Agnew

Thesis submitted in Michaelmas Term 1991 in partial fulfilment of the requirements for the degree of Doctor of Philosophy in the University of Oxford.

St. John's College

Oxford

October 1991



Abstract

A number of different aspects of Frenkel defect production are discussed in this thesis. Experiments have been performed to characterise the response of sapphire to radiation and to determine the stability, with respect to temperature and subsequent ionising radiation, of the oxygen vacancies produced. The displacement threshold of the aluminium ion has been determined by irradiating with electrons and comparing measured concentrations of the V centre with theoretical values, and evidence is presented for the stability of the F^{2+} centre at liquid helium temperatures. The efficiency of point defect production in sapphire by a variety of ion beams has been estimated by monitoring the oxygen vacancy colour centre concentration. Results are presented for H, D, He, B, N, Ne, Ar and Kr bombardment at both room temperature and 77K. Experimentally determined values of the mean number of oxygen vacancies produced per incident ion are compared with theoretical values. The latter have been computed by solving the Lindhard integral equations to determine the partitioning of energy between the oxygen and aluminium sublattices. The stopping powers and cross sections of Ziegler, Biersack and Littmark have been used in these calculations and give significantly improved estimates of the damage energy. Two main points emerge from this study. Firstly, a significant Z_1 variation of the damage efficiency is noted for low mass ions. Secondly, in contrast to metals (in particular aluminium) no reduction in efficiency has been found in sapphire with increasing ion mass. This is attributed to differences in the 'thermal spike' behaviour, as a consequence of differing thermodynamic properties, between aluminium and its oxide. The implications of both these results for irradiation characterisation are discussed. In the final chapter we discuss the interaction between conduction electrons and ions in the cooling phase of cascades in metals. Differential equations governing the transfer of heat between the two systems are derived and solved numerically, using physically reasonable parameters for cascades in copper and nickel. Large differences are found in the cooling rates of cascades in these two metals. The degree of cooling due to electronic heat transport is shown to depend on the ratio of a parameter T_0, the temperature at which the electron-phonon mean free path reduces to the radius of the Wigner-Seitz sphere, and γ_e, the coefficient of the electronic heat capacity. The participation of the electronic system in cascade evolution is shown to preclude a universal description of damage efficiency on the basis of simple atomic scaling laws.

Acknowledgements

I would like to take this opportunity to express my gratitude to my supervisor Dr. W. Hayes for his guidance and advice during the last three years. It is no exaggeration to say that without his initial interest this investigation would never have become a D. Phil. project. I wish to thank the Hayes Group for making me feel welcome at the Clarendon despite my infrequent visits. In particular, Dr. A. Fisher was very generous during a brief collaboration and a great help with matters symmetrical.

Most of the work described in this thesis was conducted at Harwell Laboratory, which has been home to me for the last six years. During that time I have profited from the supportive atmosphere in the (former) Radiation Effects Group. I am indebted to my supervisor, Mr. G.P. Pells, for his constant help and guidance throughout this project. Despite his many other responsibilities Philip was always able to find time to discuss curious results and unexpected problems. I wish to thank my group leader, Dr. C.A. English, for continuing to support the funding of this project at a time of great financial pressure. Colin's appreciation of the finer points of radiation damage were of particular help in the early stages of my research. Special thanks are due to Dr. S.N. Buckley, who first suggested the possibility of studying at Oxford, and to Dr. R. Bullough who was my Division head at the time and who first invited me to Harwell. I would like to thank Mr. Z. Sooi for his patient coaxing of the ion accelerator and Mr. M Murphy for many and varied experimental suggestions. Dr. J. Perks deserves special thanks for many things, but in particular his explanations of computers, their problems and solutions. Dr. A.J.E. Foreman provided new insights into various mathematical problems and much practical help. It is a pleasure to thank both Alan and Dr. M.W. Finnis for a very fruitful collaboration. Mike's natural gifts for physics were a joy to behold and I have learned a great deal from him. I would also like to thank Dr. A.M. Stoneham for many useful comments. Our group secretary, Mrs. L. England was very helpful in general, as were the staff of the Harwell Library.

I would like to thank Mr. L.P. Baldwin for the peace and quiet of 47 Shelley Close, where much of this thesis was written. Our mutual enjoyment of physics has been, and I hope will continue to be, a source of much pleasure.

And finally, I wish to thank Miss J.L. Ing. Judith disturbed the aforementioned peace and quiet in a most agreeable manner and provided much support and encouragement. In particular, she carefully read the entire thesis and found the mistakes everyone else had missed.

This is dedicated to my parents, who would be pleased.

Contents

Abstract

Acknowledgements

Contents

Chapter 1 – Introduction and Thesis Overview 1

§ 1.1 The Interaction of Radiation with Solids 2

§ 1.2 Modifications of Materials in a Radiation Environment 4

§ 1.3 Thesis Overview 6

Chapter 2 – Standard Models of Point Defect Production. 10

§ 2.1 The Stopping of Ions in Solids 11

§ 2.2 Simple Cascade Theory 17

§ 2.3 The 'NRT' Standard 20

§ 2.4 Failure of the 'NRT' Damage Function in Cascades 22

§ 2.5 Many-Body Interactions in the Cascade 23

§ 2.6 Effects of Crystal Structure 30

Chapter 3 – Radiation Effects in Sapphire 37

§ 3.1 Structure 37

§ 3.2 Structural Radiation Effects 38

§ 3.3 Optical Properties 40

§ 3.4 Colour Centres in Sapphire 41

§ 3.5 The Effects of Irradiation on Optical Properties 45

§ 3.6 Stability of Radiation-Induced Colour Centres 49

Chapter 4 – Theory of Damage Partitioning in Polyatomic Solids 52

§ 4.1 Integral Equations Governing Radiation Effects 53

§ 4.2 Integral Equations for Polyatomic Solids 56

§ 4.3 Scattering Cross Section and Stopping Powers 58
§ 4.4 Modifications of Stopping Powers in Ionic Insulators 62
§ 4.5 Method of Numerical Solution of Integral Equations 65
§ 4.6 Results 68
§ 4.7 Comparisons with Other Work 70

Chapter 5 – Experimental Methods and Preliminary Results 73
§ 5.1 Sample Preparation 73
§ 5.2 Variable Temperature Cryostat 74
§ 5.3 Optical Absorption Measurements 75
§ 5.4 Displacement Thresholds in Sapphire 77
§ 5.5 The Interaction of Energetic Electrons with Solids 79
§ 5.6 Thresholds : Experimental Details 84
§ 5.7 Thresholds : Results 85
§ 5.8 Thresholds : Discussion 85
§ 5.9 Annealing Behaviour of Point Defects and Colour Centres in Sapphire 87
§ 5.10 Ionisation Stability of Frenkel Pairs 89
§ 5.11 Summary 90

Chapter 6 – Damage Efficiency in Sapphire 93
§ 6.1 Evaluation of Colour Centre Concentration 94
§ 6.2 Data Analysis 98
§ 6.3 Accelerator Techniques 100
§ 6.4 Experimental Procedure 103
§ 6.5 Results 104

Chapter 7 – Discussion of Damage Efficiency 109
§ 7.1 Magnitude of Measured Efficiencies and Temperature Variation 110
§ 7.2 Validity of Damage Efficiency Results 112
§ 7.3 Damage Efficiency Variations for Low Mass Ions 114
§ 7.4 Damage Efficiency of High Mass Ions 119

§ 7.5 Irradiation Characterisation and Damage Correlation 122

Chapter 8 – Thermal Excitation of Electrons in Energetic Displacement Cascades 129

§ 8.1 Inapplicability of Bulk Thermal Conductivity 130

§ 8.2 Role of the Electron Gas 131

§ 8.3 Model of Flynn and Averback 132

§ 8.4 Theory of Finnis et. al. 134

§ 8.5 Numerical Solutions 136

§ 8.6 Atomistic Simulation with MD 138

§ 8.7 Comparison with Other Work 140

§ 8.8 MD Simulations 141

§ 8.9 Estimation of T_0 143

§ 8.10 Summary 145

§ 8.11 Conclusions 146

Appendix 1 – Numerical Integrations Involving the Divergent Thomas-Fermi Differential Cross Section 150

Appendix 2 – Units of Radiation 154

Chapter 1

Introduction and Thesis Overview

Introduction.

The modern theory of solids has been remarkably successful in explaining many of the properties of crystalline materials. One factor can be identified which has contributed to this success more than any other – that is the periodic arrangement of atoms on a lattice, extending over macroscopic distances. Our understanding of liquids and solids such as glasses, where no long range order exists, is very poor in comparison. The important role played by lattice periodicity in the theory of solids is a reflection of the physical importance of this property. If the periodicity is disturbed for some reason then the properties of the solid are likely to be modified. We must conclude then that the properties of crystalline solids are influenced not only by the intrinsic properties of the constituent atoms but also by the presence of imperfections in the otherwise perfectly ordered array of atoms.

The primary lattice defects in solids are the Schottky and Frenkel defects <1> and it is well known from thermodynamics that the second law requires *all* solids to possess these defects to a greater or lesser extent, depending on the temperature. However it is possible for these simple defects to exist in solids to a much greater degree than that required by equilibrium thermodynamics. There are several ways of introducing excess numbers of point defects into crystals. The present investigation is concerned with the manner in which Frenkel defects can be introduced by exposing the solid to energetic radiation. Simple energy arguments suggest that some tens of eV are required to break the bonds surrounding an atom and displace it from its lattice site and many measurements have shown this to be the case. Exposing a solid to radiation which is able to transfer energies of this order will result in the production of Frenkel defects. Later in this chapter we shall indicate some of the

technological consequences of this process. But first we shall briefly review the manners in which the four different types of radiation normally of interest in the field of radiation damage are able to produce lattice defects.

§ 1.1 The Interaction of Radiation with Solids.

For the purposes of radiation damage one can divide radiation into four classes: electromagnetic radiation, electrons, 'heavy' particles with mass of the order of or greater than the proton mass, and neutrons. In succeeding chapters we shall discuss the second and third of these in considerable detail but here a brief account is given of the interactions of all four.

Electromagnetic Radiation.

The low momentum associated with γ– rays (we use this generic term to imply photon energies above 10 keV) means that the direct transfer of kinetic energy to a nucleus is a very inefficient process and can be ignored. The major interaction is with the atomic electrons. This takes place via three different mechanisms: the photo-electric effect, the Compton effect and pair production. For low Z solids and energies between 1 and 10 MeV the dominant interaction is Compton scattering of the atomic electrons <2>. The photo-electric cross section is proportional to Z^5 and becomes increasingly important for large Z, but decreases with increasing energy and only becomes comparable to the Compton cross section at energies well below those capable of causing displacements. At energies greater than around 10 MeV pair production becomes the dominant interaction. The energetic electrons produced by Compton scattering or pair production carry a much greater momentum than the original photon and may produce atomic displacements by direct collision with target nuclei. In certain materials (most notably the alkali halides) excitation of the target electrons can result in lattice displacement damage. This effect is known as radiolysis and can be a much more efficient mechanism than the direct collisional process <3>.

Electrons.

Energetic electrons also interact most strongly with the target electrons, producing intense ionisation. At energies above about 100 keV they may be capable of transferring sufficient momentum to target nuclei to produce lattice displacements. However the cross section for this process is always very small compared to that for electronic excitation. In general electron irradiation produces isolated point defects and is often used to measure the minimum energy required to produce Frenkel defects – referred to as the displacement threshold energy.

Ion Irradiation.

On entering a solid an energetic ion is likely to be further stripped of orbiting electrons and so the problem to be considered is the scattering of a charged projectile from the target atoms. The large difference in mass between the target nuclei and electrons allows one to consider scattering from the nuclei and orbital electrons separately. For the important case of medium energy heavy ions the energy loss of the ion to target electrons can be treated in an analogous way to a classical particle moving in a viscous fluid, with the result that this mechanism of energy loss is proportional to the ion velocity. The interaction with the target nuclei can, to a good approximation, be treated as a two body collision with the particles interacting via a screened Coulomb potential. At high ion velocities the screening is unimportant and the interaction is described well by Rutherford's scattering formula. At lower energies screening is important and the Coulomb potential must be modified to take account of this. One fortunate aspect of this problem is that the kinematics of the collision can always be described well using classical mechanics. Simple considerations based on the Uncertainty Principle show that classical mechanics is valid for scattering by low energy ions in a solid, but becomes less so for higher energies, where quantum mechanics must be used. However, as we have just noted, at higher energies the scattering is described by a simple Coulomb potential. Now it is well known that classical mechanics and quantum mechanics (within the Born approximation) give the same formula for this type of scattering and so we are effectively able to use classical mechanics to calculate scattering cross sections throughout the whole energy range of interest in radiation damage.

Neutrons.

One must differentiate between 'thermal' neutrons (i.e. neutrons having kinetic energies of the order of kT) and fast neutrons. Although thermal neutrons are able to induce nuclear reactions where the products may produce radiation damage, they are unable themselves to produce lattice damage. Fast neutrons, being uncharged, have a weak interaction with the target compared with a protons of similar energy. Their interaction with target nuclei can, for the purposes of radiation damage, be described by a hard-sphere potential, where the hard-sphere radius is approximately equal to the nuclear radius. Fast neutrons will occasionally give up a large fraction of their energy to a target atom which, being charged, will then interact strongly with other target atoms as described above. For this reason self-ion bombardment is often used to mimic the damage production aspect of neutron irradiation.

§ 1.2 Modifications of Materials in a Radiation Environment.

A number of cases can be identified where energetic radiation exists in sufficient quantities to modify the macroscopic properties of nearby materials. In the electronics industry it is common practice to modify the properties of semiconductors by irradiating the material with an appropriate dopant ion beam in order to place the dopant at a specified depth below the surface. An undesirable product of this process is the lattice damage introduced by the bombarding ion beam. Fortunately most of this can be annealed out following the irradiation by heating the semiconductor. In space, orbiting satellites are exposed to cosmic rays and other high energy radiations which have a deleterious effect on the electronic components. However the problems of radiation damage are most acute in connection with the operation of nuclear reactors. The disintegration of a uranium or plutonium atom in the oxide fuel of a reactor produces two massive and energetic fission fragments. In being brought to rest in the surrounding material these energetic ions are able to cause many atomic displacements. Another source of damage is the abundance of fast neutrons in the reactor. Being uncharged these are able to escape from the nuclear fuel itself and cause damage in the surrounding metal structure of the reactor. The introduction of large numbers of Frenkel

defects into these materials results in important changes to their properties. Many of the problems associated with these changes have been reviewed by Bullough and Wood <4> but here we shall mention a few of the most serious. One problem associated with the production of point defects is the phenomenon of void swelling, first discovered in steels in the materials of the Dounreay fast reactor in 1966. The aggregation of vacancies into three-dimensional holes, termed voids, and the relocation of the corresponding interstitial atoms results in the material increasing in volume. One of the physical properties most dramatically affected by the production of Frenkel defects in the lattice is diffusion. In a perfect crystalline solid it is impossible for atoms to move from one lattice site to another without distorting the lattice considerably. However if vacant lattice sites are present then the random thermal motion of atoms can easily result in the transport and redistribution of atoms. For elemental solids this is often of no consequence but for multicomponent solids the ability to redistribute atoms can lead to important effects. For example, in an alloy consisting of A and B type atoms, A atoms may be rather more mobile than B atoms at a given temperature. If sinks, such as grain boundaries or dislocations exist in the system (as they do in all real materials) then regions may form in the material which are rich in one type of atom and depleted of another type. This effect is known as radiation induced segregation and can seriously degrade the properties of materials. There are a number of areas where effects of this type give rise to problems but a typical example is in the oxidation of reactor metals. Oxidation inhibitors such as chromium are often added to these materials. They act by coating the grain boundaries with an inert compound, in this case chromium oxide, which inhibits further oxidation of the bulk material. Radiation induced segregation may cause the boundaries to become depleted of chromium with the result that the bulk steel oxidises (it goes rusty).

Problems associated with metals have been most studied, due their crucial role as structural materials. However the importance of insulators in the electrically driven tokamak fusion reactors has spurred much research into radiation effects in these materials. There are several areas where compounds such as alumina, spinel and beryllia will play a role of primary importance. The windows of microwave auxiliary heating systems are particularly vulnerable. These components, which act as a vacuum break between the torus and the microwave generators, must transmit power densities of around 10 $kWcm^{-2}$ and are

subjected to considerable thermal shocks. A proportion of the incident power is absorbed by the windows, with a constant of proportionality depending upon the dielectric loss tangent, tan δ, of the material. This has been shown to increase under radiation as a result of the creation of Frenkel defects, *e.g* <5>, leading to a greater degree of window heating, thermal shock and probability of failure.

All of the technological problems we have described, and a number of others, have as their root cause the production of lattice displacements by radiation. In order to understand and predict the way in which materials will behave in a radiation environment it is therefore vital to be able to estimate the number of point defects which will be created under given irradiation conditions. Several models were devised in the 1950's to estimate defect production under energetic particle irradiation – most notably the 'Kinchin-Pease' model <6>. However it was realised at an early stage that these models, all of which gave roughly equivalent answers, considerably over-estimated residual defect production when compared to experimental values. An improved model, which we shall discuss in detail in chapter 2, was suggested in 1975 and this treats the partition of the ion energy between the target nuclei and electrons in a much more satisfactory manner. Experiments in metals have shown that this 'modified Kinchin-Pease' model succeeds in predicting the degree of defect production for electron and low mass ion irradiation, where only isolated displacements are produced. But for heavy ions and fast neutrons, where most of the displacements are produced closely together in 'cascades' (described in chapter 2), the model still gives considerable over-estimates.

§ 1.3 Thesis Overview.

The work described in this thesis is concerned with various aspects of the *efficiency* of point defect production and survival. By efficiency here we mean the ratio of the experimentally determined defect concentration to that predicted by the standard, binary collision theory of defect production based on the modified Kinchin-Pease model. A series of experiments have been performed to determine the damage efficiency in an ionic insulator,

sapphire. Although several authors have studied defect production in insulators for one or two different ions, there have been no detailed studies covering such a wide range of ions at different temperatures as is reported here. Also, previous studies have tended to use ion doses which are unsuitable for quantitative comparisons with the standard model.

In chapter 2 we review standard models of collisional defect production. The modified Kinchin-Pease model is discussed and the reasons for its failure in cascades are indicated. Molecular dynamics simulations of large collision cascades have recently been performed and since these shed further light on the breakdown of the binary collision theory we take this opportunity to review some of the more recent results that have emerged from these studies.

Since the bulk of the experimental work was conducted on sapphire, we devote chapter 3 to a discussion of radiation effects in this material. Sapphire was selected because it is one of the few technologically important insulators in which the colour centres associated with the primary point defects have been positively identified. A second reason for choosing this material is that the Frenkel defects are known to be thermally stable, at least up to room temperature. Since this is below the temperature at which any long range diffusion of defects takes place it is thus possible to determine the variation of damage efficiency with temperature. Similar experiments in metals are difficult to perform since the Frenkel defects are often mobile just above liquid helium temperatures and long range recombination can occur.

In the damage efficiency experiments conducted here measurements were only made on the colour centres associated with defects on the oxygen sublattice. Thus in order to evaluate the damage efficiency it is necessary to employ theoretical values of Frenkel pair production on the oxygen sublattice. The usual form of the modified Kinchin-Pease model is not applicable in this case since the aluminium and oxygen sublattices have different interactions strengths with an energetic ion and also have different displacement thresholds. In chapter 4 we describe a theory of energy partitioning which we use to determine how the energy of an energetic ion is shared between the two sublattices of sapphire. These results are used to obtain estimates of point defect production on the oxygen sublattice which may be compared with experimental values.

In chapter 5 we describe the basic experimental method and apparatus used. Some preliminary experiments designed to characterise the response of sapphire to radiation are described here and a number of results are reported. The results of the damage efficiency experiments are reported in chapter 6. Some of these results are quite unexpected and so in chapter 7 we initially take a closer at the irradiation conditions, to see if these results could be an artifact of the particular experimental parameters, before discussing them further. We then turn to the ways in which displacement damage is characterised, in particular with the unit of 'displacements per atom' (*dpa*), and discuss more complete methods of irradiation characterisation. It is suggested that the use of simple atomic properties as correlation parameters is incomplete and that the thermodynamic properties of the target must also be taken into account when comparing irradiations. The chapter is concluded with an illustration of the difficulties of such a procedure in metals, where the bulk values of the thermodynamic properties are shown to be inappropriate for this problem.

In the final chapter (chapter 8) we take up this problem of the thermodynamic treatment of cascades in metals in greater detail. Specifically, we shall be concerned with the manner in which heat is removed from the cascade region in metals. As noted previously, the binary collision theory predicts the degree of isolated point defect production in metals well, but gives significant overestimates when most of the Frenkel pairs are produced closely together in displacement 'cascades'. The cooling rate of a cascade is important in determining the degree of residual defect motion and hence Frenkel pair recombination. As such it is of primary importance in determining the damage *efficiency* in metals. In this chapter we discuss the mechanisms by which heat is removed from the cascade region and highlight the role played by the electron gas in the conduction process. It is shown how the thermal evolution of cascades in two such similar metals as copper and nickel can differ dramatically. This clearly has important consequences for the comparison of irradiations. A new theoretical model for the electron-ion interaction in cascades is discussed and partial differential equations describing the flow of heat from ions to electrons are derived. A method is described for incorporating the electron-phonon interaction into standard molecular dynamics simulations of cascades and we conclude with a description of some of the effects interaction produces in cascade simulations in copper.

References

<1> F.C. Brown, *The Physics of Solids* , W.A. Benjamin, New York (1967).

<2> C.M. Davisson and R.D. Evans, Rev. Mod. Phys. 24 (2), 79 (1952).

<3> P.W. Levy, Rad. Eff. in Optical Mater. SPIE Vol. 541, 2 (1985).

<4> R. Bullough and M.H. Wood, Nucl. Energy 23 (6), 371 (1984).

<5> S.N. Buckley and P. Agnew, J. Nucl. Mater. Vol. 155-157, 361 (1988)

<6> G.H. Kinchin and R.S. Pease, Rep. Prog. Phys. 18 , 1 (1955).

Chapter 2

Standard Models of Point Defect Production

Introduction

The simplest systems in which to test our theories of point defect production are perhaps solid state noble gases or covalent crystals such as iodine or diamond. These materials have two properties which simplify a theoretical treatment of the problem in that *a)* there is only one atomic species to consider and we need not worry about how the energy of an irradiating particle is partitioned amongst the different sublattices, as we must in a compound material and *b)* the electronic system does not have a continuum of states available for occupation in the energy range of the thermal phase of the cascade and thus can be entirely neglected after the first few tens of femtoseconds of the primary displacement event. This is not the case in metals (as we shall show in chapter 8) where the continuum of unoccupied states allows the electron gas to participate in the cooling of the cascade and so affect its final configuration. A standard model of point defect production has been developed to describe radiation effects in such comparatively simple materials as those mentioned above and must also form the basis for a description of the more complicated systems such as metals or ionic solids. In this chapter we present a brief review of this standard model; in later chapters we will see how the model can be modified to deal with these more complex materials. Our discussion of the stopping of ions in solids in this chapter will focus on the physical processes involved and the analytic approaches which have been used in the past to find qualitative solutions to many problems. In chapter 4 we shall then be in a position to introduce the most accurate stopping cross sections developed to date in order to find more accurate estimates of the effects of ion irradiation.

§ 2.1 The Stopping of Ions in Solids.

The large difference in nuclear and electronic mass allows us to treat the interaction of an energetic ion with these two systems separately. We may thus define nuclear and electronic stopping powers, $S_n(E)$ and $S_e(E)$, as the energy transferred per unit path length to the nuclear and electronic systems respectively by an energetic ion of energy E.

Nuclear Stopping. The transfer of kinetic energy to host atoms is described by the classical theory of scattering, *e.g.* Goldstein <1>. The collision is usually treated as a screened Coulomb collision and can be expressed as a function of two variables: the projectile's energy before the collision, E and the impact parameter, p. It is straightforward to evaluate the angle through which the projectile is scattered as

$$\Theta = \pi - \int_{r_{min}}^{\infty} \frac{2p\,dr}{r^2\left[1-\frac{V(r)}{E_c}-\frac{p^2}{r^2}\right]^{1/2}} \quad , \tag{2.1}$$

where Θ is the scattering angle in the centre of mass coordinate system, r_{min} is the distance of closest approach, $V(r)$ represents the scattering potential and E_c is the energy of the centre of mass, defined as

$$E_c = \frac{E M_2}{(M_1+M_2)} \quad . \tag{2.2}$$

Here the subscript 1 refers to the projectile and 2 refers to the stationary target atom. Equation (2.1) is known as the scattering integral. From this the energy transfer T to the target atom can be determined simply from

$$T = \gamma E \sin^2\frac{\Theta}{2} \tag{2.3}$$

$$\text{where} \qquad \gamma = \frac{4M_1M_2}{(M_1+M_2)^2}.$$

Lindhard and Scharff <2> found that a 'universal' solution of the scattering integral can be obtained if a change of variables is made such that ε becomes the reduced form of E_c and t becomes the reduced form of T as follows:

$$\varepsilon = \frac{a M_2 E}{Z_1 Z_2 e^2 (M_1 + M_2)} \tag{2.4}$$

$$\text{and} \quad t = \varepsilon^2 (T/T_m) \ .$$

Here T_m is the maximum possible energy transfer in the collision and a is a reduced radial coordinate. A common choice for this parameter is the screening radius of the Thomas-Fermi atom:

$$a = (9\pi^2/128)^{1/3} a_0 Z^{-1/3} \ , \qquad Z^{2/3} = Z_1^{2/3} + Z_2^{2/3} \ , \tag{2.5}$$

with a_0 the Bohr radius. The nuclear stopping power is found by considering all possible energy transfers in a collision up to the maximum value T_m, thus

$$S_n(E) = N \int_0^{T_m} T \, d\sigma = 2\pi N \gamma E \int_0^{p_{max}} \sin^2 \frac{\Theta}{2} \, p \, dp \ , \tag{2.6}$$

where N denotes the number density of scattering centres and p_{max} is taken to be the sum of the two atomic radii, beyond which the interatomic potential and hence the transferred energy T is zero. To proceed further it is necessary to obtain a solution of the scattering integral for a given interatomic potential, usually expressed in the form

$$V(r) = \frac{Z_1 Z_2 e^2}{r} \Phi(r/a) \ , \tag{2.7}$$

where Φ is a screening function.

Two approaches have traditionally been followed to obtain the differential cross section and nuclear stopping power. The first is to obtain analytic solutions by using a 'power law potential' in which the screening function is expressed in a power form

$$\Phi(r/a) = \frac{k}{s} (a/r)^{s-1} \ , \tag{2.8}$$

with s=1,2, *etc*, and k a numerical constant. This allows the scattering integral to be solved analytically and leads to the following expression for the scattering angle

$$\Theta = \frac{\mu k}{\varepsilon} (a/p)^s \ ,$$

(2.9)

$$\text{with} \quad \mu = \frac{1}{2}\beta\left(\frac{1}{2}, \frac{s+1}{2}\right) \approx \frac{1}{s}\left(\frac{3s-1}{2}\right)^{1/2} \quad ,$$

where β is the Beta function <3>. From this one can proceed to evaluate the differential scattering cross section as

$$d\sigma(T) = C E^{-m} T^{-1-m} dT; \qquad m = \frac{1}{s} \quad ,$$

(2.10)

$$\text{with} \quad C = \frac{\pi}{2}\lambda_m a^2 \left(\frac{M_1}{M_2}\right)^m \left(\frac{2Z_1 Z_2 e^2}{a}\right) 2m \ .$$

A rather more accurate screening function though is that of the Thomas-Fermi atom. If Φ is taken as the Thomas-Fermi screening function of a neutral atom then, providing high accuracy is not required, this simple analytic form can still be used but m must be allowed to vary with energy. Sigmund <4> gives the following criteria for choosing the appropriate value of m

$$m = \begin{cases} 1/3, & \varepsilon \le 0.2 \\ 1/2, & 0.2 < \varepsilon \le 2 \\ 1, & \varepsilon > 10 \end{cases} \qquad (2.11)$$

and also gives the values of λ_m appropriate to each m value

$$\lambda_{1/3} = 1.309; \ \lambda_{1/2} = 0.327; \ \lambda_1 = 0.5 \ . \qquad (2.12)$$

The value $m = 1$ corresponds to Rutherford (i.e unscreened Coulomb) scattering.

This analytic approach has proved powerful in the hands of the Danish school, especially Sigmund and co-workers (e.g. the review article in ref. <4>) who have shown great ingenuity in extracting analytic solutions to many problems. Greater accuracy may be achieved though by not imposing the simple form of eqn.(2.10) on the scattering cross section and resorting to numerical methods. It was first shown by Lindhard *et. al.* <5> that the so-called 'magic formula',

$$\frac{\Theta^2}{4} = \frac{-3p^{1/3}}{16E_c^2}\frac{d}{dp}\{V^2(p)p^{2/3}\} \quad , \qquad (2.13)$$

is a very accurate solution of the scattering integral for a wide variety of interatomic potentials (the requirement being that the screening function can be expressed by, perhaps different, power series over finite regions of r). In this case the solution of the scattering integral leads to a *universal* differential scattering cross section of the form

$$d\sigma = \frac{\pi a^2}{2t^{3/2}} f(t^{1/2})\, dt \quad , \tag{2.14}$$

where $f(t^{1/2})$ is a function obtained by numerical solution of the magic formula for a given potential. The most common approach is again to use the Thomas-Fermi potential and Lindhard *et. al.* <5> gave a graph of the results of such a calculation. Fig. 2.1 shows the Lindhard $f(t^{1/2})$ obtained for a Thomas-Fermi potential, the $f(t^{1/2})$ for a power law potential varying as r^{-2} (for which $f(t^{1/2})$ is a constant) and the equivalent for Rutherford scattering. Various analytic approximations to the Lindhard $f(t^{1/2})$ for a Thomas-Fermi atom have been developed, e.g. <6,7>. Some workers have chosen to use alternative universal potentials, such as the Moliere or Lenz-Jensen potentials <8>. In chapter 4 we shall discuss a new, semi-empirical, universal approximation for the scattering function $f(t^{1/2})$, which has been adjusted in the light of a detailed study of experimental results. The formula of Ziegler *et. al.* <8> is believed to give the most reliable results.

In fig. 2.2 we have calculated the differential energy transfer cross section of eqn.(2.14) for iron. This curve was obtained using the Coulter and Parkin <6> approximation to $f(t^{1/2})$. In fig. 2.3 this cross section has been used together with eqn. (2.6) to calculate the nuclear stopping power in the universal Lindhard units, making it applicable to all projectile-target combinations. This agrees very well with the original universal nuclear stopping power curve given by Lindhard *et. al.* <9>. In fact the nuclear stopping power is not particularly sensitive to the approximation used for this function and this will be seen to have important consequences later.

Electronic Stopping. The relevance of accurate electronic stopping cross sections to point defect production may not be immediately apparent. However we shall see in chapter 4 that the electronic stopping power enters the expression for the energy deposited into nuclear

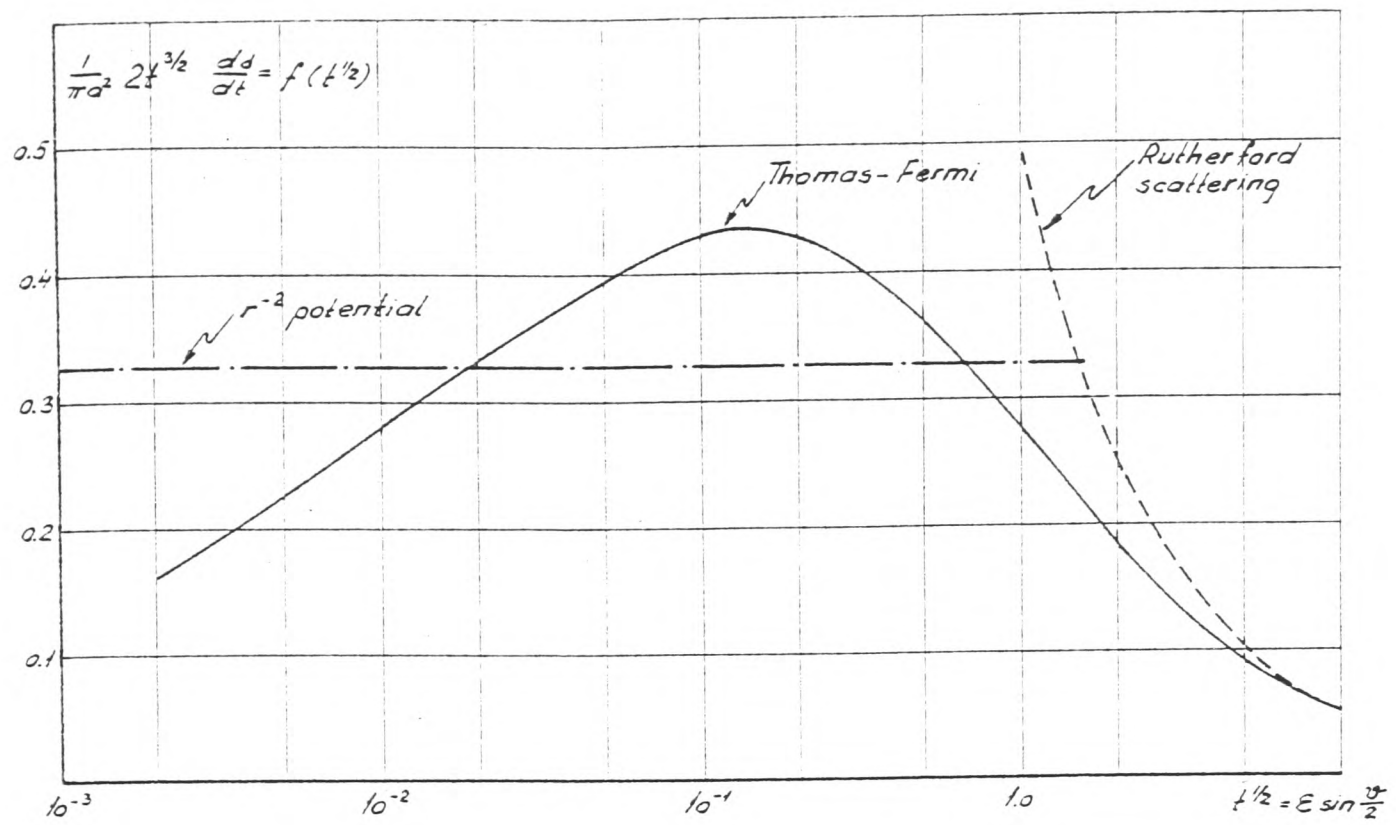


Fig. 2.1. Universal scattering function $f(t^{1/2})$ for various interatomic potentials. Ref. <9>.

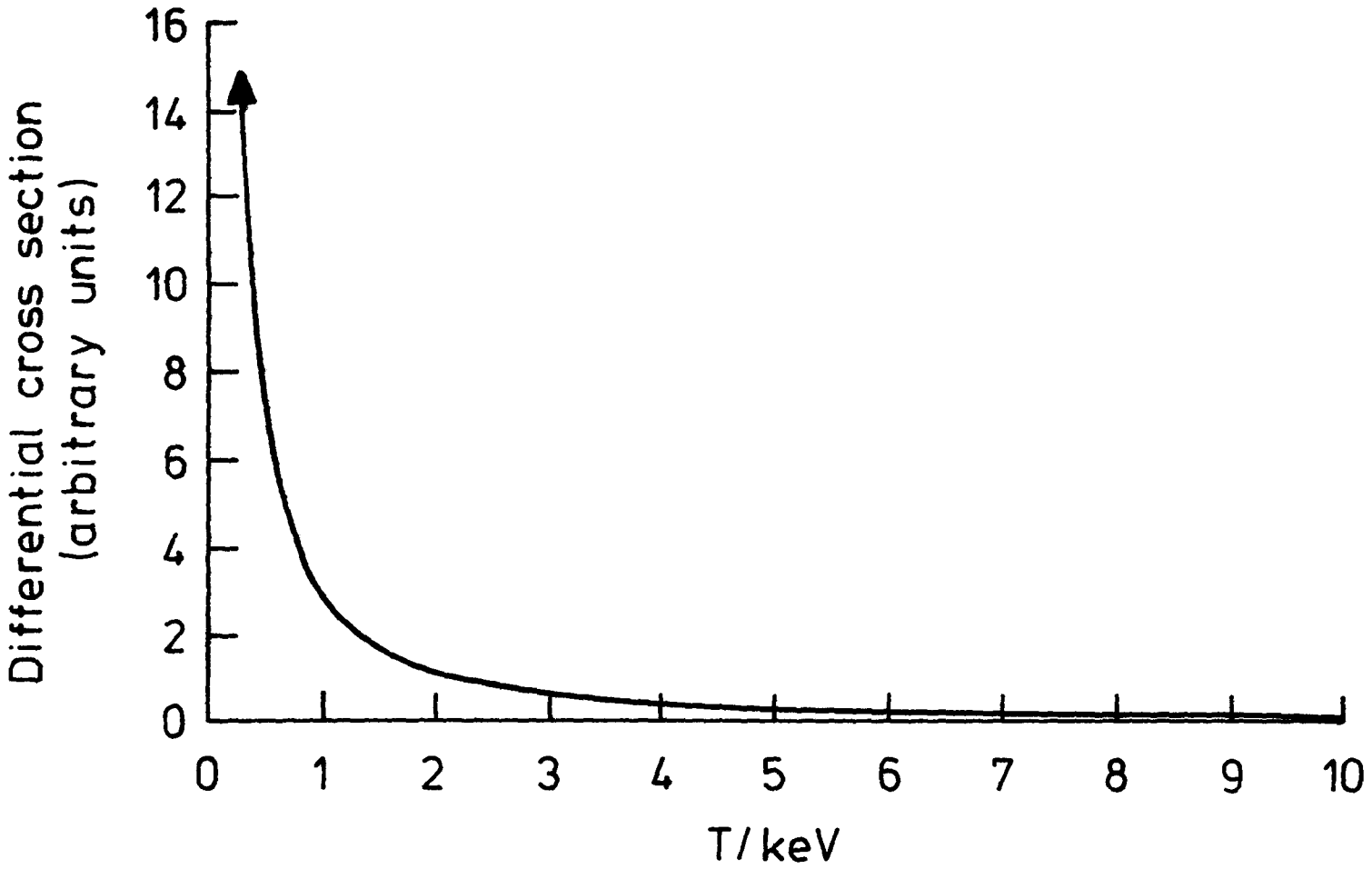


FIG. 2·2

DIFFERENTIAL ENERGY TRANSFER CROSS SECTION
FOR A 10 keV Fe RECOIL

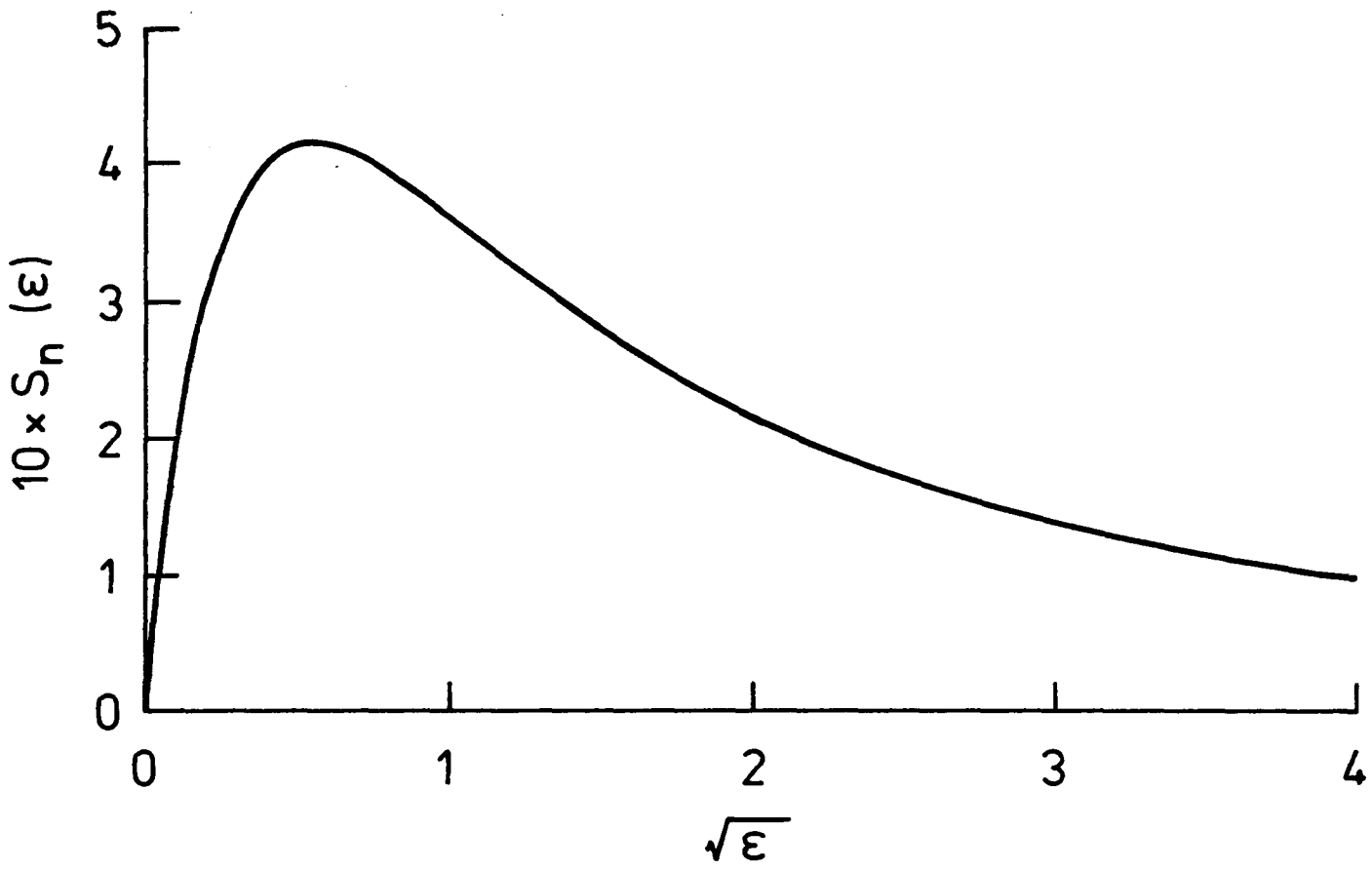


FIG. 2·3

UNIVERSAL NUCLEAR STOPPING CURVE

collisions. On simple energy considerations, if more energy is given up to electrons then less is available for displacing atoms. This subject has not been developed to the same degree of accuracy as the nuclear stopping theory and it is easy to see why when one pauses to consider some of the complex interactions of an energetic ion with the target electrons. Although the mechanics of simple ion-electron collisions have been known since the early work of Bohr <10>, Bethe <11> and Bloch <12>, the presence of the projectile in the solid causes a large perturbation to both systems so that the problem now becomes how to describe the state of both the projectile and the target as a consequence of their interaction, rather than the collision itself. Some examples may serve to make this point clear. On entering the solid an energetic ion will invariably lose some of its atomic electrons and so the charge state of the ion will, in general, depend on both the projectile energy and (to a lesser extent) the nature of the target. Bohr <13> suggested, on the basis of the Thomas-Fermi atom, that the fractional ion charge would depend on its velocity v via

$$\frac{Z^*}{Z} = \frac{v}{(v_0 Z^{2/3})} \quad , \tag{2.15}$$

where v_0 is the Bohr velocity. The Bohr criterion for fractional charge is that the atomic electrons will be stripped from the ion if its velocity exceeds the orbital electron velocity. On the other hand Lamb <14> proposed that the electron binding energy was the important stripping criterion. The problem was approached empirically by Northcliffe <15> who found that a wide variety of experimental data could be reproduced by normalizing each ion, energy and target combination of experimental stopping power to the stopping power of protons in the same target and at the same velocity. He found that a large body of data could be accurately described by the relation

$$\frac{Z^*}{Z} = 1 - a \exp\left(\frac{b}{Z^{2/3}} \frac{v}{v_0}\right) \quad , \tag{2.16}$$

introducing fitting constants a and b.

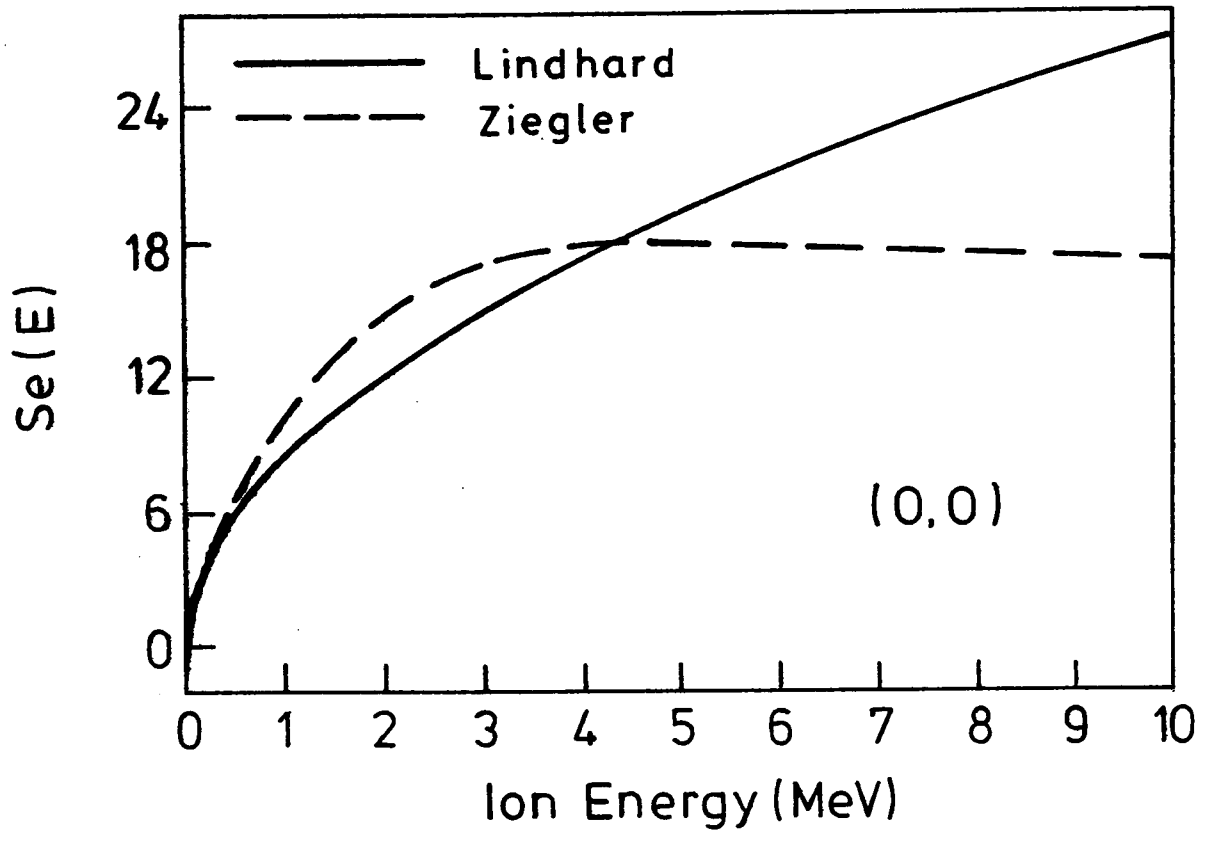
A different problem considered by Fermi and Teller <16> was to describe how the target will polarise in the presence of a rapidly moving projectile. These authors treated the target electrons as a plasma and, beginning with Maxwell's equations, they established some

estimates of the polarization of the electron gas. This work was later extended and generalised by the ubiquitous Lindhard <17>, who introduced his well-known generalised dielectric constant to obtain a many-body, self-consistent treatment of the interaction of a projectile with a free electron gas. Further improvements to electronic stopping theory awaited the development of Hartree-Fock charge density distributions for atoms in solids from the latter half of the 1970's onwards. These more realistic solid state charge distributions, together with the local density approximation (wherein each volume element of a solid is considered to be an independent plasma), has led to a full numerical treatment of the electronic stopping problem. In the field of radiation damage however, a simpler approach has generally been preferred, *e.g* <6,18> and accuracy has been sacrificed for the computational ease of the simple equation proposed by Lindhard and Scharff <19>:

$$C_e(E) = 8\pi e^2 a_0 \frac{Z_1^{7/6} Z_2}{Z} \frac{v}{v_0} \quad , \tag{2.17}$$

where $\quad Z = (Z_1^{2/3} + Z_2^{2/3})^{3/2} \quad .$

This equation may be accurate in the keV range, depending on the element involved. It was derived on the basis of the Thomas-Fermi atom and as such exhibits none of the structure which is found experimentally as the so called 'Z_1 oscillations'. This refers to the periodicity found in the electronic stopping cross section at a given ion velocity as the atomic number of the projectile (Z_1) is varied. These oscillations are known to be associated with the atomic shell structure and have been calculated theoretically by Cheshire *et. al.* <49> who used Hartree-Fock central fields to calculate the stopping cross sections rather than those derived from the Thomas-Fermi atom. If a particular projectile-target combination falls on a peak or trough of the Z_1 oscillations then the simple expression eqn.(2.17) may be significantly in error. In fig. 2.4 we present a comparison of these simple stopping powers with the more accurate ZBL electronic stopping powers, discussed in chapter 4, for the elements comprising sapphire. The simple Lindhard formula is within 20% or so of the ZBL value below 1 MeV. However for iron, fig. 2.5, differences of over 30% are apparent throughout the whole keV range. We shall see in the next section that this energy range is particularly



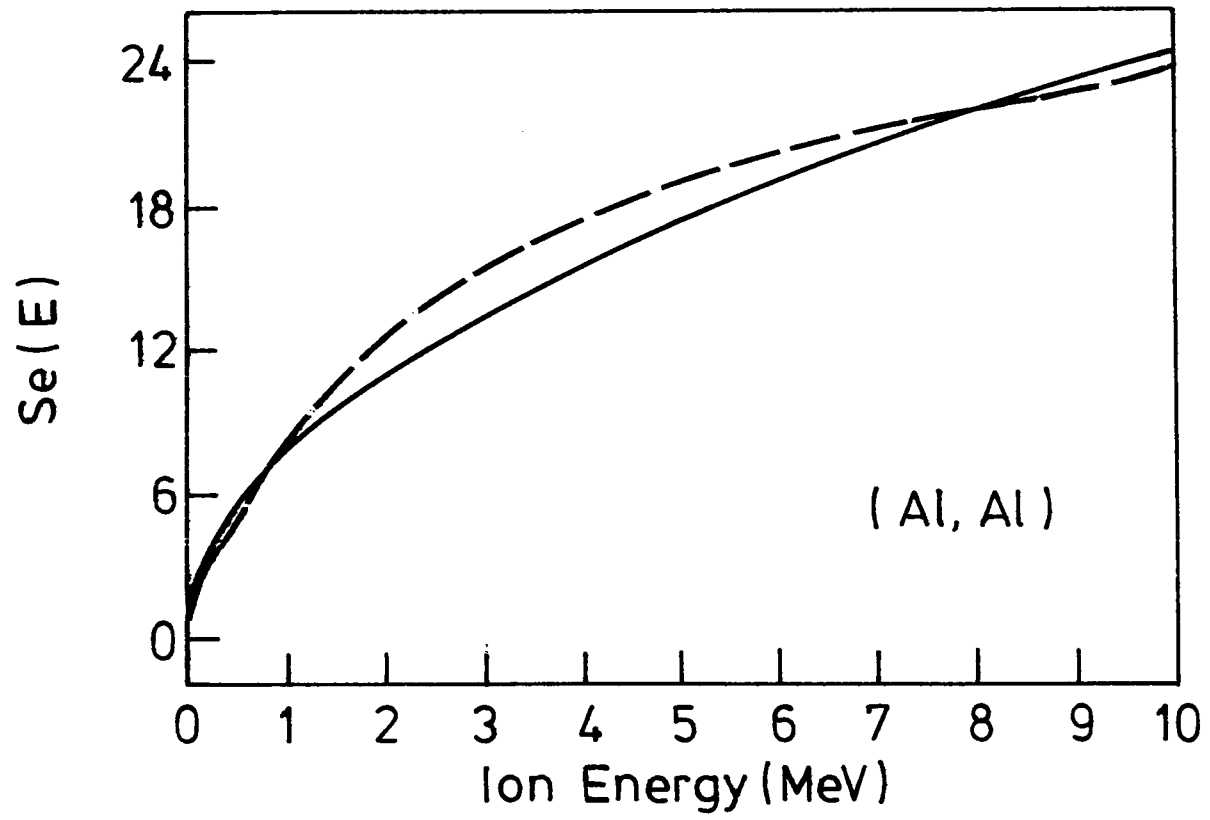
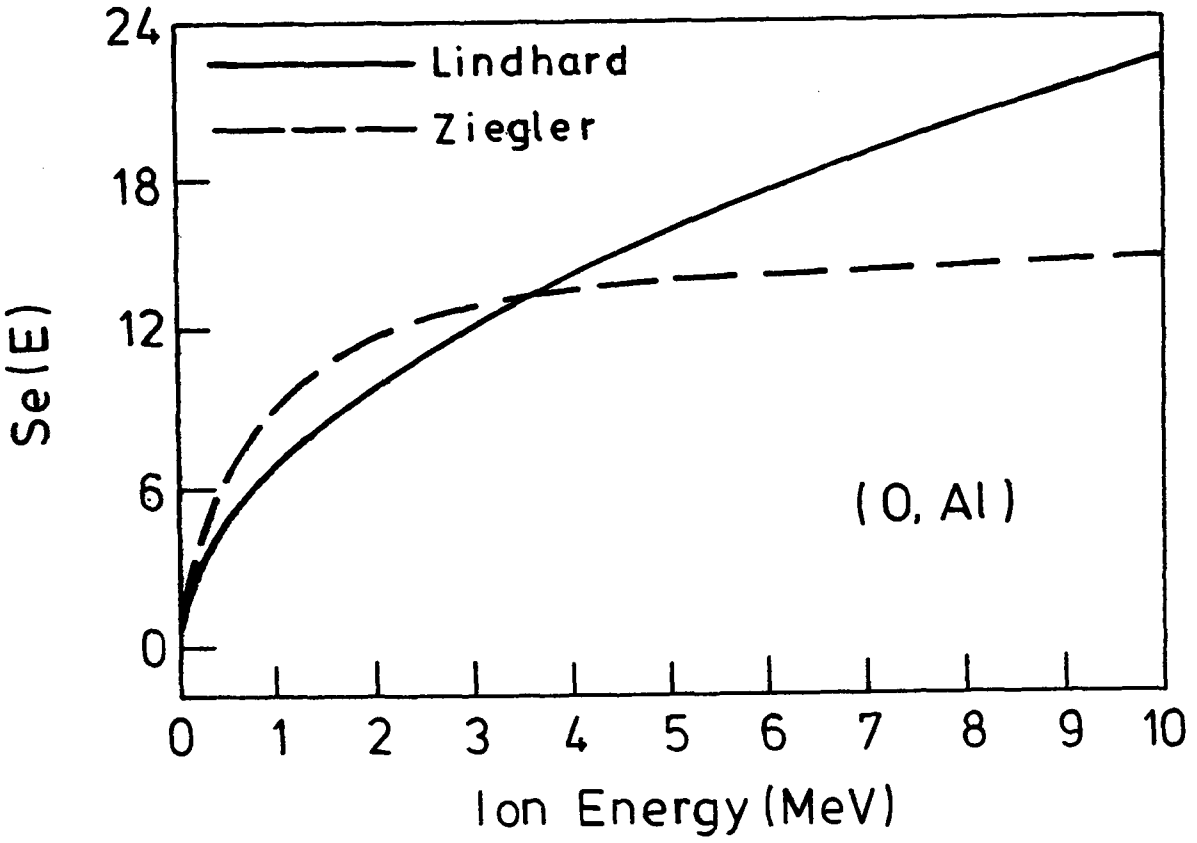


FIG. 2·4a

COMPARISON OF ZIEGLER AND LINDHARD ELECTRONIC STOPPING POWERS IN SAPPHIRE (PROJECTILE, TARGET) Se(E) UNITS ARE ARBITRARY



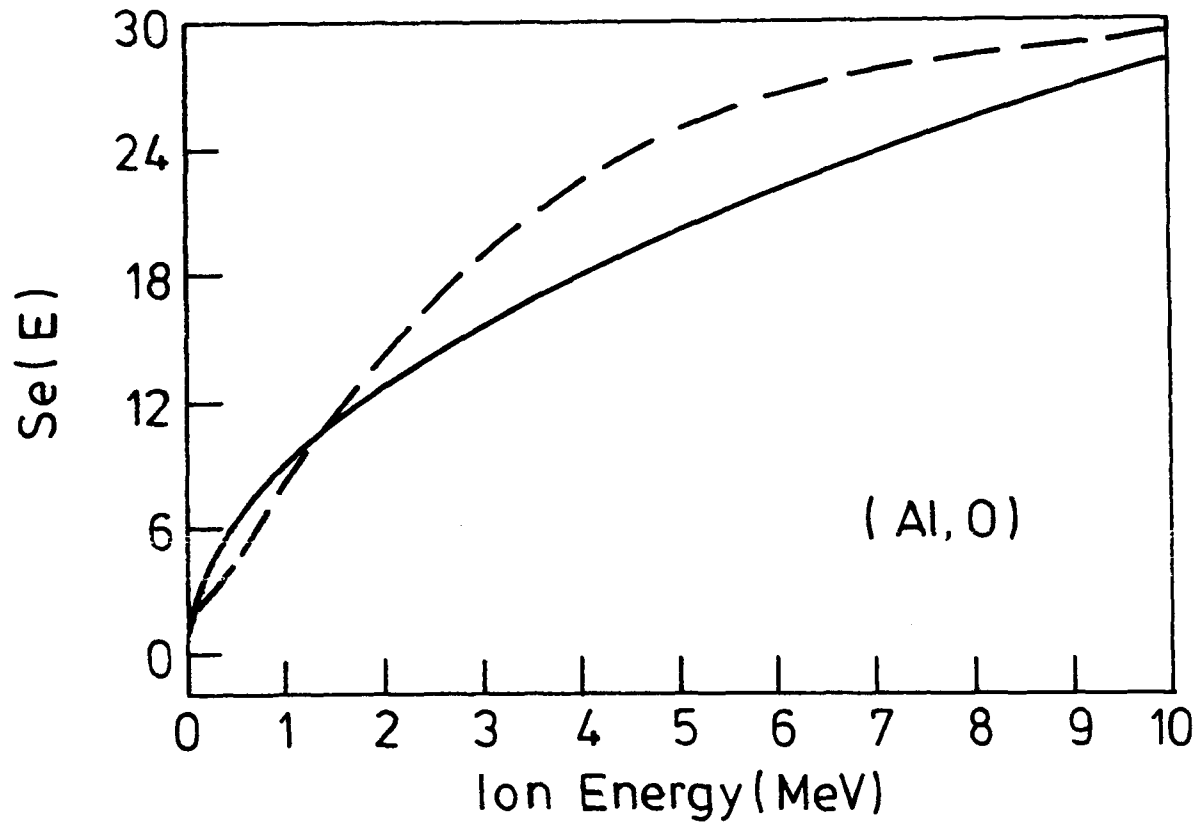


FIG. 2·4b

COMPARISON OF ZIEGLER AND LINDHARD ELECTRONIC STOPPING POWERS IN SAPPHIRE (PROJECTILE, TARGET) Se(E) UNITS ARE ARBITRARY

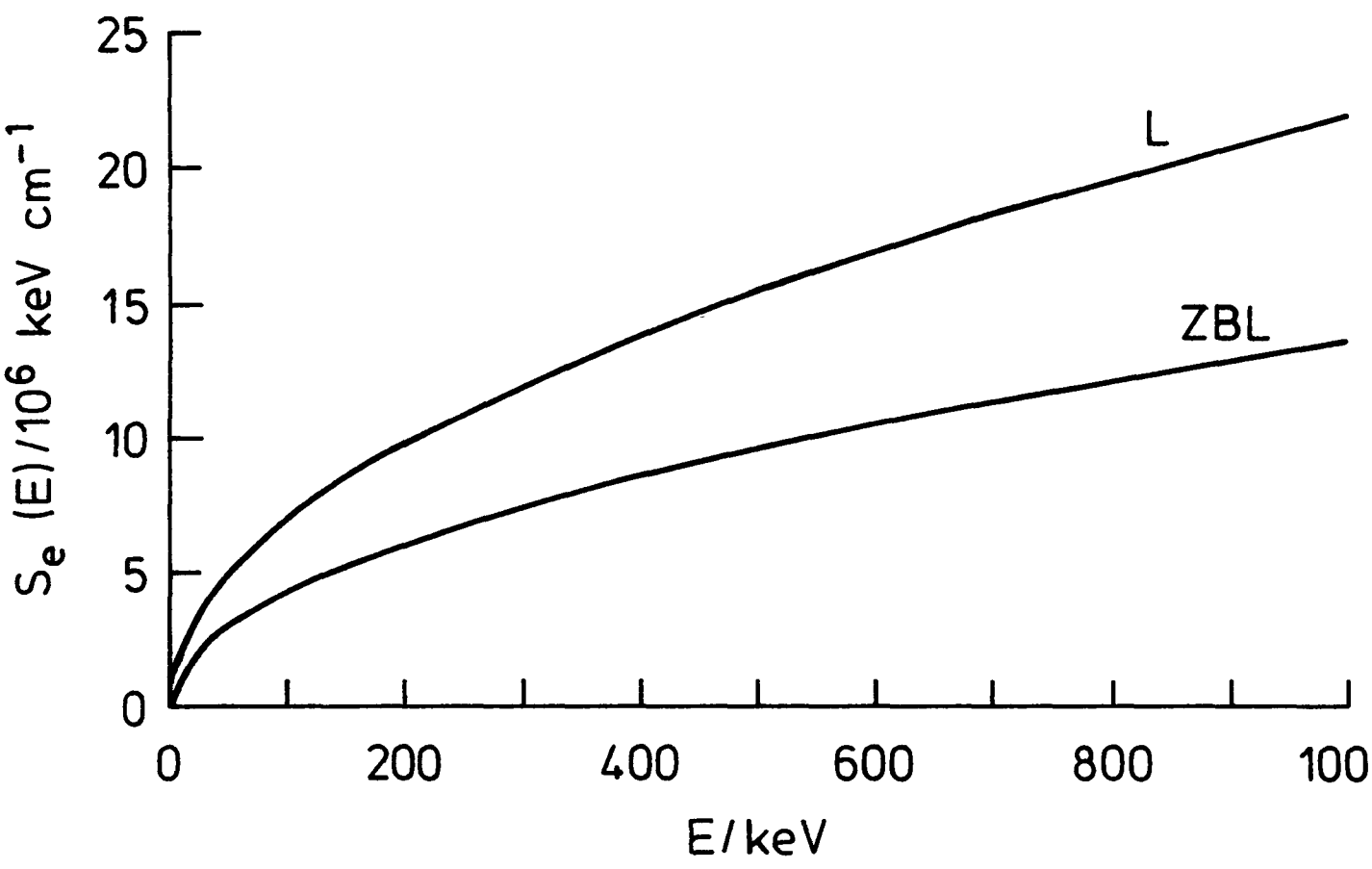


FIG. 2·5

COMPARISON OF ZBL AND LINDHARD STOPPING POWERS IN Fe

important in determining the total cross section for atomic displacements and as such it is important to use an accurate electronic stopping power in this region.

This concludes our brief review of the manner in which an energetic projectile will lose energy as it traverses a solid. The connection of these mechanisms with the production of point defects is made by assuming that if a nuclear collision is sufficiently energetic then the target atom will be expelled from its lattice site and may have sufficient energy to displace further target atoms. The cross section for the production of these primary knock-on atoms, or pka's, is found in a straightforward manner from the differential energy transfer cross section:

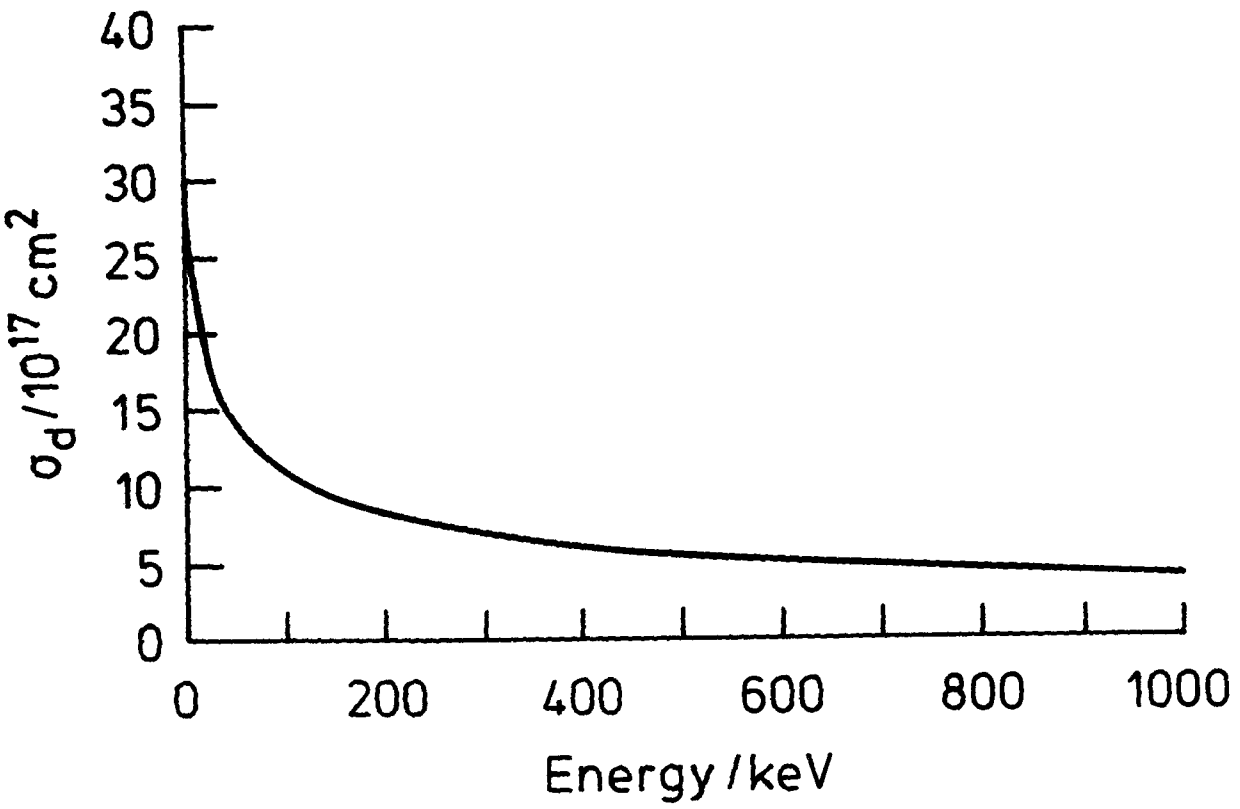
$$\sigma_d(E) = \int_{E_d}^{T_m} \frac{d\sigma(E;T)}{dT}\, dT \quad . \tag{2.18}$$

We now turn our attention to the events which follow the displacement of a pka from its lattice site by the energetic incoming ion and consider its subsequent interactions with other target atoms.

§ 2.2 Simple Cascade Theory.

In considering the interactions of the pka with other target atoms we shall, in this section, consider those interactions to be a sequence of uncorrelated binary collisions where the point defects produced are stable and do not interact with each other. This 'simple cascade theory' will serve as a starting point for more realistic models which will be discussed later.

An energetic pka, behaving like any energetic incident ion, will traverse the target causing electronic excitation and will collide with other target atoms, sharing its energy with them according to the cross sections involved. Let us calculate how the cross section for displacing other target atoms varies with the energy of this pka. In fig. 2.6 we have plotted the cross section for primary atom displacements, σ_d, as a function of pka energy for iron. We see that



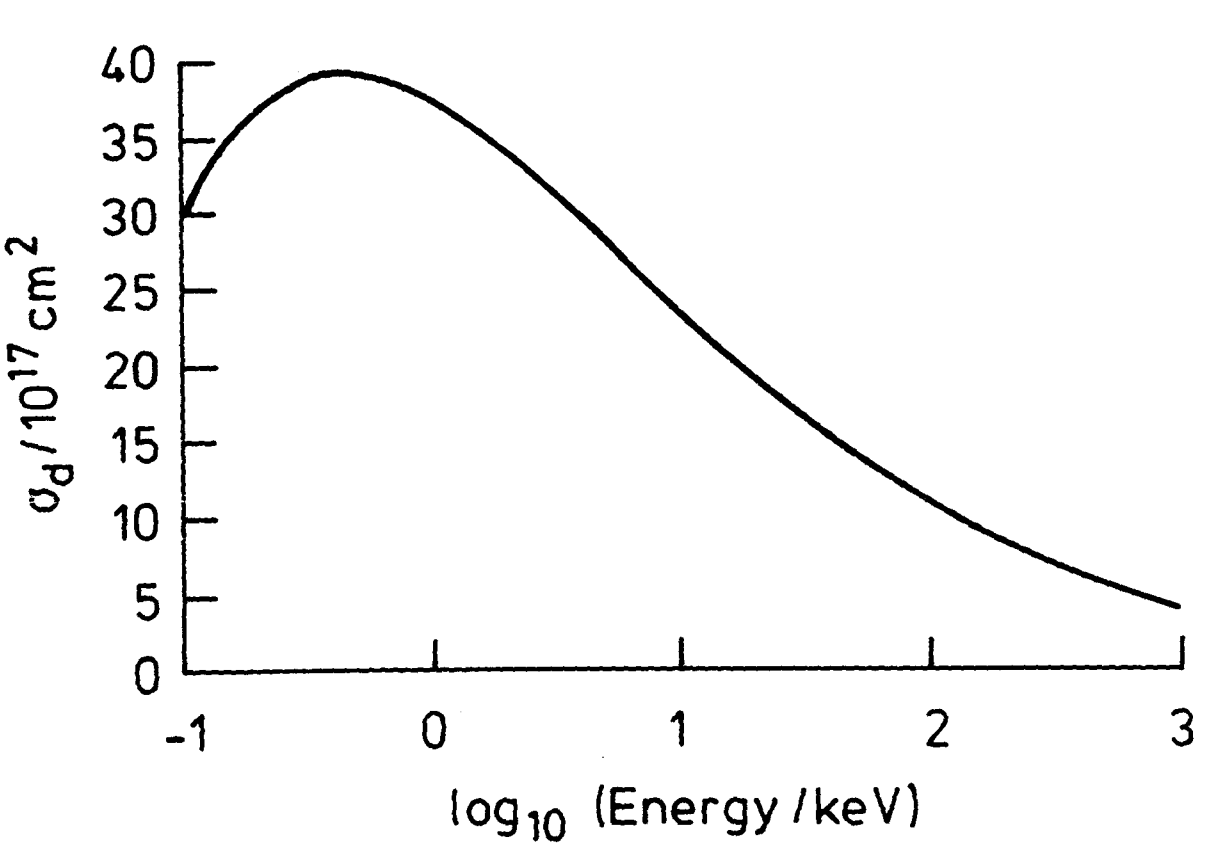


FIG. 2·6

PRIMARY DISPLACEMENT CROSS SECTION FOR Fe SELF-ION IRRADIATION SHOWN WITH LINEAR AND LOGARITHMIC ENERGY SCALES

the cross section begins to rise sharply as the pka energy falls below a certain value (which will depend on the target). As the pka reaches this threshold value it will begin to lose more and more energy, on average, in each collision with a target atom as a consequence of the larger cross section for energy transfer. In doing so it will 'move up' the curve to higher displacement cross sections in a self-reinforcing manner. What is more, the other knock-on atoms produced will also have energies in this part of the σ_d curve and have correspondingly high cross sections for displacing subsequent generations of knock-ons. In this manner a *displacement cascade* is formed whereby the knock-on atoms are produced with increasingly higher cross sections for producing further knock-ons in a cascading process. In this case the mean free path for a moving atom to transfer an energy greater than the displacement threshold to other target atoms may reduce to the order of the interatomic spacing and create a highly excited region in the solid.

A matter of primary interest is how to determine the total number of displaced atoms in the cascade. Several solutions to this problem have been proposed, differing in small details of the displacement process, but the most widely used model is associated with the names of Kinchin and Pease <20>. These authors defined a displacement threshold energy, E_d, as the minimum kinetic energy that must be transferred to a target atom before it is permanently displaced from its lattice site. Although the binding energy of the atom is neglected, the possibility of *replacement* collisions is recognised, whereby the projectile may remain trapped at the lattice site if it is left with kinetic energy less than E_d after the collision. The energy loss to electronic excitation is treated in a rather crude manner in that it is entirely neglected below a certain value of pka kinetic energy which is roughly given by the pka mass number in keV. Above this energy the opposite extreme is taken and *all* of the pka energy is assumed to be deposited in the target electronic system. To obtain an expression for the mean number of displacements, $\overline{N}_d$, produced in the cascade the following simplified argument is used: since $\overline{N}_d(E)$ is a unique function of the pka energy, E, after the first collision of the pka with another target atom in which an energy T is transferred the total potential for creating further displacements can not have been diminished and we may write the following balance equation for the total number of displacements which will ultimately be produced

$$\overline{N}_d(E) = \overline{N}_d(T) + \overline{N}_d(E-T) \quad , \tag{2.19}$$

where the first term on the right hand side is associated with the secondary knock-on and the second term with the primary knock-on. By inspection this equation is easily seen to have a simple linear solution

$$\overline{N}_d(E) = Constant \times E \quad . \tag{2.20}$$

The constant must be determined by a boundary condition which fixes $\overline{N}_d(E)$ at low energies and depends on the scattering cross section near threshold. This can be seen as follows: if a pka has energy just greater than $2E_d$ then energetically it is clearly possible for it to produce two further displacements (although the pka itself will become trapped). Alternatively it is also possible that the pka will dissipate all of its energy in sub-threshold collisions, so that no further displacements are produced. The relative probability of these two extreme cases will depend on the cross section for differential energy transfer near E_d. Kinchin and Pease <20> assumed that at these low energies the scattering is isotropic and all energy transfers are equally likely up to the maximum, so that the differential cross section for energy transfer is a constant. In this case the boundary condition is easily determined by

$$\overline{N}_d(2E_d) = Const \times 2E_d = 1 \quad . \tag{2.21}$$

Thus we arrive at the Kinchin-Pease formula

$$\overline{N}_d(E) = \frac{E}{2E_d} \quad . \tag{2.22}$$

Let us examine the assumptions and approximations which have led to this expression. Perhaps the most important aspect we have neglected is the inelastic energy loss to electrons of the moving atoms. As noted above, in the original Kinchin-Pease model this was accounted for by defining a threshold energy, above which *all* of the pka energy was dissipated inelastically and below which these losses were ignored. This proves to be a rather poor approximation, especially for low Z solids, and a significant improvement was made by Robinson <21> who used the Lindhard energy partitioning theory of the displacement cascade (which we shall discuss in detail in chapter 4 in connection with diatomic solids) to account for this energy dissipation. This model makes no such threshold assumptions but

allows inelastic losses at all energies and relates them to the electronic stopping power. The resulting energy corrected for the inelastic losses is referred to as the *damage* energy, E_{dam}, and Robinson provided analytic expressions of Lindhard's original graphical data to provide a method for calculating E_{dam} in elemental solids.

The next most important approximation is that of isotropic scattering at low energies, since this determines the value of the constant in eqn. (2.21). Sigmund <22> has investigated how this constant varies with different values of power law exponent m and finds that the number of point defects is better described by

$$\overline{N}_d(E) = \zeta(m) \frac{E}{2E_d} \quad , \tag{2.23}$$

where

$$\zeta(m) = \frac{2-2^{m+1}}{\phi(1-m)-\phi(1)} \quad . \tag{2.24}$$

Here $\phi(x)$ is the digamma function <3>. Williams <23> has given the values of $\zeta(m)$ for various m and these are reproduced in table 2.1. The hard sphere result corresponds to $m=-1$ and gives $\zeta(1)=1$ whilst for more realistic scattering cross sections, which favour smaller energy transfers, the value of ζ is less than unity. Sigmund suggests that in view of the steepness of the interaction potential at low energies, m will be only slightly greater than zero here. To be definite he does in fact choose $m=0$, giving $\zeta(0)=12\ln 2/\pi^2$ and thus

$$\overline{N}_d(E) = 0.84 \frac{E}{2E_d} \quad . \tag{2.25}$$

§ 2.3 The 'NRT' Standard.

In 1975 an international standard was proposed for calculating the number of atomic displacements produced in a displacement cascade. The 'NRT' standard <24> (after Norgett, Robinson and Torrens) was directed toward the nuclear industry and as such was primarily concerned with displacement rates in elemental metals and fission reactor alloys. The

m	$\zeta(m)$
–1	1
–1/2	0.954
0	0.842
1/4	0.744
1/2	0.598

Table 2.1. Variation of the coefficient $\zeta(m)$ in the defect production equation (2.23), with the power law exponent m.

formulae proposed by these authors incorporated the two important corrections discussed above to the simple Kinchin-Pease formula, i.e. the Lindhard partitioning theory was used to account for electronic energy losses and the correction for a more realistic scattering cross section was included. The 'modified Kinchin-Pease' formulae given were

$$\overline{N}_d(E) = 0.8\,\frac{E_{dam}}{2E_d}\ ,$$

$$E_{dam} = L(\varepsilon)E\ ,$$

$$\varepsilon = \alpha E\ ,$$

$$\alpha = a\,\frac{A_2}{Z_1 Z_2 e^2 (A_1 + A_2)}\ ,$$

$$a = \frac{0.8853\,a_0}{(Z_1^{2/3} + Z_2^{2/3})^{1/2}}\ ,$$

$$L(\varepsilon) = \frac{1}{1+\kappa_l g(\varepsilon)}\ ,$$

$$g(\varepsilon) = 3.4008\varepsilon^{1/6} + 0.40244\varepsilon^{3/4} + \varepsilon$$

$$\text{and} \qquad \kappa_l = 0.1337\,Z_1^{1/6}\,(Z_1/A_1)^{1/2}\ , \tag{2.26}$$

where A_1 and Z_1 are the atomic mass and number of the moving particle and A_2 and Z_2 are like quantities for the matrix atoms. One immediate criticism of these formulae is that by involving both A_1 and A_2 the authors imply their validity for the case of the incident atom differing from the matrix atom. They do qualify this by stating that the Lindhard formulation of these equations strictly only applies to monatomic systems but that no serious error is encountered providing the ratio Z_1/Z_2 does not differ too much from unity. In fact the Lindhard theory need not be restricted in this way and a much more satisfactory standard would have simply given the full expression for κ_l, the coefficient of the electronic stopping cross section, as Doran <25> has done:

$$\kappa_l = \frac{0.0793\,Z_1^{2/3}\,Z_2^{1/2}\,(A_1+A_2)^{3/2}}{\left(Z_1^{2/3}+Z_2^{2/3}\right)^{3/4} A_1^{3/2}\,A_2^{1/2}}\ . \tag{2.27}$$

§ 2.4 Failure of the 'NRT' Damage Function in Cascades.

Although it represents a significant quantitative improvement over the original Kinchin-Pease formula, it is found experimentally that the 'NRT' damage function described in the previous section still significantly over-estimates damage production in cascades. Fig. 2.7 shows some data obtained by Kinney *et. al.* <26> relating to point defect production in copper at low temperatures, which can be monitored via residual resistivity measurements. For electron irradiation only isolated Frenkel pairs are, in general, produced and in this case the 'NRT' damage function gives reliable estimates of point defect production. However as the energy of the pka increases, as is the case when the mass of the irradiating particle is increased, the 'NRT' damage function gives an estimate which is up to a factor of five or so too high. A similar conclusion was reached by Rehn *et. al.* <27> who monitored the degree of radiation-induced segregation in a Ni-12.7 at. % Si alloy during irradiation at temperatures from 350 to 650°C with several different ions. From these measurements they were able to infer the relative efficiency for the production of freely migrating defects by each ion and found a strong decrease in efficiency with increasing ion mass. In particular, irradiations producing average pka energies of 1.8, 2.7, 51 and 74 keV were found to be only 48%, 37%, 8% and <2% as efficient, respectively, as an irradiation with a weighted average recoil energy of 730 eV. Numerous other workers (*e.g.* <28,29,30>) have found this same qualitative behaviour in different metals.

Where has the simple cascade theory given above failed? Norgett *et. al.* <24> state that their formulae were chosen to give close accord with computer simulations of radiation damage performed at that time, *e.g.* <31>, rather than with experimental estimates of point defect production. Two areas in which the formulae could be significantly improved in their relation to experimentally observed values were recognised:

(i) the energy partitioning calculations could be extended to include experimentally determined stopping power data

(ii) point defect interactions in the cascade could be included to account for recombination processes which would reduce the point defect yield.

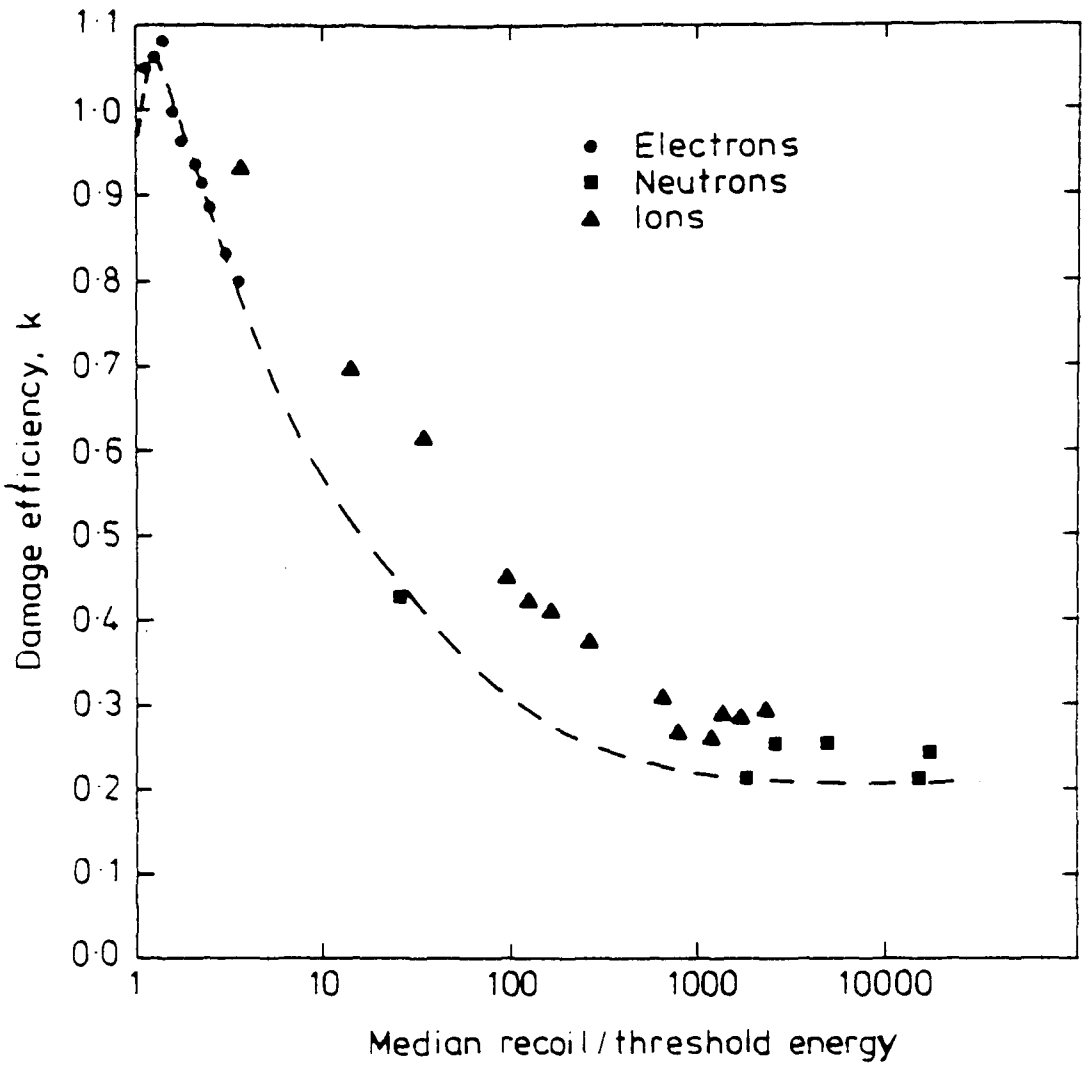


Fig. 2.7. Variation of damage efficiency with median recoil energy in copper. Ref. <26>.

The first of these points is relatively straightforward and only requires finding new solutions of the Lindhard equations, discussed in chapter 4, with the improved stopping cross sections included. But we shall see there that even when much improved values for the degree of energy partitioning are included, the decrease in the efficiency of damage production with increasing pka energy remains. In fact the second point is now known to be the source of the discrepancy. The simple cascade theory we have considered in this section has taken no account of the interactions amongst point defects in the cascade which would considerably modify their fate. We must then turn our attention to these interactions in an attempt to explain the large over-estimates given by the two-body theory.

§ 2.5 Many-Body Interactions in the Cascade.

As we have seen above, an energetic ion will be brought to rest in a solid by giving up its energy to both the target electrons and ion cores, with electronic excitation dominating for high projectile velocities and energy transfers to the ion cores becoming increasingly important as the projectile slows down. A point will eventually be reached where the mean free path for producing atomic displacements reduces to the order of the lattice constant and in this region (the collision cascade) many atoms will simultaneously be displaced and in motion. In discussing the evolution of a cascade it is possible to identify three separate stages which are characterised by both the time scales and energy transfers involved. The first stage is usually referred to as the 'displacement phase', where energy transfers are $\gtrsim E_d$ and the duration is up to the first few tenths of picoseconds (depending on the original pka energy) following the primary displacement. This is the period in which the energy of the pka proceeds to drop to values of the order of E_d and the number of displaced atoms reaches a maximum. Then follows the 'relaxation phase' during which many energy transfers of the order of some tenths of E_d take place and the lattice is in a state of constant rearrangement. Finally one usually recognises a cooling phase which begins some ten or so picoseconds after the primary event and where the cascade is in local thermal equilibrium and loses its excess kinetic energy to the surrounding lattice via *normal* thermal conduction processes. Theoretical descriptions of the first two phases are difficult due to the many body

interactions taking place. Processes involving many particle interactions are inherently difficult to describe dynamically. An analogy with the problems faced by the atomic physicist is useful. Here, an analytic solution of the Schrodinger equation for a multi-electron atom is impossible and approximate methods must be used. Two approaches to this problem have been traditionally adopted. The first, exemplified by the Hartree method, is to turn a multi-electron problem into a *one* electron problem, by focussing attention on a single electron and calculating the mean field it experiences due to all the other electrons. The motion of this electron can then be determined and the same process is then applied to all the other electrons. Iteration of this procedure to a point of self-consistency produces a solution. This method clearly becomes increasingly cumbersome for high Z atoms with large numbers of electrons. The other approach, whose usefulness actually improves with increasing numbers of electrons, is the Thomas-Fermi statistical model of the atom where one *exploits* the fact that one is dealing with a large number of particles and hence can apply statistical methods. In the problem of a displacement cascade we are perhaps dealing with hundreds or thousands of displaced atoms. With the rapid advances seen in modern computer power it is now possible to realistically simulate energetic collision cascades involving many thousands of atoms. However early workers in the field did not have this advantage and devoted most of their efforts to developing statistical ideas. This was the approach first taken by Brinkman <32,33> in his discussion of the displacement phase or displacement *spike*.

Displacement Phase. Originally considering cascades in metals, Brinkman estimated that the mean spacing of secondary displacements in copper would drop to the order of the lattice constant when the energy of the pka fell in the range 50 to 23,000 eV. He further estimated that some 10^4 atoms in a cylindrical region would be brought rather violently to the molten state and that considerable mass transport would take place. The resulting qualitative picture that emerged from this model was of a cascade region consisting of a vacancy rich central core surrounded by an outer shell rich in interstitial atoms. The 'depleted zones' which result from this mechanism have been observed directly in the field ion microscope <34> and the model is generally regarded as being valid for intermediate to large Z elements. An important feature of the displacement spike is that it clearly allows the possibility of

considerable atomic rearrangement and diffusion. One manifestation of this atomic motion on a macroscopic scale is the phenomenon of 'radiation enhanced adhesion'. In an attempt to promote the adhesion of a given material to a substrate, the coating is deposited on the substrate and then irradiated with ions of sufficient energy such that the coating is penetrated and the end of the ion's track (and hence its associated collision cascade) falls at the interface of the two materials. The ensuing displacement spike at this interface will result in such a degree of mixing of the two materials that a boundary layer is formed which binds the two materials together.

Despite the useful qualitative picture that has emerged from the displacement spike model the quantitative estimate of defect production during the collisional phase still presents problems. The binary collision approximation we have used in the treatment of defect production presented earlier clearly breaks down in a dense collision cascade and we find non-linear effects in that we can no longer expect the number of defects produced to be proportional to the energy deposited into nuclear collisions. Some aspects of non-linear cascade theory have recently been considered by Shulga *et. al.* <35>. When a heavy ion strikes a lighter target atom the ion may transfer a substantial fraction of its energy and it is quite possible that the recoiling atom has a greater speed than the final, or even the initial, projectile speed. The target atom is then able to 'run ahead' of the projectile and in scattering other target atoms will clear a path for the ion. This 'clearing-the-way' mechanism is also able to operate in the opposite way and enhance the target atomic density seen by the initial projectile. The effect is demonstrated in fig. 2.8 where the primary recoil atom, labelled 2, is scattered by the projectile and in turn scatters atoms 3 and 4 out of the projectile path. Unlike the case of light projectiles, the projectile itself need not be leading the disturbance at any point of the trajectory and so the frequency distribution of scattering processes undergone by the projectile is affected by earlier collision events. The net effect then will not be just a linear superposition of the individual binary collision events and Shulga *et. al.* refer to this as a non-linear process. These authors conducted a molecular dynamics (MD) simulation of the scattering of a 5 keV xenon ion by a copper dimer in an attempt to model this phenomenon. Despite the small number of particles involved in the simulation they found that the scattering of the projectile was indeed influenced by the Cu-Cu interaction. For dimer targets

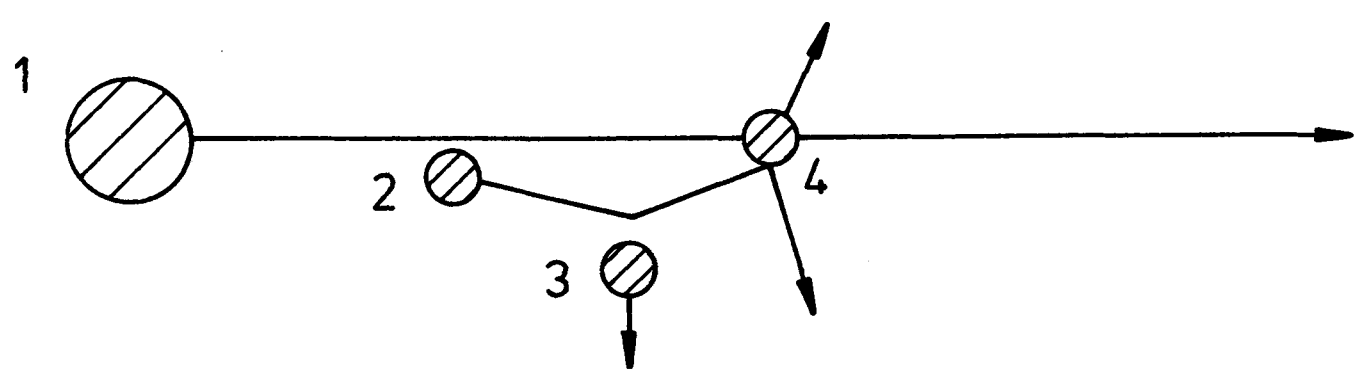


FIG. 2·8

TARGET ATOMS RECOILING FROM COLLISIONS WITH HEAVY PENETRATING ION 1 MAY CHANGE THE STRUCTURE AND STATE OF MOTION OF THE MEDIUM IN FRONT OF THE ION. FROM REF. 4. ⟨35⟩

the most pronounced feature was a wider range of impact parameters where collisions are effectively binary than one would expect from the linear superposition of two binary events. Both 'clearing-the way' and blocking mechanisms were observed in the simulations although for three-dimensional motion the former was found to dominate.

This phenomenon is not expected to have a large effect on the nuclear stopping power since it is significant only for small impact parameter collisions, whereas the nuclear stopping power is not particularly sensitive to these. The effect on point defect production is difficult to estimate without specific simulations of this phenomenon in solids, however this would be rather more sensitive to the frequency of small impact parameter collisions since these are generally the collisions which result in displacements. If one considers the collision cascade to be initiated by the pka, then since this particle has the same mass as the subsequent target particles, any further recoils cannot have a velocity greater than that of the incident pka and so the effect of this particular form of non-linearity is not likely to be significant within the cascade. A more pronounced effect could however be observed in the *production* of the pka's by more massive projectiles. Large angle scattering events with target nuclei would perhaps occur less frequently and this would manifest itself as a drop in pka production. It is clear that further atomistic simulations with a sufficiently large number of particles are necessary before one can make more detailed estimates of the consequences of this phenomenon for point defect production. Experiments sensitive only to the net number of defects would be unable to differentiate between a reduction in the number of pka's and a reduction of defect production within the cascade, but combined with techniques such as transmission electron microscopy (TEM), which are capable of probing the number of pka's produced, one may be able to observe manifestations of this phenomenon experimentally.

Relaxation Phase. We now turn our attention to the relaxation phase of the cascade which follows the displacement spike. Here the particle kinetic energies are typically about 1 eV or so and the character of the interactions is somewhere in between particle dynamics and thermodynamics. In this phase of the cascade we have a situation which is somewhat analogous to the liquid state. Theories of liquids are much less well developed than either

theories of solids or gases. In the gaseous state the energy of the particle is mostly kinetic and to a good approximation one can ignore the potential energy, as is done in the model of a perfect gas. One also exploits the random nature of the processes involved and, via the principle of equal a priori probabilities, asserts that *all* configurations of the system are equally likely to occur. In the solid state the potential energy dominates and in a low order approximation one can neglect the kinetic energy. The other great simplifying factor in crystalline solids is of course the translational symmetry which extends throughout the whole crystal. Since in the liquid state one has a situation where the kinetic and potential energies are approximately equal, one cannot neglect either and the translational symmetry is limited to short ranges. This is similar to the environment found in an energetic collision cascade where the kinetic energy of the atoms is greatly enhanced over those normally found in solids and comparable to the potential energy. The motion of the atoms also destroys the local translational symmetry and this is exhibited rather well in plots of the radial distribution function (RDF) taken during molecular dynamics simulations of cascades in copper. De la Rubia *et. al.* <36> have performed such simulations and find that the RDF during the relaxation phase is very similar to that of liquid copper. The RDF obtained by these authors is reproduced in fig. 2.9.

Clearly, an analytic description of this highly excited, liquid-like phase in terms of particle dynamics is very difficult. However a crude thermodynamic description is comparatively straightforward. Not surprisingly, the latter approach has been exploited by many authors. The concept of a 'thermal spike' following the displacement spike was originally introduced by Seitz and Koehler <37> in 1956 and has since been the subject of much discussion, even controversy. These authors recognised that as the moving atoms in a cascade slow down, a point is reached where they no longer have sufficient energy to cause further displacements but will dissipate their remaining kinetic energy in sub-threshold collisions with target atoms. The energy transferred in these collisions will, in general, be large in comparison to the normal vibrational energies of the surrounding lattice and the initial distribution will be random. But after a time of the order of half a picosecond or so it is expected that an approximate equipartition of this energy will be achieved and so one can associate a temperature with the region. The problem can then be analysed as if the lattice has suddenly

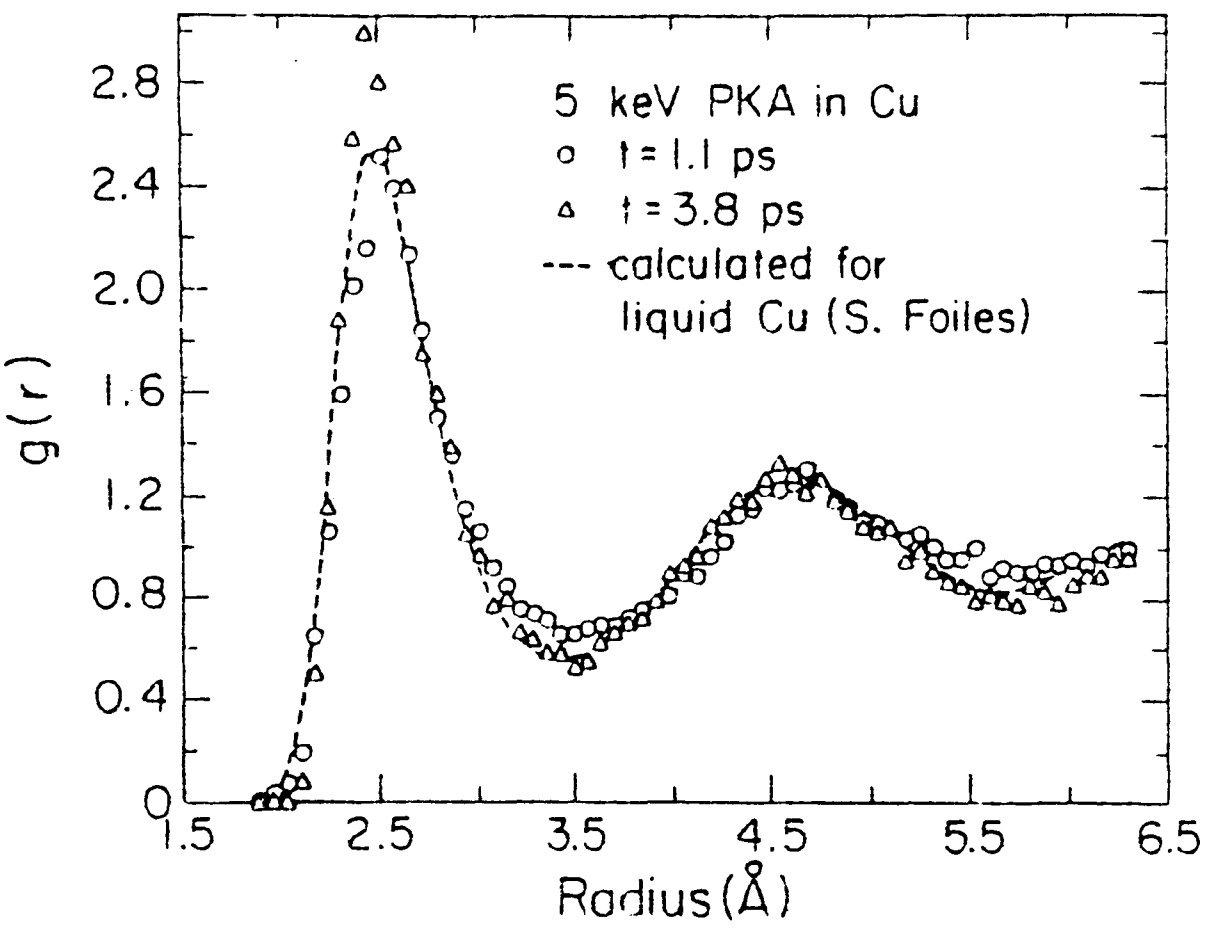


Fig. 2.9. Comparison of radial distribution function of liquid copper with that of a 5 keV cascade. Ref. <36>.

been heated to a high temperature in a restricted region and simple thermodynamic arguments applied to predict the transport of mass and energy within the cascade region. The usual approach in applying the thermal spike model has been to select a specific geometry appropriate to the problem (usually spherical or cylindrical) and solve the non-linear heat conduction equation:

$$\frac{\partial T}{\partial t} = \nabla \kappa \cdot \nabla T \quad , \tag{2.28}$$

where κ is the thermal diffusivity. A significant problem here is in selecting a value for κ. In most metals the normal thermal conductivity is dominated by electronic conduction, but in the aftermath of a displacement spike the cascade kinetic energy is associated with only the ion cores. Furthermore, the cascade dimension is typically less than or of the order of the electron-phonon mean free path at room temperature and so the electrons may not 'see' the thermal spike until it has spread out into the surrounding lattice. The appropriate thermal conductivity will clearly not then be the bulk value. However by using only the lattice conductivity one will neglect *any* interaction with the target electrons. This problem has only recently been addressed and we shall return to it in chapter 8, but we note here that it has been partly responsible for the controversy surrounding the thermal spike model. Another reason for this controversy was concerned with the very applicability of equilibrium thermodynamics to the extreme conditions encountered in the cascade. This question was addressed by a number of authors using computer simulations of collision cascades. King and Benedek <38> performed a molecular dynamics simulation of a 500 eV cascade in copper at absolute zero temperature, with nearly 17,000 atoms and monitored their energy distribution as the cascade evolved. The distributions found by these authors are reproduced in fig. 2.10, where it can be seen that during most of the displacement phase the spectrum is far from the thermal equilibrium Maxwell distribution. But after about 7ps approximate equipartition of energy is achieved and the energy distribution is close to that expected for an ensemble of atoms in thermal equilibrium at 17 K. These results have been confirmed by other workers for higher energy cascades. Foreman *et. al.* <39> have simulated 1 keV

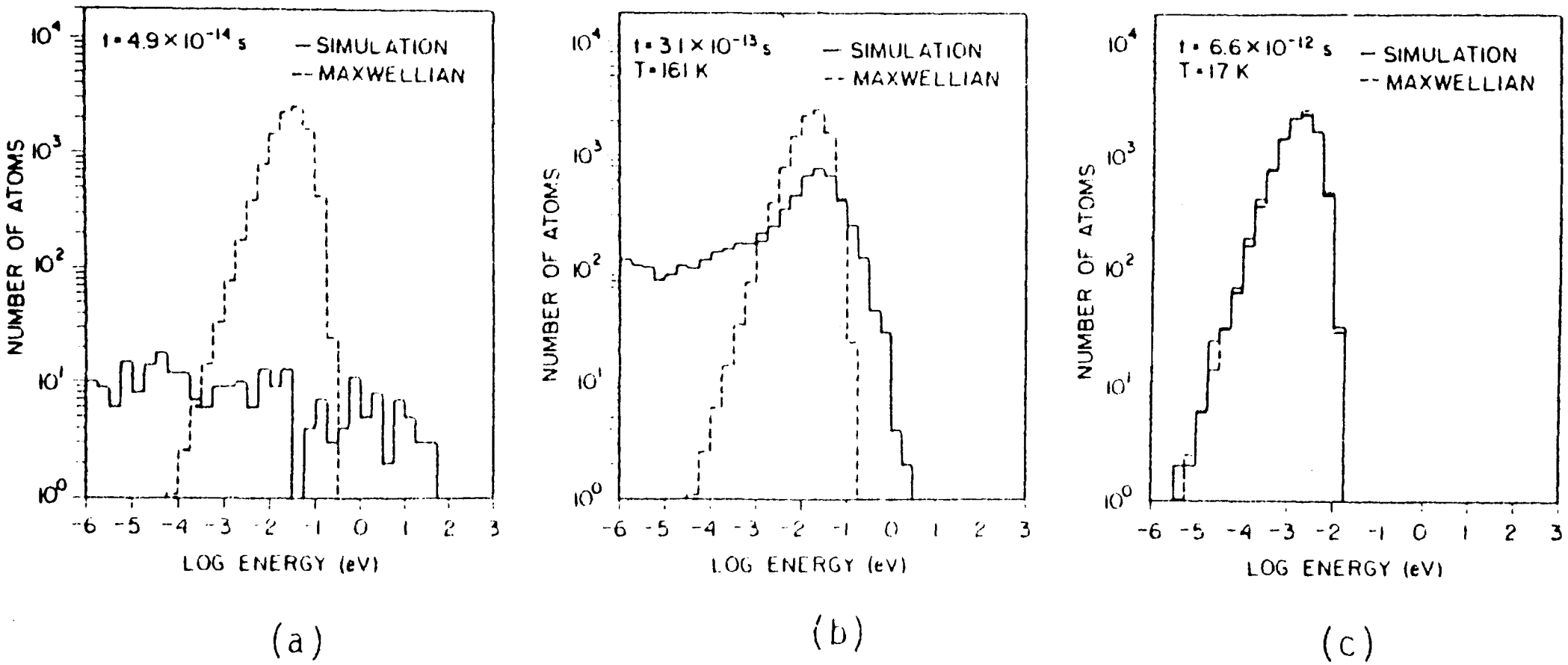


Fig. 2.10. Cascade energy distribution compared to the equilibrium Maxwell distribution. Ref. <38>.

cascades in copper and find an approximate equipartition after about 0.25ps, with this time also corresponding to maximum disorder in the cascade.

The relaxation phase has a large effect on the final number and configuration of the point defects produced during the displacement phase. King and Benedek <38> monitored the number of point defects during the evolution of their 500 eV cascade simulation and found that the number at the beginning of the relaxation phase was in close agreement with that calculated from the modified Kinchin-Pease expression, discussed in § 2.3. However as the relaxation phase progressed a large amount of Frenkel pair annihilation occurred and at the end of this phase the number of point defects fell to about 15% of this value. Foreman *et. al.*, in their MD study of cascades in copper, found that the number of point defects produced was significantly overestimated by the modified Kinchin-Pease expression for all cascades above 100 eV ! They performed over one hundred cascade simulations, with energies ranging from 60 eV to 2 keV, in order to obtain a good statistical sample and found a sharp initial drop in the displacement efficiency at around 100 eV, followed by a slowly decreasing reduction with increasing energy up to 2 keV. Their data are reproduced in fig. 2.11. This represents a much lower threshold for the breakdown of simple cascade theory than has been suspected before and these authors related this behaviour to the onset of a thermal spike regime. It is clearly of primary importance to obtain a good theoretical description of the relaxation phase of the cascade. The observation of Foreman *et. al.* that the maximum number of point defects and the achievement of thermal equilibrium coincide temporally has especially important consequences for the description of the relaxation phase since this indicates that one *is* justified in using thermal spike concepts during the period of the cascade evolution which has such a large influence on the final defect number and configuration.

Cooling Phase. Finally we come to the cooling phase of the cascade, which actually requires little comment since its description is straightforward. Around some tens of picoseconds after the primary displacement event the majority of recombination events have taken place and the energy of the cascade can be transported via normal thermal conduction processes. Sufficient lattice conduction has taken place to have increased the spatial extent of

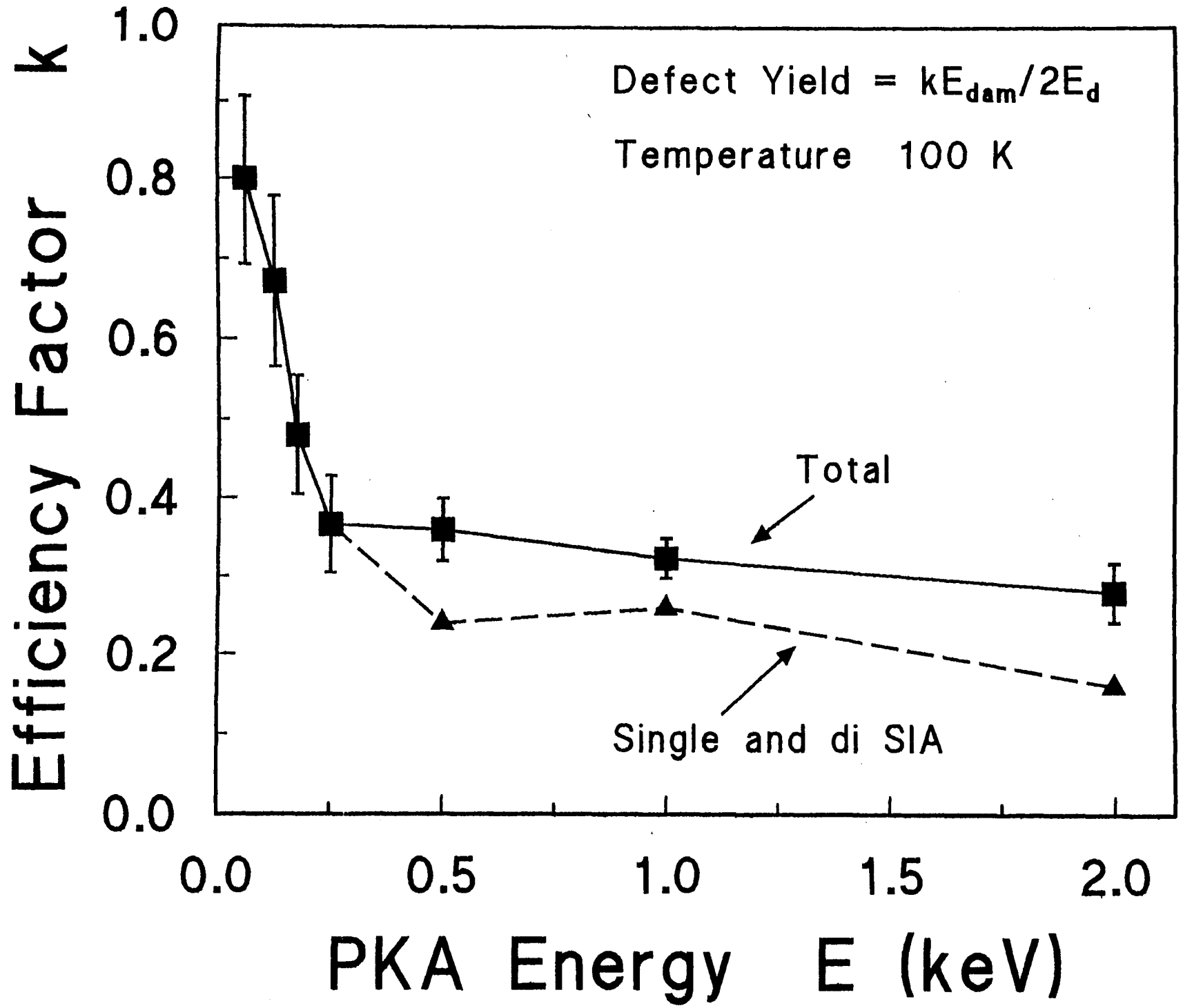


Fig. 2.11. Damage efficiency variation with pka energy in Cu, predicted by molecular dynamics simulation. Ref. <39>.

the hot region, enabling the electron gas to participate in the conduction of heat away from the excited region. Local thermal equilibrium can be assured during this phase and the mass or energy transport can be estimated using the appropriate (temperature dependent) macroscopic diffusion coefficients.

This completes our review of many body effects in the displacement cascade. We have seen that the simple cascade theory we presented earlier gives reasonable estimates of point defect production providing they are produced as isolated Frenkel pairs, but is unable to predict the net defect production in energetic displacement cascades, where many displacements are created closely together in both space and time. We shall conclude our review of standard models of point defect production by considering what new effects arise when the target atoms are arranged on a crystal lattice. We shall see that this new feature is also capable of reducing the defect yield compared to a similar amorphous target.

§ 2.6 Effects of Crystal Structure.

The cascade theories presented above all disregard the translational symmetry of the solid and treat the target as amorphous. On simple physical considerations however one would expect the crystalline nature of the target to have some influence on the nature of radiation damage processes. For example, the atomic potential well in a crystal lattice exhibits considerable anisotropy and one would expect this to be reflected in the crystallographic dependencies of E_d. Such effects are well documented, *e.g* <40>, but rather more spectacular effects of the crystal lattice are possible. In the early 1960's it became apparent that the penetration of ions into crystalline and amorphous solids showed notable differences. In the latter the distribution of implanted ions was approximately Gaussian whilst polycrystalline samples exhibited a skewness with a deeply penetrating tail. This phenomenon attracted little attention until a computer simulation of radiation damage in copper under neutron bombardment, performed by Robinson and Oen <41> in 1963, indicated some exceptionally long trajectories for pka's produced along certain crystallographic directions. The

phenomenon of *channelling* subsequently attracted a great deal of interest and was soon demonstrated experimentally by several groups <42,43,44>. The channelling process is demonstrated in fig. 2.12, which shows that if an incident ion enters a crystallographic channel it will undergo low angle scattering rather than suffer head-on collisions and in this way it can, under certain conditions, be repeatedly steered towards the middle of the channel, recoiling from one layer of atoms to the other. A channelled projectile is expected to have a reduced nuclear stopping power since it will only undergo collisions having large impact parameters. A reduction in the electronic stopping power is also to be expected since the target electronic density will be smaller in the channel and these two effects have the consequence that the projectile range will be significantly increased. An analytic theory of the channelling process was first given by Lindhard <45> who used a continuum description of the channelling planes and a screened Coulomb potential for the ion-plane interaction to derive the subsequent motion of the channelled particle as it oscillates between the planes. A comparison of the stopping powers for channelled and non-channelled copper atoms is reproduced from Nelson <46> in fig. 2.13.

As well as having consequences for projectile range distributions, the phenomenon of channelling also has important consequences for point defect production. As described above, a channelled particle is prohibited from suffering small impact parameter collisions and these are just the collisions which are likely to result in displacement events. Thus a beam of channelled particles will be much less efficient in producing point defects than a similar unchannelled beam. In investigating the production of point defects in cascades then, it is necessary to ensure that the incident particles are not directed down a crystallographic axis. Even if this is achieved though there is a likelihood of local channelling of displaced atoms within the cascade. The effect of this on point defect production in the cascade was first analysed by Oen and Robinson <47> who included a channelling dependent term in the integral equation for point defect production (see chapter 4). By assuming that the probability of a pka channelling is independent of its energy (a rather unrealistic assumption in fact), these authors were able to solve the integral equation and obtained the following expression for the number of defects produced by a pka of energy E

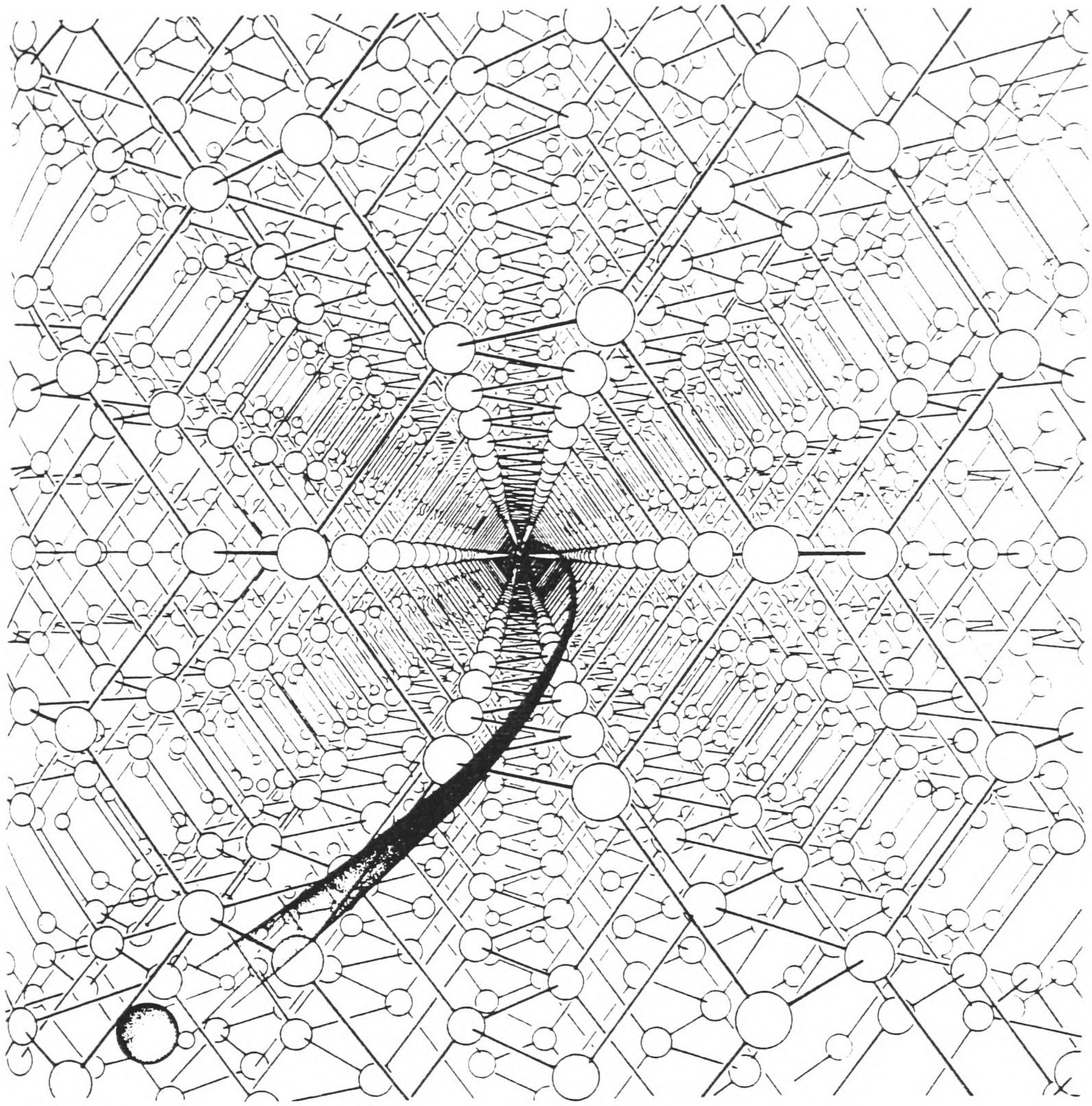
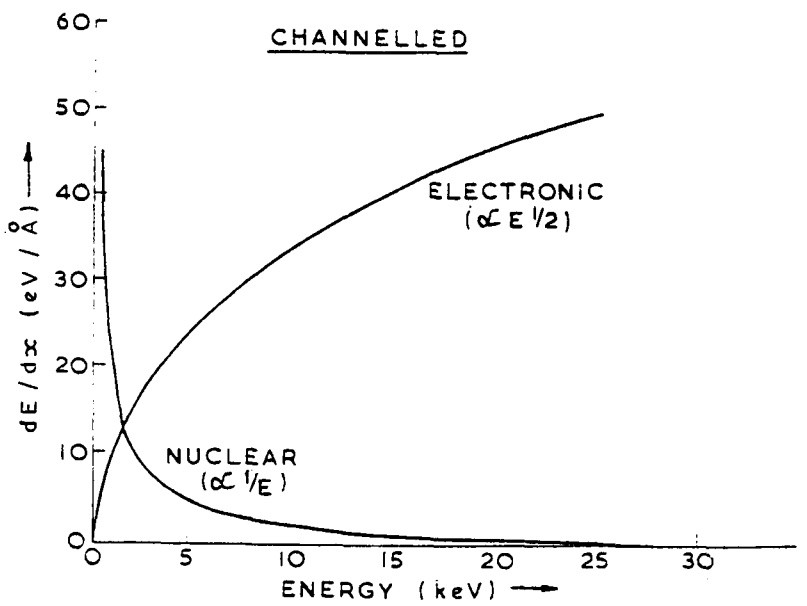


Fig. 2.12. Artists representation of the channelling process. Ref. <50>.

(a)



(b)

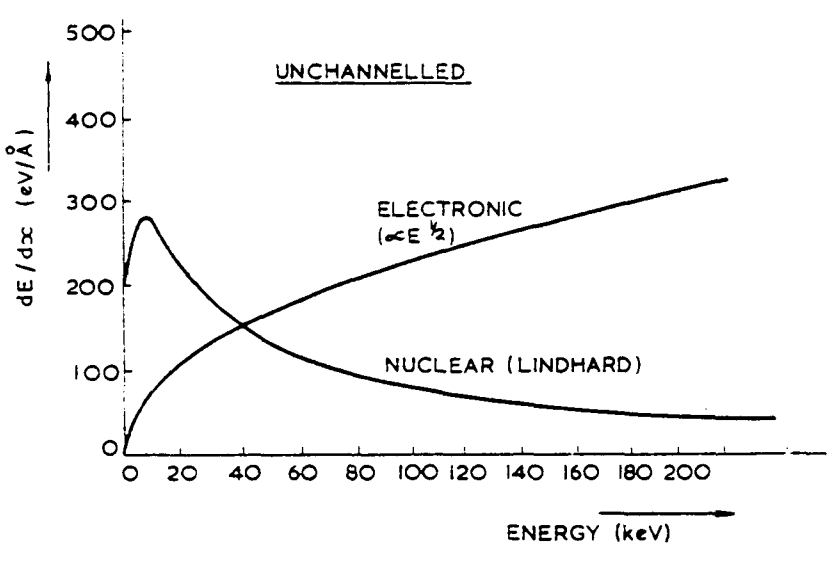


Fig. 2.13. Comparison of theoretical estimates for the channelled and unchannelled stopping powers in Cu. Ref. <46>.

$$N_d(E) = \frac{1-P}{1-2P}\left(\frac{E}{2E_d}\right)^{1-2P} - \frac{P}{1-2P} \quad , \tag{2.29}$$

where P represents the probability of the pka channelling. This equation reduces to the Kinchin-Pease result for $P=0$. The channelling of a primary beam in sapphire has been demonstrated by Naramoto *et. al.* <48>, using the technique of 'Channelling Rutherford Backscattering Spectroscopy'. In this technique a beam of particles with sufficiently low mass and sufficiently high energy to ensure purely Rutherford scattering (typically 2 MeV helium ions), are directed onto the sample and the backscattered ions detected by a solid-state radiation detector set at about 160° to the incident beam. The sample is mounted on a goniometer and the channels are located by monitoring the number of backscattered particles as the sample orientation is varied. As a channel is approached the backscattering yield decreases and reaches a minimum as the beam is directed parallel to a channel. A typical spectrum is reproduced from the data of Naramoto *et. al.* <48> in fig. 2.14. Channelling RBS is now widely used as an analytical technique to probe the crystal lattice. For example these authors were able to deduce that Cr ions implanted into sapphire occupy entirely substitutional sites on the aluminium sublattice.

One other phenomenon associated with a periodic lattice and of considerable importance in the cascade is that of *focussing*. This refers to the transfer of energy and momentum by nearly head-on collisions along a row of atoms. In elements, the next nearest neighbour atoms are identical and so the momentum transfer can be 100% efficient between successive atoms and will propagate with relatively little attenuation. If the energy transfer is greater than E_d then a 'replacement collision sequence' or RCS is possible whereby neighbouring atoms in the row move one lattice site along. The importance of such events in the cascade is two-fold. Firstly, their ability to separate the vacancy-interstitial pair by many lattice constants means that the probability of subsequent recombination is significantly reduced. Secondly, the transport of energy along the row of atoms provides a mechanism for removing energy from the cascade region and so reducing the temperature of the thermal spike. The recent work of Foreman *et. al.* <39> in performing MD simulations of cascades indicates that the first of these mechanisms is the most important in terms of defect production. These authors found that the mean length of an RCS increases with pka energy

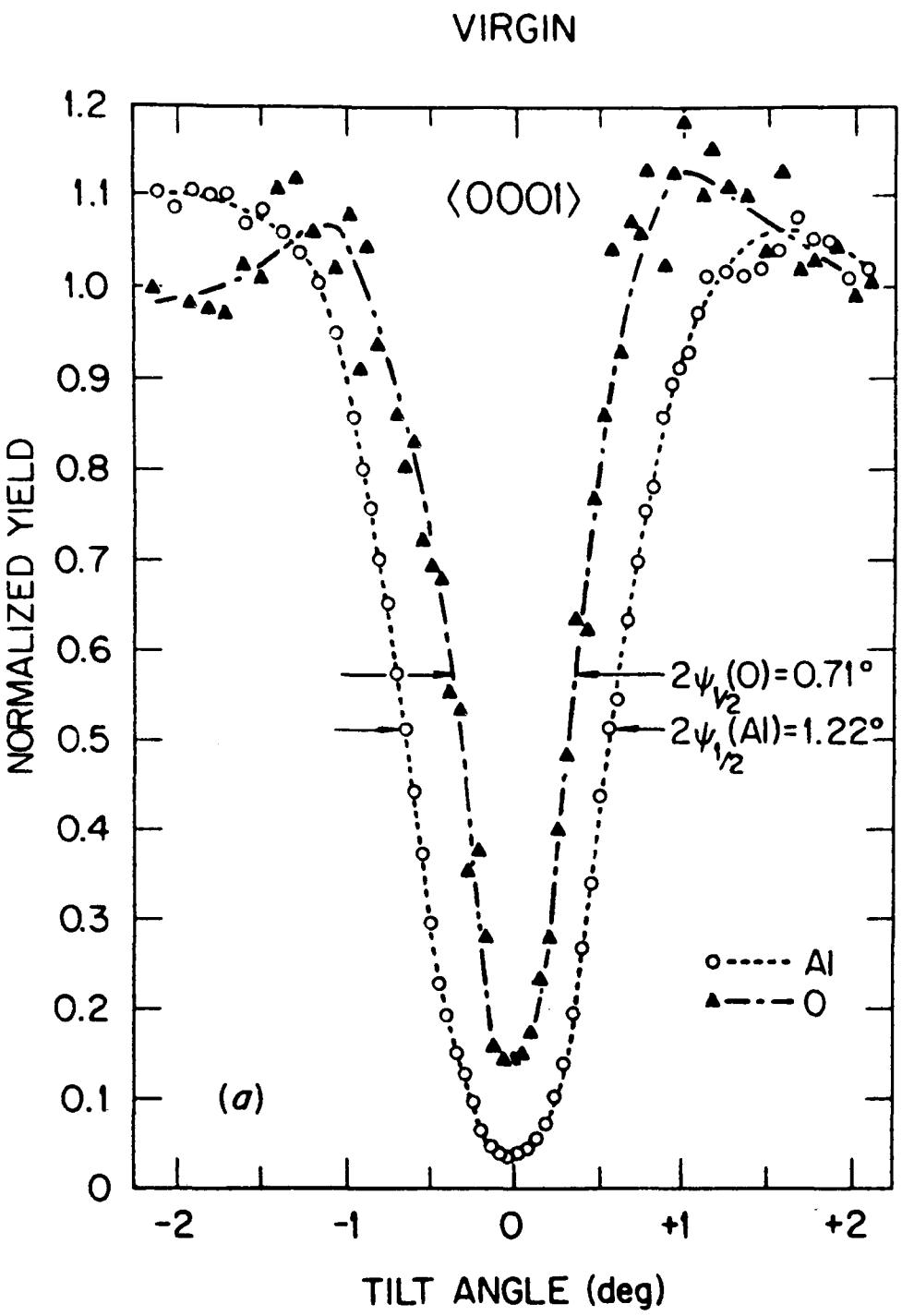


Fig. 2.14. Variation of backscattering yield with angular deviation from the <0001> direction in sapphire. Ref. <48>.

in the range 125 to 2000 eV, going from 4.3 ± 2.0 to 6.1 ± 2.5 replacements. They observed an eleven-atom replacement sequence in a 2 keV cascade, which represents a very efficient mechanism for defect separation. The percentage of the pka energy, E, removed via the RCS mechanism was found to decrease with E, going from 9% to 1.6% for values of E of 125 eV and 2 keV respectively.

This completes our review of the standard models of point defect production. We have seen how the simple binary collision theory is able to describe the production of relatively isolated Frenkel pairs. It also gives a rough estimate of the point defect concentration at the end of the displacement phase of energetic cascades, but we demonstrated how subsequent defect interactions in the excited region invariably lead to a reduction in this number. These standard models have mainly been developed to describe defect production in metals and this is also where the bulk of experimental investigations have been concentrated. When we come to consider defect production in ionic materials we must recognise the possibility of variations from both the quantitative *and* qualitative predictions of the theory outlined above and in chapter 4 we shall explore such differences. However, before doing so we shall review the experimentally observed effects of both ionising and particle irradiation on a typical ionic insulator, sapphire.

References

<1> H. Goldstein, ' Classical Mechanics ', Addison-Wesley Publishing Company (1980).

<2> J. Lindhard and M. Scharff, Phys. Rev. 124 , 128 (1961).

<3> M. Abramowitz and I.A. Stegun, editors, ' Handbook of Mathematical Functions ', National Bureau of Standards, U.S.A. (1964).

<4> P. Sigmund, Rev. Roum. Phys., 17 , 823 (1972).

<5> J. Lindhard, V. Nielsen and M. Scharff, Mat. Fys. Medd. Dan. Vid. Selsk. 36 , No. 10 (1968).

<6> C.A. Coulter and D.M. Parkin, J. Nucl. Mater., 88 , 249 (1980).

<7> K.B. Winterbon, P. Sigmund and J.B. Sanders, K. Dan. Viden. Selsk. Mat. Fys. Medd. 37 , No.14 (1970).

<8> J.F. Ziegler, J.P. Biersack and U. Littmark, ' The Stopping and Range of Ions in Solids ', Pergamon Press (1985).

<9> J. Lindhard, V. Nielsen, M. Scharff and P.V. Thomsen, Mat. Fys. Medd. Dan. Vid. Selsk. 33 , No. 10 (1963).

<10> N. Bohr, Phil. Mag., 25 , 10 (1913).

<11> H.A. Bethe, Ann. Physik, 5 , 325 (1930).

<12> F. Bloch, Ann. Physik, 16 , 285 (1933).

<13> N. Bohr, Phys. Rev. 58 , 654 (1940).

<14> W.E. Lamb, Phys. Rev. 58 , 696 (1940).

<15> L.C. Northcliffe, Phys. Rev. 120 , 1744 (1960).

<16> E. Fermi and E. Teller, Phys. Rev. 72 , 399 (1947).

<17> J. Lindhard, Mat. Fys. Medd. Dan. Vid. Selsk. 28 , No. 8 (1954).

<18> Y. Matsutani and S. Ishino, J. Appl. Phys. Vol. 48, No. 5, 1822 (1977).

<19> J. Lindhard and M. Scharff, Phys. Rev. 124 , 128 (1961)

<20> G.H. Kinchin and R.S. Pease, Rep. Prog. Phys. 18 , 1 (1955).

<21> M.T. Robinson, Proc. BNES Conf. on ' Nuclear Fusion Reactors ', Culham, England, 364 (1969).

<22> P. Sigmund, Rad. Eff., 1 , 15 (1969).

<23> M.M.R. Williams, Prog. Nucl. Energy, Vol. 3, No. 1, 1 (1979).

<24> M.J. Norgett, M.T. Robinson and I.M. Torrens, Nucl. Engrg. Des. 33 , 50 (1975).

<25> D.G. Doran, Nucl. Engrg. Des. 33 , 63 (1975).

<26> J.H. Kinney, M.W. Guinan and Z.A. Munir, J. Nucl. Mater., Vol. 122-123, 1028 (1984).

<27> L.E. Rehn, P.R. Okamoto and R.S. Averback, Phys. Rev. B 30 , No. 6, 3073 (1984).

<28> R.S. Averback, R. Benedek and K.L. Merkle, Phys. Rev. B 18 , 4156 (1978).

<29> R.S. Averback, R. Benedek, K.L. Merkle, J. Sprinkle and L.J. Thompson, J. Nucl. Mater. 113 , 211 (1983).

<30> M.A. Kirk, and L.R. Greenwood, J. Nucl. Mater. 80 , 159 (1979).

<31> M.T. Robinson and I.M. Torrens, Phys. Rev. B, Vol. 9, No. 12, 5008 (1974).

<32> J.A. Brinkman, J. Appl. Phys., 25 , 961 (1954).

<33> J.A. Brinkman, Am. J. Phys., 24 , 246 (1956).

<34> M.I. Current and D.N. Seidman, Nucl. Instrum. and Methods, 170 , 377 (1980).

<35> V.I. Shulga, M. Vicanek and P. Sigmund, Phys. Rev. A, Vol. 39, No. 7, 3360 (1989).

<36> T. Diaz de la Rubia, R.S. Averback, H. Hsieh and R. Benedek, J. Mater. Res., Vol. 4, No. 3, 579 (1989).

<37> F. Seitz and J.S. Koehler, in ' Solid State Physics ', *Ed.* F. Seitz and D. Turnbull, Vol. 2, Academic Press, New York (1956).

<38> W.E. King and R. Benedek, J. Nucl. Mater., 117 , 26 (1983).

<39> A.J.E. Foreman, W.J. Phythian and C.A. English, Unclassified 'AEA Technology' Report, AEA-TRS-2031, Jan. 1991.

<40> J.N. Lomer and M. Pepper, Phil. Mag. 16 , 1119 (1967).

<41> M.T. Robinson and O.S. Oen, Phys. Rev. 132 , 1385 (1963).

<42> J.A. Davies, F. Brown and M. McCargo, Can. J. Phys. 41 , 829 (1963).

<43> R.S. Nelson and M.W. Thompson, Phil. Mag. 8 , 1677 (1963).

<44> H.O. Lutz and R. Sizmann, Phys. Letts. 5 , 113 (1963).

<45> J. Lindhard, Mat. Fys. Medd. Dan. Vid. Selsk, 34 , No. 14, 1 (1965).

<46> R.S. Nelson, ' The Observation of Atomic Collisions in Crystalline Solids ', North-Holland Publishing Company (1968).

<47> O.S. Oen and M.T. Robinson, Appl. Phys. Lett., 2 , 83 (1963).

<48> H. Naramoto, C.W. White, J.M. Williams, C.J. McHargue, O.W. Holland, M.M. Abraham and B.R. Appleton, J. Appl. Phys., 54 , 683 (1984).

<49> I.M. Cheshire, G. Dearnaley and J.M. Poate, Proc. Roy. Soc. A. 311 , 47 (1969).

<50> W. Brandt, *Channelling in Crystals,* Scientific American (1968).

Chapter 3

Radiation Effects in Sapphire

Introduction.

Sapphire is one of the best studied insulators by both pure and applied scientists and a large body of literature has developed concerning both the intrinsic properties of the perfect crystal and the defect state. It is of interest to the solid state theorist as offering perhaps the next degree of complexity compared to the simple alkali halides and MgO. This extra complexity arises both due to its more complicated structure and the fact that it exhibits a significant degree of covalency in its bonding. Sapphire has also been the subject of intense research by applied scientists due to its numerous technological uses. Its excellent electrical, thermal and optical properties, together with its high chemical stability, allow it to be used under adverse conditions in a variety of applications. Most of the defect production experiments described herein have been performed with this material and so in this chapter we review its fundamental properties and discuss how they are modified by radiation.

§ 3.1 Structure.

Sapphire is the common gem name for single crystal $\alpha - Al_2O_3$ (alumina), though it is also often referred to by its mineral name of *corundum*. This also lends its name to the generic crystal structure which sapphire takes. The arrangement of atoms in the corundum structure was first determined by Pauling and Hendricks <1> and is rather complicated. The Bravais lattice is trigonal or rhombohedral, where all the primitive lattice vectors are of equal length $a=9.694$ atomic units and the angle between any two of them is $\beta=55°6'$. The preferred coordination number for aluminium is six so that with a valence of three there is a 'bond

strength' of one half; this requires four Al^{3+} ions adjacent to each O^{2-}. This is achieved by *nearly* hexagonal close-packing of the oxygen ions, with aluminium ions filling two thirds of the octahedral sites. Pairs of Al ions are stacked along the *c*–axis and are surrounded by trigonally distorted octahedra of oxygen ions. This pair of Al atoms 'shares' the equilateral triangle of oxygen atoms lying between them. The Al-O distance in this case is 1.969A. The other triangle of each octahedron is larger and lies closer to the Al ion than does the first. This Al-O distance is 1.865A and thus the site symmetry of the Al ion would be C_{3V} if no other distortions occurred. However the upper and lower triangles are rotated away from the σ_V planes by 2°8.5′ in opposite directions, thus destroying the reflection symmetry. This loss of symmetry is so slight that the site symmetry may be assumed to remain C_{3V} for most purposes. This will be seen to have significant consequences when we consider the optical properties of the Al vacancy. However we note here that the octahedral symmetry of the cation site in sapphire is responsible for some interesting and beautiful optical effects.

§ 3.2 Structural Radiation Effects

The effects of irradiation on the structure of insulators varies significantly from one material to another. Some, such as CaO and CaF_2, retain their crystallinity to very high doses, whilst others, including SiO_2, become amorphous at relatively low doses. The question of whether sapphire will become amorphous under ion bombardment is of some importance to the present investigation since a local crystalline-to-amorphous transition in the vicinity of the displacement cascade at the end of an ion track would alter the structure of point defects in that region and hence alter the characteristics of the associated colour centres. Matzke and Whitton <2> have suggested that the resistance to amorphisation can be correlated with the structure of the unirradiated material since they found that several non-cubic materials, including TiO_2 (rutile), became amorphous at relatively low doses whereas many cubic materials maintained their crystallinity to high doses. Three qualitative reasons for differences in amorphisation behaviour were suggested by these authors: (i) materials which are polymorphous are likely to show less resistance to amorphisation since they are naturally able to accommodate different structural arrangements (ii) similarly,

materials which have different cation-anion distances for different nearest neighbours are more able to accommodate the amorphisation and (iii) anisotropic materials will tend to undergo amorphisation at lower doses due to the extra lattice strains induced following irradiation.

More quantitative requirements for amorphisation have been outlined by Naguib and Kelly <3> and two different criteria were given. The first states that amorphisation should occur whenever the ratio (crystallisation temperature/melting temperature) exceeds a certain value. The argument is that the disturbed region of the displacement cascade at the end of the ion's track can be considered as a thermal spike (as described in the previous chapter) and hence to have a liquid-like structure. This region cools rapidly and crystallisation begins when the local temperature falls below the melting point, T_m. The diffusion equation for a point source can be solved in a straightforward manner and an estimate obtained of the number of atomic jumps that can be made as the zone cools from T_m to the crystallisation temperature, T_c. Naguib and Kelly suggest that the crystallinity will be preserved if the distance moved by the crystallisation front into the disordered region is 'sufficiently greater than the mean atomic spacing'. They proceed to show that this criterion can be simply expressed as amorphisation occurring when $T_c/T_m > 0.3$. Sapphire has a ratio T_c/T_m somewhat larger than this value (in fact a value of 0.43) and so this criterion would suggest that it will not show a large resistance to amorphisation. The second criterion is of a more empirical origin and states that loss of crystallinity should occur whenever the ionicity is ≤ 0.47. Here the Pauling ionicity is defined by

$$ionicity = 1 - \exp[-0.25(X_a - X_b)^2] \qquad (3.1)$$

where X_a and X_b are the electronegativities of the two ions, as tabulated in *e.g* ref. <4>. Sapphire has a Pauling ionicity defined in this way of 0.59, suggesting a significant resistance to amorphisation, in contrast to the previous prediction. Clearly these criteria are only approximate and the conclusion we must draw on these bases is that sapphire is intermediate in its resistance to a crystalline-amorphous transition following irradiation. The experimental evidence has been reviewed by White *et. al.* <5> who conclude that although sapphire will eventually become amorphous, large doses (e.g. $\geq 5\times10^{17}$ cm $^{-2}$, 200 keV Fe)

are required. In all of the ion bombardment experiments on sapphire reported in the present investigation, the levels of deposited energy are well below the value at which amorphisation is expected to occur and we shall always assume that the target is in the crystalline state.

§ 3.3 Optical Properties.

High purity sapphire is transparent in the visible part of the spectrum through into the vacuum ultra-violet (with a band gap of around 9eV) although its impure forms provide an array of spectacularly coloured gemstones. These colours may be produced by several different mechanisms <6>. However several of the most common are caused by the optical absorption bands of transition metal ion impurities. A few atomic percent of chromium occupying substitutional cation sites produces the familiar deep red hue of ruby, whilst a similar level of iron impurity induces predominantly blue or green colours, depending on the concentration and the presence of other ions. The transition elements are characterised by having unoccupied outer *d* orbitals which are degenerate in the free atom, with its full rotational symmetry. This symmetry is broken if the atom is embedded in a crystal matrix causing, in general, a splitting of the *d* orbitals. In cubic symmetry electric dipole *d–d* transitions remain forbidden. However the lack of inversion symmetry at the cation site in the corundum structure permits such transitions and these are responsible for many of the beautiful colours found in impure sapphire. In a classic paper on the optical spectra of transition-metal ions in sapphire, McClure <7> used a point charge model of the impurity ions to calculate the crystal field splitting of the atomic terms and produced reasonable quantitative agreement with experimental spectra of Ti^{3+}, V^{3+}, Cr^{3+}, Mn^{3+}, Co^{3+} and Ni^{3+} ions resident in sapphire.

In the unirradiated material at room temperature the point defect population and hence the colour centre concentration, is extremely small due to the high free-energy of formation for thermal vacancies. However, subjecting a previously unirradiated crystal to a high X-ray flux will introduce additional absorption bands around 400 nm and 230 nm <8,9>, which have been ascribed to the colour centres associated with the aluminium and oxygen vacancies (see

below). There is a growing consensus that the small but finite number of intrinsic point defects are Schottky in nature <10>.

§ 3.4 Colour Centres in Sapphire.

The main effects of energetic particle bombardment on the optical properties of sapphire are caused by the introduction of colour centres. Before discussing the consequences of each type of irradiation therefore, I have chosen to first discuss our present state of knowledge regarding the few colour centres which have been positively identified with a specific structural defect. Historically, of course, the identification of colour centres was preceded by an understanding of the type of defects each type of radiation was capable of producing and this historical approach has been taken by Crawford <11> in a more comprehensive review article. In practice we shall mostly be concerned with the colour centres of the primary defects – oxygen and aluminium vacancies and will limit this review to these defects and one or two others of particular interest.

The Oxygen Vacancy.

The oxygen vacancy is able to exist in two stable charge states, giving rise to two colour centres, the F and the F^+ centres. The former consists of two electrons with opposing spin trapped at the vacancy and the latter just a single electron. The bare oxygen vacancy is usually assumed to be unstable due to its large Coulomb attraction <11>. However in chapter 5 we shall present evidence for the existence of this defect. The site symmetry of the oxygen vacancy is C_2, with the C_2 axis being perpendicular to the crystal c–axis (the <0001> direction). This point group has just two, one dimensional irreducible representations. Thus no orbital degeneracy can remain and p–type orbitals will split into three distinct levels. La *et. al.* <12> have performed a point ion calculation of the wave functions and energy levels of the oxygen vacancy centre using a symmetry adapted basis set consisting of s, p and d orbitals. Linear combinations of the correct symmetry type were found using the variational principle and approximate eigenvalues deduced from these. The resulting energy scheme is

shown in fig. 3.1. Three transitions from the ground state are possible: from 1A to 1B, 2A and 2B, with calculated transition energies of 2.26, 3.39 and 5.15 eV respectively. The low site symmetry means that some of these transitions cannot be excited with light of a certain polarisation. With the coordinate system shown in fig. 3.2 it is straightforward to show that the following transition matrix elements are zero on the grounds of symmetry alone: $<2A|E_x|1A>$, $<2A|E_y|1A>$, $<1B|E_z|1A>$ and $<2B|E_z|1A>$. Here the subscript on the electric field vector indicates its direction. The second of these matrix elements can be more usefully expressed as $<2A|E_{//}\,c|1A>=0$, to indicate that this transition cannot be excited with light having its electric vector parallel to the crystal c-axis. The polarisation properties of the absorption bands in sapphire irradiated with both fast neutrons and 2 MeV electrons were first investigated by Mitchell *et. al.* <13> who found that the most prominent band at 6.02 eV was optically isotropic whilst bands appearing at 5.4 and 4.8 eV were strongly and oppositely polarised. In a later series of bleaching and polarized light experiments on neutron irradiated sapphire, Evans and Staplebroek <14> confirmed that bands at 4.8, 5.4 and 6.3 eV exhibited the polarisation behaviour predicted for the F^+ centre, *i.e.* the 5.4 eV band (1A ~ 2A) did not appear with light polarised $E_{//}\,c$. The 4.8 and 6.3 eV bands were visible with light having this same polarisation but were considerably stronger when probed with light having $E_{//}\,c$ polarisation. Evans and Staplebroek found that excitation with 4.8 and 5.4 eV photons produces emission at 3.8 eV and they associated this emission with the 1B ~ 1A transition. Although the absolute values of the transition energies predicted by the point-ion calculations of ref. <12> are rather inaccurate, the qualitative scheme agrees very well with experiment and in view of the deficiencies of point-ion calculations in general (*e.g.* neglect of extended ion effects, polarization and lattice distortion about the defect) the absolute errors are to be expected.

The most prominent absorption band in irradiated sapphire appears at around 6.02 eV and, as mentioned above, is optically isotropic. It was first determined to be an electron centre by Turner and Crawford <15> in a series of bleaching experiments conducted on lightly neutron irradiated samples. The results which made it possible to determine whether this band was a transition of the F or F^+ centre were described by Lee and Crawford <16> who found that bleaching neutron bombarded sapphire with 6.02 eV light substantially decreased the

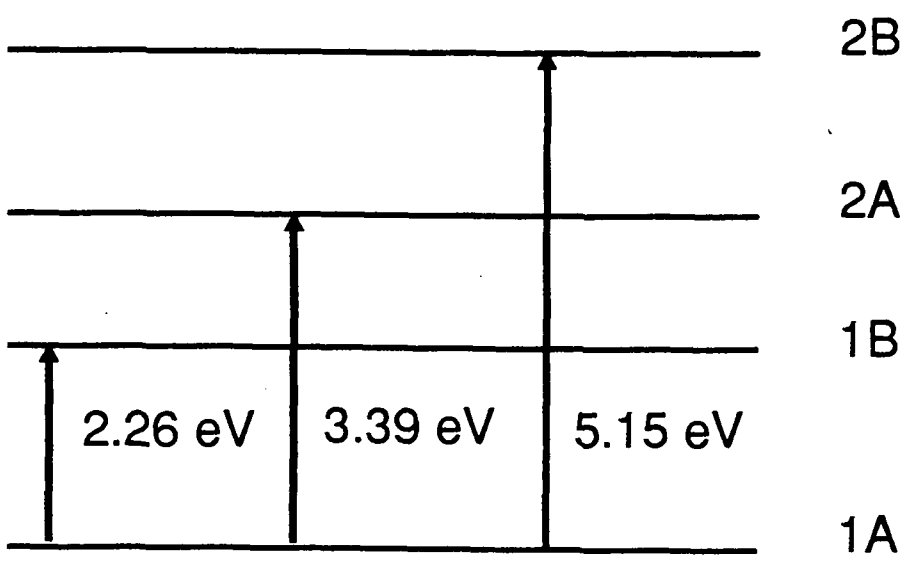


Fig. 3.1. Energy level scheme of the F^+ centre in sapphire, together with calculated transition energies. Ref. <12>.

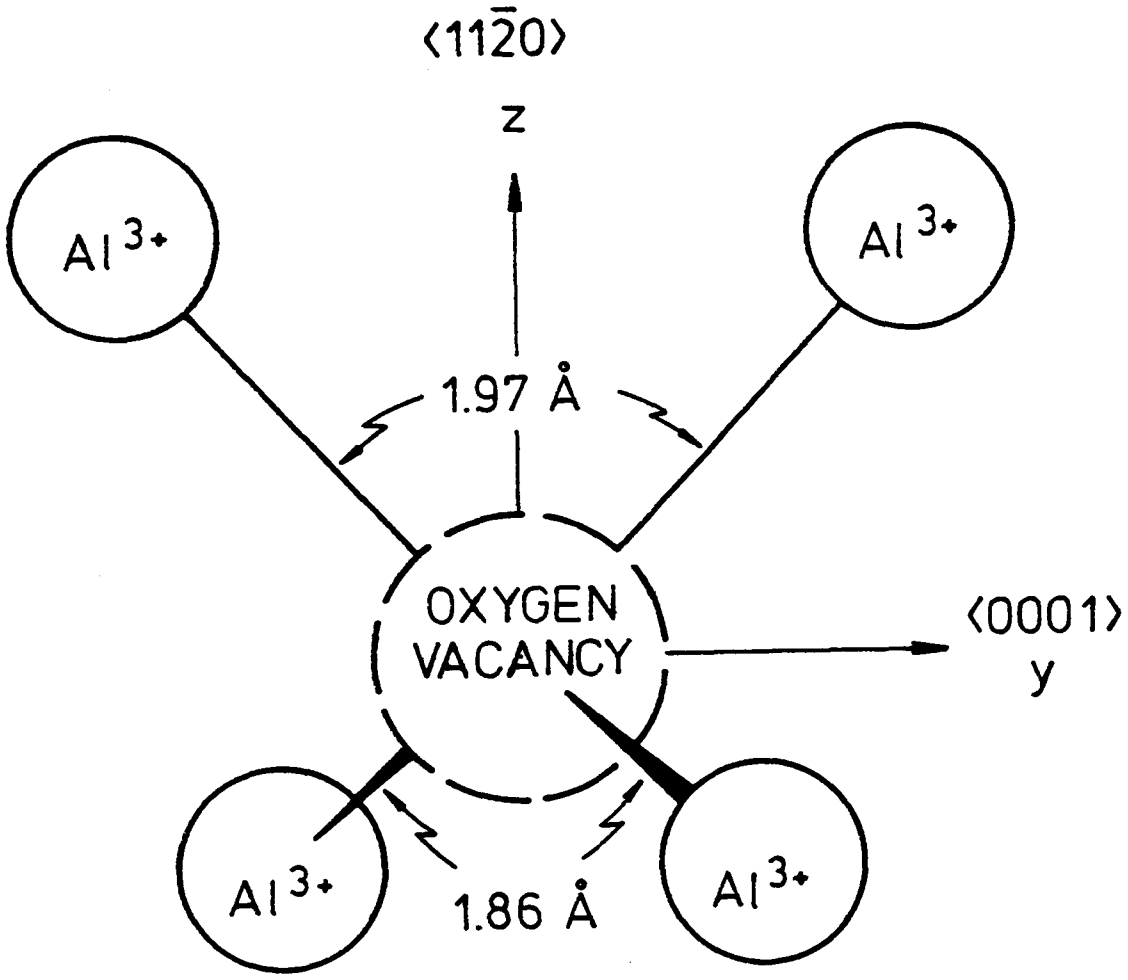


Fig. 3.2. Coordinate system used in the description of the F^+ centre in α–Al_2O_3. The x axis is out of the plane of the paper.

intensity of the 6.02 eV absorption band and *increased* absorption at 5.4 eV, 4.8 eV and in other parts of the spectrum. The inference from this is that bleaching releases electrons from the F centre which becomes an F^+ centre, allowing the electrons released in this process to occupy other colour centres. This leads us to assign the 6.02 eV band to the F centre and the 5.4 and 4.8 eV bands to the F^+ centre. More recent work by Dalal *et. al.* <17> on the growth of absorption bands during ion irradiation shows that the 6.3 eV band is enhanced in parallel with the 5.4 and 4.8 eV bands, confirming this band as the 1A ~ 2B transition of the F^+ centre. The wavelengths and corresponding energies of the absorption bands associated with the single oxygen vacancy are listed in table 3.1.

Several outstanding problems regarding the above assignments have recently received attention. There is one puzzling question regarding the nature of the excited states of the F centre. Given that this centre has the same site symmetry as the F^+ centre one would expect a similar degree of splitting (i.e. three-fold) of its first excited state. Only one band has been assigned to the F centre though. This problem is illuminated by the work of Draeger and Summers <18> who found, in a study of the photoconductivity of sapphire, that excitation into the 6.02 eV band produces photoconductivity at least down to 10K. Hence the unrelaxed excited state must lie very close to, if not *in*, the conduction band, indicating that the wave function is highly extended. Thus although splitting no doubt would occur, it is probable that its magnitude is less than the half widths of the component bands and cannot be resolved.

The Aluminium Vacancy.

The first steps in identifying the colour centres associated with the aluminium vacancy were aided considerably by comparisons with known colour centres in MgO. Turner and Crawford <19> subjected 55mm long crystals of sapphire to γ–rays and found bands in the infra-red which were analogous to bands found in MgO and known to be associated with OH^- ions situated adjacent to Mg^{2+} vacancies. Given confidence by the analogies found in the I.R. spectra, these authors associated the wide band at around 3.0 eV in sapphire with several trapped hole centres. Further investigations <15,20,21> involving e.s.r., thermoluminescence and optical absorption measurements firmly identified a number of

Centre	λ / nm	E / eV
F	203	6.02
F^+	260	4.8
F^+	230	5.4
F^+	197	6.3

Table 3.1. Wavelengths and corresponding energies of the absorption bands associated with the single oxygen vacancy in sapphire.

hole centres, including the V^{2-} (an O^- ion adjacent to an aluminium vacancy), the V^- (two O^- ions adjacent to an aluminium vacancy) and the V_{OH}^- (an O^- ion adjacent to an aluminium vacancy which also has an OH^- as a nearest neighbour). All of these centres absorb near 3.0 eV. The charge complimentarity of the 3.0 eV and 5.4 eV bands was confirmed by Turner and Crawford <15> who showed that the latter could be completely destroyed by irradiating into the 3 eV band, which was also bleached in the process.

Multiple Defect Centres.

Of all the defects involving more than a single vacancy, only the colour centres associated with the oxygen divacancy have been identified. Plane polarised light absorption experiments were employed by Welch *et. al.* <22> to demonstrate that the transition moment of a band appearing at 3.46 eV (358 nm) in both proton and neutron, heavily irradiated samples, was aligned with that expected of two nearest neighbour oxygen vacancies. Atobe *et. al.* <23> performed a series of annealing studies on neutron irradiated samples and found bands at 450 and 570 nm which were tentatively identified with the F_2^+ centre. A band at 302 nm was associated with the F_2 centre. Further investigation by Pogatshnik *et. al.* <24> indicated that the 450 nm band was composed of at least two components, the narrow component of which should be assigned to the F_2^{2+} centre. On the basis of a number of photobleaching experiments these authors proposed an energy level scheme for the F_2 centre and its charged derivatives which is reproduced in fig. 3.3.

For all of these multiple defect bands high levels of lattice damage are necessary for their visibility. For example the samples analysed by Welch *et. al.* <22> had been irradiated with 1 and 3 MeV protons up to doses of 3×10^{18} cm $^{-2}$. The levels of lattice damage produced in the present damage efficiency investigation are around one thousand times less than that observed by these authors and so, not surprisingly, no evidence of multiple defect absorption bands was found in all the damage efficiency experiments conducted.

Having described the basic colour centres one might expect to find in irradiated sapphire we shall now discuss the characteristic effects of each particular type of radiation and the colour centres they are likely to produce.

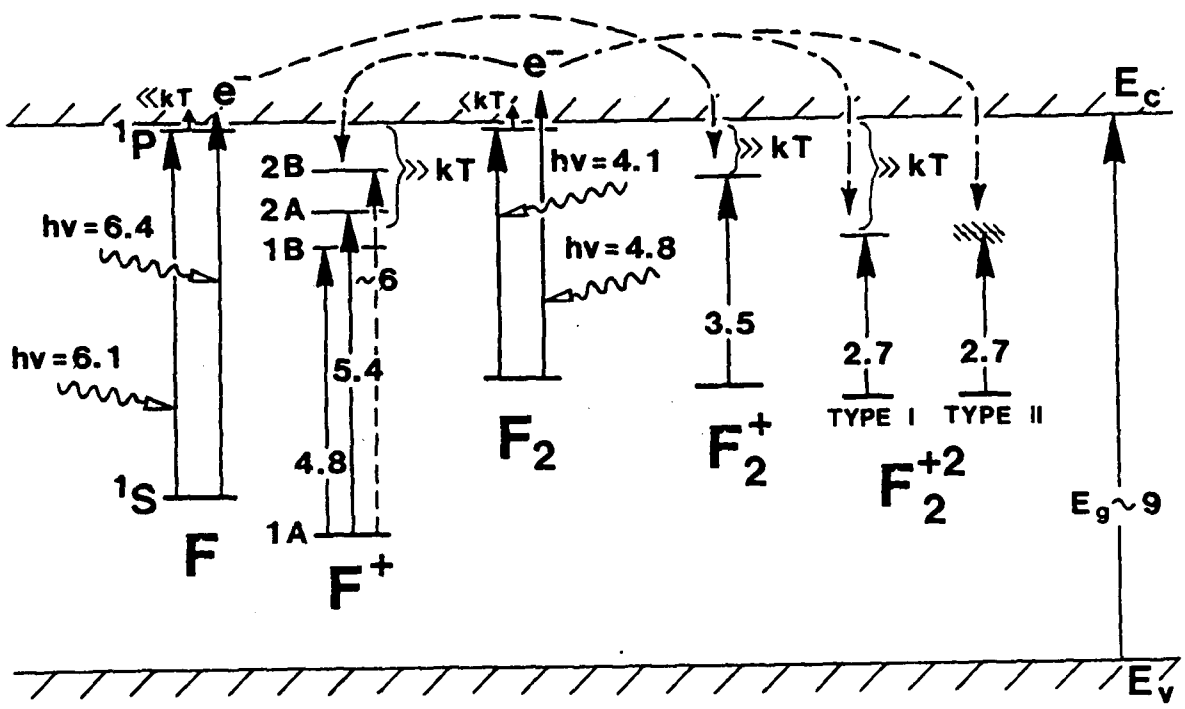


Fig. 3.3 Energy levels of some anion vacancy centres in sapphire. The positions of the conduction and valence bands are denoted by E_C and E_V respectively. Energies are expressed in eV. Ref. <24>.

§ 3.5 The Effects of Irradiation on Optical Properties.

From the very early investigations into the different effects of the various types of radiation on sapphire it was apparent that a distinction could be drawn between the effects of the predominantly ionising radiations (X-rays, γ–rays and electrons) and radiation capable of producing lattice displacements as described in chapter 2. In considering the interaction of radiation with sapphire we shall arrange the four different classes we defined in chapter 1 into two groups: (i) ionising radiation and (ii) heavy particle bombardment.

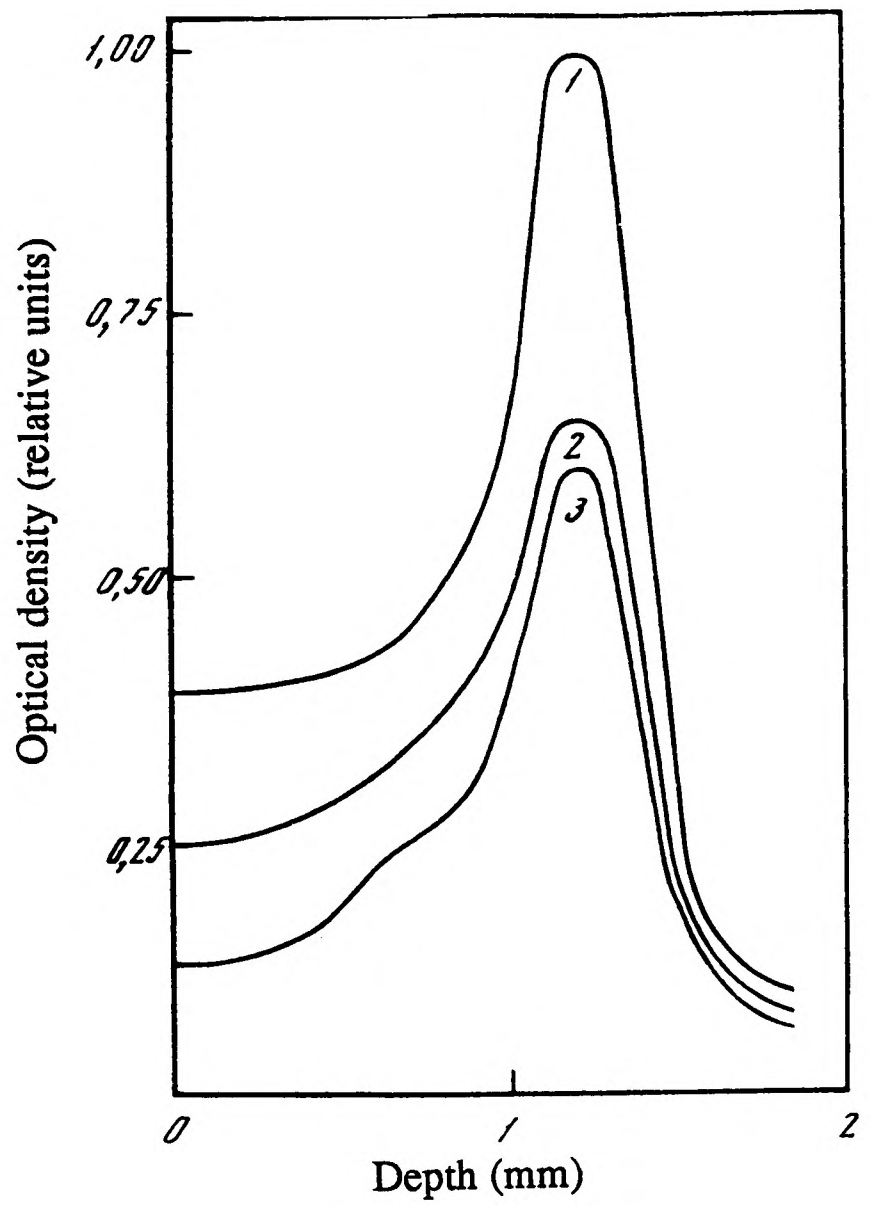
Ionising Radiation.

The finite number of intrinsic structural defects will, if suitably populated by electrons or holes, give rise to characteristic absorption bands. Ionising radiation such as X- or γ–rays provide a convenient way of populating colour centres with charge. Rehavi and Kristianpoller <9> subjected pure sapphire to X-rays at 80K and found absorption bands at 290, 260 and 230 nm, together with a steep increase in absorption near 200 nm. Thermal annealing at 200K resulted in an increase of the 230 and 260 nm band and a slight decrease of the band near 200 nm. These results are consistent with the assignments above for the absorption bands of the F and F^+ centres and are interpreted simply as a redistribution of electrons amongst the oxygen vacancies present.

Radiations which only excite the target electrons have long been supposed to be incapable of producing lattice displacements in sapphire and only able to influence pre-existing lattice imperfections such as vacancies or impurities. Levy <25> subjected sapphire to an initial dose of 3×10^4 rad of Co ^{60} γ–rays (which have energies of 1.1 and 1.3 MeV) and found a small initial change in the absorption spectrum. Subsequent doses up to 10^9 rad were unable to produce any further changes. Similar experiments reported by Compton and Arnold <26> involving electron irradiation below the displacement threshold have also failed to produce any features in the optical spectra which increase with dose. Some evidence *supporting* the production of defects by ionising radiation has been presented by Vakhidov *et. al.* <27>. These authors bombarded sapphire with 18 MeV protons, which are intensely ionising. They employed a specially designed scanning spectrophotometer to monitor the F centre

concentration along the whole 1.15mm range of the protons and hence obtained a profile of the defect production along the ion path. Their profiles are reproduced in fig. 3.4, together with a graph of the vacancy distribution predicted by binary collision theory, assuming a purely collisional mechanism of defect production. The correspondence is rather good, confirming that the collisional mechanism of vacancy production is dominant. However *F* centres were found well below the peak in nuclear stopping power and it was suggested that some form of ionisation assisted displacement mechanism was responsible. A somewhat naive argument was used by these authors in that they assumed the protons were incapable of producing displacements until their energy had dropped below 4 MeV. This is clearly unrealistic and is likely to be the source of the discrepancy. Another possibility is that defects had migrated during the irradiation. The intense ionisation and significant vacancy concentrations introduced by bombardment with 18 MeV protons could quite possibly result in radiation enhanced diffusion of point defects from the peak of the damage into the relatively undamaged regions. Also, no details are given of temperature control during the irradiation and again a rise in temperature would promote vacancy diffusion. We shall thus assume for the purposes of all the damage efficiency measurements conducted herein that the electronic stopping power makes no contribution to the production of lattice defects.

Energetic electrons lose the vast majority of their energy to target electrons, but if sufficiently energetic to transfer energy greater than the displacement energy to target nuclei, are also capable of causing lattice displacements. In general though the recoils produced only have energies of the order of E_d and so the damage produced by electrons generally consists of isolated Frenkel pairs. With electron energies below about 410 keV the major effect is to change the charge state of existing lattice defects and in this way small absorption bands may be produced, as for X-rays. Again though, these effects do not grow with dose and saturate at low electron doses. Above this energy one observes growth of both the *F* and F^+ bands, indicating the displacement of oxygen atoms. No evidence for multiple defects, such as the 358 nm band, is apparent. In view of the low oscillator strength of the *V* band, this feature is not easily observed with electron irradiation. However an experiment involving irradiation of sapphire just above the threshold for oxygen displacement is reported in chapter 5 and evidence for the production of aluminium vacancies is presented. It is thus apparent that all



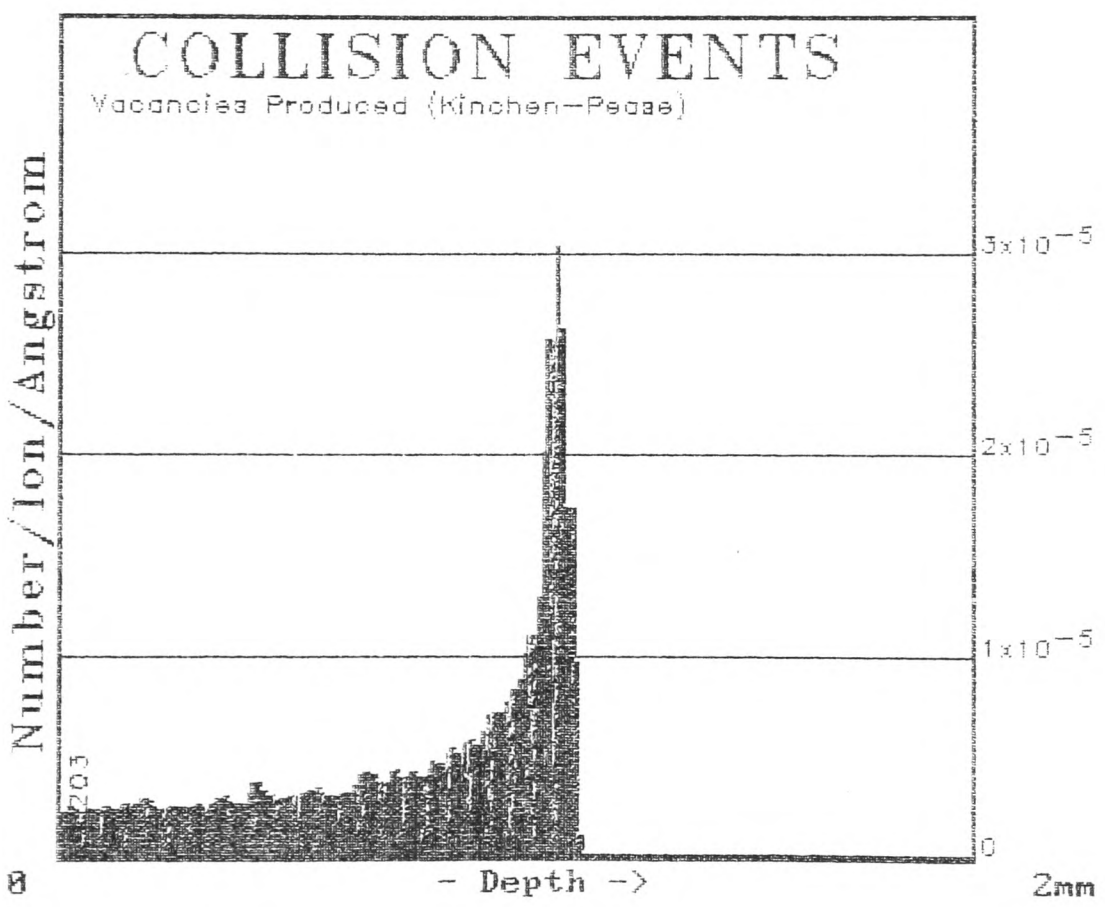


Fig. 3.4. Comparison of *F* centre concentration profile from ref. <27> with the vacancy profile calculated by the Monte Carlo code TRIM <33>. This assumes vacancies are created by direct nuclear collisions.

of the primary defects in sapphire can be generated by sufficiently energetic electron irradiation.

Heavy Particle Bombardment.

Energetic charged particle bombardment will, in general, provide a source of both ionising radiation and lattice displacements. The low average atomic number of sapphire means that for all but the heaviest incident particles the electronic stopping power is much greater than the nuclear stopping power for most of the ion's range. Thus not only will lattice defects be created, but there will also be sufficient electronic excitation to ensure that these defects are populated with the requisite holes or electrons, enabling them to become optically active. In view of the more energetic recoil atoms produced under ion bombardment one would also expect a greater likelihood of multiple defect centres in addition to the primary defects. Similar arguments may be made in the case of neutron bombardment. This is most conveniently carried out inside a thermal reactor and generally produces the greatest number of different colour centres. This is because in the reactor environment, *all* of the four types of radiation distinguished in chapter 1 are present in abundance. The high energy recoils produced by the fast neutrons are able to produce multiple defects and there is ample ionising radiation, from both the energetic recoils and the γ–rays resulting from radioactive decay and fission processes, to ensure that all the lattice defects produced are populated with the necessary optically activating charge. One of the first analyses of neutron irradiated sapphire was performed by Levy <25>, who found seven bands resulting from thermal reactor irradiation. This large number of bands is characteristic of reactor irradiation and is to be expected on the basis of the arguments just presented.

Further evidence for the more complicated defect structures encountered in neutron irradiated samples is given by luminescence studies. It is well known <28> that a blue luminescence at 3.0 eV is associated with the *F* centre. In the case of fast neutron irradiated samples, *F* band excitation produces a very weak luminescence of this kind, in contrast to the strong emission observed upon *F* band excitation of thermochemically coloured crystals <16>. The emission efficiency of neutron irradiated samples can be greatly enhanced by

annealing in the range 200°C to 500°C. As the *F* band intensity decreases by about a factor of seven the ratio (luminescent intensity/absorption coefficient) increases by a factor of one hundred <29>. This is interpreted by Jeffries *et. al.* <30> as suggesting that the *F* centres introduced by fast neutron bombardment are localized within disordered regions (displacement cascades) where the local symmetry is so disturbed that coupling to the lattice is enhanced and non-radiative decay dominates over the radiative decay which results in luminescence. Annealing results in recombination in the cascade thus decreasing the local *F* centre concentration and increasing the luminescent efficiency until it approaches the value expected for isolated, uniformly distributed *F* centres as one finds in thermochemically coloured crystals. Crawford <29> also notes that the F^+ centre, whose wave function is not so extended in comparison with the *F* centre and whose concentration is much less, shows no such quenching.

Variations in the relative proportion of bands under irradiation by different ions have been investigated by Dalal *et. al.* <17>. These authors attempted to produce a variation in the ratio of (*F* centre concentration / F^+ centre concentration) by varying the ion mass and hence the defect density at the end of the ion track. In dense cascade regions one might expect that competition amongst the large number of oxygen vacancies for stabilising charge is considerable and so F^+ centres will predominate. This was indeed found to be the case, with this ratio being 8:1 for electron irradiation and dropping to 2:1 for He irradiation. For the case of Ne and Ar irradiation they were unable to fully resolve the *F* band and suggested that in this case the *F* centres are only a minor fraction of the defects present or that they are strongly perturbed by the interactions with neighbouring lattice defects. Rather curiously, these authors find the same 8:1 ratio for neutron irradiated samples as they do for electrons. This is difficult to interpret with this same model since the character of the damage produced by electrons and neutrons is quite different, as noted above. No details of the neutron irradiated samples are given though and so further speculation is difficult.

§ 3.6 Stability of Radiation Induced Colour Centres.

One of the great difficulties in performing quantitative defect production experiments in metals is that all measurements must be conducted close to 4K. This is because point defects in metals possess significant mobility above this temperature and hence a large fraction of the Frenkel pairs would recombine. This difficulty is alleviated in sapphire where the Frenkel pairs are largely stable up to room temperature. Pells <31> has conducted a series of isochronal anneals on sapphire and finds that the *F* centre first starts to anneal at around 200°C and then reduces in a stepwise fashion as the temperature is increased up to 700°C, at which point the annealing is virtually complete. This data is reproduced in fig. 3.5 along with the annealing behaviour of the aluminium vacancy. The *V* centre is much more stable and does not start to anneal until temperatures above 400°C have been reached. It is fully annealed at around 1100°C. Pells' data were obtained on samples which had been neutron irradiated at temperatures between 60°C and 250°C. Further measurements on neutron irradiated sapphire with irradiation temperatures of 15 K and 360 K have been reported by Atobe and Nakagawa <32>. These authors found that for samples irradiated at 15 K and then warmed to 360 K, the *F* centre concentration fell by about 20%. Subsequent annealing to a series of higher temperatures caused the reductions indicated in fig. 3.6. These results clearly imply that *F* centres created at temperatures below ~ 300 K are quite stable and there is no large scale thermal recombination immediately following the irradiation.

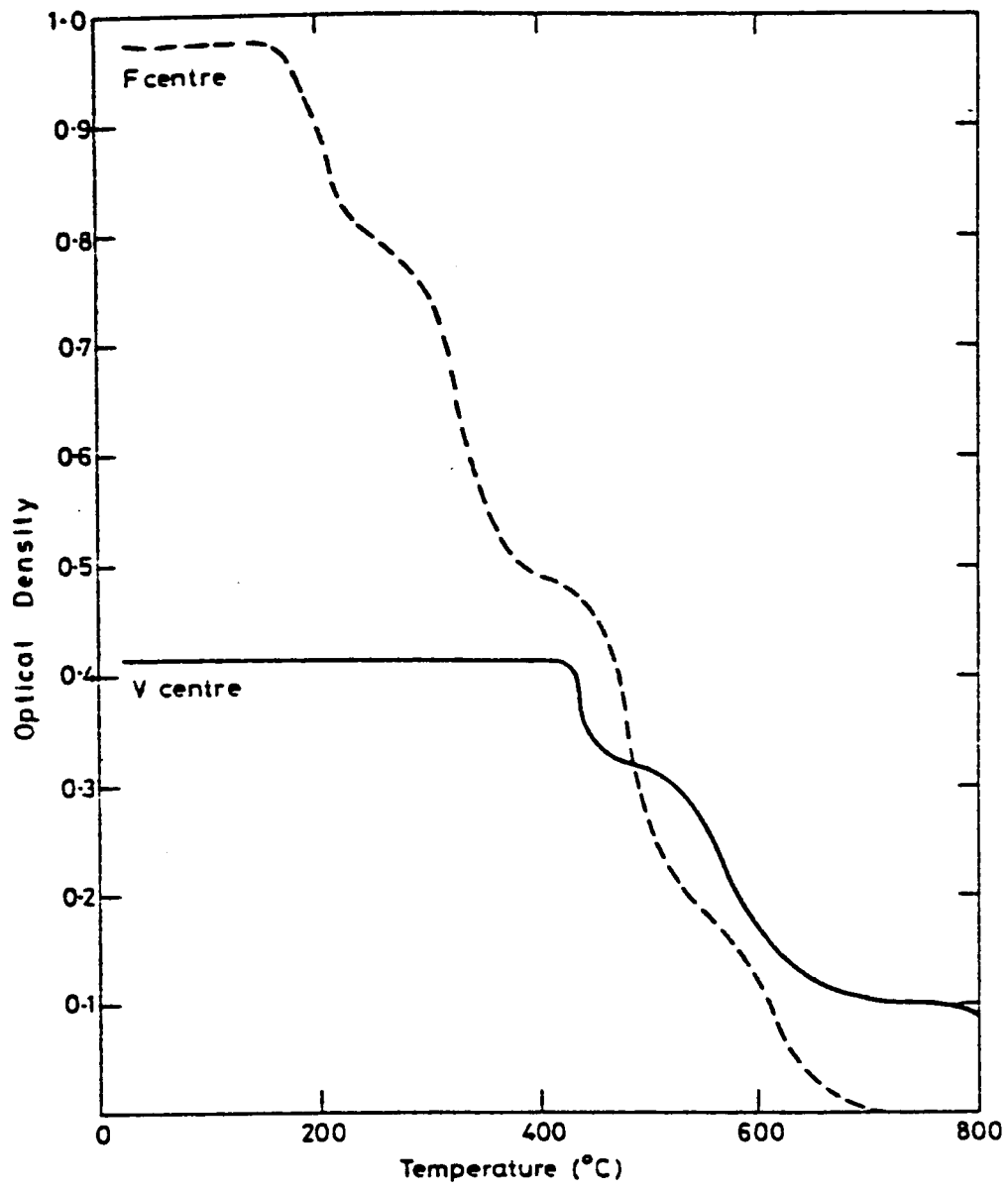


Fig. 3.5. Isochronal annealing curves for the *F* and *V* centres in fast neutorn irradiated sapphire. Ref. <31>.

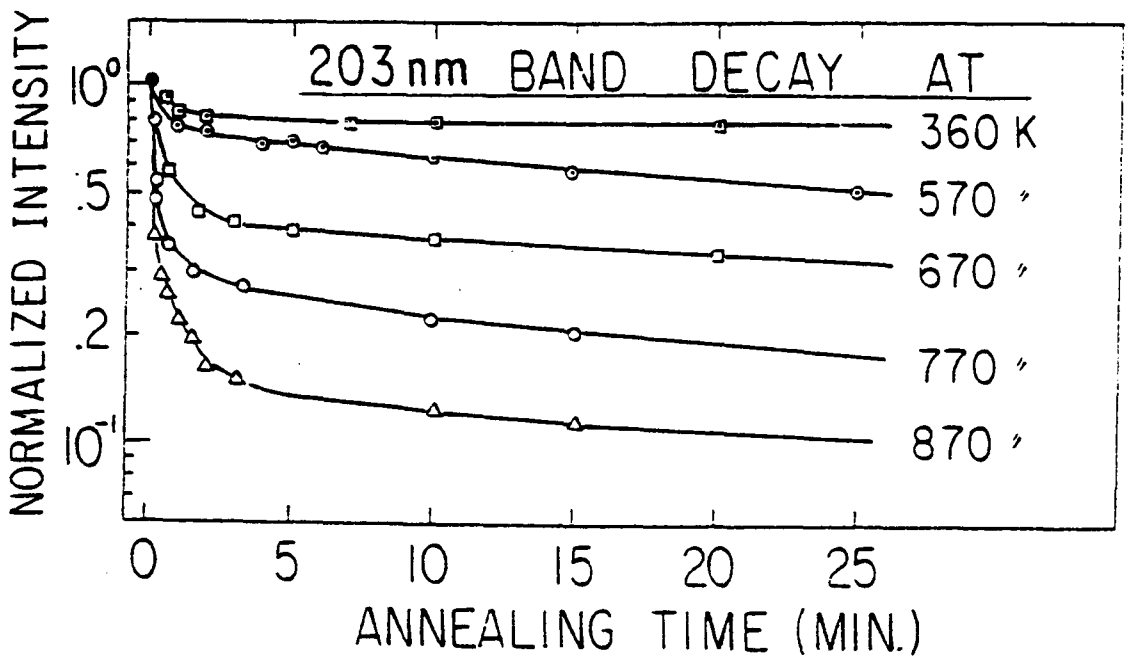


Fig. 3.6. *F* centre annealing characteristics for low temperature irradiations. Ref. <32>.

References

<1> L. Pauling and S.B. Hendricks, J. Am. Chem. Soc 47 , 781 (1925).

<2> Hj. Matzke and J.L. Whitton, Can. J. Phys 44 , 995 (1966).

<3> H.M. Naguib and R. Kelly, Rad. Eff. 25 , 1 (1975).

<4> S.S. Batsanov, Russ. Chem. Rev. 37 , 332 (1968).

<5> C.W. White, C.J. McHargue, P.S. Sklad, L.A. Boatner and G.C. Farlow, Mater. Sci. Rep., Vol.4, No. 2,3 (1989).

<6> 'Gems and Gemology', Summer edition 1988

<7> D.S. McClure, J. Chem. Phys. Vol. 36, No. 10, 2757 (1962).

<8> R.A. Hunt and R.H. Schuler, Phys. Rev 89 , 664 (1953).

<9> A. Rehavi and N. Kristianpoller, Phys. Stat. Sol. (a) 57 , 221 (1980).

<10> 'Advances in Ceramics' Vol. 10, 'Structure and Properties of MgO and Al_2O_3 Ceramics.' Ed. W.D. Kingery, pub. The American Ceramic Society, 1984.

<11> J.H. Crawford Jr., J. Nucl. Mater. 108 & 109, 644 (1982).

<12> S.Y. La, R.H. Bartram and R.T. Cox, J. Phys. Chem. Solids, 34 , 1079 (1973).

<13> E.W.J. Mitchell, J.D. Rigden and P.D. Townsend, Phil. Mag. 5 , 1013 (1960).

<14> B.D. Evans and M. Staplebroek, Phys. Rev. B, Vol.18, No. 12, 7089 (1978).

<15> T.J. Turner and J.H. Crawford, Phys. Rev. B13, 1735 (1976).

<16> K.H. Lee and J.H. Crawford, Phys. Rev. B19, 3217 (1979).

<17> M.L. Dalal, M. Rahmani and P.D. Townsend, Nucl. Instr. Meths. in Phys. Res. B32, 61 (1988).

<18> B.G. Draeger and G.P. Summers, Phys. Rev. B19, 1172 (1979).

<19> T.J. Turner and J.H. Crawford, Solid State Commun. 17 , 167 (1975).

<20> F.T. Gamble, R.H. Bartram, C.G. Young, O.R. Gilliam and P.W. Levy, Phys. Rev. 134 A589 (1964).

<21> R.T Cox, Solid State Commun. 9 , 1989 (1971)

<22> L.S. Welch, A.E. Hughes and G.P. Pells, J. Phys. C: Solid State Phys., 13 , 1805 (1980).

<23> K. Atobe, N Nishimoto and M. Nakagawa, Phys. Stat. Sol. (a) 89 , 155 (1985).

<24> G.J. Pogatshnik, Y. Chen and B.D. Evans, IEEE Trans. Nucl. Sci., Vol. NS-34, No. 6, 1709 (1987).

<25> P.W. Levy, Phys. Rev. Vol. 123, No. 4, 1226 (1961)

<26> W.D. Compton and G.W. Arnold, Jnr., Disc. Far. Soc. No. 31, 130 (1961).

<27> Sh.A. Vakhidov, Zh.D. Ibragimov, I. Nuritdinov and K. Khatamov, Dokl. Akad. Nauk SSSR 288 , 348 (1986).

<28> J.A. Valbis, P.A. Kulis and M.J. Springis, Izv. Akad. Nauk Latv. SSR, Ser. Fiz. Tekh. No. 6, 22 (1979).

<29> J.H. Crawford, Semicond. and Insul. Vol. 5, 599 (1983).

<30> B. Jeffries, G.P. Summers and J.H. Crawford, J. Appl. Phys. 51 , 3984 (1980).

<31> G.P. Pells, Radiat. Phys. Chem. Vol. 22, No. 6, 1053 (1983).

<32> K. Atobe and M. Nakagawa, Cryst. Lattice Defects Amorphous Mater. Vol. 17, No. 1-2, 229 (1987).

<33> J.F. Ziegler, J.P. Biersack and U. Littmark, 'The Stopping and Range of Ions in Matter', Pergamon Press (1985).

Chapter 4

Theory of Damage Partitioning in Polyatomic Solids

Introduction.

The models of point defect production described in chapter 2 were developed for elements. When we come to consider the interaction of an energetic particle beam with multi-component systems, such as ionic solids, the simple cascade theory presented there cannot be applied. The net interaction is clearly not just the sum of the projectile interactions with each distinct atom type – for the pka's produced on each sublattice may interact both with target atoms of the same *and* different kinds. Since the damage production experiments to be described in chapter 6 are, in general, only capable of detecting lattice defects on the anion sublattice, in order to obtain estimates of the damage *efficiency* we need a theory which is able to describe the partitioning of the radiation effects amongst the two sublattices. In this chapter then, we review the Lindhard theory of energy partitioning. We show how the integral equations originally developed for monatomic solids can be modified in a manner which allows one to calculate how the energy of the incoming ion partitions, firstly between the electrons and ions of the solid, and then between the sublattices of a polyatomic solid. Having developed the appropriate integral equations we discuss the 'ZBL' cross sections and stopping powers used in the calculations. These are amongst the most accurate currently available and yield improved estimates over the simple Lindhard stopping powers for the energy deposited into nuclear collisions during particle irradiation. The effect of the target ionicity on the stopping cross sections is also discussed. We proceed to describe a method of numerical solution for the case of diatomic solids and then the results of partial damage energy calculations for various materials are presented. Finally, we use these partial damage energy functions to evaluate the number of point defects produced on both the oxygen and aluminium sublattices of sapphire under energetic particle bombardment.

§ 4.1 Integral Equations Governing Radiation Effects.

The modern approach to theoretical studies of radiation damage was first described in 1963 by Lindhard *et. al.* <1> in a remarkable paper. The equations derived were of such generality that nearly thirty years on they still form the basis for most studies of radiation effects. For this reason we present here a derivation of the basic integral equation, following closely the reasoning of the original authors. For the moment we confine ourselves to the case of self-ion irradiation of a monatomic solid.

Consider some physical quantity ϕ , as yet unspecified and arbitrarily taken to be zero prior to the irradiation, which will increase additively during the course of the irradiation. This may be, for example, the number of ion pairs in a gas or the number of electron-hole pairs in a semiconductor or indeed the number of colour centres in a crystal. Here we shall ultimately be interested in the case where ϕ represents the energy deposited into elastic nuclear collisions, the *damage* energy. Let the average value of ϕ following irradiation by an energetic particle of energy E (referred to as the ion) be $\overline{\phi}(E)$. If the ion moves a path length dR in a medium which has N atoms per unit volume then there is a probability $NdRd\sigma_{n,e}$ for a collision involving a transfer of energy T_n to the centre of mass of the struck atom, together with energy transfer T_{ei} to the target electrons. Here electrons are given the label i and $d\sigma_{n,e}$ represents the cross section for the total event. The collision will reduce the ion energy to the value $E-T_n-\sum_i T_{ei}$ and it will have a $\overline{\phi}$ value equal to $\overline{\phi}(E-T_n-\sum_i T_{ei})$. At the same time the struck atom will receive a $\overline{\phi}$ value of $\overline{\phi}(T_n-U)$, where U is the energy dissipated in breaking the atomic binding. The energetic electrons produced as a result of the collision may, in the general case, also be able to contribute to ϕ and so they must be described by another ϕ function, denoted as $\overline{\phi}_e$. Their contribution to $\overline{\phi}$ after the collision is then $\sum_i \overline{\phi}_e(T_{ei}-U_{ei})$, where U_{ei} are the corresponding ionization energies. The above probability multiplied by the total $\overline{\phi}$ value *after* the collision gives the contribution of this collision to $\overline{\phi}(E)$. We now integrate over all possible collisions, noting that if there is no collision the $\overline{\phi}$ value remains $\overline{\phi}(E)$. We may write a balance equation for $\overline{\phi}$ values as

$$\bar{\phi}(E) = NdR\int d\sigma_{n,e}\{\bar{\phi}(E-T-\sum_i T_{ei})+\bar{\phi}(T_n-U)+\sum_i \bar{\phi}_e(T_{ei}-U_{ei})\} + \ldots$$

$$\ldots+\bar{\phi}(E)\left(1-NdR\int d\sigma_{n,e}\right) . \qquad (4.1)$$

The last term in this equation expresses the probability of no collision occurring. Rearranging this leads to the basic integral equation governing the effects of the irradiation:

$$\int d\sigma_{n,e}\{\bar{\phi}(E-T_n-\sum_i T_{ei})-\bar{\phi}(E)+\bar{\phi}(T_n-U)+\sum_i \bar{\phi}_e(T_{ei}-U_{ei})\} = 0 . \qquad (4.2)$$

This equation has a simple physical interpretation which is that the $\bar{\phi}$ value of the incident particle before the collision is equal to the sum of the $\bar{\phi}$ values after the collision of, respectively, the particle itself, the struck atom and the excited electrons, averaged over the probability of occurrence of the individual processes with the cross section $d\sigma_{n,e}$. It is clear from the arbitrary nature of $\bar{\phi}$ that this integral equation is capable of describing many irradiation phenomena. Here, we have ignored any recombination processes which may subsequently reduce $\bar{\phi}(E)$ as these may be accounted for separately later. The only requirement has been that the physical quantity $\bar{\phi}(E)$ is additive. The theory will now be developed with the production of lattice defects in mind.

Lindhard *et. al.* <1> consider five schemes for simplifying eqn.(4.2), which they call approximations A, B, C, D and E. These names are frequently used by workers in the field and we shall follow this notation. The first approximation, A, is $\bar{\phi}_e = 0$. This is a mathematical statement of the fact that the energetic electrons produced during the slowing down of the incident ion are incapable of producing displacement damage. This is not the case in, for example, the alkali halides where energetic electrons are well known to produce lattice defects. However sapphire, as discussed in chapter 3, does not suffer from radiolysis and this assumption is valid for this material. Approximation B involves neglecting the binding energy of the atoms and is equivalent to setting U in eqn. (4.2) to zero. As a rough

guide, the binding energy is usually between one fifth to one quarter of the displacement threshold energy, which gives U values for sapphire of around 15 eV and 5 eV for oxygen and aluminium ions respectively. This is a good approximation in most radiation damage calculations, where recoil energies are usually much larger than atomic binding energies. The third approximation, C, is to assume that energy transfer to electrons is small compared to energy transfer to ions, *i.e.* $T_{ei} \ll E - T_n$. Again, this is valid when one considers recoils of an energy typically found in radiation damage studies.

The final levels of approximation, D and E, are the most widely used in the field of radiation damage. The first of these involves the added assumption of the separability of the nuclear and electronic coordinates. Here the idea is that a negligible part of the electronic excitation occurs at the small impact parameters where large kinetic energies are likely to be transferred to nuclei. Gathering all these approximations together allows eqn.(4.2) to be written in approximation D as

$$\bar{\phi}'(E)\, C_e(E) = \int d\sigma_n \{ \bar{\phi}(E - T_n) - \bar{\phi}(E) + \bar{\phi}(T_n) \} \ , \tag{4.3}$$

where $d\sigma_n$ is the cross section for differential energy transfer for elastic nuclear collisions, $C_e(E)$ is the electronic stopping cross section and the prime on $\bar{\phi}$ denotes differentiation with respect to energy. The final level of approximation, E, is to realise that the energy transferred in elastic nuclear collisions, T_n, is generally small compared to the ion energy E. The reason for this is that although the maximum energy transfer between two particles may be quite large (in fact it is equal to the ion energy if the masses are the same), $d\sigma_n$ is strongly biased towards small energy transfers, making the probability of an energy transfer of the order of E comparatively small. Expanding the first term in eqn.(4.3) in a Taylor series, approximation E amounts to retaining only the leading term and then the basic integral equation may be written as

$$\bar{\phi}'(E) \{ C_e(E) + C_n(E) \} = \int d\sigma_n \, \bar{\phi}(T_n) \ , \tag{4.4}$$

where we have written

$$C_n(E) = \int d\sigma_n(T_n) \quad . \tag{4.5}$$

This important quantity is known as the nuclear stopping cross section and its precise form will be discussed later. However we note here that it is simply related to the nuclear stopping power via

$$S_n(E) \equiv (dE/dx)_n = NC_n(E) \quad . \tag{4.6}$$

Equations (4.3) and (4.4) form the basis of most radiation damage calculations, *e.g.* <2,3,4> and are the approximations to the basic integral equation we shall be concerned with in this study. They are integro-differential equations with the unknown function $\bar{\phi}(E)$ occurring on the left-hand side as a derivative and on the right-hand side under an integral sign. Analytic solutions of these 'exciting but treacherous integral equations', as Sigmund has referred to them <5>, are possible if one uses simplified cross sections and neglects the electronic stopping cross section (see for example ref. <5>). This approach is useful in giving a qualitative indication of how $\bar{\phi}(E)$ varies at low energies, but an accurate determination requires a numerical solution. The method of obtaining such a solution will be discussed in § 4.5.

§ 4.2 Integral Equations for Polyatomic Solids.

As noted above, the unspecified nature of ϕ allows one to apply the above technique to determine the energy deposited elastically into the material by each pka type. Let us consider such a material with n components. Following the above reasoning we see that as a primary knock-on atom of type i moves through the material it will lose energy through electronic excitation and in elastic collisions with the various types of host atoms, sharing its energy amongst them in some proportion to be determined. Coulter and Parkin <2> have defined the damage energy function $\nu_k(E)$ to be the energy deposited elastically into the material by a type k pka with energy E and derived, within approximation D, the equation it must obey.

The present investigation requires more information than this. The experiments to be described in chapter 6 are only capable of determining the concentration of optically active oxygen vacancies and hence it is this quantity that must be calculated for comparison with experiment. For this purpose we define a *partial* damage energy matrix, ν. The meaning of the matrix element $\nu_{ij}(E)$ is that it represents the energy deposited elastically into the j nuclear system by an i type pka of energy E. Within approximation D, $\nu_{ij}(E)$ obeys the following equation,

$$\nu_{ij}'(E)\,S_e^{(i)}(E) = \sum_k N_k \int d\sigma_{ik}(E;T)\{\,\nu_{kj}(T) - \nu_{ij}(E) + \nu_{ij}(E-T)\,\}\ , \tag{4.7}$$

whilst within approximation E this simplifies to <4>

$$\nu_{ij}'(E)\,S_t^{(i)}(E) = \sum_k N_k \int d\sigma_{ik}(E;T)\{\,\nu_{kj}(T)\,\}\ . \tag{4.8}$$

In these equations $d\sigma_{ij}$ denotes the cross section for a type i projectile colliding with a type j atom (we have made the dependences explicit here: in the expression for $d\sigma_{ij}$, E appears as a parameter and T as a variable). $S_e^{(i)}(E)$ denotes the electronic stopping power of a type i ion in the compound material whilst $S_t^{(i)}(E)$ denotes the *total* stopping power (nuclear plus electronic) of a type i ion in the compound material. The relationship with the quantity $\nu_k(E)$ defined by Coulter and Parkin <2> is simply

$$\nu_k(E) = \sum_{j=1}^{n} \nu_{kj}(E)\ , \tag{4.9}$$

whilst the total energy deposited elastically into the j sublattice is given by

$$\nu_j(E) = \sum_{i=1}^{n} \nu_{ij}(E)\ . \tag{4.10}$$

Having characterised the energy deposited into a given sublattice by the various pka's we

are now in a position to estimate point defect production. We use the NRT model described in chapter 2 but replace the damage energy with the *partial* damage energy and use the displacement threshold appropriate to the sublattice. Then the number of displacements produced on the j^{th} sublattice by irradiation with a foreign ion, type k and energy E, is given by the following double integral

$$N_{dj}(E) = \sum_i \int_{E_{di}}^{E} \left\{ \frac{N_i \int_{E_{di}}^{T_m^{ki}} \Psi_{ij}(T)\, d\sigma_{ki}(E';T)}{S_t^{(k)}(E')} \right\} dE' , \qquad (4.11)$$

where

$$\Psi_{ij}(T) = \begin{cases} 0, & T < E_{dj} \\ 1, & E_{dj} \le T \le 2E_{dj}/\kappa \\ \dfrac{\kappa \nu_{ij}}{2E_{dj}}, & T > 2E_{dj}/\kappa \end{cases} . \qquad (4.12)$$

This is the equation evaluated in the present work, with κ set equal to the NRT value of 0.8. We now describe the various functions and parameters used in these calculations.

§ 4.3 Scattering Cross Section and Stopping Powers.

The solution of eqn.(4.8) and the evaluation of eqn.(4.11) requires knowledge of the scattering cross section and both electronic and nuclear stopping cross sections. If an explicit expression is not available for $C_n(E)$ then it may be calculated directly from the form of $d\sigma_n$ via eqn.(4.5).

Nuclear Stopping. As shown in chapter 2, the nuclear stopping cross section can be derived by solving the scattering integral for the scattering angle Θ, once the interatomic potential is known. Many authors (e.g. refs. <2,3,4>) have followed Lindhard *et. al.* <1> and used an interatomic potential derived from the Thomas-Fermi atom. Other authors have used the Moliere <6> or Lenz-Jensen <7> potentials. These semi-classical, universal potentials have the useful property that the results scale from one atomic number to another in a simple

manner, but the accuracy of the results is not high. In the late 1970's Hartree-Fock atomic charge distributions were first used to perform more accurate estimates of stopping and collision cross sections <8>. This work has recently been extended by Ziegler, Biersack and Littmark (ZBL) <9> who have derived potentials from solid-state, rather than atomic, charge distributions and developed a universal interatomic potential. Defining the interatomic screening function as

$$\Phi = \frac{V(r)}{(Z_1 Z_2 e^2/r)} \ , \tag{4.13}$$

they find that Φ is well represented by

$$\Phi = 0.1818\, e^{-3.2x} + 0.5099\, e^{-0.9423x} + 0.2802\, e^{-0.4028x} + 0.02817\, e^{-0.2016x} \ , \tag{4.14}$$

where $x = r/a_u$ is a reduced length and a_u is the ZBL screening parameter

$$a_u = \frac{0.8554\, a_0}{(Z_1^{.23} + Z_2^{.23})} \ . \tag{4.15}$$

This reduced radial coordinate was found by these authors to give a much tighter grouping of the data than the Thomas-Fermi screening function mentioned in chapter 2. The scattering integral was solved by ZBL using this universal potential and values of the stopping cross section were calculated with eqn.(4.5). To enable efficient numerical evaluation of nuclear stopping powers the following function was fitted to the calculated values of $C_n(\varepsilon)$

$$C_n(\varepsilon) = \frac{\ln(1 + a\,\varepsilon)}{2(\varepsilon + b\varepsilon^c + d\varepsilon^{1/2})} \ , \tag{4.16}$$

where ε is the Lindhard reduced energy and the fitting coefficients are

$$a = 1.1383 \, ; \ b = 0.01321 \, ; \ c = 0.21226 \, ; \ d = 0.19593 \ .$$

For values of $\varepsilon > 30$ the screening becomes negligible and the nuclear stopping becomes Rutherford – like. In this case the unscreened stopping cross section is

$$C_n(\varepsilon) = ln(\varepsilon)/(2\varepsilon) \ . \tag{4.17}$$

Scattering Cross Section. Having obtained a functional form for the nuclear stopping cross section one may invert eqn.(4.5) to obtain an analytic expression for the scattering cross section in terms of ε. In this way we find

$$d\sigma = \{\frac{-\pi a_u}{2}\} \frac{f(t^{1/2})\,dt}{t^{3/2}} \quad , \tag{4.18}$$

with

$$f(x) = \frac{d}{dx}\,[xC_n(x)] \quad . \tag{4.19}$$

Evaluating this derivative gives

$$f(x) = \frac{\ln A}{2B} + \frac{ax}{2AB} - \frac{x(\ln A)(1 + bcx^{c-1} + d/(2x^{1/2}))}{2B^2} \quad ,$$

with (4.20)

$$A = (1+ax) \text{ and } B = (x+bx^c+dx^{1/2}) \quad .$$

Note the misprint in ref.<9>, where the first term in the expression for B should only appear to the *first* power, as shown here. Some comments are in order regarding the validity of a differential cross section derived in this way. Eqn.(4.5) may be regarded as the first moment of the energy transfer distribution and by inverting this formula to obtain the differential scattering cross section we are of course assured that this cross section will generate the correct nuclear stopping power. There is no guarantee though that the higher moments of the distribution will be correctly described by this cross section and it is these higher moments which control point defect production near the displacement threshold. It may then be necessary to impose other physical arguments to give a good account of defect production and this is in fact the procedure adopted in the modified Kinchin-Pease approach.

Electronic Stopping. This subject is very complex and we shall only mention the briefest details of the ZBL scheme here. A complete discussion can be found in ref.<9>. Although these stopping cross sections involve considerably more computational and programming effort than the simple Lindhard expression mentioned in chapter 2, the increased effort is rewarded with much higher accuracy. ZBL claim an accuracy of better than 10% for light ion stopping and an accuracy of better than 5% for helium and proton stopping.

The main idea of these semi-empirical stopping cross sections is to use a scaling law relating heavy ion stopping to equivalent proton stopping via the relation

$$C_{HI} = C_P(Z^*_{HI})^2 = C_P Z_{HI}{}^2 \gamma^2 \ , \qquad (4.21)$$

where the subscript *HI* refers stands for heavy ion and the P for proton. Z^* indicates the effective charge state of the ion as it moves through the solid and the right-hand equality shows that this is normally written as the product of the full nuclear charge and γ, the *fractional* effective charge. This procedure of scaling proton stopping cross sections has been applied to the prediction of helium stopping powers and has produced very reliable results. This is significant since helium stopping cross sections have been measured more often and with greater accuracy than for any other ion as a consequence of the need for an extensive data base for helium Rutherford Back-Scattering (RBS) materials analysis. Applying this scaling theory to heavy ion stopping involves a number of steps:

(a) the relative velocity of the ion with respect to the target Fermi velocity is calculated

(b) the fractional ionization of the ion is calculated

(c) the screening length of the ion is calculated as a function of the ion's charge state

(d) the fractional effective charge, γ, of the ion is calculated

(e) the equivalent proton stopping cross section is calculated

(f) and finally the ion stopping cross section is found using eqn.(4.21).

The proton stopping cross sections must be calculated separately for each element and ZBL have provided a data base of fitting constants to enable their evaluation for all ninety two naturally occurring elements.

A computer program was written to evaluate both electronic and nuclear ZBL stopping cross sections, following the method given above by these authors in ref. <9>. In fig.2.4 of chapter 2 a comparison of ZBL and Lindhard stopping cross sections up to 10 MeV was given for the elements comprising sapphire. The differences in the electronic stopping cross sections are most pronounced above several MeV but are significant even below 1 MeV. These differences will be carried over to the partial damage energy calculations, since the electronic stopping power appears in eqn.(4.8) and so one can expect improved accuracy for estimates of defect production by using the ZBL values.

§ 4.4 Modifications of Stopping Powers in Ionic Solids.

The original literature on stopping theory and most recent works have considered the target to be either neutral atoms or metals in which the charged ionic core is fully screened outside the Wigner-Seitz cell. We now wish to consider how the stopping and scattering cross sections described above must be modified in ionic insulators where (i) the Coulomb force of an ion core extends beyond many nearest neighbours and (ii) the band gap may prohibit certain electronic excitations. These problems appear to have first been addressed by Biersack and Stadele <10>.

Nuclear Stopping. The long range nature of the Coulomb force in ionic solids allows a transfer of energy between an energetic ion and distant target atoms. In a classical theory of stopping this would yield an infinite nuclear stopping cross section but quantum theory removes this divergence by taking into account the bound states of the target ions in the lattice. For example, if the ions are held in their lattice positions by potential wells which correspond to an oscillation frequency f of around 10^{13} Hz, then the quantisation of the oscillator energy forbids energy transfers to these atoms which are less than ~ 10^{-2} eV. This minimum energy transfer effectively limits the Coulomb interaction to finite ranges and one is able to define a maximum impact parameter, p_ω, beyond which no energy transfers may take place. If we further define a parameter p_s, which corresponds to the impact parameter for a neutral Thomas-Fermi atom beyond which there is no energy transfer, then the extra contribution to the nuclear stopping cross section made by the ionic nature of the target atoms is

$$C_n^* = \varepsilon \int_{p_s}^{p_\omega} \sin^2 \frac{\theta}{2}\, d(p^2) \ , \tag{4.22}$$

in reduced units. Biersack and Stadele evaluate this integral for a purely Coulombic interaction and obtain

$$C_n^* = \frac{\phi_\infty{}^2}{4\varepsilon} \ln\left[\frac{T_m / hf}{1+(2\,\varepsilon p_s / \phi_\infty)^2}\right] \ , \tag{4.23}$$

where

$$\phi_\infty = \frac{Z_1^* Z_2^*}{Z_1 Z_2} \quad . \tag{4.24}$$

Here, Z_1^* and Z_2^* represent the *ionic* charges of the projectile and target ions respectively. The lattice frequency selected by Biersack and Stadele for use with this formula is that of the longitudinal optical (LO) phonon.

Evidence for this enhanced nuclear stopping in ionic solids has recently been presented. Izsak *et. al.* <11> have used RBS to measure the range of low energy ions incident on sapphire. They estimate that their technique is capable of resolving range differences of the order of 10 Å and so is able to follow the stopping of ions down to reduced energies of around 2×10^{-4}. These authors measured the range of Au, Cs and Xe in sapphire and found that at low energies Cs showed a relatively strong deviation towards lower ranges than those predicted on the basis of a non-polar target. Xe ranges agreed well with theory whilst Au was intermediate between the two. The data is reproduced in fig. 4.1, where the effect can be seen to cause a reduction of about a factor of three in the range of Cs ions with a reduced energy of 10^{-3}. The effect produces negligible differences in range for energies greater than about 10^{-2}. These results appear to support the Biersack and Stadele theory. The enhanced nuclear stopping cross section depends on the effective charge of the projectile Z_1^* and these results suggest that Z_1^* (Cs) > Z_1^* (Au) > Z_1^* (Xe). This is reasonable given the binding energies of valence electrons in these atoms which are 3.89, 9.22 and 12.13 eV respectively <12>. Thus Xe^+ can pick up an electron from the host lattice (most probably from O^{2-} in sapphire), but Cs will remain ionized. Au represents an intermediate case. The data of Izsak *et. al.* indicate that Z_1^* (Cs) ~ 1, Z_1^* (Au) ~ 0.4 and Z_1^* (Xe) ~ 0.

At first sight the existence of an enhanced nuclear stopping power at low ion energies might appear to have serious implications for damage production in ionic solids since the stopping power is intimately related to the scattering cross section. However the nature of this effect is to effectively increase the number of *low* energy scattering events rather than those collisions which result in the displacement of the target atom. For example, a collision involving the transfer of energy of some tens of eV (a typical displacement energy) requires

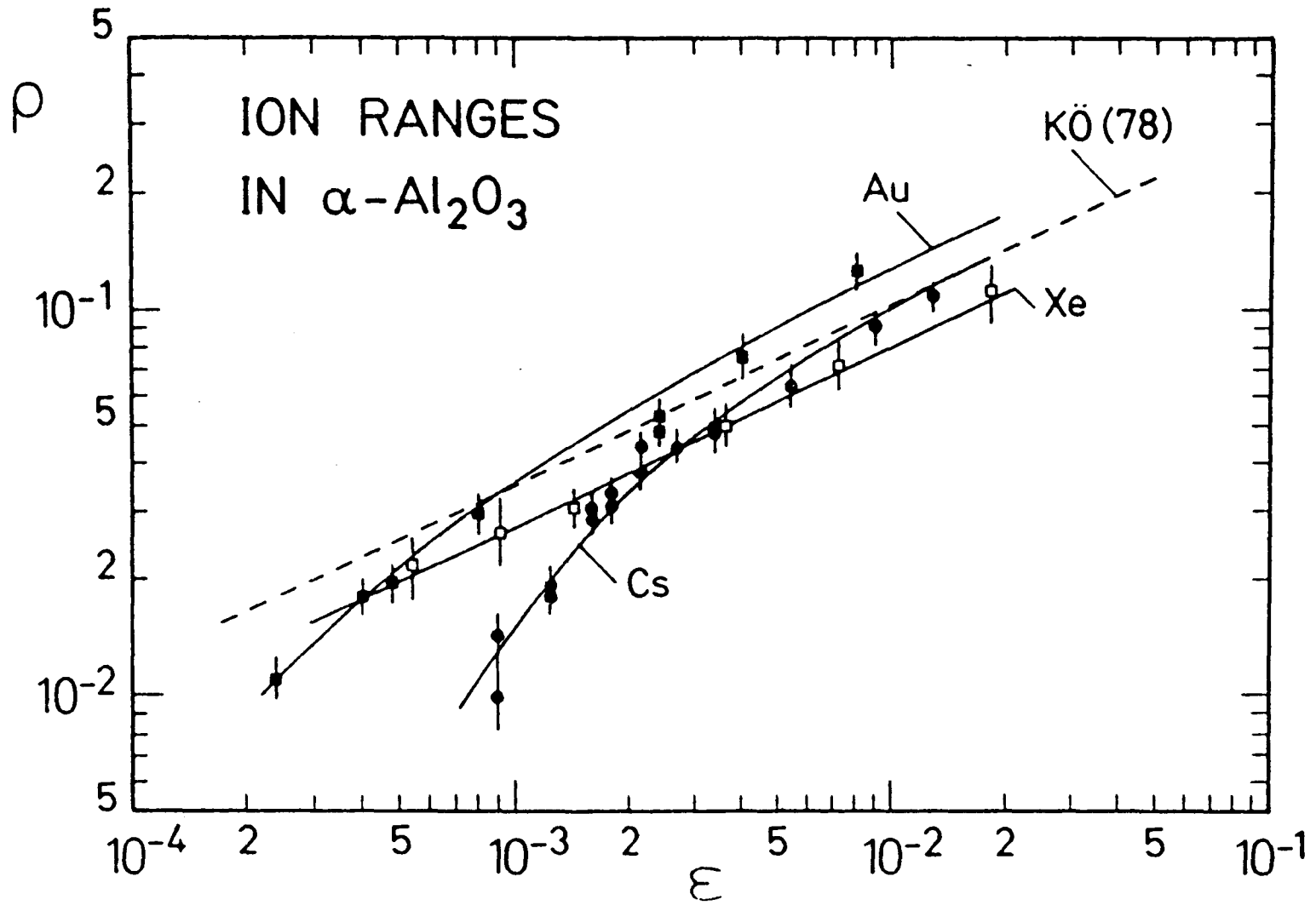


Fig. 4.1. Comparison of experimental (points) and theoretical (dased line) range variation with energy, in reduced units, for Au, Xe and Cs. At low energies Cs shows a relatively strong deviation towards lower energies. Ref. <11>.

the impact parameter to be somewhat less than 1 Å, so that these collisions are governed by the 'normal' repulsion of ion cores. The long range Coulomb forces have very little influence on such collisions. Thus for the purposes of calculating displacement rates in ionic solids we are justified in using a scattering cross section which ignores the polar character of the target.

Additional mechanisms of energy loss to the nuclear system in ionic solids have been considered by Biersack and Stadele. They point out that although the interaction time of a projectile with a target atom may be too short to allow the transfer of one quantum of vibrational energy, the transient electric field of the passing ion may be so sharply peaked that its photons carry enough energy to excite LO phonons in the lattice. This would be the case if the interaction time corresponds to a frequency $hf > hf_{LO}$. Thus although any given single ion does not receive sufficient energy to excite one vibrational quantum, a large number of them acting in a collective motion may still absorb the energy into lattice vibrations. It was found in actual calculations though that this mechanism made only a small correction to the nuclear stopping power at low energies, and for the purposes of damage production is negligible.

Electronic Stopping. As discussed above, modern treatments of the electronic stopping cross section involve the treatment of each volume element of the target as an independent plasma (the local density approximation). The lower the ion velocity becomes the less able it is to penetrate the high electronic density regions of the target atomic cores and so at low velocities only the valence electrons contribute to the stopping. In an ionic solid then, where the outermost electrons are tightly bound and separated from higher unoccupied states by a band gap of several eV, a slow moving projectile may become unable to excite *any* target electrons and the electronic stopping power would vanish. Various experimental data have been analysed by Biersack <13> who found no evidence for such an effect. Electronic stopping cross sections which were determined for elemental targets appeared to be well applicable for insulators and so no adjustments have been made to the ZBL electronic stopping powers used in the partial damage energy calculations reported here, to account for the polar nature of targets.

We now return to the integral equations which the partial damage energies must obey and discuss the method of their solution.

§ 4.5 Method of Numerical Solution of Integral Equations.

The present calculations were mostly performed within approximation E and so we give below the equations for the deposition of energy into the type 1 sublattice of a diatomic solid explicitly, since the number of subscripts in eqn.(4.8) may cause some confusion.

$$\nu'_{1,1}(E)\, S_t^{(1)}(E) = N_1 \int d\sigma_{1,1}(E;T)\{\nu_{1,1}(T)\} + N_2 \int d\sigma_{1,2}(E;T)\{\nu_{2,1}(T)\}$$

(4.25)

$$\nu'_{2,1}(E)\, S_t^{(2)}(E) = N_1 \int d\sigma_{2,1}(E;T)\{\nu_{1,1}(T)\} + N_2 \int d\sigma_{2,2}(E;T)\{\nu_{2,1}(T)\} \quad .$$

Since the unknown functions appear on both sides of the equation an iterative technique must be used whereby a trial functional form is assumed for the $\nu_{ij}(E)$ and this is used to evaluate the integral appearing on the right-hand side. This is done for a number of energies E, enabling the derivative appearing on the left-hand side to be integrated with respect to energy. We then have a single value of the partial damage energy function. This procedure is repeated at a number of different energies sufficient to cover the range of interest. In the present case the calculations were taken up to 800 keV. This process is repeated for $\nu_{2,1}(E)$ using the trial function. At this stage we have a first order approximation to both partial damage energy functions $\nu_{1,1}(E)$ and $\nu_{2,1}(E)$. These functions can then be inserted on the right-hand side of eqn. (4.8) and the whole process repeated, each iteration giving an improved estimate of the partial damage energy functions. In an important paper, Miller and Boring <14> have shown that for a monatomic solid this iterative process can be given a simple physical interpretation. They demonstrated that successive iterations correspond to 'allowing' further generations of the knock-on atoms to lose energy in electronic excitation processes. Thus not only is the final damage energy function of interest, but the amount of ionisation associated with each generation of knock-on atoms can also be determined. As pointed out by Matsutani and Ishino <4>, this simple correspondence does not hold strictly in a diatomic solid, but nevertheless the idea is still qualitatively useful in interpreting the results of such calculations.

The iteration process must start somewhere and several trial functions suggest themselves from physical considerations. One normally tries to choose a trial function which also represents the low energy behaviour of the cascade and can act as a boundary condition to the numerical integration. The simplest choice is to set $\nu_{ij}(E) = n_j E$ where n_j is the atom-fraction of j type atoms. Physically this corresponds to the case where the incident ion but not the pka's are allowed to lose energy in electronic excitation. Two possible trial functions are suggested by Matsutani and Ishino. Defining

$$\eta_{il}(E) = \frac{N_l C_n^{(il)}(E)}{\sum_j N_j C_n^{(ij)}(E)} \quad , \tag{4.26}$$

where $C_n^{(il)}$ is the nuclear stopping cross section for type i atoms bombarding type l atoms, they suggest either

$$\frac{\nu_{ij}(E)}{E} = \lim_{E \to 0} \eta_{ij}(E) \tag{4.27}$$

or, in the case of a binary target,

$$\frac{\nu_{1,1}(E)}{E} \cong \frac{\nu_{2,1}(E)}{E} = \lim_{E \to 0} \frac{\eta_{2,1}(E)}{\eta_{1,2}(E) + \eta_{2,1}(E)}$$

and (4.28)

$$\frac{\nu_{1,2}(E)}{E} \cong \frac{\nu_{2,2}(E)}{E} = \lim_{E \to 0} \frac{\eta_{1,2}(E)}{\eta_{1,2}(E) + \eta_{2,1}(E)} \quad .$$

These authors show that the first case corresponds to only considering a partition of energy amongst *primary* knock-ons whilst the second set of equations result when subsequent branches of the cascade are included. A boundary condition which is not restricted by the assumption of vanishing electronic losses at low energies can also be introduced. This has the form

$$\nu_{ij}(E) = \int_0^E \frac{N_j C_n^{(ij)}(T)}{\sum_k N_k C_n^{(kj)}(T)} \, dT \quad . \tag{4.29}$$

Calculations were performed using this both as the trial function for $\nu_{ij}(E)$ *and* as a boundary condition for its value below 200 eV. Although from a theoretical point of view this is more satisfactory, the calculations take considerably longer to run and the results did not differ significantly from those obtained with the simpler boundary conditions of eqn.(4.28). In practice the results do not appear particularly sensitive to the choice of boundary condition. Matsutani and Ishino find differences of several percent between the results calculated using eqn.(4.27) rather than (4.28) and this was confirmed with the present calculations.

In practice about five or six iterations are required to achieve convergence to within one or two per cent. At the end of each cycle the functions obtained are divided into three ranges:

$$0 \le E \le 0.2\,, \quad 0.2 < E \le 10, \quad \text{and} \quad 10 < E \le 800 \ \text{keV}\ . \tag{4.30}$$

The value of the partial damage energy function in the first range is determined solely by the boundary conditions discussed above. In the second range $\nu_{ij}(E)$ is fitted to a function of the form

$$\nu_{ij}(E) = \frac{E}{1+\alpha E^{.15}+\beta E^{.75}+\gamma E}\ . \tag{4.31}$$

This type of function was first used by Robinson <15>, following the deduction by Lindhard *et. al.* <1> of the asymptotic behaviour of the damage energy. However the particular form used here was found by Coulter and Parkin <2> to give a somewhat more accurate representation of Lindhard's original data. In the third range a generalised form of the Robinson function was used

$$\nu_{ij}(E) = \frac{E}{1+aE^{.15}+bE^{.75}+cE+dE^{.2}+eE^{.3}+fE^{.5}}\ . \tag{4.32}$$

The reason for this division of the energy range is that it is difficult to find a single function with variable coefficients which will represent the partial damage energy function over the whole range of interest. Although more terms could be added to the expression in eqn.(4.32), quotients of this form have one troublesome quality – if one or more of the fitting coefficients are negative the denominator can have one or more roots, making the function singular at these points. This invariably wrecks the numerical integration scheme. It was

found empirically that these singularities usually occur below 10 keV so in this region a separate Robinson function was used. The six fitting coefficients of the high energy range, together with the two of the intermediate range (one point is fixed by the boundary conditions) allows us to calculate the partial damage energy function at eight energies throughout the range of interest. The fitting coefficients were then determined by solving eqns.(4.31) and (4.32) using a matrix inversion subroutine.

§ 4.6 Results.

The iteration procedure for solving eqn.(4.25) is illustrated in fig. 4.2, where the results of successive iterations for two of the partial damage energies for sapphire are shown. As noted earlier, each iteration gives an indication of the degree of ionisation associated with successive generations of knock-ons. In the six pages comprising fig. 4.3 we present the partial damage energy curves for Al_2O_3, MgO, CaO, ZnO, TaO and UO_2. The curves are all set out in the form

Oxygen – Oxygen	Cation – Oxygen
Oxygen – Cation	Cation – Cation

where first species given is the energetic ion and the second is the sublattice. Thus

Aluminium Oxide

Al – O

indicates that this is the curve giving the energy deposited into the oxygen sublattice by aluminium knock-ons in sapphire.

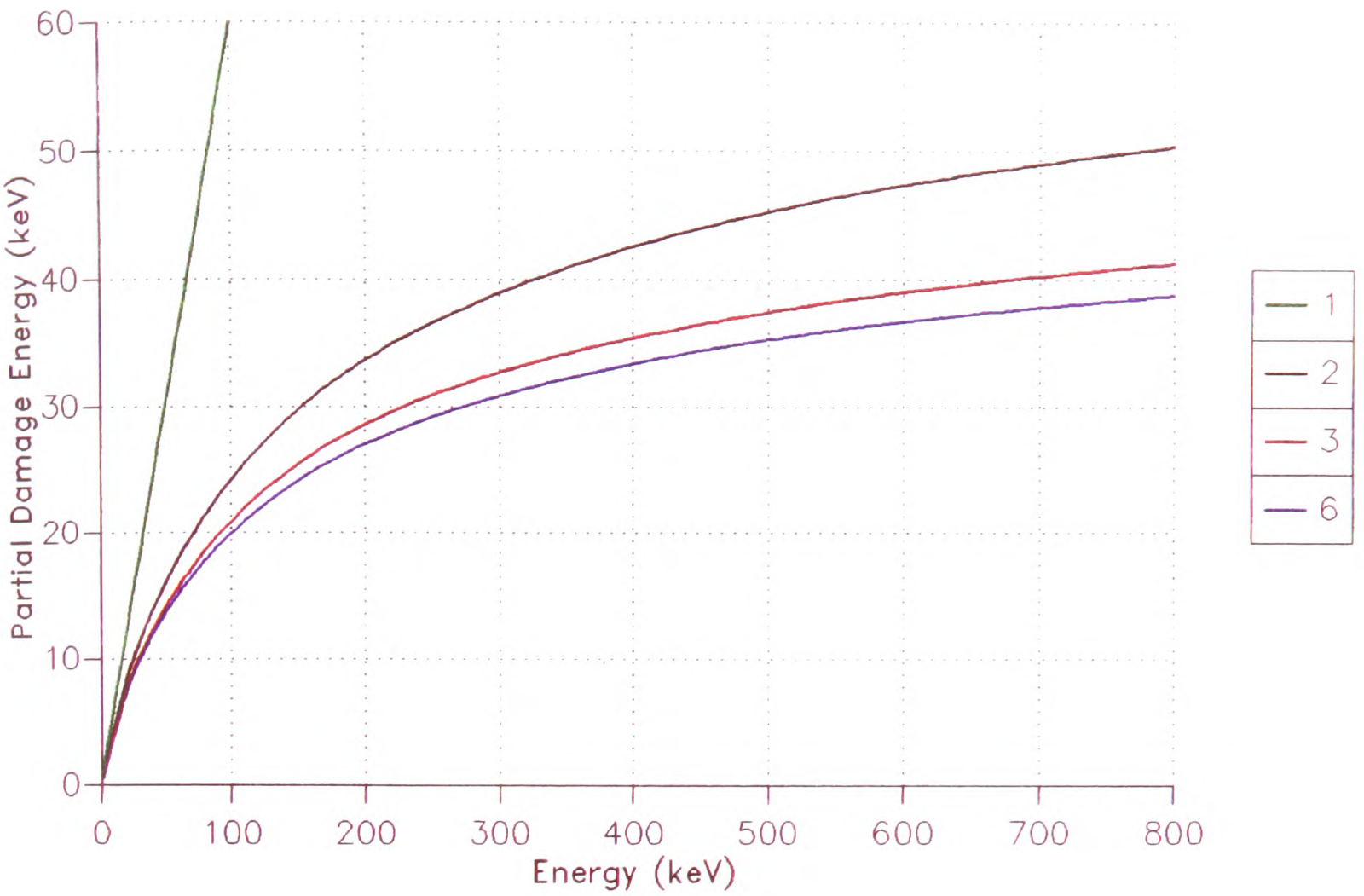
The results for Al_2O_3 are, of course, central to the present investigation. Results are also presented for UO_2 due to its technological importance as a nuclear fuel. Calculations for the oxides of magnesium, calcium, zinc and tantalum were performed to illustrate the effect of increasing cation mass on the energy deposited into the oxygen sublattice. The interaction between the two sublattices can clearly be seen here by noting differences in the O-O curve for each material. The energy deposited into the O sublattice by energetic O pka's is seen to

increase slowly as the cation mass increases from Mg through to Zn. This is due to the fact that an O pka can deposit energy into the O sublattice either by the direct mechanism of colliding with O target atoms or by the indirect mechanism of first colliding with cations which *then* collide with O atoms. In fact a quasi-infinite number of such indirect mechanisms exist where collisions with different sublattices are made by different generations of knock-on. The partial damage energy curve represents the weighted summation of all these possible pathways. The trend of increasing O-O partial damage energy with mass appears to be broken in going from zinc oxide to tantalum oxide. This can be traced to the enhanced O-Zn interaction over that of O-Ta. Thus for a given energy, O knock-ons are able to produce more energetic cation knock-ons in Zn than Ta (this is the outcome of a complex balancing of the different atomic numbers, masses and electronic stopping powers of the interacting atoms). The Zn knock-ons are then able to deposit more energy in the O sublattice in subsequent collisions.

It is often useful to have an analytic expression for the partial damage energies and so the final iteration of each partial damage energy was fitted with three coefficients in an equation of the form of eqn.(4.31). These are given in table 4.1. Following this, in fig. 4.4, we present the curves giving the number of displacements produced on both the oxygen and aluminium sublattices in sapphire under ion irradiation. These are the results of evaluating eqn.(4.11) for each ion, for a range of energies. These calculations were performed for the following ions: H, D, He, B, N, O, Ne, Al, Ar, and Kr. The values of displacement threshold used were 24 and 79 eV for the aluminium and oxygen sublattices respectively. The measurements on which these values are based are described in the next chapter.

Fig. 4.2. Iterative steps in the solution of eqn.(4.25). Here we show the first, second, third and sixth iterations in the approach to convergence of the partial damage energy functions for oxygen knock-ons in the oxygen sublattice of Al_2O_3 and aluminium knock-ons in the aluminium sublattice.

O-O


Partial Damage Energy (keV)
60
50
40
30
20
10
0
0
100
200
300
400
500
600
700
800
Energy (keV)
1
2
3
6

Al-Al

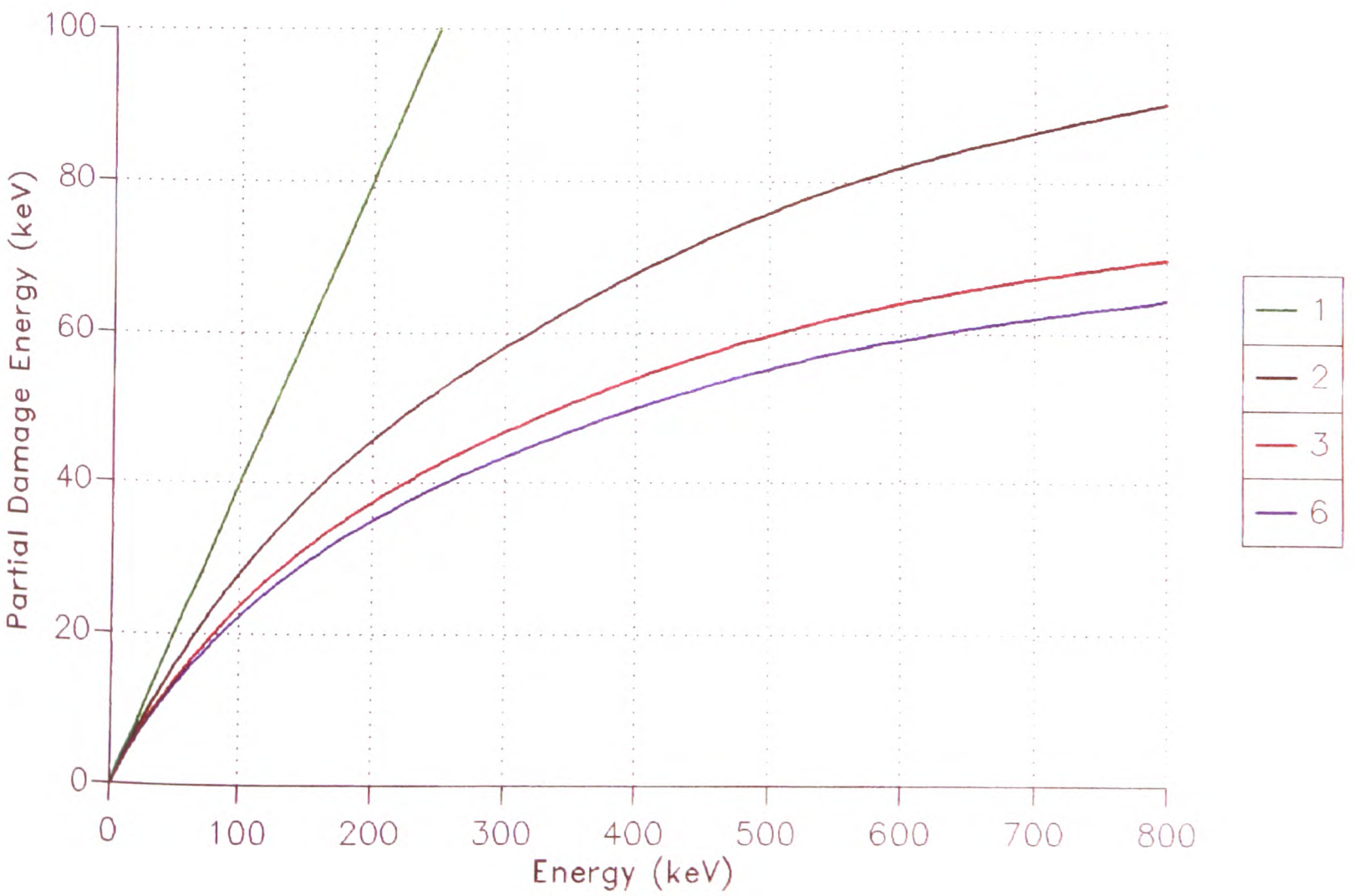
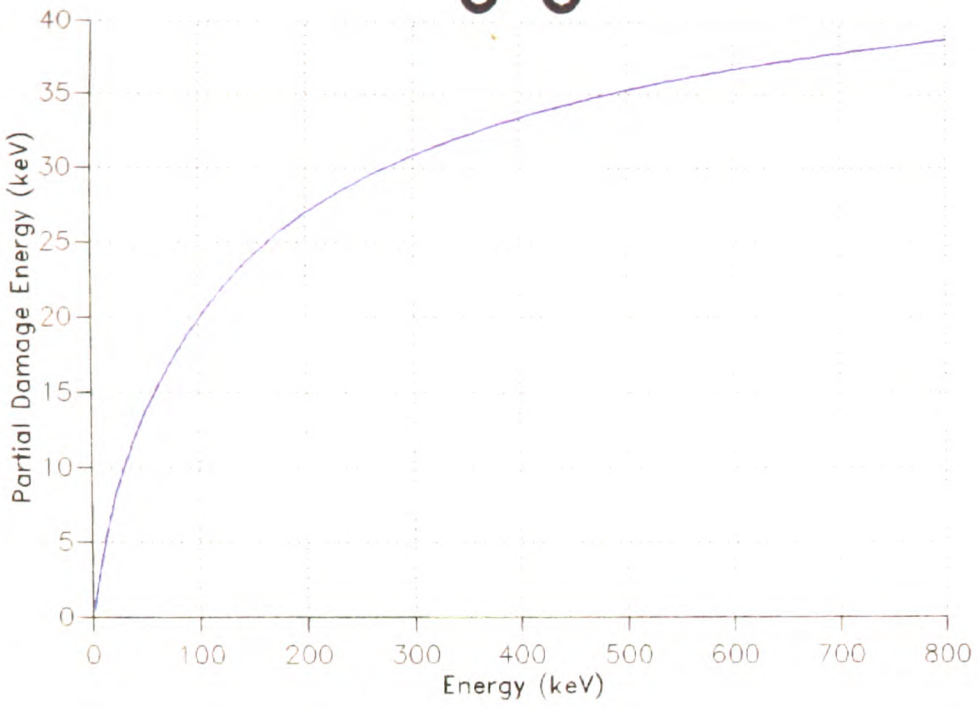
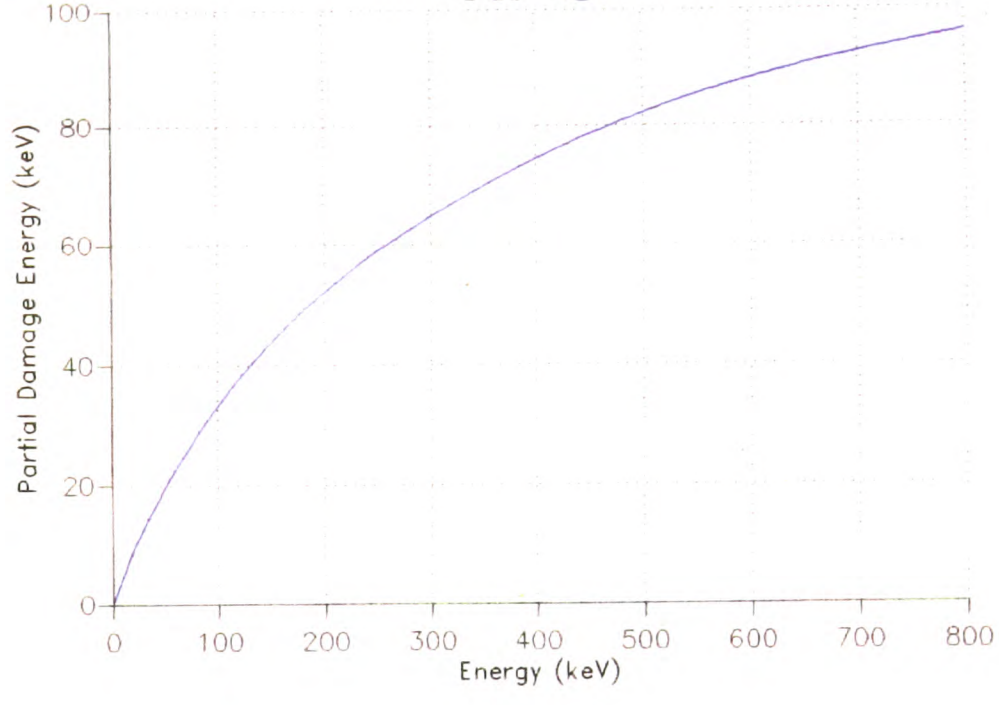

Partial Damage Energy (keV)
100
80
60
40
20
0
0
100
200
300
400
500
600
700
800
Energy (keV)
1
2
3
6

Fig. 4.3. Partial damage energy curves for Al_2O_3, MgO, CaO, ZnO, TaO and UO_2.

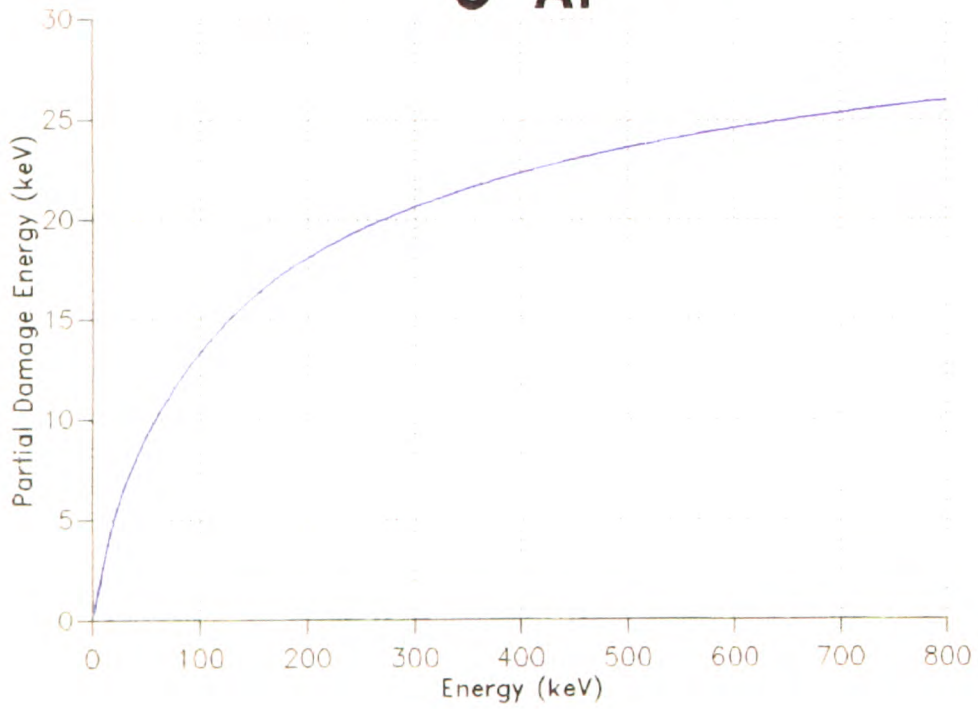
Aluminium Oxide
O-O



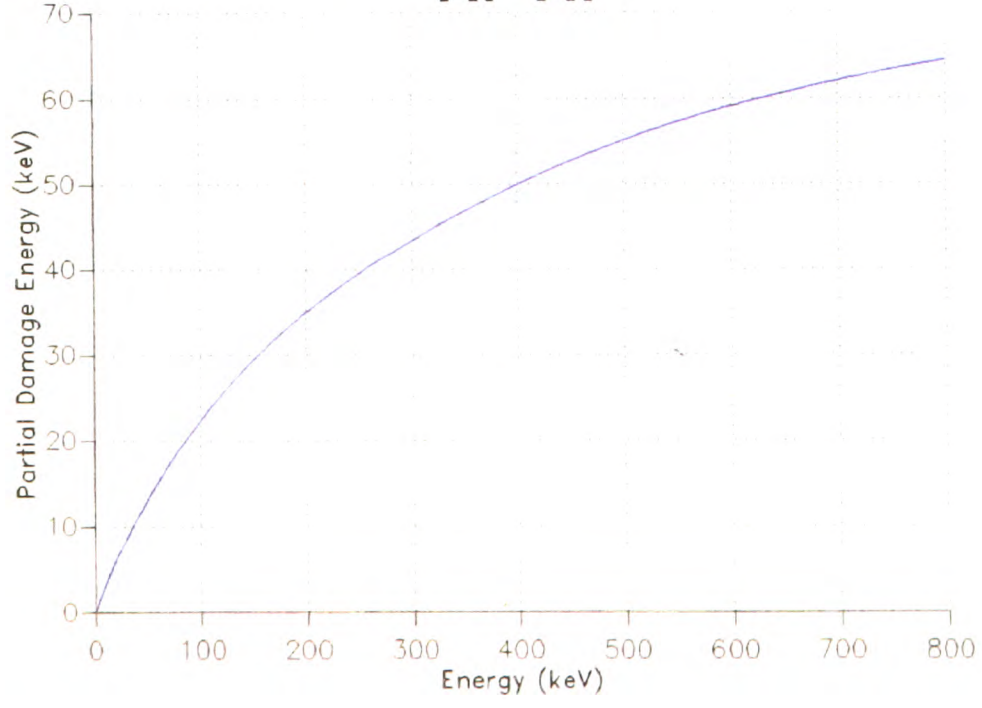
Aluminium Oxide
Al-O



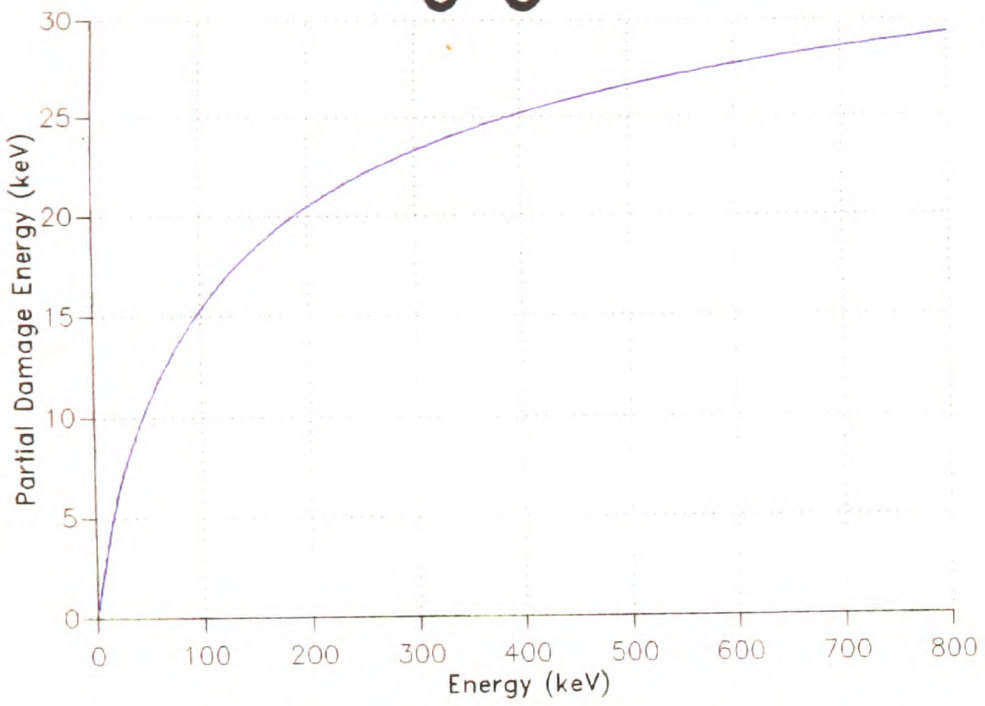
Aluminium Oxide
O-Al



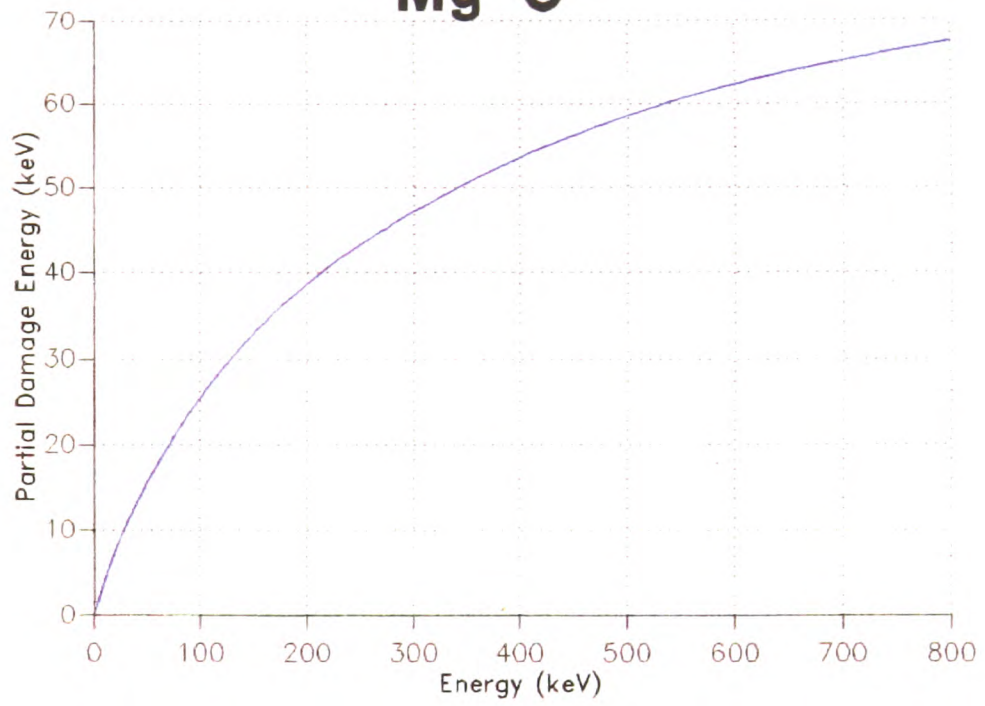
Aluminium Oxide
Al-Al



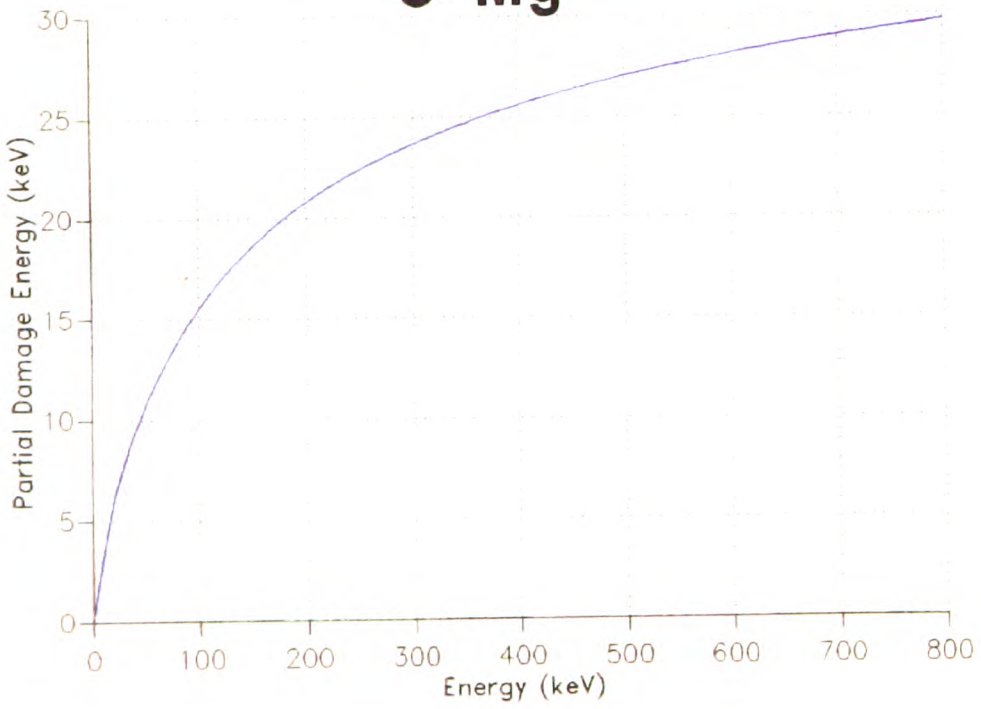
Magnesium Oxide
O-O



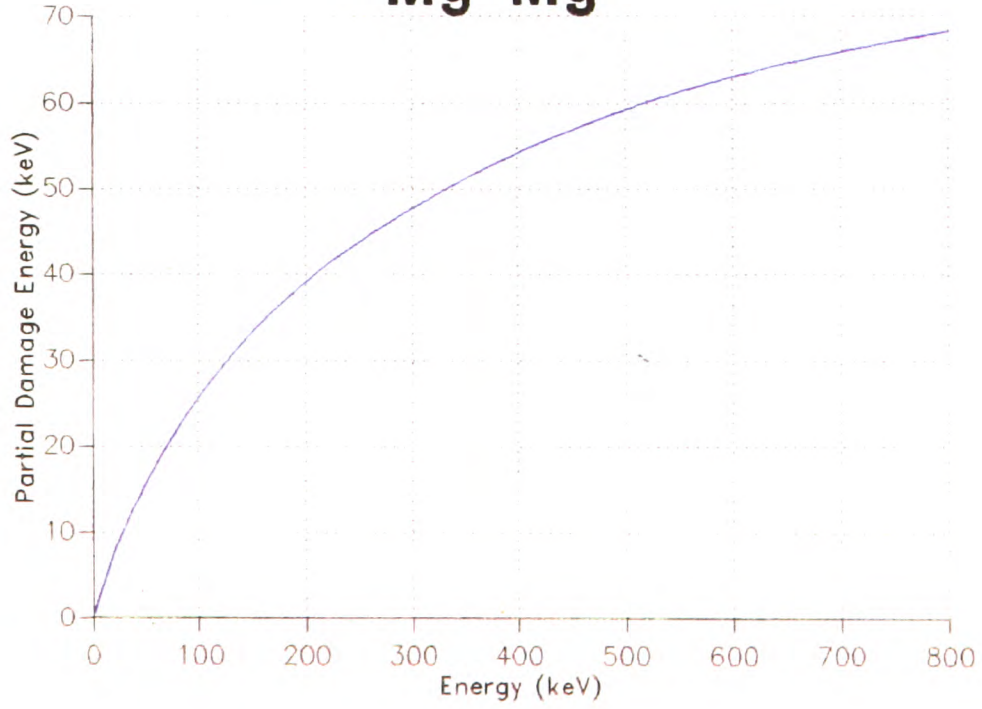
Magnesium Oxide
Mg-O



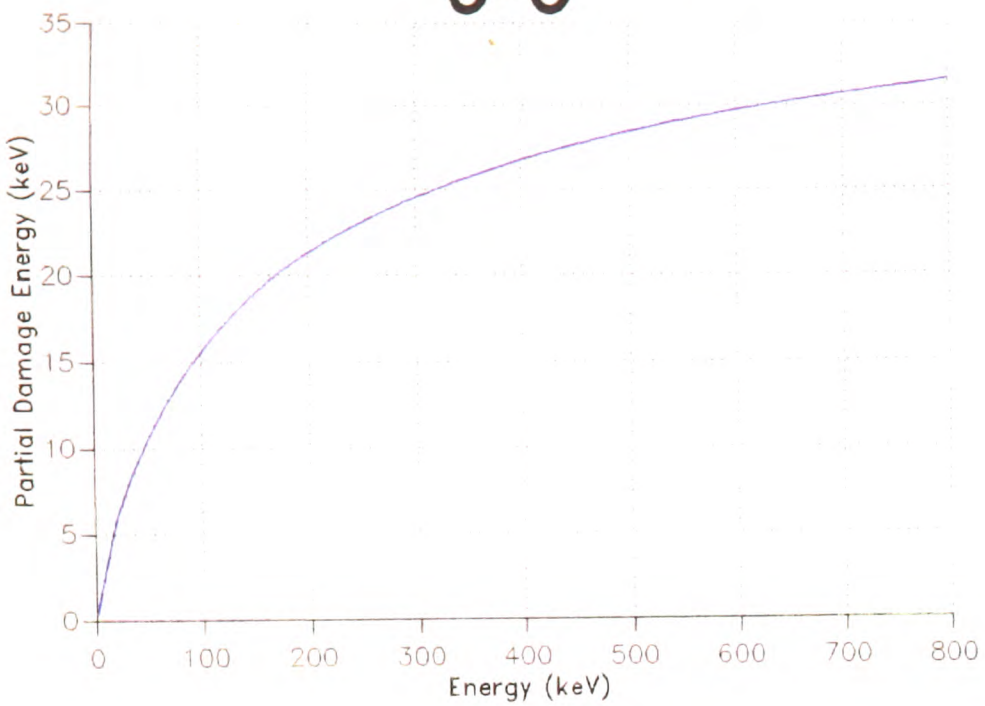
Magnesium Oxide
O-Mg



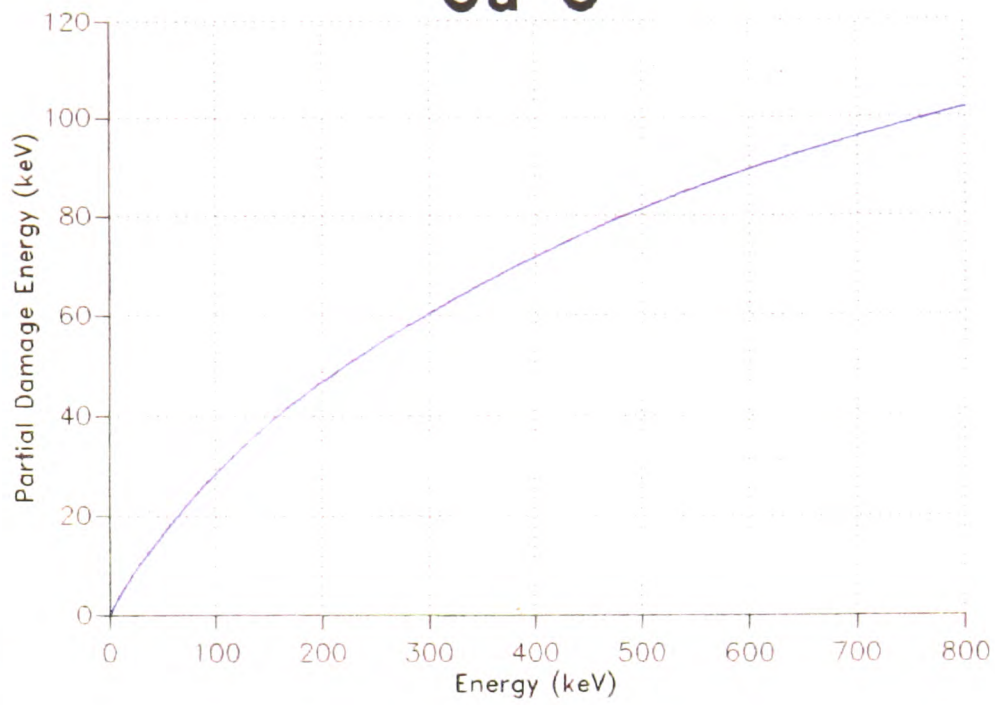
Magnesium Oxide
Mg-Mg



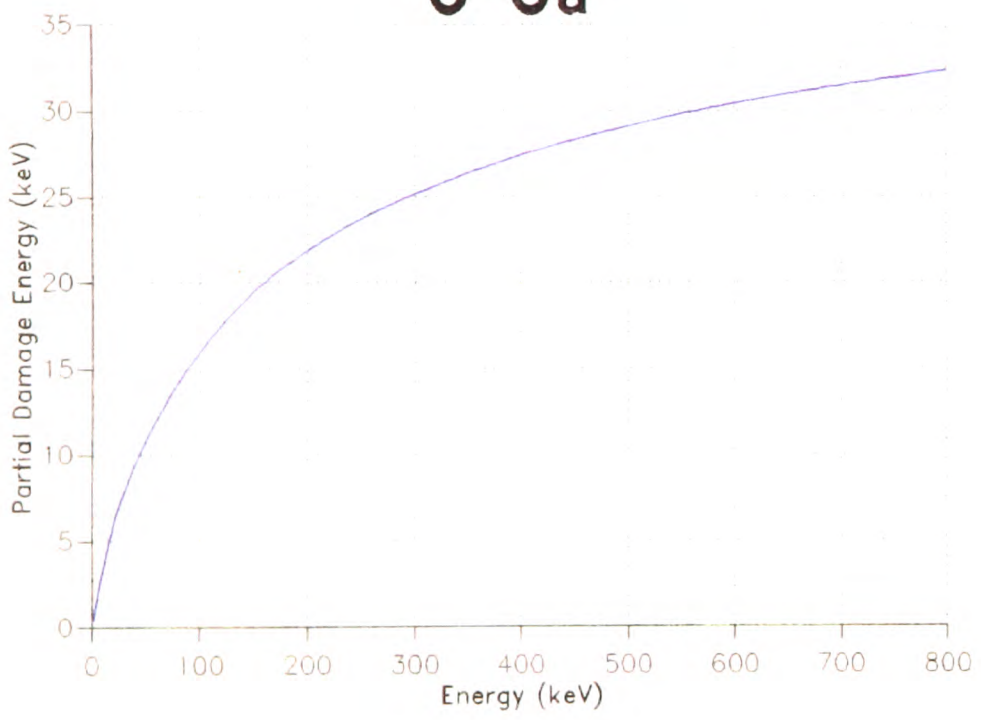
Calcium Oxide
O-O



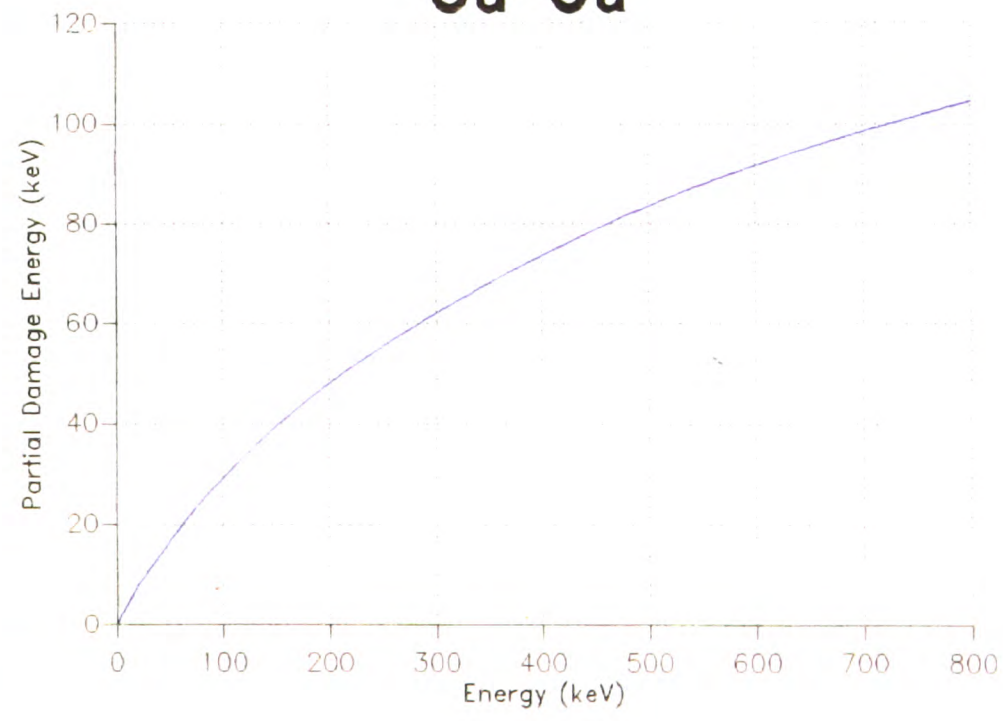
Calcium Oxide
Ca-O



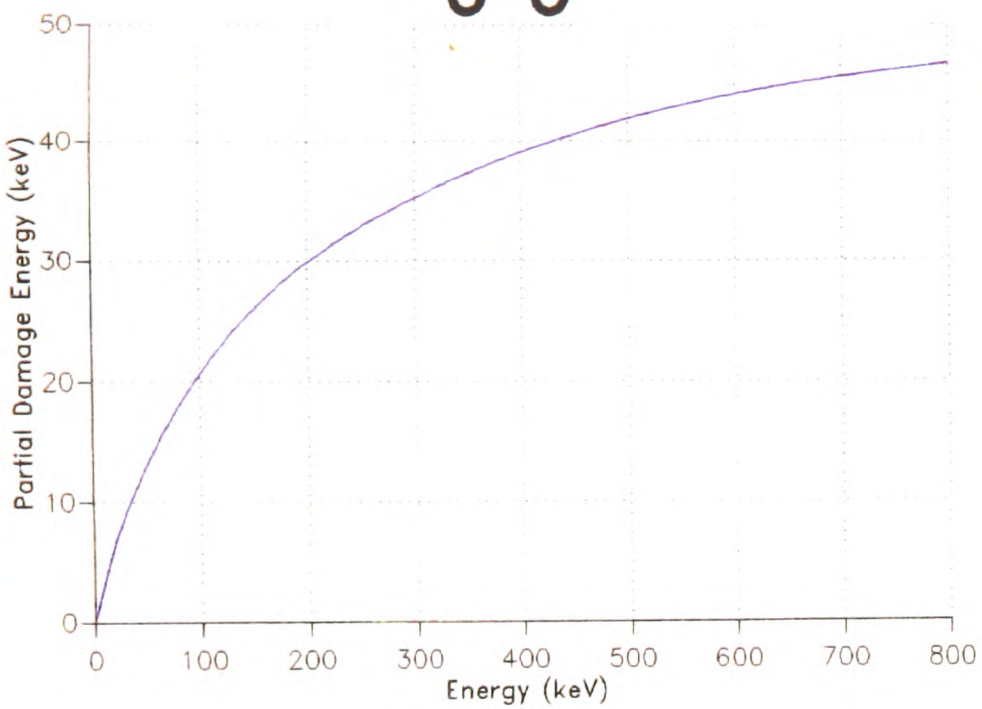
Calcium Oxide
O-Ca



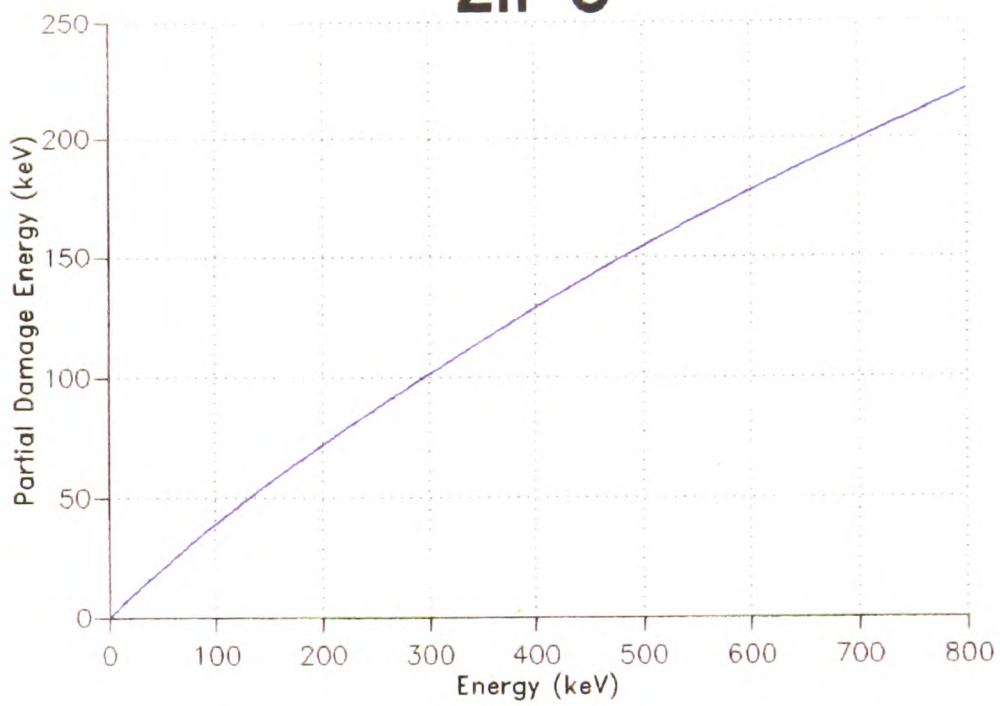
Calcium Oxide
Ca-Ca



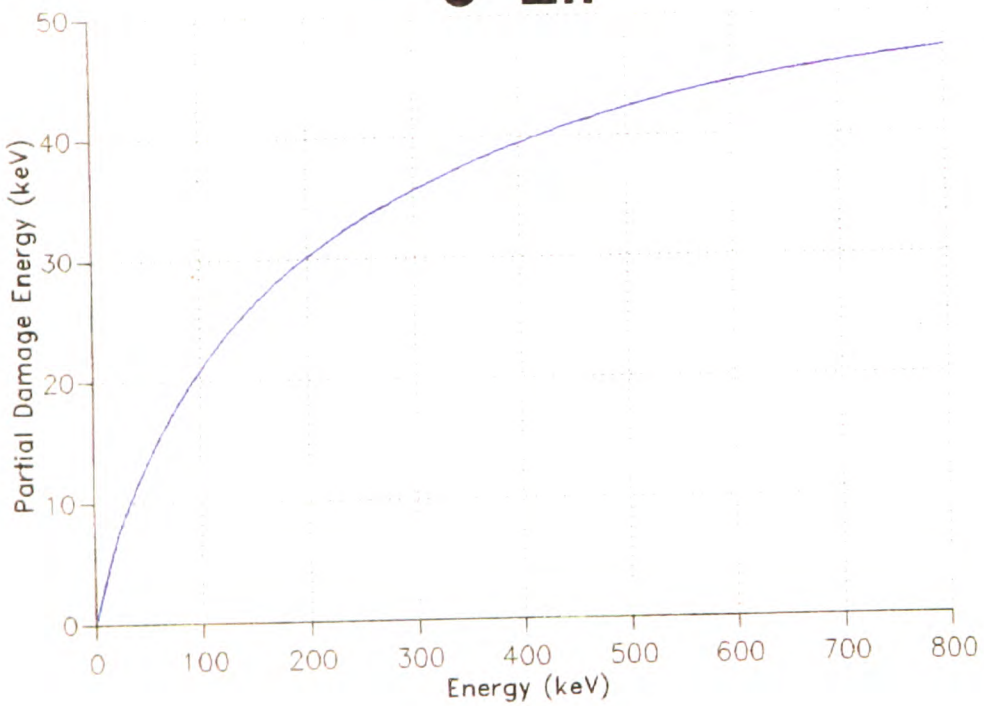
Zinc Oxide
O-O



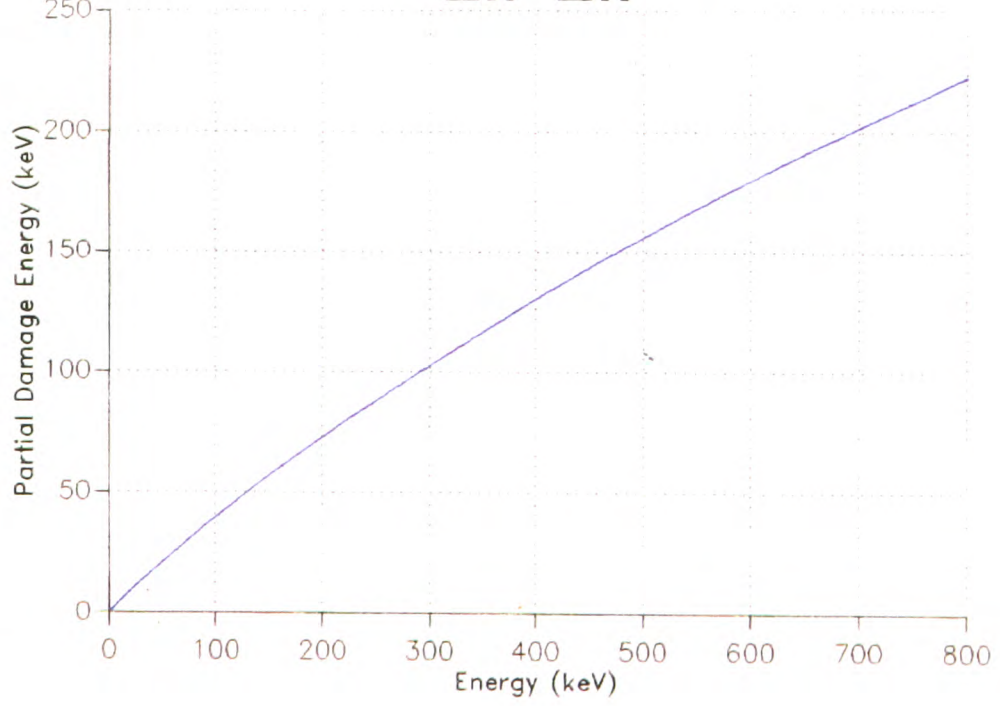
Zinc Oxide
Zn-O



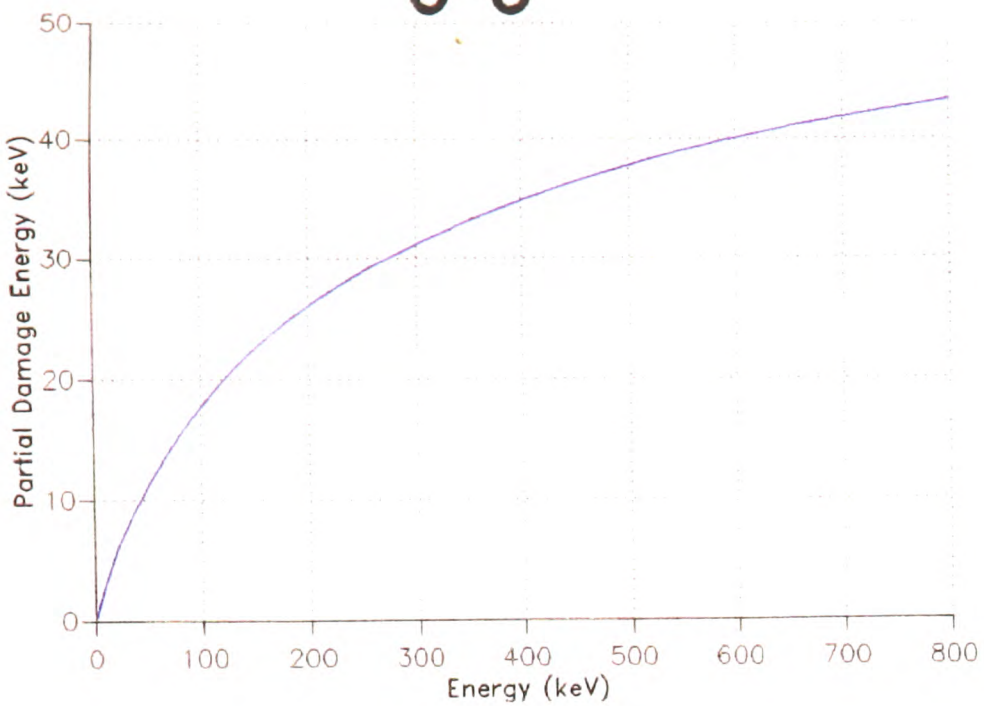
Zinc Oxide
O-Zn



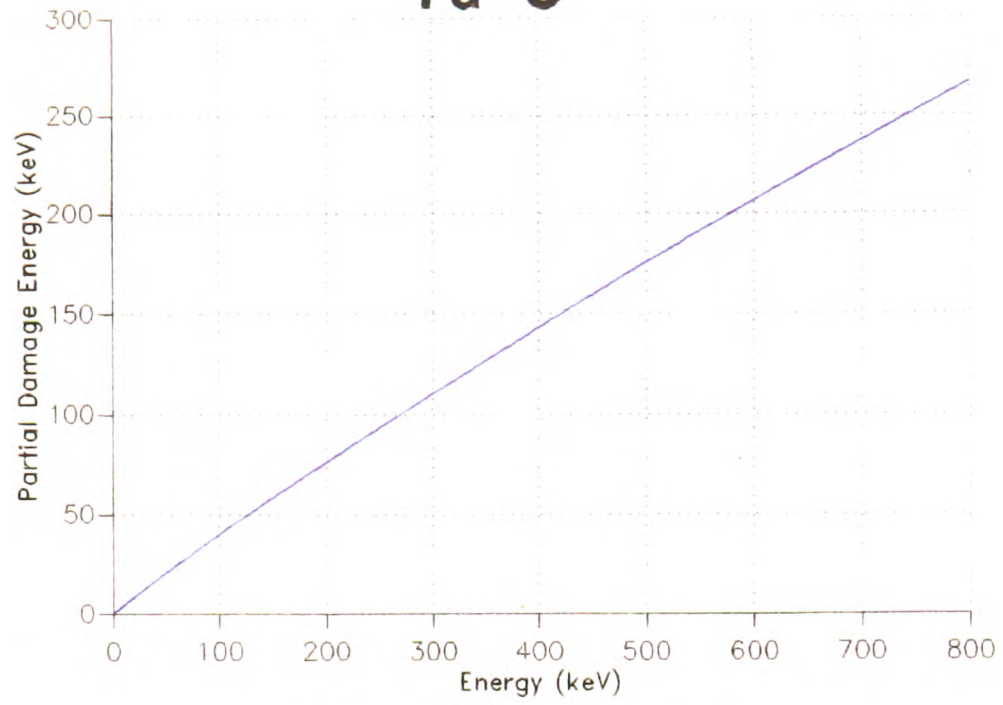
Zinc Oxide
Zn-Zn



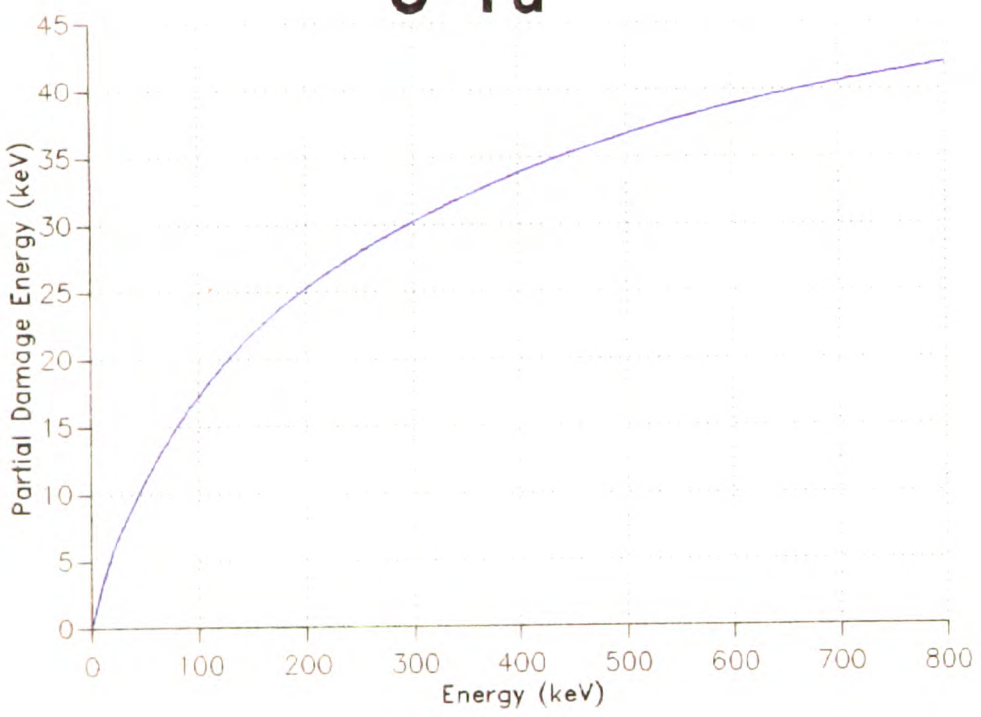
Tantalum Oxide
O-O



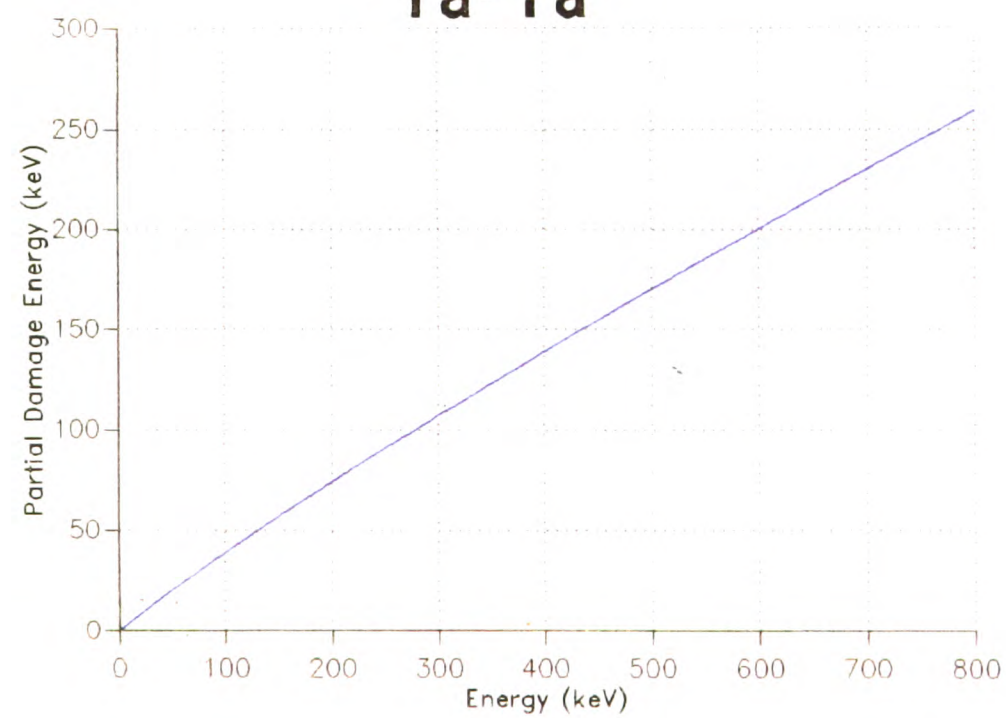
Tantalum Oxide
Ta-O



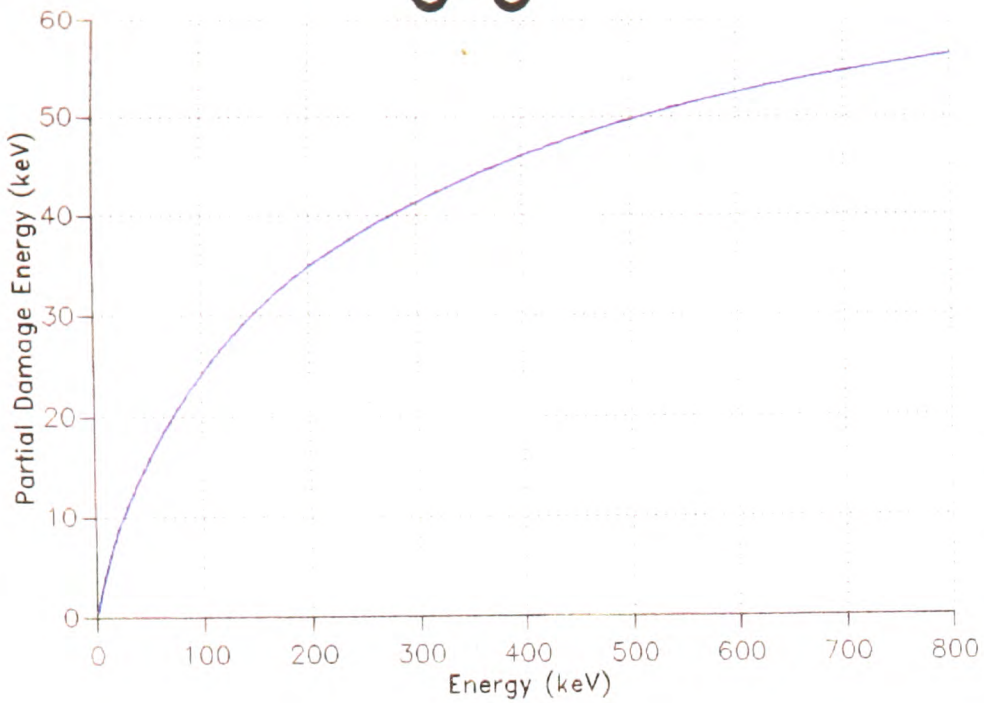
Tantalum Oxide
O-Ta



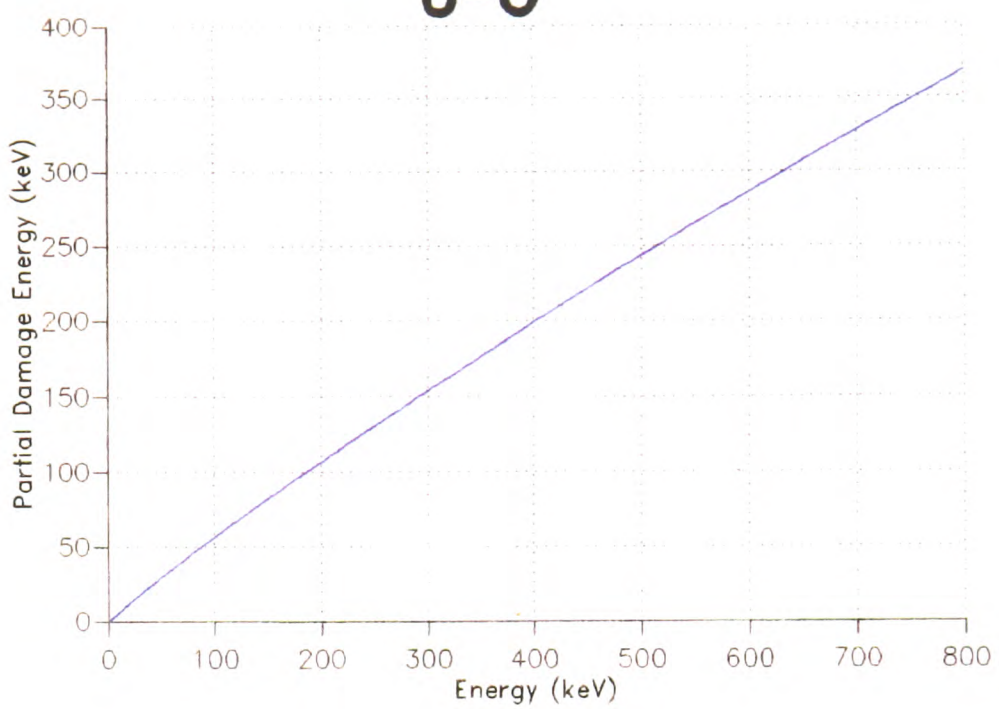
Tantalum Oxide
Ta-Ta



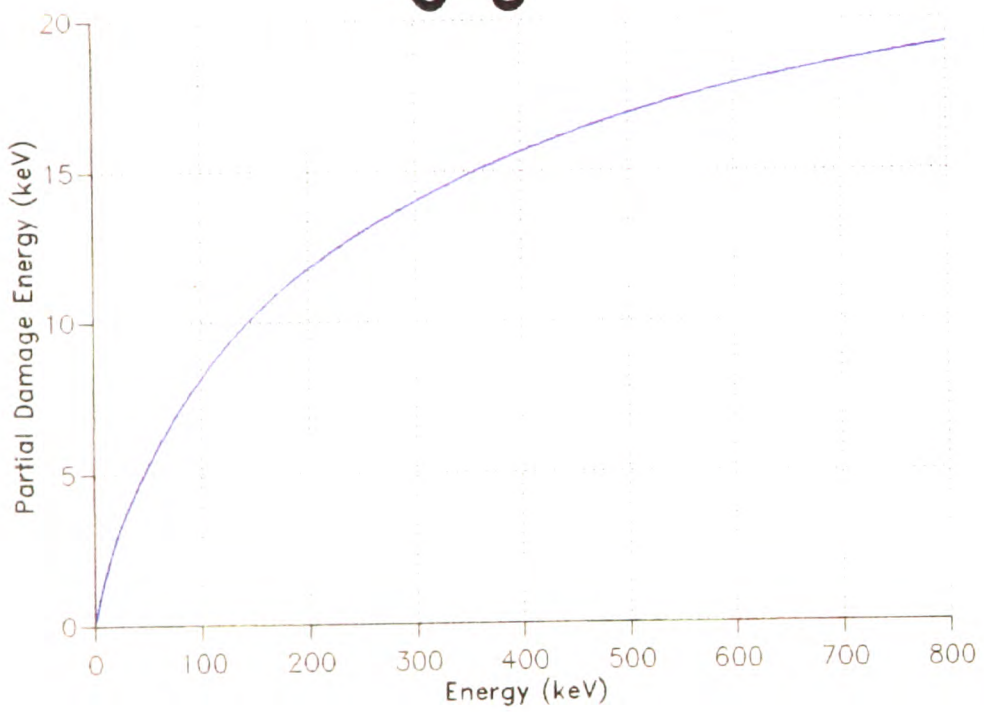
Uranium Oxide
O-O



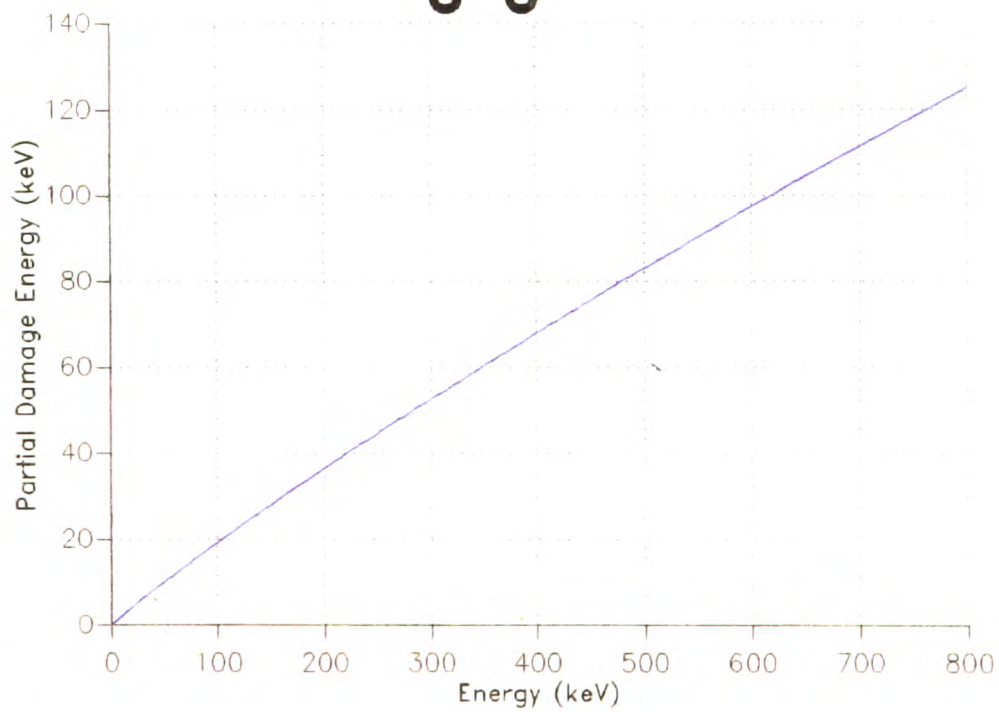
Uranium Oxide
U-O



Uranium Oxide
O-U



Uranium Oxide
U-U

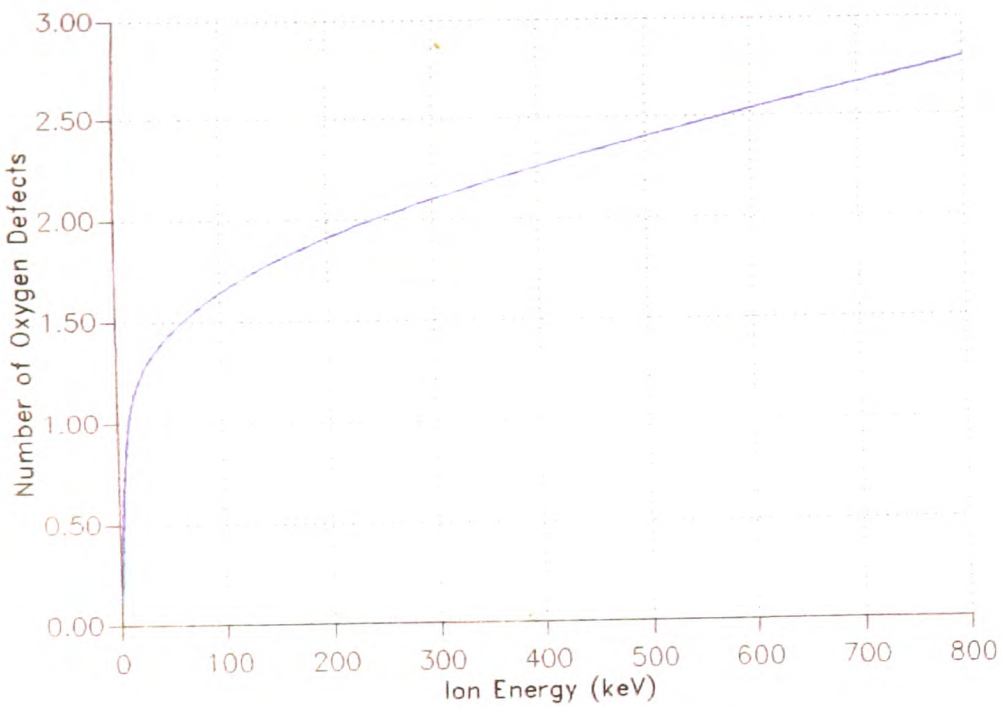


Species	α	β	γ
Al_2O_3			
O-O	0.752	0.0218	0.0179
Al-O	0.688	-0.00323	0.00743
O-Al	1.46	0.0223	0.0280
Al-Al	1.36	-0.0144	0.0123
MgO			
O-O	1.06	0.0351	0.0226
Mg-O	0.991	-0.00415	0.0110
O-Mg	1.04	0.0345	0.0224
Mg-Mg	0.969	-0.00372	0.0108
CaO			
O-O	1.15	0.0339	0.0202
CaO	1.04	-0.00209	0.00544
O-Ca	1.10	0.0332	0.0197
Ca-Ca	0.994	-0.00153	0.00523
ZnO			
O-O	1.08	-0.000233	0.0165
Zn-O	0.845	-0.0111	0.00250
O-Zn	1.07	-0.000244	0.0164
Zn-Zn	0.829	-0.0107	0.00244
TaO			
O-O	1.35	0.0143	0.0146
Ta-O	0.850	-0.0113	0.00174
O-Ta	1.42	0.0137	0.0152
Ta-Ta	0.896	-0.0122	0.00187
UO_2			
O-O	0.678	0.0258	0.00930
U-O	0.380	-0.000283	0.000226
O-U	3.37	0.0360	0.0327
U-U	2.46	-0.0350	0.0226

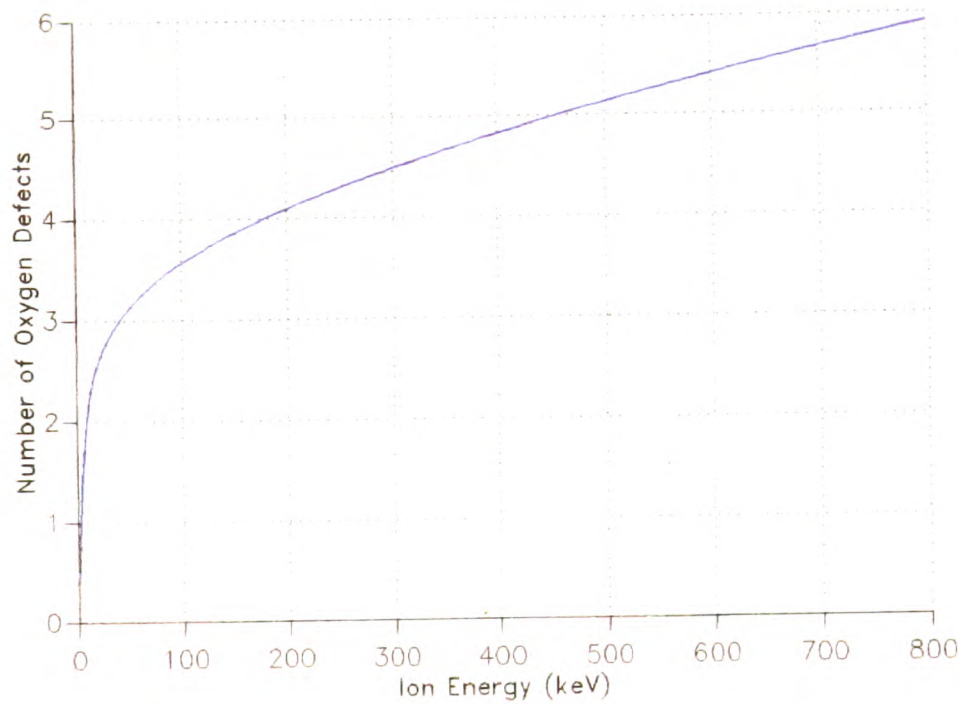
Table 4.1. Partial Damage Energy Coefficients

Fig. 4.4. Number of defects created on the oxygen and aluminium sublattices of Al_2O_3 under ion irradiation. Curves are presented for H, D, He, B, N, O, Ne, Al, Ar, and Kr.

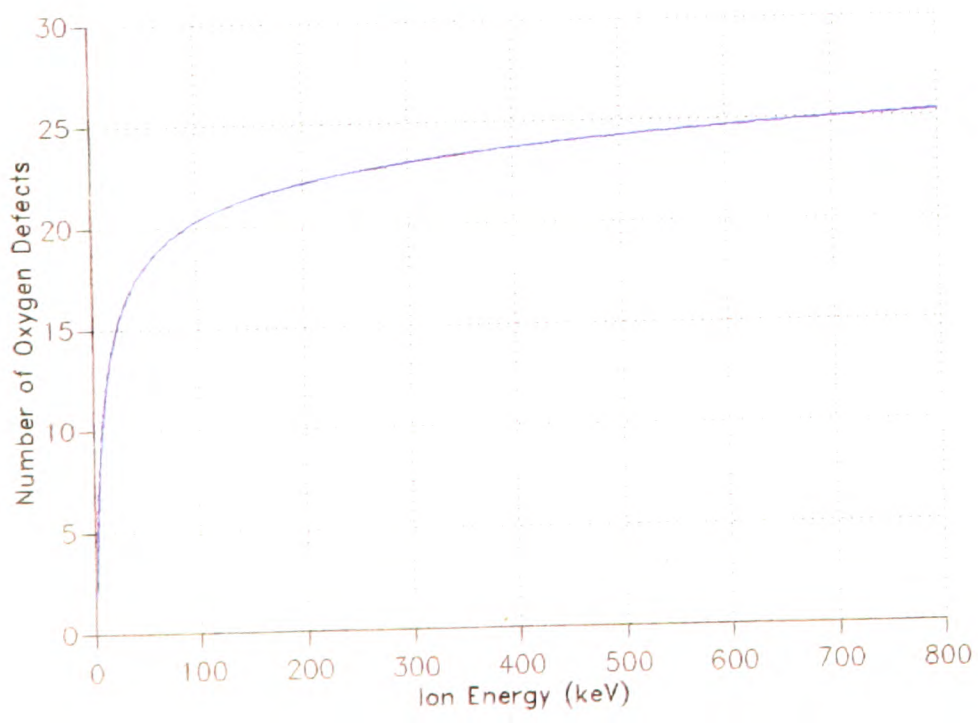
Protons



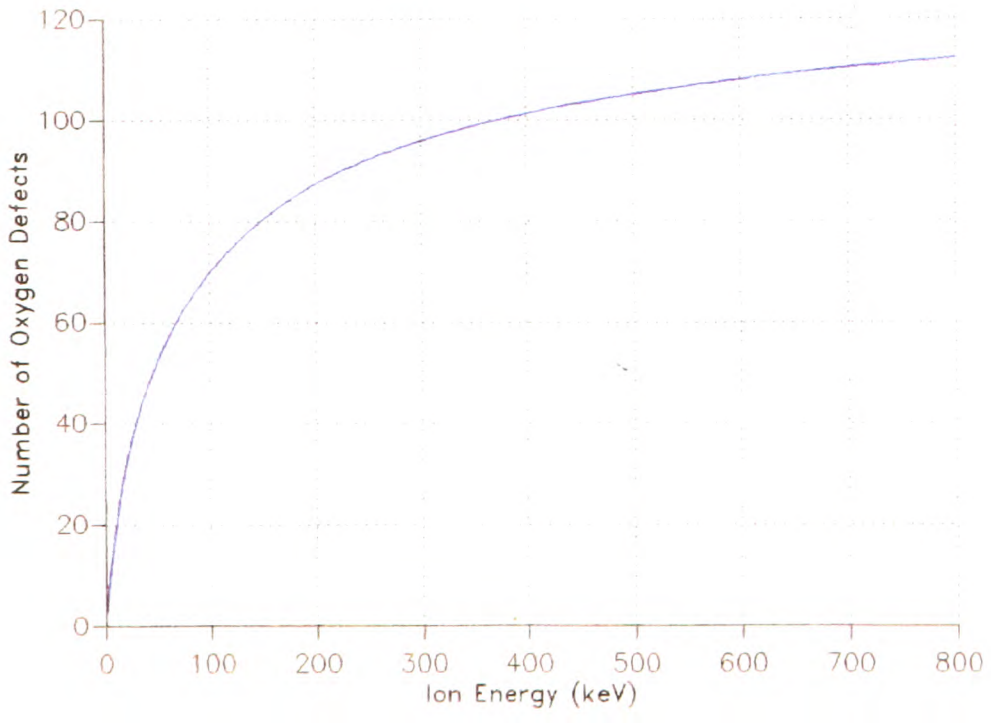
Deuterium



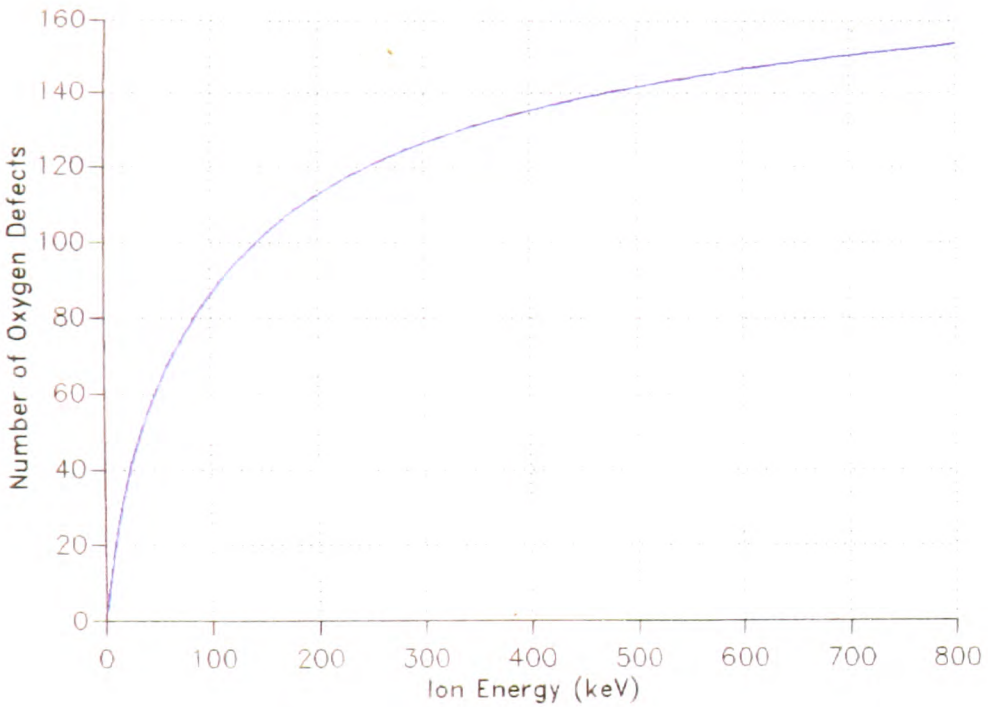
Helium



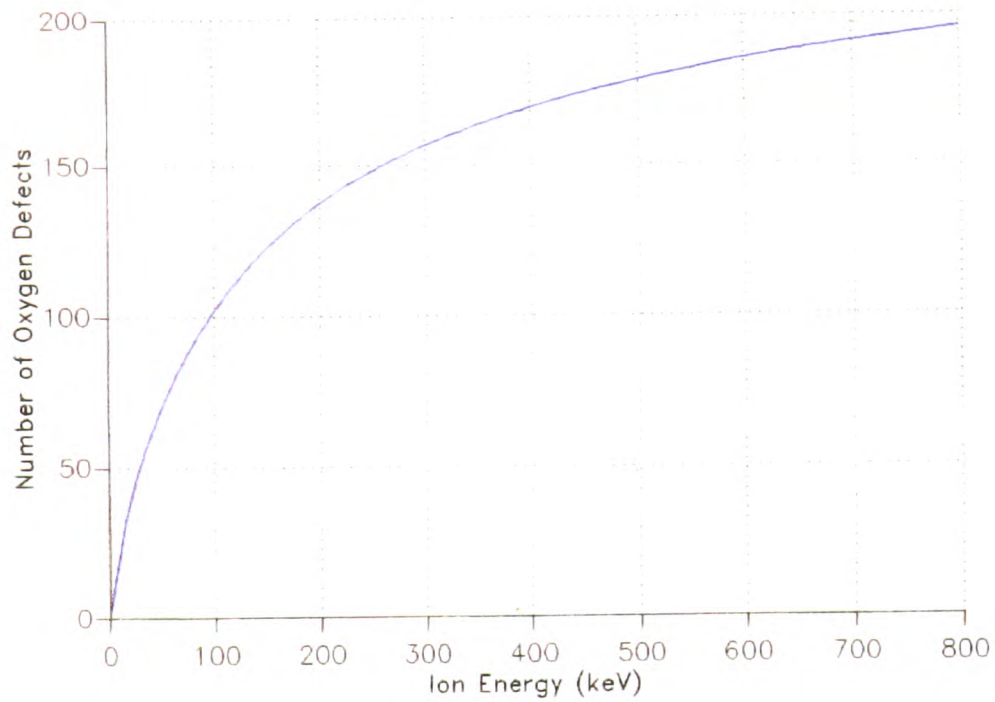
Boron



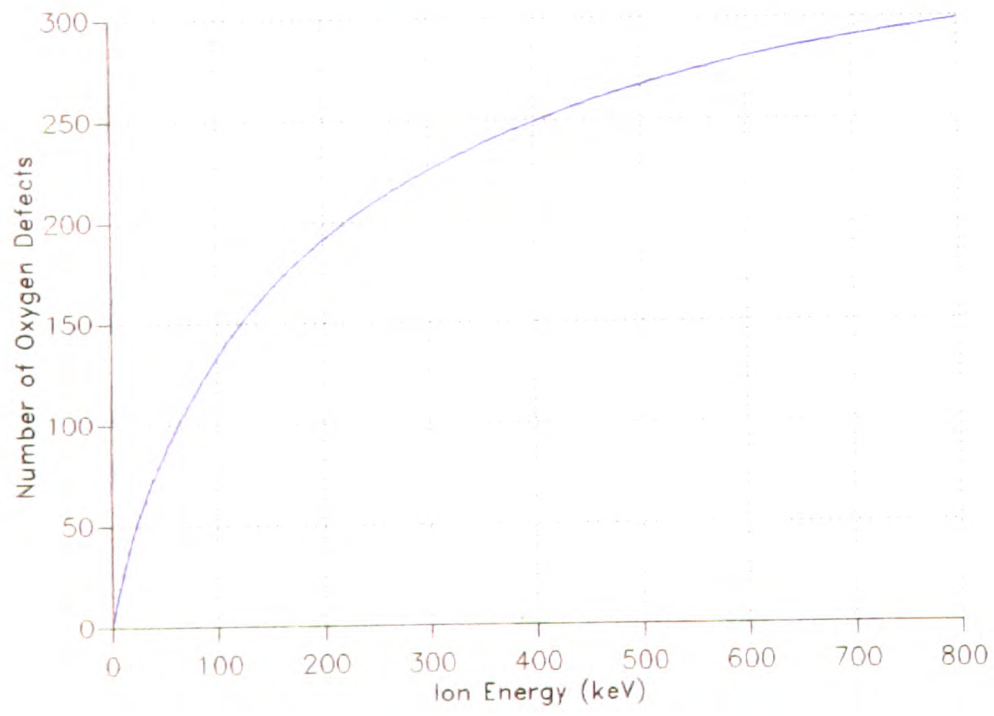
Nitrogen



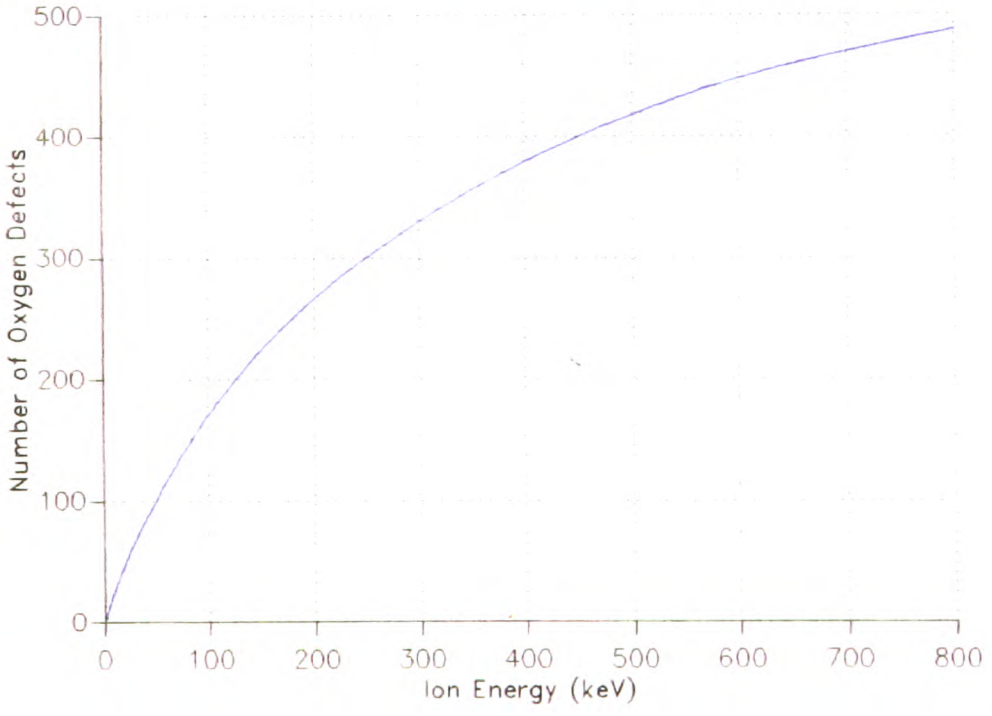
Oxygen



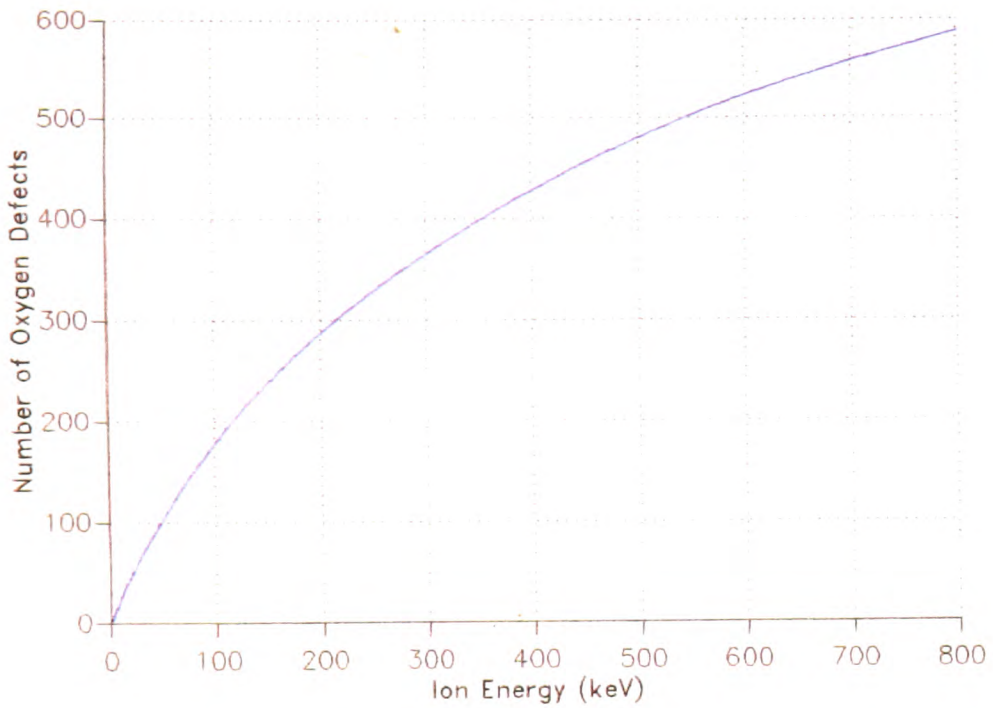
Neon



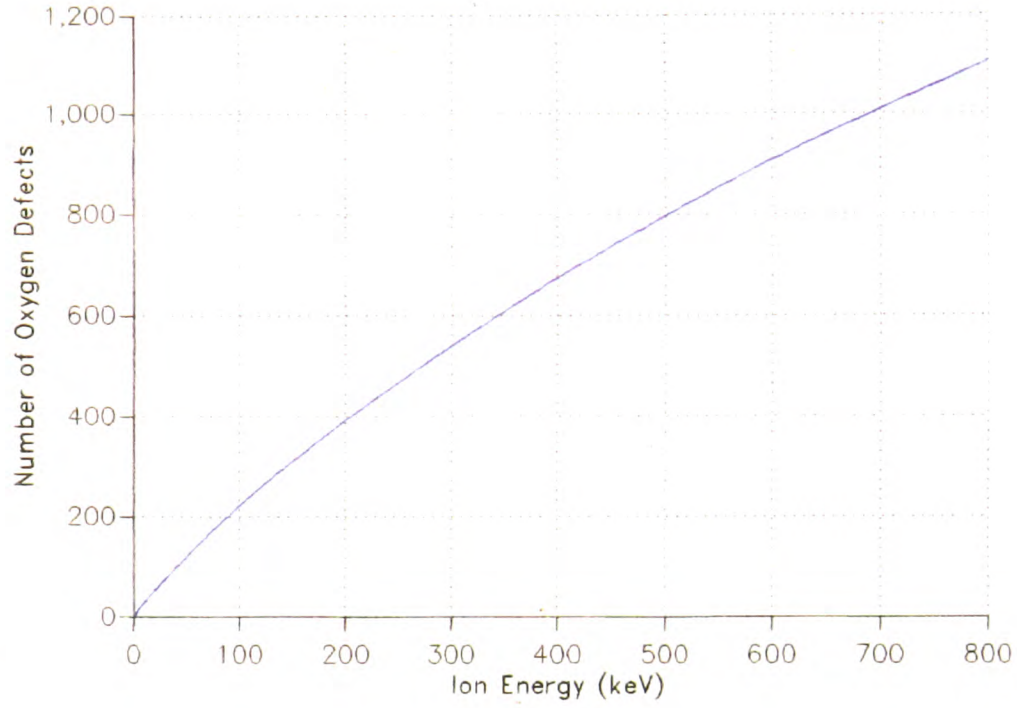
Aluminium



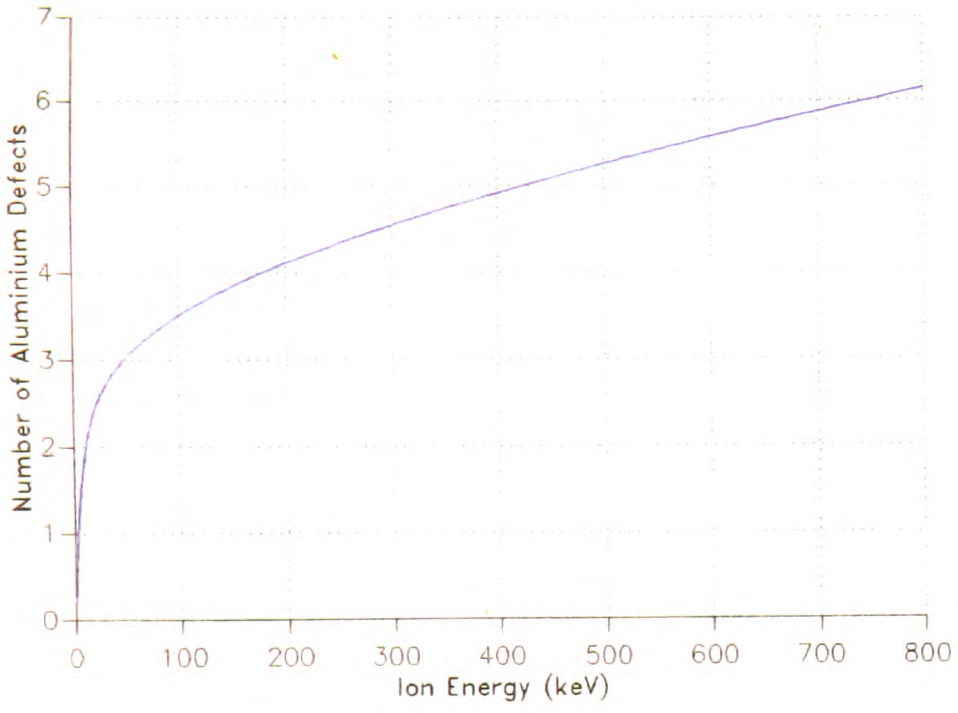
Argon



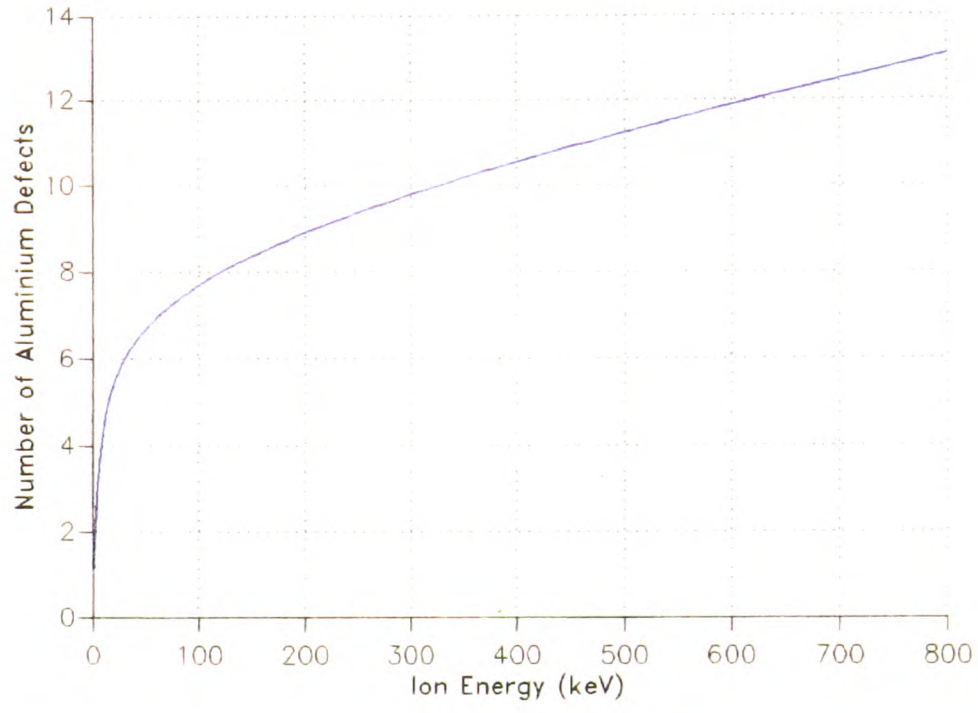
Krypton



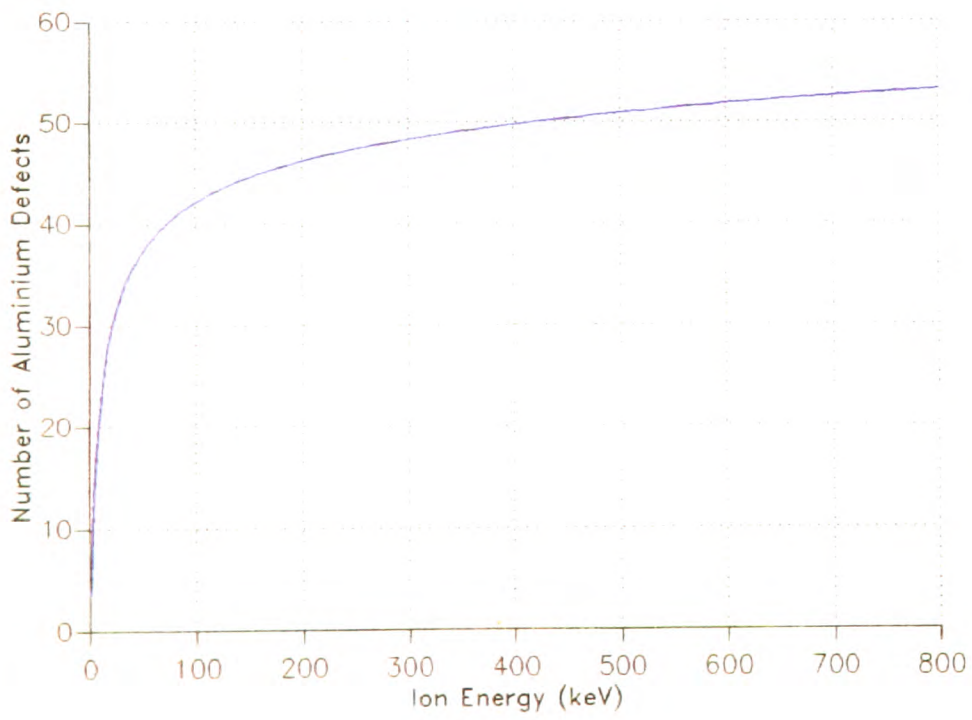
Protons



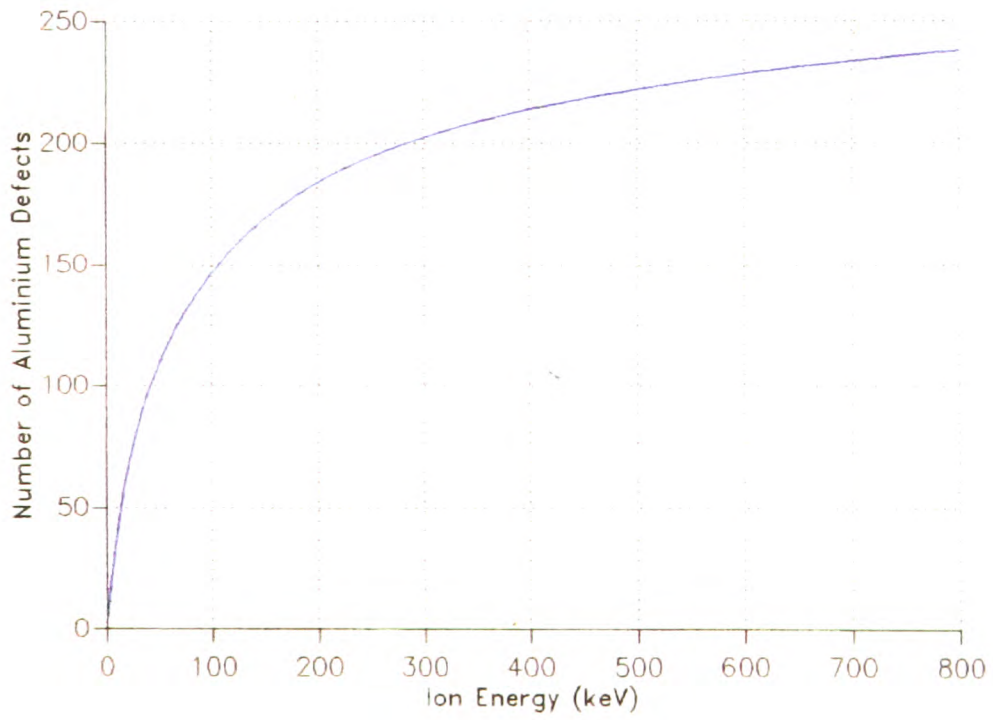
Deuterium



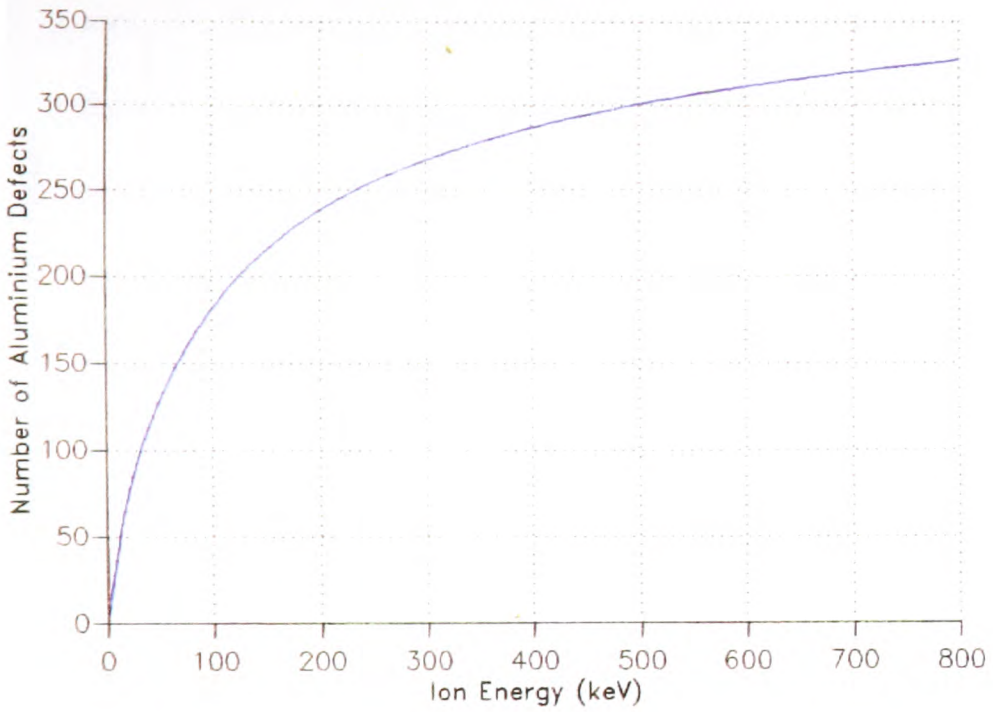
Helium



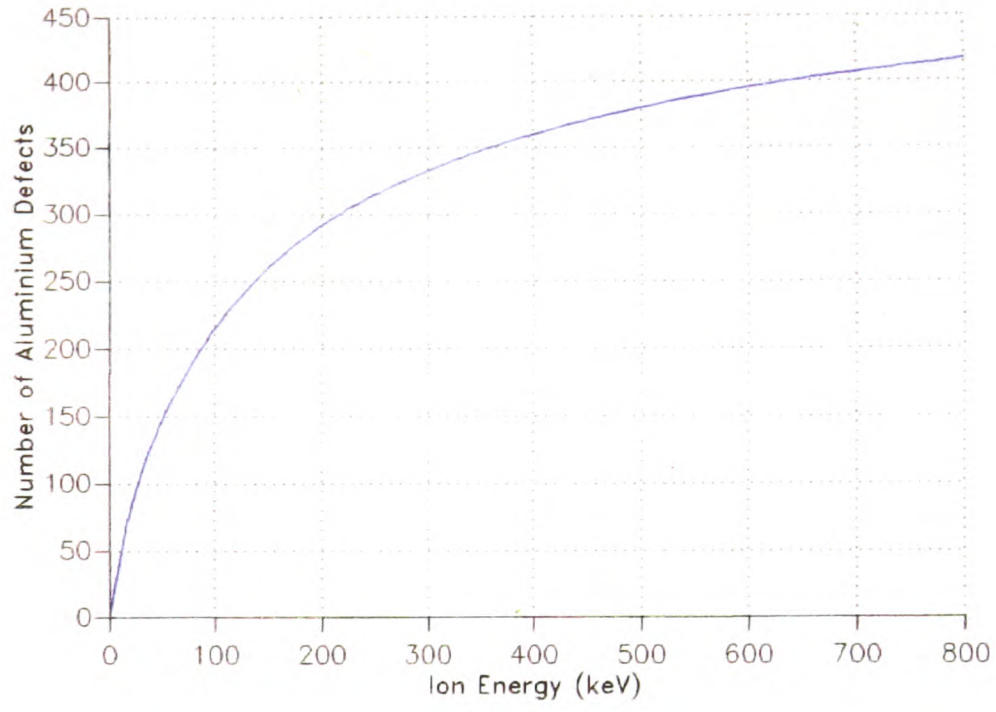
Boron



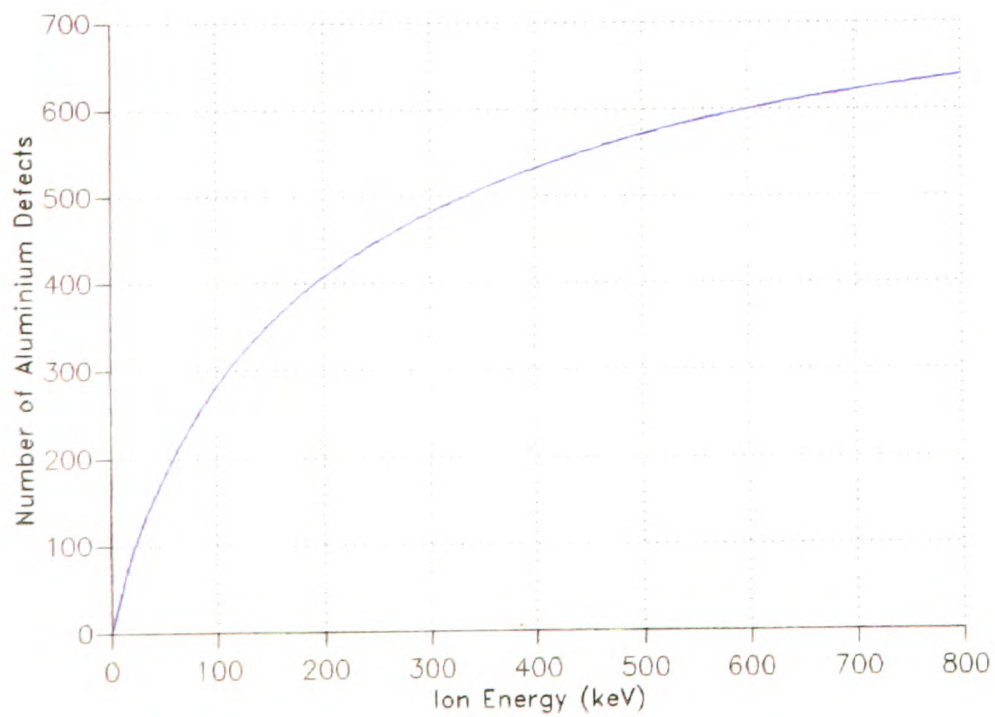
Nitrogen



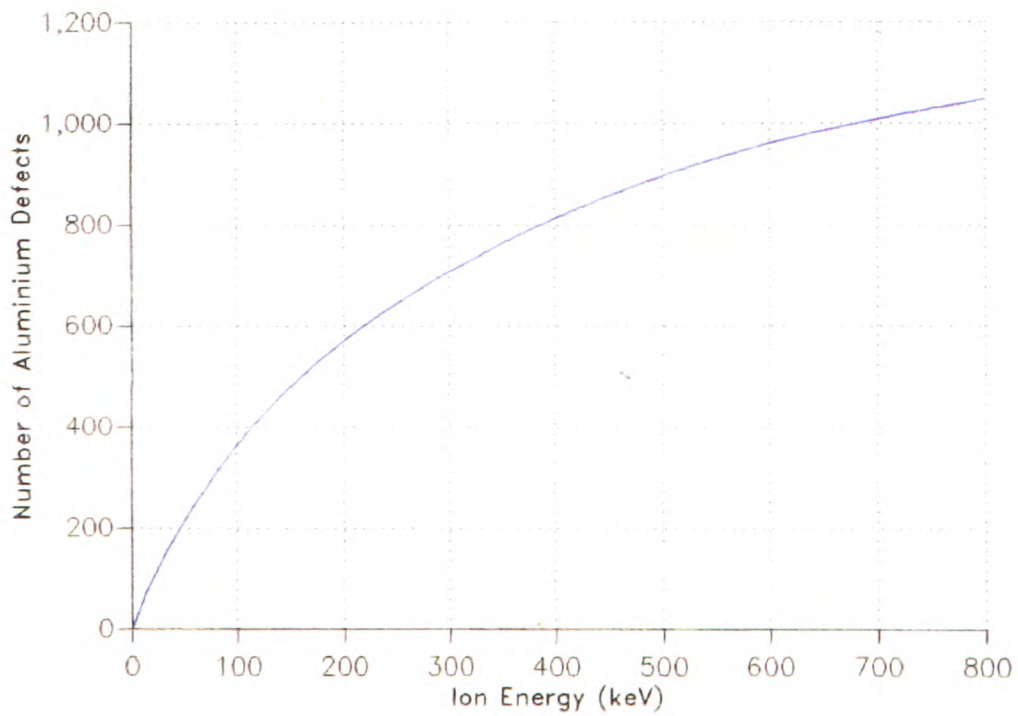
Oxygen



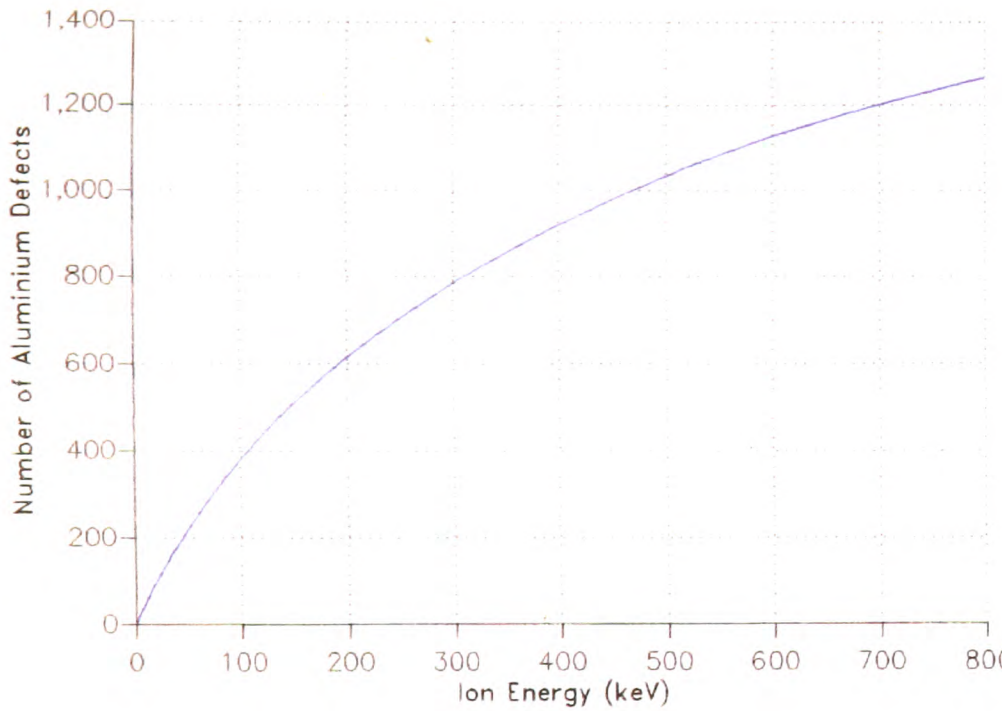
Neon



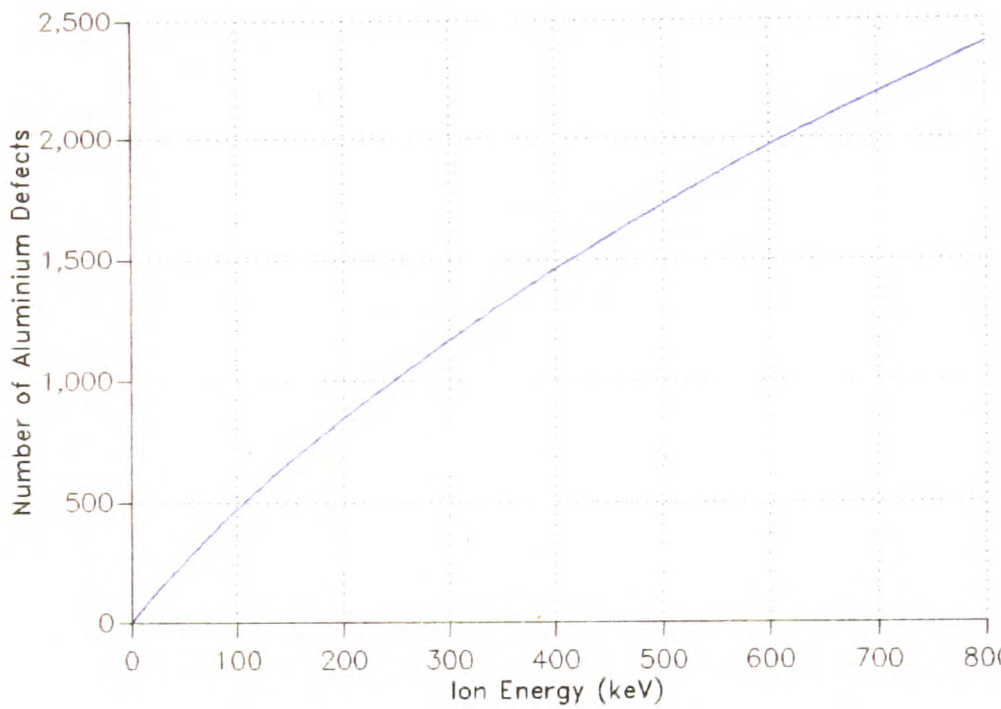
Aluminium



Argon



Krypton



§ 4.7 Comparisons With Other Work.

Partial damage energy functions for sapphire do not appear to have been published by any other workers and so our comparisons will not be entirely straightforward. But before we do this it is worthwhile comparing the various methods used to estimate damage production. Although the NRT formalism is widely used on a regular basis in the nuclear industry it does have a number of important limitations which have led researchers to adopt other methods. For example the manner in which the threshold energy is introduced is somewhat artificial and it is easy to see that the method used to derive the fundamental integral equation for the damage energy could easily be modified to obtain a similar equation giving the number of atomic displacements directly, rather than go via the intermediary of a damage energy. This approach has been taken by Parkin and Coulter <16> who defined a total *displacement* function and estimated deviations from stoichiometric defect production in a number of compounds including sapphire. Unfortunately they did not give details of the *partial* displacement functions (although they must have calculated these implicitly) and so their results could not be used for the present study. It is also worth noting that Parkin and Coulter used the simple Lindhard stopping cross sections and not the more accurate ZBL values. Dell and Goland <17> have made detailed comparisons of the different approaches to estimating point defect production. These authors employed the three following methods:

(i) they applied Robinson's original form of the damage energy function for elements to each component of the compound separately and then assumed that the damage energy partitioned between the sublattices in the stoichiometric ratio.

(ii) They repeated this approach but instead of assuming stoichiometric partitioning of the damage energy they used the Coulter and Parkin <16> damage energy functions mentioned in § 4.2.

(iii) Finally they used the Parkin and Coulter *displacement* functions.

They found that the first two methods gave equivalent results to the third for low Z compounds, but differed by about 30% for the higher Z compound TaO. They concluded that the major error in the first two methods (in the case of TaO) was the assumption that the damage energy partitions stoichiometrically, rather than the use of the damage energy to

characterise displacements. The calculations of damage production performed in the present study do not suffer from this limitation since we make no assumptions about the partitioning of the damage energy. It seems likely then that defect production calculated by the partial damage energy formalism would agree well with partial displacement functions.

It is also possible to make limited comparisons with the well known TRIM code of Biersack and Littmark <9>. TRIM (TRansport of Ions in Matter) is a Monte Carlo code which follows the trajectory of energetic ions at an atomistic level and gives details of useful parameters such as the mean ion range, the straggling and the damage profiles. Compound targets may be specified but these are treated simply as amorphous mixtures of the two elements. The code is able to follow the displacement of atoms at an atomistic level and if a given target atom receives a kinetic energy greater than E_d it is recorded as a displacement (providing the incident ion is not left with a kinetic energy *less* than E_d). The code uses the same ZBL stopping cross sections we have used and so ought to give similar results to ours. Unfortunately though it does not record the *type* of atom displaced (although there seems no reason why this could not be done) and so direct comparisons with the estimates of defect production obtained above are not possible. However if we specify the same value of E_d for both sublattices and assume that the damage energy partitions stoichiometrically then comparisons are possible. We have compared defect production in this way with the TRIM code and find good agreement with the results presented here.

The estimates of point defect production on the oxygen sublattice in sapphire obtained in this chapter will be compared to experimental values in chapter 6. In the next chapter we describe the basic experimental methods used in this investigation and report the results of some preliminary experiments designed to characterise the response of sapphire to radiation.

References

<1> J. Lindhard, V. Nielsen, M. Scharff and P.V. Thomsen, Mat. Fys. Medd. Dan. Vid. Selsk. 33 , No. 10 (1963).

<2> C.A. Coulter and D.M. Parkin, J. Nucl. Mater., 88 , 249 (1980).

<3> K.B. Winterbon, P. Sigmund and J. Sanders, Mat. Fys. Medd. Dan. Vid. Selsk. 37 , No. 14 (1970).

<4> Y. Matsutani and S. Ishino, J. Appl. Phys. Vol. 48, No. 5, 1822 (1977).

<5> P. Sigmund, Rad. Eff. 1 , 15 (1969).

<6> G. Moliere, Z.f. Naturforsch A2 , 133 (1947).

<7> W. Lenz, Z.F. Physik 77 , 713 (1932).

<8> J.F. Ziegler, ' Helium Stopping Powers and Ranges in All Elements,' Pergamon Press, New York (1978).

<9> J.F. Ziegler, J.P. Biersack and U. Littmark, ' The Stopping and Range of Ions in Solids,' Pergamon Press (1985).

<10> J.P. Biersack and M. Stadele, Rad. Eff. Vol. 64, No. 1-4, 51 (1982).

<11> K. Izsak, J. Berthold and S. Kalbitzer, Nucl. Instr. Meths. in Phys. Res. B15, 34 (1986).

<12> ' Atomic Energy Levels,' NBS Circular 467 (1958).

<13> J.P Biersack in ' Ion Beam Modification of Insulators ', Ed. P. Mazzoldi and G.W. Arnold, Elsevier (1987).

<14> M.S. Miller and J.W. Boring, Phys. Rev. A, Vol. 9, No. 6, 2421 (1974).

<15> M.T. Robinson, Proc. BNES Conf. on ' Nuclear Fusion Reactors, ' Culham, England, 364 (1969).

<16> D.M. Parkin and C.A. Coulter, J. Nucl. Mater. Vols. 85 and 86, 611 (1979).

<17> G.F. Dell and A.N. Goland, J. Nucl. Mater. 102 , 246 (1981).

Chapter 5

Experimental Methods and Preliminary Results

Introduction.

This chapter describes the basic experimental techniques and apparatus used to perform some preliminary irradiations and optical measurements in order to characterise the behaviour of the colour centres in sapphire under a variety of conditions. A quantity of primary importance in determining displacement rates is the displacement threshold energy and since some disagreement exits in the literature concerning the value of these parameters for both sublattices in sapphire, an attempt was made to re-determine them in an improved experiment, where the irradiation was more closely controlled and the possibility of concurrent ion bombardment removed. The stability of irradiation-induced F bands was investigated up to 380 K by irradiating with energetic ions at liquid helium temperatures and performing a series of anneals. Finally, the effect of subsequent ionising radiation on the F centre was investigated by subjecting the sample to electron irradiation following ion bombardment. Temperature control during these experiments was achieved by mounting the sample on the stage of one of two cryostats, a constant temperature cryostat being used for irradiations at 4 K, 77 K and ambient temperature whilst a variable temperature cryostat was used for intermediate temperatures. We begin then with a description of general techniques and apparatus.

§ 5.1. Sample Preparation.

Samples of Czochralski-grown u.v. grade sapphire measuring 1cm × 1cm × 300 μm and oriented with the c-axis perpendicular to the face were obtained from Roditti International

Ltd. This material is the highest quality sapphire commercially obtainable – an important consideration in quantitative damage production experiments, where low mass impurities can introduce more efficient energy transfer processes. The samples were then ground and polished on both sides to an optical finish using a Malvern Instruments Multipol 2 grinding and polishing machine with diamond based cutting fluids. Finally, they were ultrasonically cleaned in acetone. After this process the samples were typically between 240μm and 270μm thick.

§ 5.2. Variable Temperature Cryostat.

The variable temperature cryostat was designed, jointly at Harwell by Mr. G.P.Pells and Oxford Instruments Ltd, as a general purpose facility to enable samples to be irradiated on a variety of particle accelerators and subsequently transported to the location of measuring apparatus, with the specimen stage held at any temperature in the range 4 K to 800 K. The specimen stage was designed to supply sufficient cooling power to hold the sample at 4 K under a beam heating load of up to 5 Watts. The sample is cooled by passing helium gas over a heat exchanger mounted inside a 'cold finger' assembly. The cryostat internal reservoir provides a source of liquid helium which is drawn through a series of capillary tubes into the heat exchanger at the sample stage. The helium is evaporated and in so doing, cools the sample. The flow of helium is effected by evacuating the capillary tube at the exhaust side of the heat exchanger with an Edwards E2M80 rotary pump. The degree of helium flow (and hence cooling) is controlled by opening/closing the needle valve between the pump and the heat exchanger or by opening/closing the needle valve between the helium reservoir and the heat exchanger. A schematic diagram of the cooling circuit is shown in fig. 5.1. Temperature control at the sample stage is achieved using a Watlow firerod heater cartridge in combination with the helium coolant. An Oxford Instruments ITC4 Intelligent Temperature Controller is interfaced to two thermocouples – one at the sample stage and another at the base of the cold finger assembly. The desired temperature may be set with the controller and the ITC4 will then adjust the electrical current supplied to the heaters to achieve the correct temperature at the sample stage. For temperatures above 300 K it is beneficial to close off the

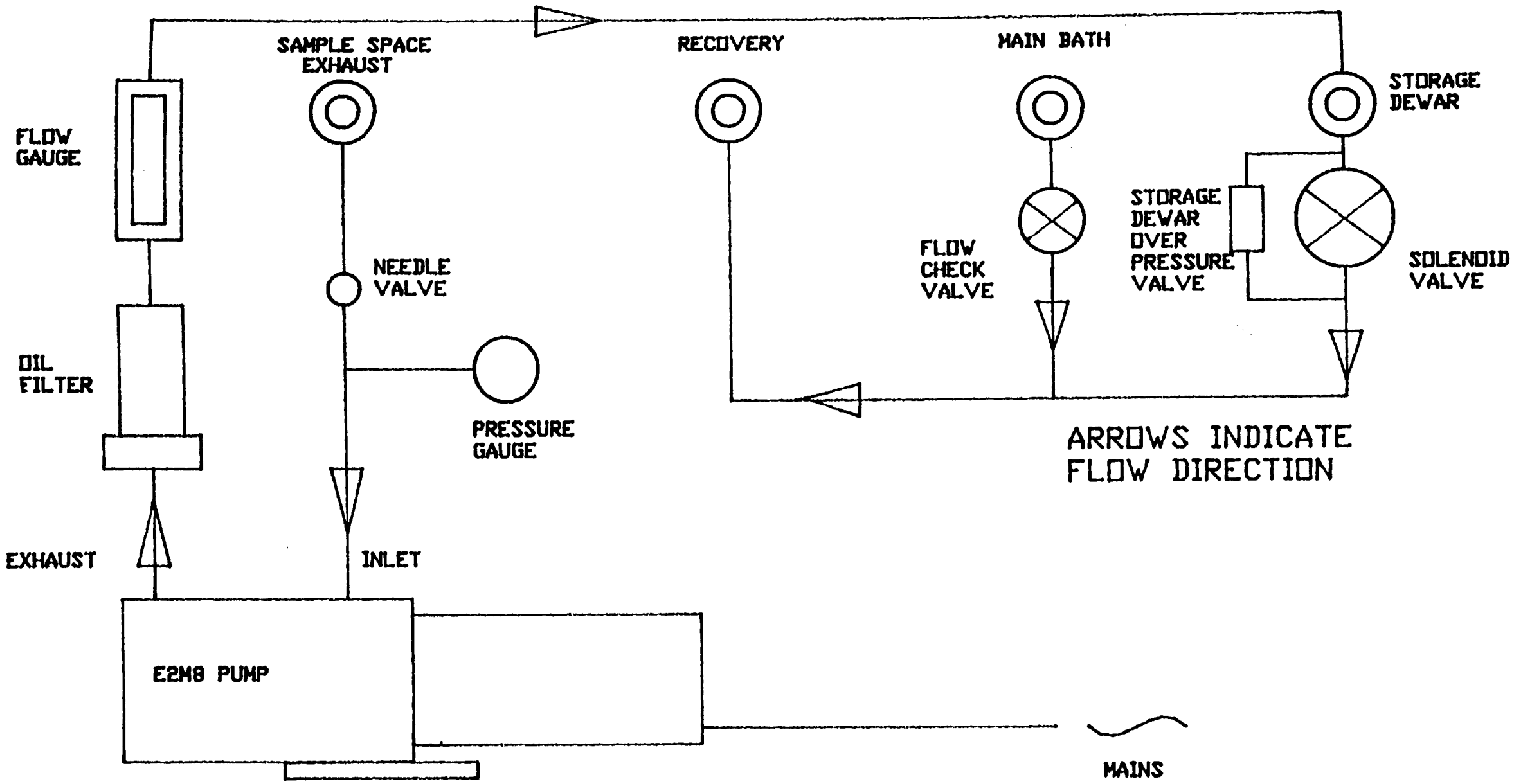


Fig. 5.1. Schematic drawing of the cooling circuit of the variable temperature cryostat.

helium coolant altogether, since clearly no cooling is required above ambient temperature. Automatic replenishment of the helium reservoir may be achieved by using the exhaust from the rotary pump to pressurise the liquid helium dewar, as shown in fig. 5.1. This excess pressure of about 5 psi forces liquid helium through a transfer tube into the helium reservoir of the cryostat. The helium level in the reservoir is monitored by an Oxford Instruments HLM2 liquid helium level meter which consists of a length of superconducting niobium alloy wire, interfaced to a resistance meter. When totally immersed in liquid helium the wire has zero resistance but as the helium level drops part of the wire returns to the normal state and a resistance is measured. The resistance meter may then be calibrated to read directly the amount of helium remaining in the reservoir.

Since the irradiations and subsequent optical measurements are generally performed at physically separate locations it is necessary that the cryostat be capable of maintaining the sample at pre-set temperatures during transit. Transit inevitably requires that the cryostat be disconnected from the pumping set and temperature controller, thereby removing the excess pressure to drive coolant through the heat exchanger. This could result in undesirable warming of the sample but the problem is overcome by fixing two check valves to the exhaust ports on the cryostat which open only when the internal pressure rises above 0.5 psi. In this way the helium which evaporates during transit is used to provide the impetus for driving coolant into the heat exchanger. The system is self-correcting in that if the sample should warm slightly and thereby evaporate more coolant, this will in turn increase the excess pressure on the liquid helium reservoir (to a limit of 0.5 psi) and increase the flow rate of coolant, hence cooling the sample.

The cold finger assembly, on which the sample is mounted, is capable of rotation through $\pm 180°$. This feature allows the sample to be oriented with the plane face towards the particle beam during the irradiation and then rotated through 90° to allow optical analysis.

§ 5.3. Optical Absorption Measurements.

The growth of optical absorption bands induced by radiation were monitored using a Perkin-Elmer Lambda – 9 spectrophotometer. The Lambda – 9 is a general purpose,

computer-controlled u.v / visble / i.r spectrophotometer capable of performing optical measurements over the range 190 to 3000 nm. For the series of experiments described here the Lambda – 9 was used exclusively in the transmission mode, i.e. the light beam is passed through the sample and detected with a photomultiplier tube. The effect of variability of the light source is removed by the double beam system employed which takes two light beams from the source through the optical system inside the machine and detects them separately, one having passed through the sample and one through only a reference chamber. The optical density of the sample is then calculated internally by comparison with the reference beam.

Some modifications were made to the Lambda – 9. The sample compartment was mechanically modified to accommodate both the constant and variable temperature cryostats. To minimize the absorption of light by atmospheric oxygen in the ultra-violet part of the spectrum all exposed parts of the optical path were continuously flushed with dry nitrogen gas. Although the optical grating is capable of operating down to 170 nm (in a manually operated mode) the output from the light source proved too weak to obtain reliable measurements below 190 nm, despite flushing with dry nitrogen. Attempts were made to reduce the signal-to-noise ratio by flushing the photomultiplier tube with dry nitrogen gas cooled to around 275 K but in practice temperature reductions of only a few degrees could be obtained at the photomultiplier body and this produced no significant improvement in the signal-to-noise ratio.

The Lambda – 9 spectrophotometer was interfaced to a Perkin-Elmer computer to allow subsequent manipulation and storage of the optical spectra taken. Spectra were normally taken over the range 900 to 190 nm with data being recorded every 1 nm. The exit slit of the grating was set to give a resolution of 1nm. All spectra were recorded in terms of optical density (or absorbance – the two are used interchangeably) versus wavelength since the relevant optical parameters for estimating colour centre concentration are obtained by subtracting pre-irradiation values of optical density from post-irradiation values (as shown in chapter 6). This subtraction of spectra was performed on the Perkin-Elmer computer and these 'difference' spectra were then transferred to an IBM 3040 Q mainframe computer for further analysis, as described in chapter 6.

§ 5.4. Displacement Thresholds in Sapphire.

In a diatomic solid such as sapphire, each atomic species may have different values of E_d, leading to the possibility of non-stoichiometric damage production. Electron irradiation is ideally suited to the determination of displacement thresholds since the low electron – to – ion mass ratio causes the cross section for displacement to vary rapidly as the electron energy is varied. The most common method of determining thresholds (the so-called 'bracketing' technique) is to simply monitor the production of vacancies (in this case via the associated colour centres) as a function of electron energy and determine the point at which no further vacancies are created. Some preliminary experiments of this kind were performed in order to check the oxygen displacement threshold, using the Harwell 500kV electron accelerator. However the values obtained were consistently lower than previously reported thresholds. Values of E_d for both species in sapphire have been reported by Pells and Phillips <1> and Pells and Stathopoulos <2> who both found 18 eV and 76 eV for aluminium and oxygen respectively. Their method mainly involved the monitoring of loop formation in a high voltage electron microscope (HVEM) where the point defects themselves were not observed but rather a product of their formation and agglomeration, namely interstitial dislocation loops. One possible source of error in thresholds determined with electron irradiations is that free ions can be formed at the electron source, either by evaporation from the hot filament stage or field assisted emission from the high accelerating voltage. These ions will then be accelerated along with the electron beam and on striking the sample will produce many more displacements than each electron. Furthermore, there will no cutoff point below which they are incapable of producing damage, making threshold determinations impossible. In collaboration with Dr. L. Canham of RSRE Malvern, this source of error on the Harwell 500 kV Van de Graaff electron accelerator was investigated by placing some etchable ion track (a special plastic developed by the nuclear physics department of the University of Bristol) in the beam path and operating the electron accelerator under a variety of conditions. Subsequent etching of the test materials showed clearly that it is practically impossible to obtain an electron beam which is not contaminated with damage producing ions. Both mechanisms of ion production mentioned above are likely since ion tracks were detected even with the filament switched off, indicating field assisted

emission. However ion production was enhanced considerably with a hot filament. To overcome the problem a 5μm thick, pinhole free aluminium foil, obtained from Goodfellow Metals Ltd, was inserted in the flight tube to prevent any heavy ions travelling with the electron beam from striking the target. Further tests with etchable ion track showed no evidence of ion damage.

The HVEM experiments of Pells and Phillips were less likely to suffer this problem since care was taken to 'condition' the microscope before the measurements were performed. However the results obtained in this way were apparently confirmed by measurements of the colour centre concentrations induced following electron bombardment in a Van de Graaff accelerator. No precautions were taken to avoid the possibility of concurrent ion bombardment and, as discussed above, it is likely that they suffered from ion beam damage. Having said this though we also note that the values of E_d for oxygen obtained by these authors is in fair agreement with other reported values, where precautions may well have been taken to avoid ion damage. Compton and Arnold <3> obtained the value 70 ± 10 eV whilst Arnold and Compton <4> found the value 90 ± 5 eV. Unfortunately no other data are available for aluminium but the value of 18 eV is rather low in comparison with similar materials; for example in MgO the threshold for Mg has been reported as 60 eV by Pells <5>. The most reliable results of Pells and Phillips were those obtained from the HVEM experiments. However threshold determinations performed by colour centre measurements are, where possible, to be preferred over determinations involving loop production, since in the former case the primary defect itself is being monitored. In view of the importance of E_d to any quantitative damage investigation, both thresholds were re-determined via colour centre measurements with the precaution of an ion-blocking foil.

The low oscillator strength and large width of the *V* band (i.e. the band associated with the aluminium vacancy) mean that it is impractical to apply the usual 'bracketing' method of reducing the electron energy until no further defects are produced. An alternative method is to compare optical measurements of the *V* centre induced by electron bombardment with values calculated from scattering theory. This was in fact the method employed by Arnold and Compton <4> but they did not allow for the fact in their calculations that secondary

damage (i.e displaced atoms may proceed to create further displacements) may occur. The results presented in this chapter do account for this and it appears especially important to do this in sapphire, where the thresholds differ widely for the two sublattices.

The displacement of atoms by electrons in elements has been discussed before by several authors, including Oen and Holmes <6> and Cahn <7>. Some modifications are necessary in the case of a diatomic solid and we shall now discuss these complications, following a brief review of the characteristics of electron interactions.

§ 5.5. The Interaction of Energetic Electrons with Solids.

On entering a solid an energetic electron may lose energy in three ways :

(i) the electron is subjected to large accelerations and hence will radiate energy

(ii) it may interact with the atomic nucleus and transfer energy to the atom as a whole

(iii) it may excite the electrons of the target atoms in ionization processes.

Of these three mechanisms, the last is by far the greatest source of energy loss for the range of energies considered here. Bethe and Ashkin <8> have estimated the ratio of energy loss through radiation to energy loss through ionization and find

$$\frac{(-dE/dx)_{rad}}{(-dE/dx)_{ioniz}} \approx \frac{Z \times E}{800} \quad , \tag{5.1}$$

where $(-dE/dx)$ is the stopping power, Z is the atomic number of the target atoms and E is the electron energy in MeV. The interaction with the nucleus is of course the interaction responsible for the displacement of atoms and as such is of primary importance. However it does not represent a significant source of energy loss.

The stopping power due to excitation and ionization of the target atoms has been derived by Bethe and Askin <8> and is

$$\frac{-dE}{dx} = \frac{2\pi N Z e^4}{m_e \beta^2 c^2} \times \left\{ \log \frac{m_e \beta^2 c^2 E}{2I^2(1-\beta^2)} - (2\sqrt{1-\beta^2} - 1 + \beta^2)\log 2 + ... \right.$$

$$\left. ... + 1 - \beta^2 + \frac{1}{8}(1-\sqrt{1-\beta^2})^2 \right\} \quad \text{ergs/cm} \ . \tag{5.2}$$

Here c.g.s units are employed and the symbols have the following meaning : E is the kinetic energy of the electron, N is the number density of the target atoms, m_e is the rest mass of the electron, e is the electronic charge in e.s.u., c is the speed of light in vacuo, Z is the atomic number of the target atoms, β is the ratio of the electron velocity to the speed of light in vacuo and I is the mean excitation potential energy of the target atoms. Values of I may be calculated using the following empirical formula suggested by Segrè <9>

$$I = 9.1Z\left(1 + 1.9Z^{-2/3}\right) \quad \text{eV} \ . \tag{5.3}$$

Alternatively, and indeed preferably, experimentally determined values of I are given for many elements in the comprehensive article by Ahlen <10>.

The interaction of energetic electrons with the atomic nucleus is described in the work of Mott <11> who expresses his results for the differential cross section in the form of conditionally convergent series. These are cumbersome to handle both numerically and analytically and so several approximations have been developed. The one most widely used, and the one used in the present work, is the McKinley-Feshbach cross section <12>. This cross section best approximates Mott's results for low Z elements; in fact Curr <13> has estimated it is accurate to one per cent for values of Z up to 40. The McKinley-Feshbach differential cross section for energy transfer is

$$\frac{d\sigma}{dT} = \pi r_0^2 \left(\frac{Z^2}{\beta^4\gamma^2}\right)\left(\frac{T_m}{T^2}\right)\left\{1 - \beta^2 \frac{T}{T_m} + \pi\alpha\beta\left[\sqrt{T/T_m} - T/T_m\right]\right\} \ , \tag{5.4}$$

where the symbols have the following meaning : r_0 is the classical radius of the electron, α is $Z\times$ (fine structure constant) $\approx \frac{Z}{137}$, T_m is the maximum energy the electron can transfer to the nucleus and γ is equal to $(1-\beta^2)^{-1/2}$.

The cross section for an energetic electron to produce a primary displacement is equivalent to the cross section for the electron to transfer kinetic energy greater than or equal to E_d to an atom and is given by the expression

$$\sigma_p(E_d, T_m) = \int_{E_d}^{T_m} \left(\frac{d\sigma}{dT}\right) dT \ . \tag{5.5}$$

Evaluation of this integral for the McKinley-Feshbach cross section is elementary and is

$$\sigma_p(E_d, T_m) = \frac{\pi r_0^2 Z^2}{\beta^4 \gamma^2} \left\{ [(T_m/E_d) - 1] - \beta^2 \ln(T_m/E_d) + \ldots \right.$$

$$\left. \ldots + \pi\alpha\beta \left\{ 2[\sqrt{T_m/E_d} - 1] - \ln(T_m/E_d) \right\} \right\} \ . \tag{5.6}$$

This is the cross section used by Oen and Holmes <6> in their calculations. However a much more useful quantity is the cross section for producing any displacements, be they primaries, secondaries or otherwise. In the case of an elemental solid this is simply given by incorporating the damage function as follows :

$$\sigma_t(E_d, T_m) = \int_{E_d}^{T_m} \Psi(T) \left(\frac{d\sigma}{dT}\right) dT \ . \tag{5.7}$$

Using the Kinchin-Pease damage function the expression can be evaluated analytically. The result for this total cross section is

$$\sigma_t(E_d, T_m) = \frac{\pi r_0^2 Z^2}{\beta^4 \gamma^2} \times \left\{ \frac{T_m}{2E_d} - \beta^2 \ln 2 + \ldots \right. \tag{5.8}$$

$$\ldots + \pi\alpha\beta \left\{ [\sqrt{1/E_d} - \sqrt{1/2E_d}]\, 2\sqrt{T_m} - ln2 \right\} + \ldots$$

$$\left. \ldots + \frac{kT_m}{2E_d} \times \left\{ \ln(T_m/2E_d) + \beta^2 [(2E_d/T_m) - 1] + \pi\alpha\beta[(2E_d/T_m) + 1 - 2\sqrt{2E_d/T_m}] \right\} \right\} \ .$$

This is the expression used by Cahn <7>.

Having obtained expressions for the displacement cross sections we may proceed to calculate, on average, how many atoms an energetic electron may displace in slowing down to rest in an elemental solid. The small number of displacement interactions, $d\bar{n}$, of an electron with energy E in a small path length dx is

$$d\bar{n} = \sigma_T N dx \ , \tag{5.9}$$

where N is the number density of target atoms. The total number of displaced atoms is found by integrating over the path length :

$$\bar{n}(E_0) = \int_0^{X_0} N \sigma_T \, dx \ , \tag{5.10}$$

where E_0 is the initial electron energy and X_0 is the total path length. It is difficult to obtain σ_T as a function of x. However the integral can be written as a function of energy by incorporating the stopping power :

$$\bar{n}(E_0) = \int_0^{E_0} \frac{N \sigma_T (E) \, dE}{(-dE/dx)} \ . \tag{5.11}$$

This is the expression used to calculate the average number of atoms displaced when an electron of initial energy E_0 comes to rest in an elemental solid. In practice the lower limit is taken to be that electron energy below which no atoms can be displaced. This is calculated from the equation

$$T_m = \frac{560.8}{A} y(y+2) \quad \text{eV} \ , \tag{5.12}$$

where y is the electron energy expressed in units of its rest energy, 0.511 MeV and A is the atomic mass in a.m.u. This is the well known relativitistic form of the standard expression for the maximum energy transfer between two colliding particles. One may easily consider the case of electrons leaving the solid, with say energy E_1, by replacing the lower integration limit with this value.

To extend these results to sapphire we must modify both the cross sections and stopping powers to take account of the fact that we have a diatomic lattice. The question of stopping powers is quite straightforward. Electrons in oxygen and aluminium atoms have different binding energies and this manifests itself as two different values of the mean ionization potential energy. We make the assumption that the total stopping power is just the sum of the individual stopping powers of each sub lattice (the Bragg rule), i.e

$$\left(\frac{-dE}{dx}\right) = \sum_i \left(\frac{-dE}{dx}\right)_i \ , \tag{5.13}$$

where the summation is taken over each component.

To deal with the problem of partial cross sections we use the partial damage functions calculated in chapter 4. The symbol σ_{ij} is taken to mean the cross section for the event of electrons displacing type i atoms and these pka's proceeding to displace type j atoms.

$$\sigma_{ij}(E) = \int_{E_{di}}^{T_{mi}} \Psi_{ij}(T)\left(\frac{d\sigma_i}{dT}\right)dT \ , \tag{5.14}$$

where E is the initial electron energy, E_{di} is the displacement energy of type i atoms, $(d\sigma_i/dT)$ is the McKinley-Feshbach cross section evaluated for the interaction of electrons with type i atoms and T_{mi} is the maximum energy an electron with kinetic energy E can transfer to a type i atom. This expression must be evaluated over the three regimes of the partial damage function. This cross section is then used in eqn. (5.11) to calculate the average number of point defects created on each sublattice by each type of pka. The total number of point defects on each sublattice is just the sum of such terms over each atom type.

Numerical Method. – The rapid variation of the differential cross section near the origin and much slower variation further out makes a straightforward linear integration very inefficient. Greater efficiency is obtained by re-writing the integral in eqns. (5.14) and (5.11) with respect to the logarithm of T. In this way the integration step size, being of equal size in $\ln(T)$, gives a shorter step size near the origin and a larger one further out. A five point quadrature integration technique was used and was tested by setting the damage energy equal to the energy and comparing the result with the analytic formula, eqn. (5.8). Accuracy to four significant figures was achieved using one hundred steps.

Results. – To illustrate the trend followed by $\bar{n}(E_0)$, in fig. 5.2 we show the variation in the mean number of oxygen displacements produced per incident electron assuming a variety of E_d values. The important point to note is that when the threshold is changed by a small amount (5% here) a much larger change occurs in $\bar{n}(E_0)$ when we are close to the threshold

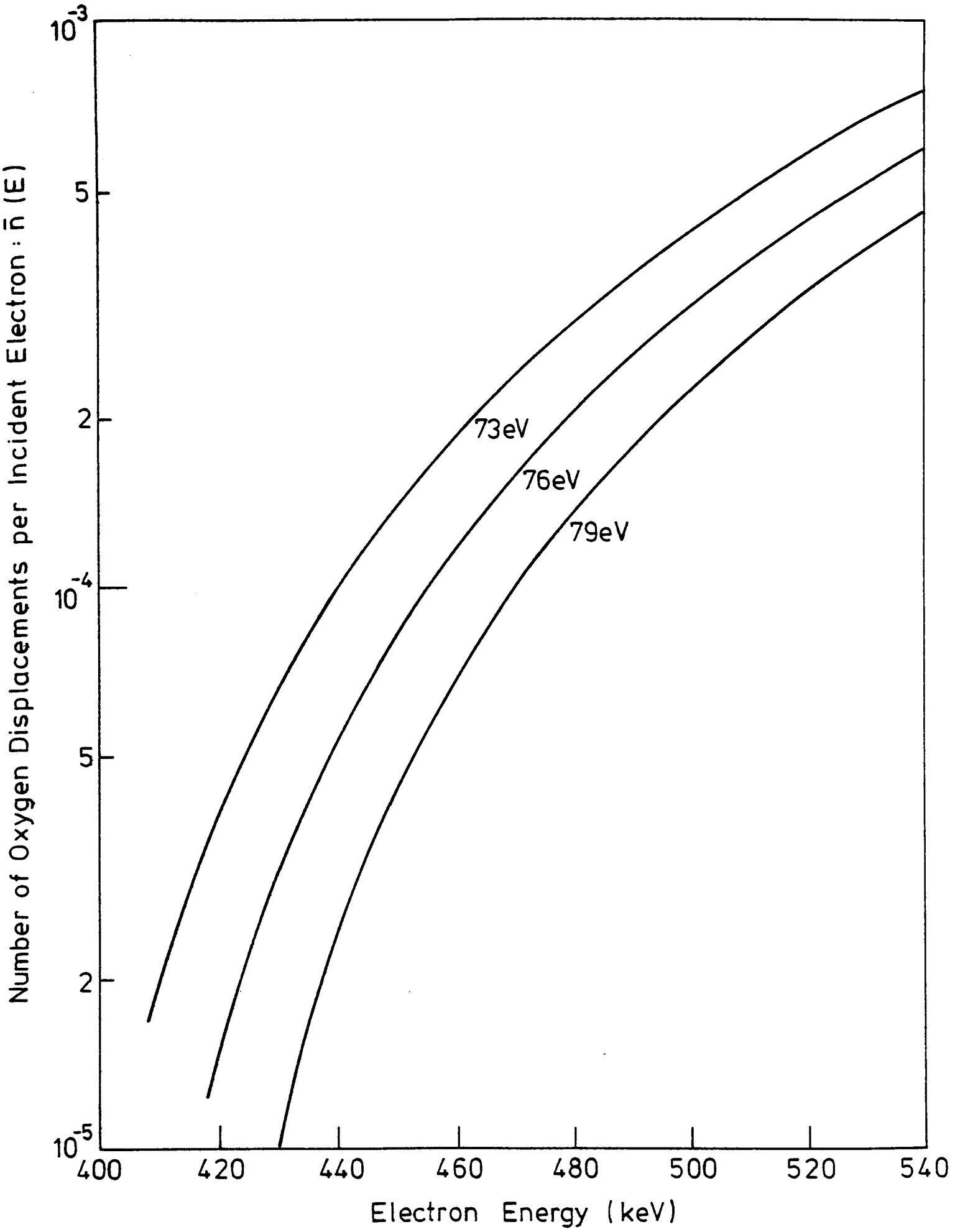


Fig. 5.2. Variation in the number of oxygen atoms displaced by energetic electrons. Three slightly different values of E_d have been used to illustrate the sensitivity of $\bar{n}(E)$ to this parameter near threshold.

energy. The value of E_d for aluminium was found by selecting trial values in the calculation of $n(E_0)$ and comparing these with the measured value. The determination of E_d is thus actually rather insensitive to the measured value of defect concentration and it is this property which makes the technique valuable.

§ 5.6. Thresholds : Experimental Details.

The oxygen threshold was determined by monitoring the *F* centre production following irradiation with a given energy and then lowering the energy for the next irradiation until no increase could be observed in the band height. The electron energy loss in the blocking foil was estimated to be 2.2 keV by integrating the Bethe stopping power, eqn.(5.2), for 450 keV electrons over the thickness of the foil. In both threshold experiments a short irradiation was performed, delivering about $10^{15}\ cm^{-2}$, 400 keV electrons and the spectrum was then recorded. The purpose of this was to account for any effects of ionization on impurities and pre-existing defects in the initial spectrum. These effects would then cancel out when this initial spectrum was subtracted from subsequent spectra. The dose of ionizing radiation required to saturate intrinsic colour centres was estimated from the work of Pells *et. al.* <14>, who consistently find no further colouring of Roditti sapphire after a dose of 10^6 rad. The initial dose delivered in the present experiment corresponds to around 5×10^7 rad and should be more than sufficient to ensure saturation.

In the case of the aluminium threshold the low oscillator strength of the *V* centre means that a large concentration of point defects must be built up before one can observe the associated optical absorption band. This in turn meant in practice it was only possible to obtain two data points due to the long irradiation times required. The electron energy was raised to 450 keV and a beam current of 5μA was obtained at the target (scattering from the aluminium foil significantly reduces the available beam current). For each data point a further fluence of $1.5 \times 10^{17}\ cm^{-2}$ was delivered. The initial spectrum was subtracted from these two to reveal the effect of the irradiation.

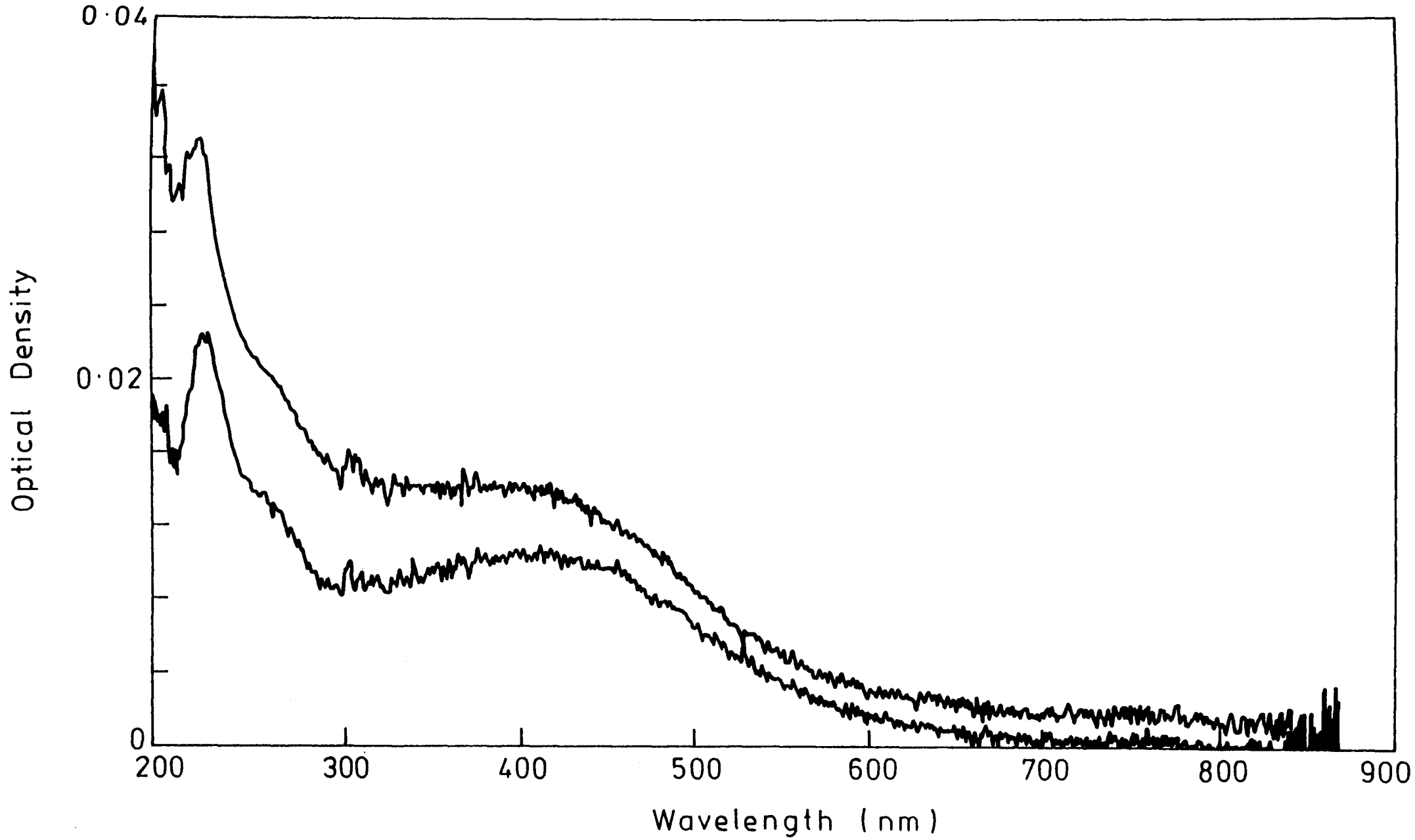


Fig. 5.3. Optical spectrum of sapphire following doses of $1.5\times10^{17}\,cm^{-2}$ and $3.0\times10^{17}\,cm^{-2}$, 450 keV electrons.

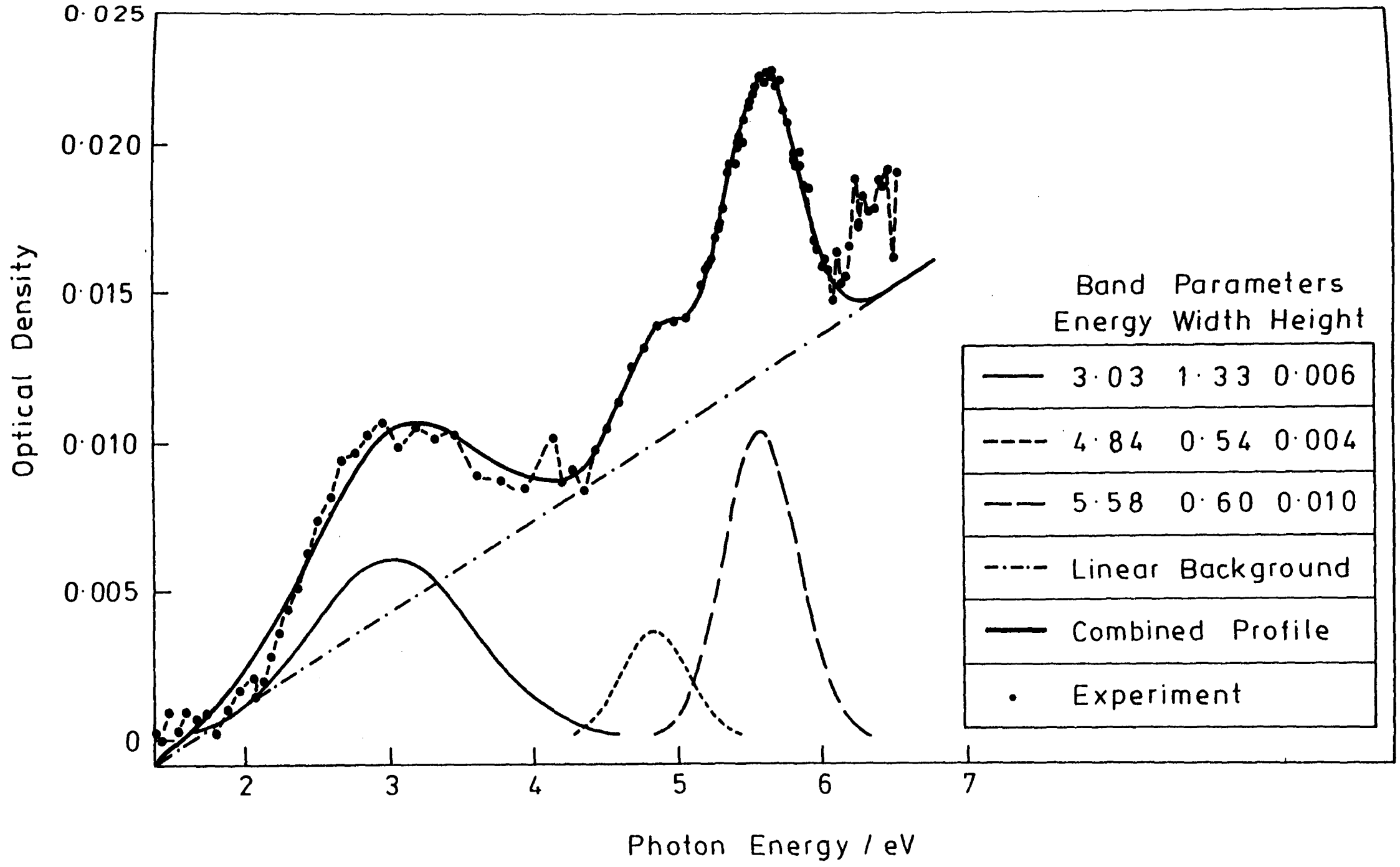


Fig 5.4. Resolution of absorption bands induced by 450 keV electron irradiation. The *V* band (aluminium vacancy) peaks at around 3 eV.

E_d/eV	$n(E_o)$
18	1.3×10^{-2}
23	6.2×10^{-3}
24	5.3×10^{-3}
25	4.6×10^{-3}
30	2.2×10^{-3}
40	4.1×10^{-4}

Table 5.1. Mean number of Al vacancies produced per electron (450 keV), assuming different values of E_d.

§ 5.7. Thresholds : Results.

Oxygen threshold. – Beginning with a 400 keV electron irradiation, a fluence of $2.78\times10^{17}\ cm^{-2}$ was delivered and no *F* centre production was observed. The energy was raised to 430 keV and following a fluence of $2.32\times10^{17}\ cm^{-2}$ a small *F* band was detected. The energy was subsequently lowered several times until at 410 keV a fluence of $5.5\times10^{17}\ cm^{-2}$ was delivered, resulting in no further colour centre production. The threshold voltage was determined to be 415 ± 4 keV, which, after accounting for the energy loss through the foil, gave a displacement threshold for the oxygen ion of 79 ± 2 eV.

Aluminium threshold. – The effects of the electron irradiation on the optical spectra are shown in fig. 5.3. In fig. 5.4 the lower spectrum has been re-plotted in terms of photon energy and resolved into absorption bands together with a linearly rising background feature. The *V* band is clearly visible, peaking at around 3 eV, together with bands at 4.8, 5.6 and 6.3eV. The number of aluminium displacements created by each electron was estimated from Smakula's equation (discussed in chapter 6). The refractive index of sapphire was calculated from Abramov *et. al.* <15> to be 1.79 at 400 nm. The oscillator strength of the *V* centre in sapphire has not been measured so a value of 0.1 was chosen to agree with the value reported for MgO by Henderson and Wertz <16>. This analogy does not seem unreasonable since in both cases the cation vacancy has six-fold coordination with respect to doubly charged oxygen ions. With these values the number of aluminium vacancies measured per incident electron was 5.6×10^{-3}.

In table 5.1 we present values of $n(E_0)$ calculated from scattering theory assuming different values of E_d. A value of 24 eV most closely reproduces the measured value. As mentioned earlier, the value of E_d is seen to be very insensitive with respect to $n(E_0)$.

§ 5.8. Thresholds : Discussion.

The value of E_d obtained for oxygen is in good agreement with other values in the literature and requires little further comment except to note that it is about three times greater than that of aluminium and hence in terms of a simple damage production model one would expect around three times more aluminium displacements than oxygen displacements

following ion or neutron irradiation. The estimated value for aluminium requires some qualification. The largest source of uncertainty in the present result must be regarded as the value assumed for the oscillator strength, which could conceivably be as much as a factor of two in error. In this case the value of E_d would either fall closer to Pells' value of 18 eV or rise to around 30 eV depending on the correction to be made. Another possible source of significant error is that the apparent efficiency of displacement damage is known to decrease with increasing levels of damage, as we shall show in the next chapter, making the observed value too low. This source of error is difficult to quantify but would lead to an over-estimate of E_d.

The optical spectrum shown in fig. 5.3 deserves further comment. The F^+ centre is known to have absorption bands at 4.8 eV, 5.6 eV and 6.3 eV, as discussed in chapter 3. The F centre absorption band maximum occurs at 6.02 eV. Following ion irradiation one usually sees all four bands, albeit in varying proportions depending on the irradiation conditions and ion used. For example Dalal *et. al.* <17> attempted to vary the relative proportion of F and F^+ centres produced in sapphire by varying the incident ion mass and hence the density of vacancies at the end of the ion track. The higher concentrations of vacancies produced under Ar and Ne bombardment compared to He bombardment were expected to produce local competition for electrons in the damaged regions and hence favour F^+ production. This was indeed found to occur, to the extent that for Ar and Ne bombardment the 6.02 eV band could not be resolved. A similar effect has been noted in CaO by Krefft <18>, who found that whilst both F and F^+ centres could be produced with proton irradiation, Ar or Ca irradiation produced *only* F^+ centres. In the spectrum presented in fig. 5.3 all the bands associated with the F^+ centre appear. However there is no evidence for the F band at 6.02 eV. This is probably associated with the fact that the low defect concentrations observed are similar to the impurity concentrations and competition from other electron traps will limit the number of electrons available for colour centre production.

The linearly rising background feature is commonly observed following particle irradiation of sapphire (though not usually so pronounced) and as yet has no explanation. Evans <19> has suggested a rise in the background in the U.V. part of the spectrum of

radiation damaged MgO may be associated with exciton bands perturbed by the displacement damage. The strength of this feature and the high level of non-stoichiometric damage in the present case certainly suggests that the two are related.

One curious feature of *V* centre production in sapphire is that it appears to be very difficult to produce *V* bands in the absence of *F* bands. All attempts to observe the *V* band independently by irradiating with electrons below the threshold for oxygen displacement have been unsuccessful. Since it is difficult to see how the actual displacement of aluminium ions could be affected by the displacement of oxygen ions some distance away, we suggest that this is more likely to be associated with the visibility of the aluminium vacancy centre rather than its production. An analogous situation, but with the role of anion and cation reversed, exists in zinc oxide where Locker and Meese <20> have suggested that zinc displacements must be present in order to activate oxygen colour centres. These authors suggest that oxygen vacancies will not be populated until zinc vacancies are produced and are able to pull the Fermi level below the oxygen donor levels by trapping electrons from the conduction band. The large band gap ($\sim 9eV$) of sapphire would make charge transfer processes with impurities or defects rather more likely. However analogous processes may similarly limit *V* centre visibility in sapphire and be linked with the appearance of the F^+ bands rather than the *F* band.

§ 5.9. Annealing Behaviour of Point Defects and Colour Centres in Sapphire.

In order to make meaningful estimates of the efficiency with which ion irradiation produces displacement damage it is necessary that no long range diffusion and subsequent recombination of Frenkel pairs should take place. If one is monitoring the defect concentration via colour centre absorption, as in the present investigation, then it is also necessary that these centres are optically active. As discussed in chapter 3, the measurements of Pells <21> on neutron irradiated samples indicate that the *F* centre in sapphire appears to be largely stable up to around room temperature. We also mentioned there that the F^{2+} centre is generally supposed to be unstable due to its large Coulomb attraction. Since these two

facts are of central importance to the present investigation experiments were performed to check their validity.

First we address the question of the stability of the F^{2+} centre. A standard sapphire sample was mounted on the stage of the variable temperature cryostat and cooled to 13 K. A beam of 100 keV He ions was used to produce a significant concentration of Frenkel pairs in the sample whilst avoiding a cascade-like configuration of defects. A dose of about $1.7\times10^{15}\ cm^{-2}$ was delivered and the spectrum in fig. 5.5 shows the induced optical absorption. The subsequent behaviour of oxygen vacancies was monitored as the sample temperature was raised. In fig. 5.6 we show the spectra which result from subtracting this baseline spectrum from those taken at 27, 49, 78, 90, 200, 230 and 255 K. The initial temperature rise causes both the F and F^+ bands to appear and the background absorption to steadily increase as the temperature is raised further. The three bands associated with the F^+ centre appear particularly clearly in the spectrum taken at 255 K. The implication of this is that bare oxygen vacancies are able to exist at liquid helium temperatures and only become unstable as the sample is warmed. At first sight this result would appear to have important consequences for low temperature damage efficiency studies, since it suggests all the vacancies may not be optically active. The effect is rather small though. In this experiment the colour centre concentration rises by less than ten percent as the sample temperature is raised. It is possible that more dense defect configurations (produced by irradiating with heavier ions) may have somewhat different characteristics, as the competition for electrons varies. However the degree of colour centre visibility is not expected to change dramatically and we conclude that meaningful estimates of damage efficiency can be obtained at low temperatures.

In a subsequent experiment the thermal stability of Frenkel pairs was confirmed. A dose of $1.1\times10^{15}\ cm^{-2}$, 200 keV He was delivered to a standard sapphire sample held at 13 K. A series of spectra were taken as the sample was warmed up and again an increase in the colour centre concentration was noted, similar to that just described. This time the sample temperature was increased above room temperature, to 330 K. A spectrum taken after the sample had been held at this temperature for half an hour revealed a reduction in the colour

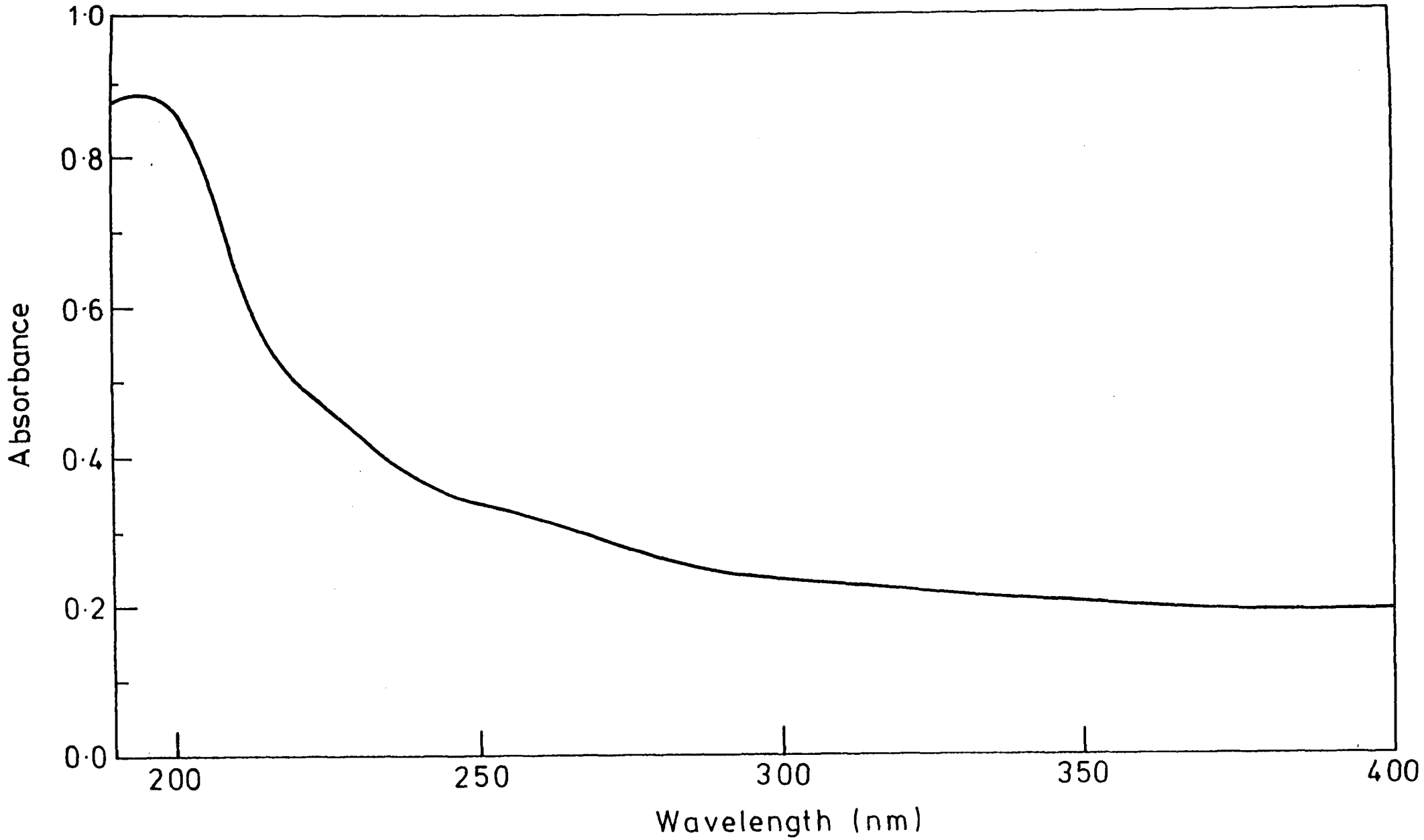


Fig. 5.5. Optical absorption following 1.7×10^{15}, 100 keV He cm^{-2}.

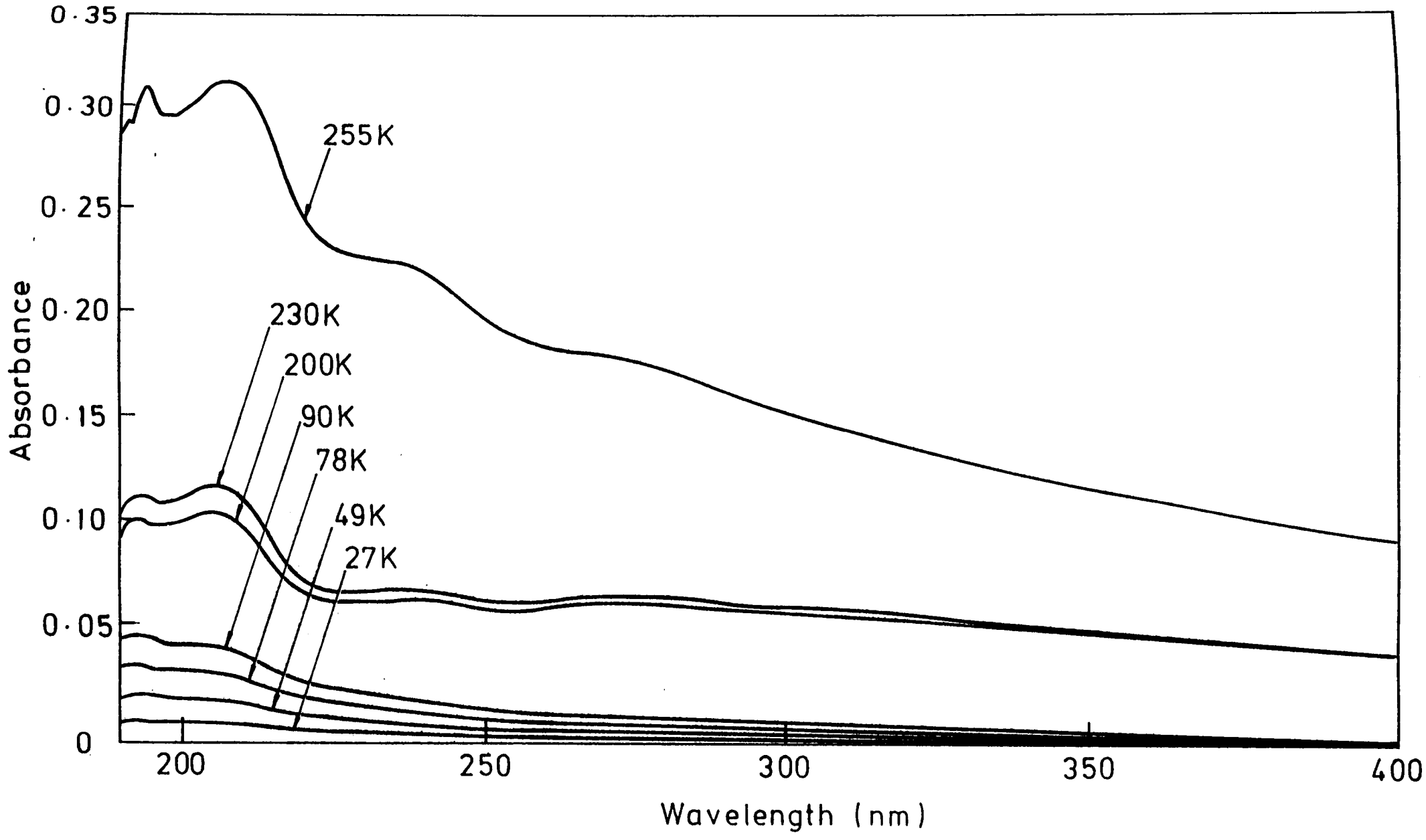


Fig. 5.6. 'Difference' spectra showing the appearance of F and F^+ centres as the sample is warmed.

centre concentration of a few percent. Increasing the temperature to 360 K produced a reduction of around fifteen percent and further heating to 380 K increased this to about twenty percent. This was sufficient to confirm the thermal stability of Frenkel pairs under the conditions used in the present experiments.

§ 5.10. Ionisation Stability of Frenkel Pairs.

One further question which must be addressed is the stability of lattice defects with respect to ionising radiation. There have been suggestions that if, following ion beam irradiation of insulators, one subjects the damaged sample to ionising irradiation, then some Frenkel pair recovery will take place. The implications of this for damage efficiency determinations are quite serious since the ratio of electronic to nuclear stopping differs widely between the low and high mass ions. Such an effect would complicate the interpretation of these experiments enormously. Let us review the evidence. Krefft <18> used a novel cantilever beam technique to monitor the volume changes of CaO which had been irradiated with various ions and then irradiated with protons or electrons. The creation of Frenkel pairs results in expansion of the damaged region which can be detected by making the sample act as a capacitor in a resonant LCR circuit. This author was also able to monitor the F and F^+ colour centre concentrations and the results suggested that in this material the effect of the ionising radiation was to actually destroy lattice vacancies in an ionisation stimulated annealing process. In an earlier study of sapphire, Arnold *et. al.* <22> found that the expansion caused by exposing samples to heavy ion irradiation was diminished when they were subsequently irradiated with protons or electrons. However this was attributed to a change in the charge state of the defects caused by the ionising radiation, rather than their annihilation. Firmer evidence for the stability of Frenkel pairs in sapphire under ionising irradiation was provided by Luera <23>, who used the technique of 'channelled proton induced X-rays' (CPIX) to monitor lattice damage. In the CPIX technique X-rays produced in the stopping of channelled protons in the target are monitored. Dechannelling of the protons due to displacement damage can be detected and the degree of lattice disorder inferred. This technique measures the total displacement damage directly, in contrast to optical techniques which measure only specific colour centre

concentrations. Luera's firm conclusion was that the number of displaced atoms produced in sapphire by ion implantation at room temperature is not affected by the deposition of additional energy into electronic processes.

For the purposes of the present investigation it seemed desirable to determine the effect of intense ionising radiation on pre-existing colour centres. A standard sapphire sample was irradiated with 100 keV He to a dose of about $5.8\times10^{14}\ cm^{-2}$ and its optical spectrum recorded. The sample was then irradiated with 400keV electrons to a dose of around 5×10^{7} rad and another spectrum recorded. The results are shown in fig. 5.7. There is a significant reduction in the height of the F band but a similarly significant increase in the F^{+} bands. If one assumes that all oxygen vacancies are present as either F or F^{+} centres then a closer examination of the spectra suggests that about eight percent of the total number of single oxygen vacancies have been annihilated. The main effect of ionising radiation appears to be the movement of charge between F and F^{+} centres, rather than the annihilation of Frenkel pairs. The small degree of annihilation suggested by these optical measurements is in contrast to that found by the CPIX technique. This is probably due to the fact that not all of the oxygen vacancies are present as F or F^{+} centres. A small proportion are likely to be present as divacancies and similar clusters, which cannot be detected optically due to their low oscillator strengths. The action of ionising radiation may be to transfer charge to these other centres or to cause single vacancies to combine and form clusters. These would still be detected by CPIX but would not be detected by optical absorption measurements.

§ 5.11. Summary.

In this chapter we have determined the threshold displacement energy for both the oxygen and aluminium sublattices in sapphire and found the values 79 and 24 eV respectively. We have confirmed the thermal stability of colour centres on the oxygen sublattice in the temperature range to be used in the damage efficiency measurements. Evidence was presented for the unexpected stability of the bare oxygen vacancy, the F^{2+} centre, at liquid helium temperatures. It was demonstrated that only a small fraction of the oxygen vacancies present were in the form of these optically inactive centres and one could still make

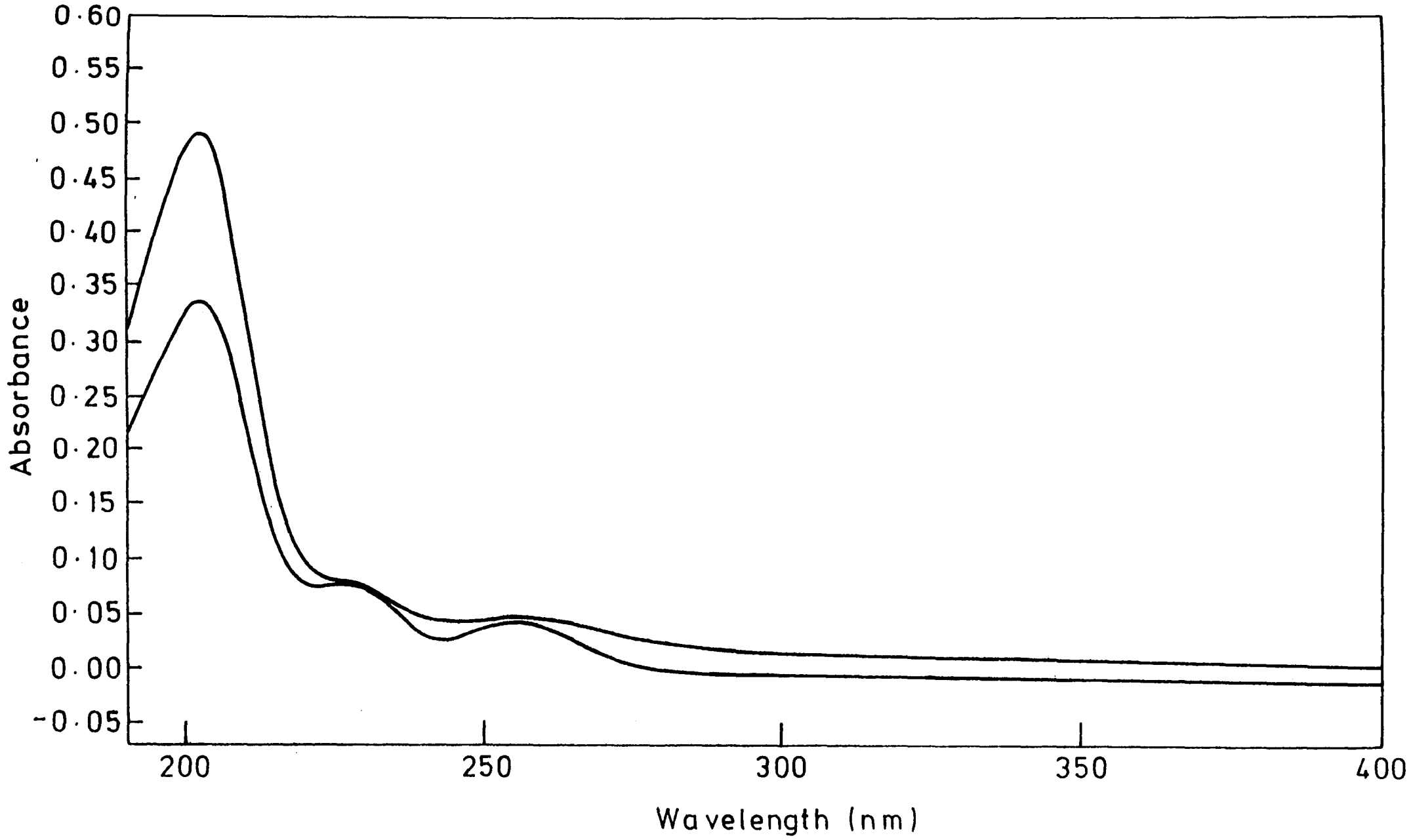


Fig. 5.7. Upper spectrum shows the absorbance following 100 keV He irradiation. The lower spectrum was taken after this sample had been exposed to 50 Mrad of ionising electron irradiation.

meaningful estimates of Frenkel pair production in sapphire at low temperatures via colour centre measurements. Finally, the single oxygen vacancy colour centres produced by ion bombardment were shown to be largely stable with respect to subsequent ionising radiation. A small amount of annealing was observed but this was attributed to the movement of charge between centres and the clustering of lattice defects rather then their annihilation. Having characterised the behaviour of sapphire in the experiments described here, we shall proceed with the determination of the efficiency of Frenkel pair production on the anion sublattice in sapphire under various conditions.

References

<1> G.P. Pells and D.C. Phillips, J. Nucl. Mat., 80 , 207, (1979).

<2> G.P. Pells and A.Y. Stathopoulos, Rad. Eff., 74 ,181, (1983).

<3> W.D. Compton and G.W. Arnold, Disc. Faraday Soc. 31 , 130, (1961).

<4> G.W. Arnold and W.D. Compton, Phys. Rev. Letts., 4 (2), 66, (1960).

<5> G.P. Pells, Rad. Eff., 64 ,71, (1982).

<6> O.S. Oen and D.K. Holmes, J. Appl. Phys. 30 , No. 8, 1289 (1959).

<7> J.H. Cahn, J. Appl. Phys. 30 , No. 8, 1310 (1959).

<8> H.A. Bethe and J. Ashkin, in *Experimental Nuclear Physics* , Ed. E. Segrè , Vol.1, John Wiley & Sons, Inc (1953).

<9> E. Segrè, *Nuclei and Particles* , W.A. Benjamin (1964).

<10> S.P Ahlen, Rev. Mod. Phys. 52 (1), 121 (1980).

<11> N.F. Mott, Proc. Roy. Soc. (London) A124 , 425 (1929).

<12> W.A. McKinley and H. Feshbach, Phys. Rev. 74 , 1759 (1948).

<13> R.M. Curr, Proc. Roy. Soc. (London) A68 , 156 (1955).

<14> G.P. Pells, A.J. Fudge, M.J. Murphy and M. Wilkins, 4th ASTM – Euratom Symp. on Reactor Dosimetry, Gaithersburg, Maryland U. S.A. (1982).

<15> V.N Abramov, B.G. Ivanov and A.I. Kuznetsov, Phys. Stat. Sol. (a) 48 ,287, (1978).

<16> B. Henderson and J.E. Wertz, *Defects in the Alkaline Earth Oxides* , Taylor & Francis Ltd., London (1977).

<17> M.L. Dalal, M. Rahmani and P.D. Townsend, Nucl. Instr. and Meths. in Phys. Res. B32 , 61 (1988).

<18> G.B. Krefft, Rad. Eff., 60 , 223 (1982).

<19> B.D. Evans, Phys. Rev. B, 9 (12), 5222, (1974).

<20> D.R. Locker and J.M. Meese, IEEE Trans. Nucl. Sci. NS- 19 (4), (1972).

<21> G.P. Pells, Rad. Phys. Chem. 22 (6), 1053, (1983)

<22> G.W. Arnold, G.B. Krefft and C.B. Norris, Appl. Phys. Letts., 25 (10), 540 (1974).

<23> T.F. Luera, J. Appl. Phys. 51 (11), 5792 (1980).

Chapter 6

Damage Efficiency in Sapphire

Introduction.

A major part of the experimental work of this investigation into point defect production involved the irradiation of sapphire with a variety of ion beams under various conditions. In this chapter we describe the methods employed and report the results of these experiments. The idea of using induced colour centre concentrations to investigate point defect production is not new and the ability to make such experiments quantitative can be traced back to the important paper by Smakula <1> in 1930, where the formula relating the colour centre concentration to the optical properties of the material was derived. Since that time numerous other workers, *e.g.* <2 to 7>, have used this technique in an attempt to assess the accuracy of theories of point defect production. However this has often been a secondary aim of the investigation and so the experimental parameters have tended to be rather unsuitable. One common example is the use of ion doses which are well suited to producing easily observable absorption bands but are then usually much too large to obtain reliable estimates of defect production by single ions, due to the interactions between overlapping regions of damage. The use of a sensitive double beam spectrophotometer combined, with the ability to digitally record spectra and perform accurate subtractions of one spectrum from another, enabled the ion doses used in the present investigation to be kept to a minimum.

Another criticism of earlier work in this field is that the theoretical estimates of defect production, to which experimental results are then compared, were often based on rough approximations and used inaccurate stopping powers or cross sections. We saw in chapter 2 how the Lindhard electronic stopping powers differ significantly from the more accurate ZBL values. However the Lindhard stopping powers are almost universally adhered to in

radiation damage calculations due to their analytic simplicity. Since the materials employed in colour centre studies are usually diatomic and the point defects are usually only detected on one sublattice, proper account must be taken of the damage energy partitioning but this is usually only done in an approximate manner (*e.g.* Luera <8>). In the present study we have used the estimates given by the calculations described in chapter 4 and, as we pointed out there, we believe these are amongst the most accurate currently available. We begin this chapter with a description of the basic theory and experiments used to measure the point defect concentration in sapphire.

§ 6.1 Evaluation of Colour Centre Concentration.

We wish to determine the number of point defects present in a sample of sapphire. As we have seen in chapter 3 the primary defects (oxygen and aluminium vacancies) are able to trap charge (electrons or holes respectively) and in doing so become optically active. Following Smakula, Dexter <9> has given a theory of the absorption of light by optically active centres in solids and derived the following relationship between the number of absorbing centres N and the integrated optical absorption coefficient μ:

$$N = \frac{n m^* c}{\pi e^2 h f_{ij}} \left(\frac{E_0}{E_{eff}}\right)^2 \int \mu(E)\, dE \ . \tag{6.1}$$

Here f_{ij} is the oscillator strength for the transition giving rise to the absorption band in question, n is the refractive index, m^* is the effective electron (or hole) mass, E_0 is the average electric field in the medium and E_{eff} is the effective field. The ratio of these last two quantities accounts for the fact that the perturbing field experienced by the electron at the defect is actually the sum of the 'applied' field due to the photon and the induced field as the surrounding medium is polarised. The most common approximation used for this, and the one we shall use, is that of the Lorentz-Lorenz local field which gives

$$\frac{E_{eff}}{E_0} = 1 + \frac{n^2 - 1}{3} \ . \tag{6.2}$$

Dexter states that in reality this approximation is unlikely to be reliable for most systems and

that to predict the value of the square of E_{eff}/E_0 within a factor of two is as much as one can hope for. This must be borne in mind if one wishes to make absolute determinations of colour centre concentration. For a Gaussian absorption band the integral can be performed to give the spatial average of the colour centre concentration $\overline{N}$ in terms of the maximum absorption coefficient μ_{max} and the fwhm U in eV :

$$\overline{N} = 0.87\times10^{17}\ \frac{n}{f_{ij}\,(n^2+2)^2}\ \mu_{max}\,U \qquad cm^{-3}\ . \tag{6.3}$$

So if the refractive index, the oscillator strength of the transition and the band height are known it is a simple matter to deduce the colour centre concentration. The refractive index of sapphire has been accurately measured by Abramov *et. al.* <10> and the following formula reproduces the measured values to five significant figures:

$$n^2 - 1 = \frac{C_1\lambda^2}{\lambda^2-\lambda_1^2} + \frac{C_2\lambda^2}{\lambda^2-\lambda_2^2} + \frac{C_3\lambda^2}{\lambda^2-\lambda_3^2}\ . \tag{6.4}$$

λ is the wavelength of the light in micrometres, $C_1=1.023789$, $C_2=1.058264$, $C_3=5.280792$, $\lambda_1=0.06144821$, $\lambda_2=0.1106997$ and $\lambda_3=17.92656$.

The oscillator strength for the transition from ψ_0 to ψ_i for light polarised along $x_j=x,y$ or z is defined, in Slater atomic units, as

$$f_{ij} = (E_i-E_0)\,|<\psi_i\,|x_j|\,\psi_0>|^2\ . \tag{6.5}$$

Reliable measurements of oscillator strengths are difficult to obtain. The usual approach is to obtain a sample with a known concentration of a given colour centre and then invert eqn.(6.3) to obtain f_{ij}. This was the method used by Silsbee <11> to determine this parameter for the alkali halides. This author measured the concentration of F centres via electron spin resonance (e.s.r.) and then compared this with the result of optical absorption measurements. We immediately face a problem if we wish to use the same technique with sapphire because here the F centre contains two electrons and cannot be detected with e.s.r. Despite this problem some estimates of the f_{ij} for the F and F^+ centres have been suggested. Lee and Crawford <12> performed a series of bleaching experiments on neutron irradiated sapphire

and recorded changes in the 6.1 and 4.8 eV bands. They assumed that the change in the number of centres producing the 6.1eV band is equal to the change in the number of centres responsible for the 4.8 eV band and used Smakula's equation (eqn. 6.1) to deduce that the oscillator strength of the 6.1 eV band is about twice that of the 4.8 eV band. We now know that these bands are associated with the F and F^+ centres respectively so that this factor of two is what one would expect. Turner and Crawford <13> placed $f_{6.1}$ in the range 1 to 2 so this would place $f_{4.8}$ in the range 0.5 to 1. In an attempt to calculate the oscillator strengths of the F^+ centre from first principles using eqn.(6.6), Evans and Staplebroek <14> used the wave functions of La *et. al.* <15> to give the values shown in table 6.1. For the estimates of point defect concentration reported in this chapter we shall use the values $f_{6.1} = 1.3$ and $f_{5.4} = 0.66$ for the respective oscillator strengths, together with the measured fwhm values at room temperature of 0.73 eV and 0.36 eV for the F and F^+ centres respectively. The corresponding values used for 77 K measurements are 0.62 eV and 0.35 eV.

In summary then we may say that the absolute values of colour centre concentration $\overline{N}$ determined with Smakula's equation must be treated with caution due to the many approximations and uncertainties associated with its use. However the largest uncertainties may be absorbed into a constant of proportionality between $\overline{N}$ and the band parameters so that we can make accurate *relative* measurements of radiation induced colour centre concentration.

The form of Smakula's equation given in eqn.(6.3) is not immediately applicable to experimentally measured quantities. It contains the absorption coefficient μ from the Beer-Lambert law

$$I = I_0 e^{-\mu t} \quad , \tag{6.6}$$

where I_0 is the incident light intensity and t is the sample thickness. We must ensure that the value of μ used in eqn.(6.3) only represents light absorbed by colour centres. However a straightforward measurement of the light transmitted by a sample will also include light lost by reflection from the surface (the normal Fresnel losses). Two simple experimental procedures are able to overcome this problem. The first involves using the double beam

f_{ij}	i = 1 1A -> 1B	i = 2 1A -> 2A	i = 3 1A -> 2B
f_{ix}	0.601	0.0	0.013
f_{iy}	0.292	0.0	0.414
f_{iz}	0.0	0.664	0.4

Table 6.1 Calculated oscillator strengths of the F^+ centre <14>

capability of the spectrophotometer and placing an identical, but unirradiated, sample in the reference chamber so that the Fresnel losses cancel out. The other possibility is to record a pre-irradiation spectrum of the sample which may then be subtracted from subsequent spectra to reveal the effect of irradiation. We prefer to use the latter technique since it does not rely on the reference sample being *identical* to the irradiated sample and is in practice somewhat easier to implement. Indeed, if the sample is contained within an optical cryostat then the former method also requires that one place equivalent windows in the reference chamber. These 'difference' spectra are necessary when one is dealing with very weak absorption bands and so this single subtraction of the pre-irradiation spectrum takes care of both problems. One potential error which may arise is if the reflection coefficient R of the sample changes as a result of the irradiation, for this would be indistinguishable from a change in absorption coefficient on the basis of a simple measurement of transmitted light. We wish to show that the error introduced by this effect is negligible for a realistic change in R. Consider a sample prior to irradiation with absorption coefficient μ_1, refractive index n_1 and intensity reflection coefficient R_1. The latter two quantities are related by the usual Fresnel equation for normal incidence

$$R_1 = \left(\frac{n_1 - 1}{n_1 + 1}\right)^2 \quad . \tag{6.7}$$

For a light beam of intensity I_0 incident on the surface of a sample of thickness t, it is straightforward to show that the transmitted light has an intensity given by

$$I_t = \frac{I_0 (1 - R_1)^2 \, e^{-\mu_1 t}}{1 - R_1^2 \, e^{-2\mu_1 t}} \quad . \tag{6.8}$$

Now consider the sample following irradiation. A similar equation may be written for the transmitted intensity but we allow for the fact that the reflection coefficient may have been altered to R_2 and the absorption coefficient will have increased by an amount $\Delta\mu$, which is the quantity we actually require for Smakula's equation. Now the optical density or its equivalent, the absorbance number, A (we use the two terms interchangeably), is the quantity recorded by the Lambda-9 spectrophotometer and is defined as

$$A = \log_{10}\left(\frac{I_0}{I_t}\right) \quad . \tag{6.9}$$

The difference spectrum obtained by subtracting pre- from post irradiation measurements will give the quantity

$$A_2 - A_1 = \log_{10}\left\{\frac{1-R_2^2\, e^{-2t(\mu_1+\Delta\mu)}}{1-R_1^2\, e^{-2t\mu_1}}\right\} + \log_{10}\left\{\frac{e^{t(\mu_1+\Delta\mu)}}{e^{t\mu_1}}\right\} + 2\log_{10}\left\{\frac{1-R_1}{1-R_2}\right\} \quad . \quad (6.10)$$

Considering the first term, the negative exponentials have a maximum value of unity whilst $R_1^2 \approx R_2^2 \approx 0.01$ so that the quantity in brackets is very close to unity and its logarithm tends to zero. A binomial expansion of the argument of the third term shows that this has a similar behaviour for realistic values of R. In this case both of these terms can be neglected in comparison to the second term. Numerical calculations have been made for the case where R_2 differs substantially from R_1 and even in the extreme case of it doubling, the neglected terms only introduces a 5% error. So we may write the following expression for $\Delta\mu$:

$$\Delta\mu = 2.303\, \frac{(A_2 - A_1)}{t} \quad . \quad (6.11)$$

With this relationship it is straightforward to show that the following more useful form of eqn.(6.3), giving the number of colour centres produced per incident ion, N_ϕ, in terms of the peak optical density of the difference spectra, ΔA, and ion fluence ϕ, is also valid:

$$N_\phi = 2.00 \times 10^{17}\, \frac{n}{f_{ij}\, \phi (n^2+2)^2}\, U\, \Delta A \quad . \quad (6.12)$$

§ 6.2 Data Analysis.

The colour centre concentration can be derived from the peak optical density of the difference spectra as shown above. However the spectrum in the vicinity of any given band generally contains contributions from other centres and a proper evaluation of the band parameters requires the separation of these other features. To achieve this a data fitting program was written which allows one to 'guess' an experimental spectrum by adding together features of known absorption bands, and this spectrum is then optimised in a least squares manner to obtain the best fit to the experimental data. It was invariably found that the experimental spectrum could not be accurately reproduced by a simple combination of

known absorption bands – the 'background' feature, discussed in chapter 5, was also present which interfered with the *F* band. To account for this the program was modified to allow one to include either a constant, linear, quadratic or exponential background feature in the optimisation procedure and this produced much better fits to the true data. This procedure may be criticised since there is at present no theoretical understanding of this 'background' absorption and hence no guide as to which functional form might best approximate it over the range of interest. In order to gain a better guide as to the best way to account for this background absorption it proved necessary to extend the range of measurements into the vacuum ultra-violet (v.u.v) part of the spectrum. A short series of experiments were performed with a v.u.v spectrophotometer at the National Physical Laboratory (NPL) with the aid of Dr. G. Freeman of the Quantum Metrology Department. The NPL spectrophotometer is a single beam, manually operated system hence the number of data points taken was limited. Three samples were measured – one unirradiated, one irradiated with 50 keV protons and one with 100 keV helium. The spectrum of the unirradiated sample is shown in fig. 6.1. The difference spectra of the irradiated samples were obtained by subtracting the values for the unirradiated sample. These are shown in figs. 6.2 and 6.3 for the H and He irradiated samples respectively. The background absorption on which the *F* band is superimposed is higher on the high energy side of the peak but does not rise particularly sharply. These spectra, which show the full extent of the *F* band, are useful in giving a guide to the resolution of other spectra where data cannot be obtained beyond the 6.5 eV (190 nm) limit of the Lambda – 9 spectrophotometer. The background absorption used in the analysis need only be realistic in the vicinity of the bands of interest. As an example of the data analysis process we present figs. 6.4 and 6.5 which show typical experimental spectra of sapphire damaged by He and Kr respectively (replotted in terms of photon energy), together with the Gaussian bands and background fitted by the analysis program.

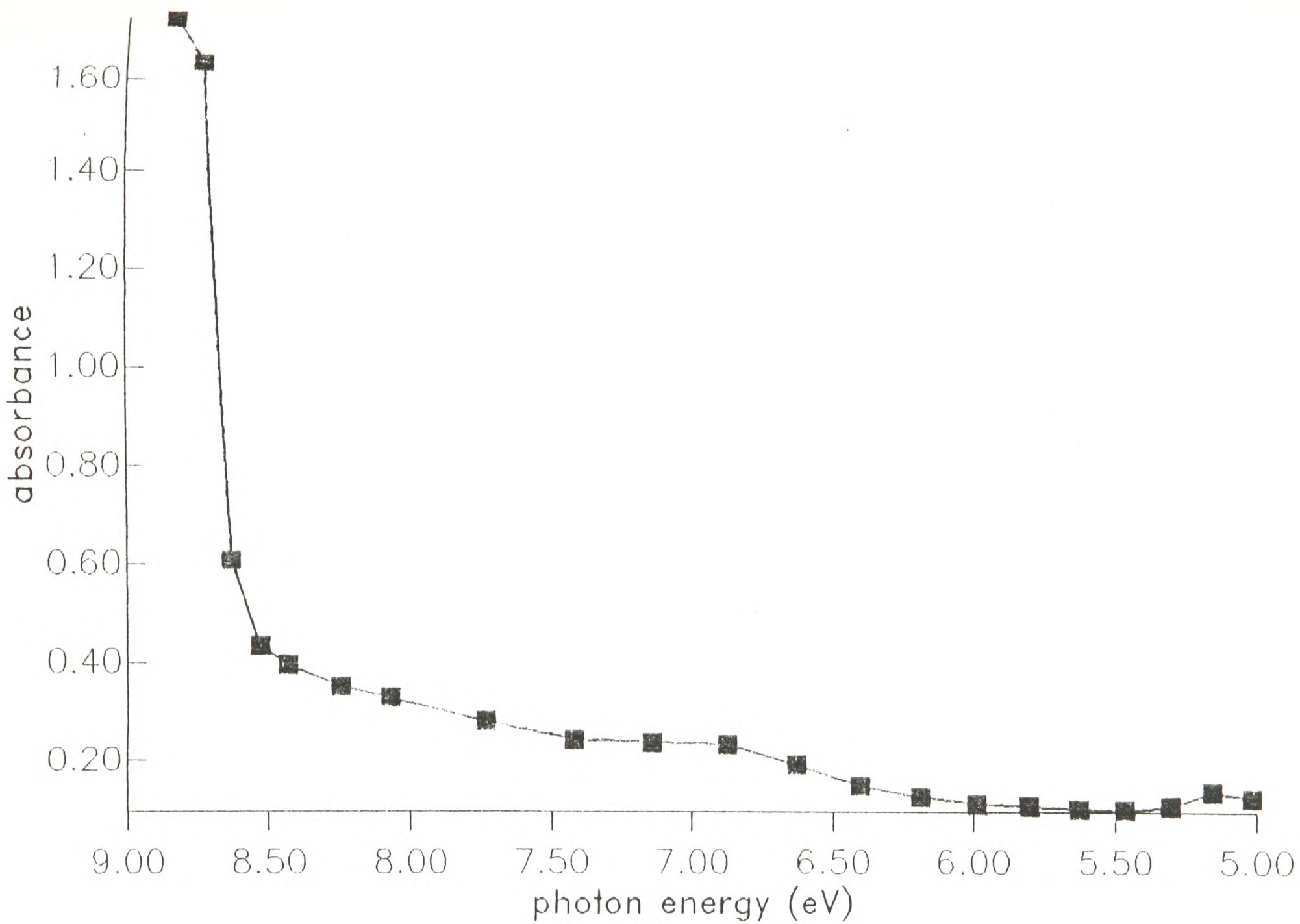


Fig. 6.1. Optical absorption spectrum of unirradiated sapphire, extending into the vacuum ultra-violet.

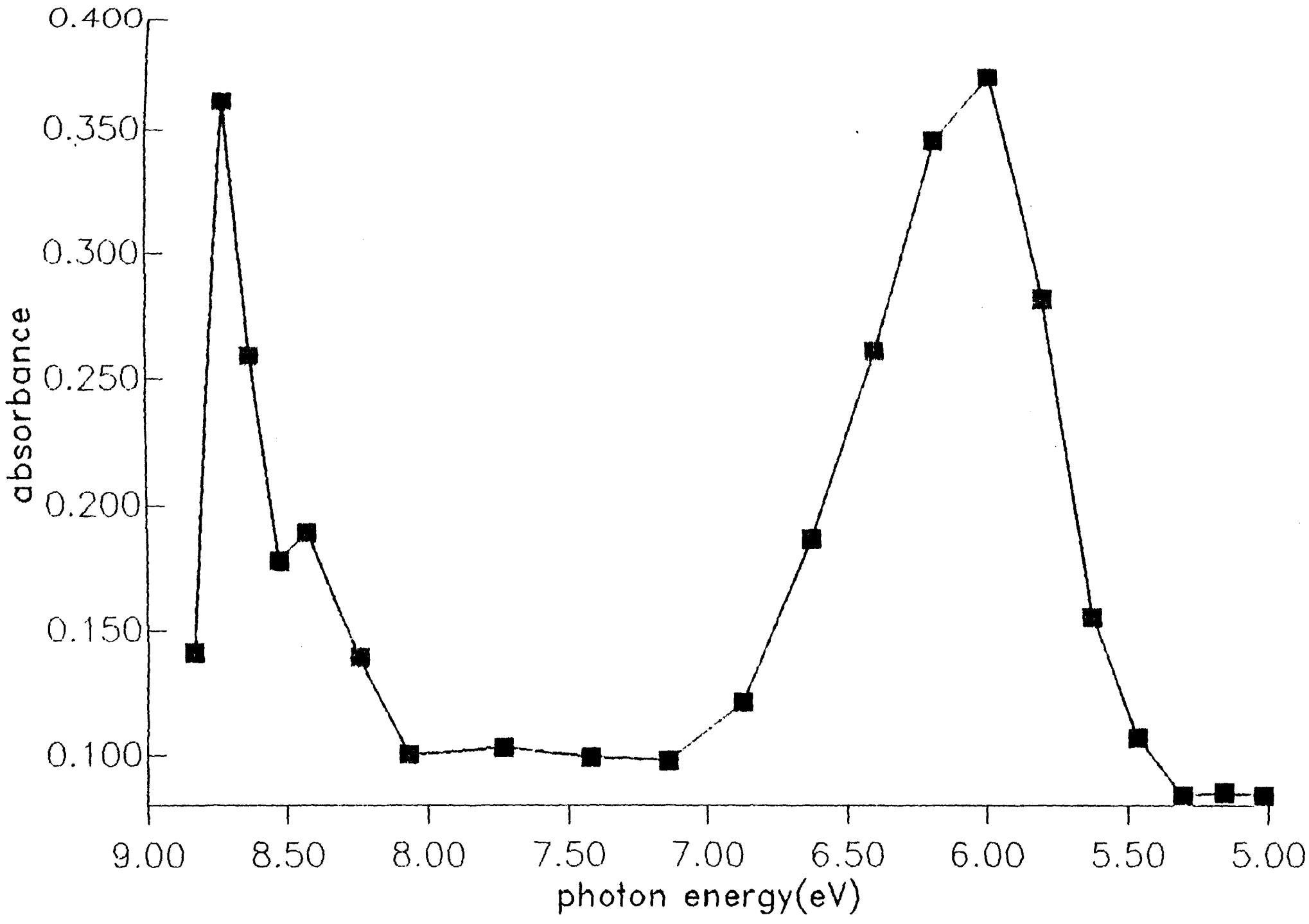


Fig. 6.2. Optical absorption spectrum of proton irradiated sapphire, extending into the vacuum ultra-violet.

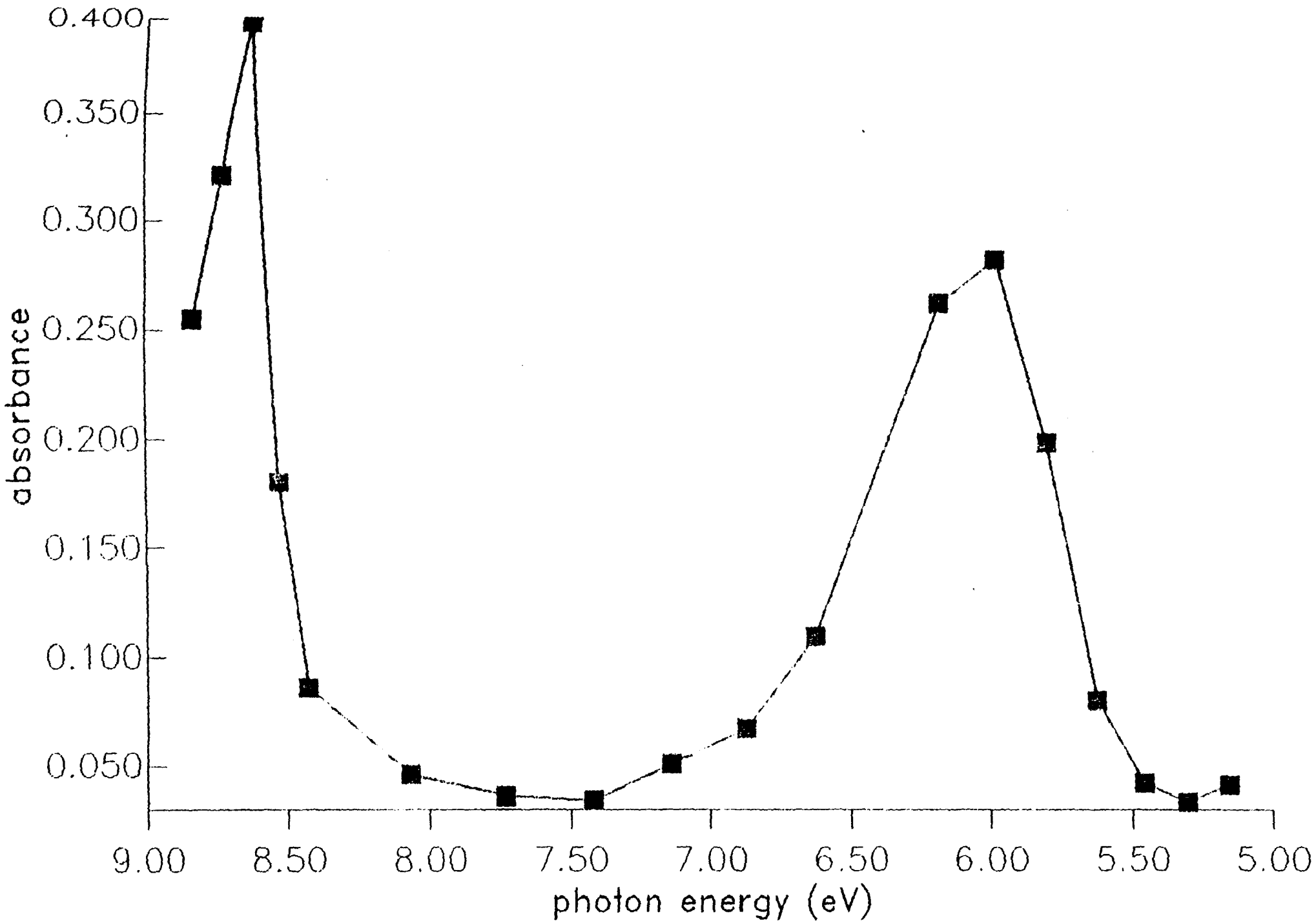


Fig. 6.3. Optical absorption spectrum of helium irradiated sapphire, extending into the vacuum ultra-violet.

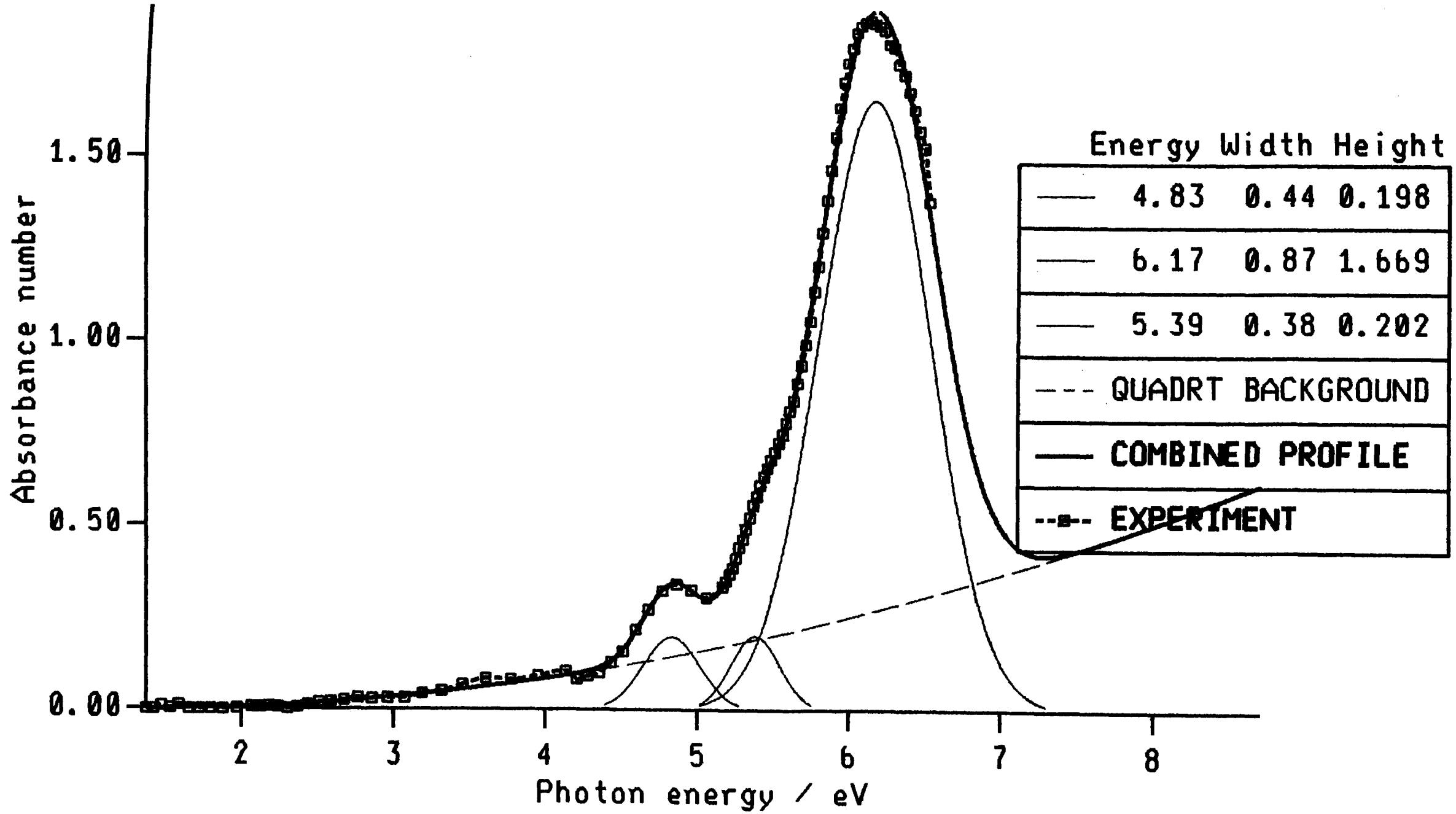


Fig. 6.4. Example of curve fitting program for He irradiation.

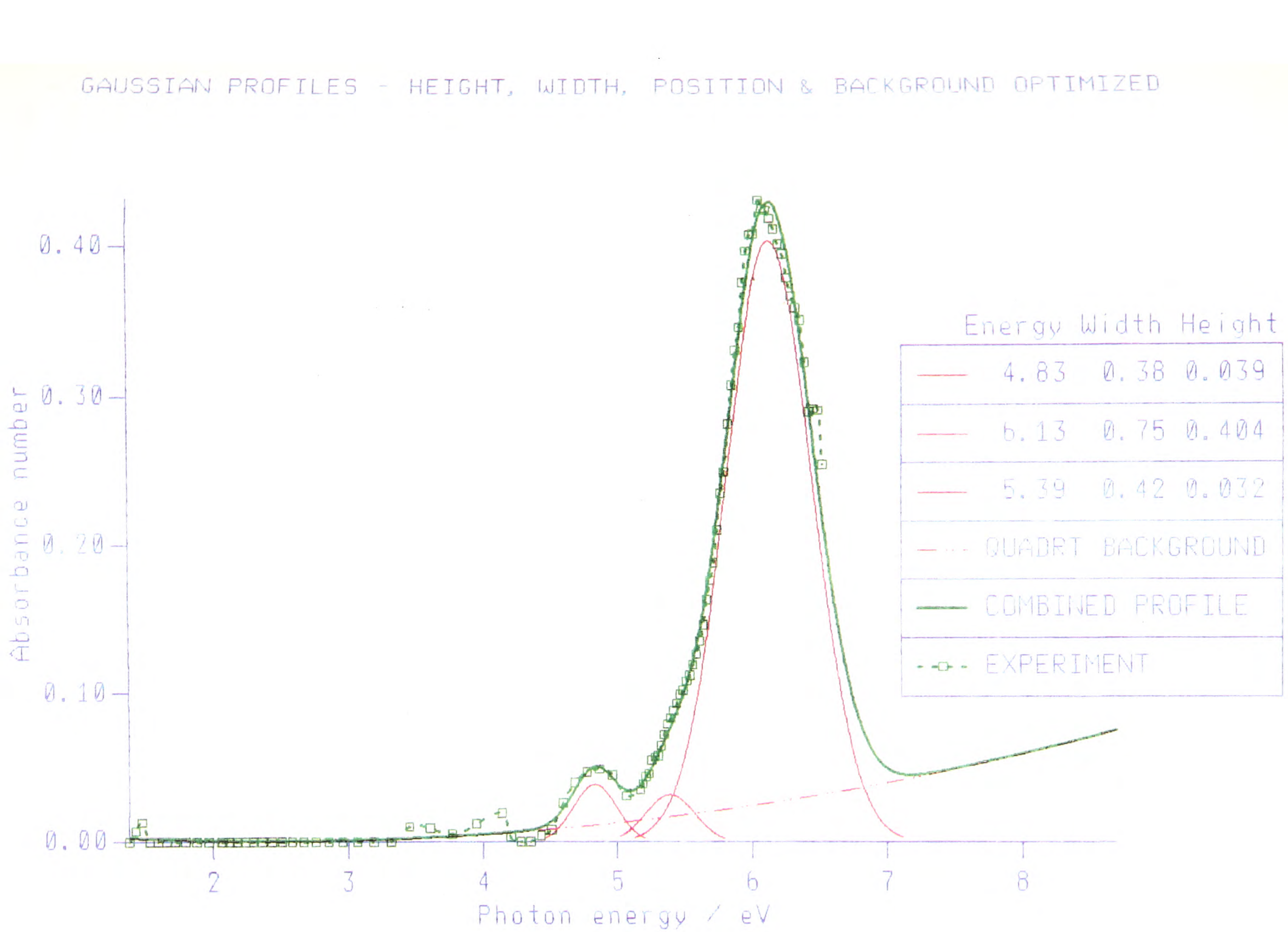


Fig. 6.5. Example of curve fitting program for Kr irradiation.

§ 6.3 Accelerator Techniques.

The majority of the ion irradiations were performed with a 'Danfysik' 200 kV accelerator, shown in fig. 6.6. The accelerator consists of a motor generator providing a stable, isolated power supply, a 'mini-separator' and an accelerator column, all contained within a high voltage enclosure. The mini-separator contains the ion source, ion extraction system, analysing magnet and vacuum pumping system. The ion source consists of a titanium or tungsten filament which is heated by passing a current of about 20A, surrounded by a small oven capable of operating at 1800°C. The oven allows ion beams of solid substances such as boron, carbon or metals to be produced by vaporising the solid. During operation the filament current is increased until an arc is struck in the source and the ions formed are then extracted through a 0.5 mm aperture by a 30 kV potential. The beam current can be controlled by adjusting either the filament current, the arc voltage or the gas pressure inside the ion source. The particular ion beam required is magnetically separated from all others with a 90°, double-focussing analysing magnet. This magnet has a radius of 50 cm and can analyse mass-to-charge ratios in the range 1 to 250 a.m.u. per unit ionic charge, with a resolving power of about 500.

The accelerator has an automatically controlled vacuum system, operated by an Edwards 2002 vacuum controller. A vacuum is produced by four pumps at various positions on the accelerator. The ion source is pumped by a diffusion pump whilst a turbo-molecular pump provides the vacuum in the accelerator section. The central section of the beam line is separated from both the accelerator section and the target chamber by automatically actuated valves and is held at a pressure of around 10^{-7} torr by a diffusion pump. A cryopump is fitted to the target chamber in order to provide a high pumping speed, low ultimate pressure and to avoid contamination of the chamber with the organic molecules produced by the action of diffusion pumps. A low pressure is particularly important for low temperature irradiations since thin films may freeze on the surface of the sample. This has two undesirable consequences. The first is that the energetic ions are slowed down by the thin film and enter the sample with a reduced energy. The second is that the deposited layer may grow to such proportions as to produce an interference film, visible to the naked eye, which distorts the

Fig. 6.6. The Harwell 200 kV Heavy Ion Accelerator. The constant temperature cryostat is shown in position at the end of the beam line.



A E A TECHNOLOGY
CULHAM / HARWELL
PHOTOGRAPHIC GROUP

HRC 29542

optical measurements. Under typical experimental conditions the target chamber was held at a pressure of around 2×10^{-7} torr during the irradiation. This proved sufficient to avoid the build up of optically detected films.

There are a number of problems associated with the operation of an accelerator of this kind, the most tiresome of which is due to the ion source. The filaments generally have a lifetime of around ten hours under typical operating conditions, which is sufficiently small to make it rather likely that one will expire at some point during a days irradiation. If protons are to be produced and the filament is operated in an atmosphere of hydrogen then this lifetime is reduced to about two hours. In order to replace a filament the ion source must be exposed to the atmosphere and subsequent pumping down to produce an acceptable vacuum takes about an hour. Then there is a further hour or so to wait since the filament can only be slowly heated to its operating temperature due to the large amount of outgassing which occurs.

A potentially more important problem was encountered in the production of beams of multiply charged noble gases, due to the gas supply system to the ion source. Gas is fed into the ion source from one of a number of small valved bottles, along a common feed pipe with a further valve. The gas is selected by simply opening the valve on the appropriate bottle. The noble gases are more commonly used than any others and so these are kept permanently 'on-line' but with the valves closed. However if a valve is slightly leaky or if a given gas has previously been in use then traces of this gas will fill the common feed pipe. This means that along with the required gas there will also be traces of other gases in the ion source. Now usually the presence of a number of different ions in the ion source is of no consequence since these are separated from the required beam by the analysing magnet. But the noble gases have the property that the charge to mass ratio of, for example, doubly charged krypton is just the same as the charge to mass ratio of singly charged argon and similarly for other neighbouring pairs in the periodic table. Thus if one wishes to accelerate doubly charged krypton and some argon is also present in the ion source, the analysing magnet will be unable to differentiate between the desired beam and singly charged argon ions. For a given ion the ratio of doubly to singly charged species is very small so even if only a small amount of

argon is present it may give a beam comparable to the doubly charged krypton. This problem actually came to light in the course of a damage efficiency determination for doubly charge krypton which produced much less damage than expected. The solution is straightforward and involves making sure the other gas bottles are disconnected from the common feed pipe and that this is well pumped out before the run to ensure that only the desired gas atoms are present in the source.

Dosimetry was performed by integrating the current passing between the cryostat (which was electrically isolated) and earth with a Danfysik 554 current integrator. There are several problems associated with using a simple current measurement to perform ion beam dosimetry, one of which is the emission of secondary electrons from the beam collimator. If these reach the target where the ion current is being measured they will cause an apparent reduction in the dose. The solution to this problem is to apply a positive potential to a plate in front of the collimator and attract any emitted electrons. An electron suppression system is fitted to the target vacuum chamber and was operated with an applied voltage of 280 V. However tests showed that the secondary electron current was generally negligible compared to the ion current. Another common source of error in dosimetry is the ejection of electrons from the target which appear electrically as the arrival of an equal positive charge and would thus give an overestimate of the ion dose. However the geometry of the cryostat (shown attached to the ion accelerator in fig. 6.6) is such that it acts as a Faraday cage and any electrons emitted from the target are highly likely to be subsequently reabsorbed at another electrically connected point on the cryostat. We can obtain a rough estimate of the fraction of electrons which escape the cryostat from simple geometric considerations. The end of the entrance tube to the cryostat is about 18 cm from the sample stage and has a diameter of 3.0 cm. The solid angle subtended at the end is thus 0.022 sterads. If we assume that electrons are ejected from the target isotropically then less than 0.2% will escape form the cryostat. A more realistic distribution of ejection angles will not change this crude estimate dramatically. Finally, tests were carried out to ensure that there were no special problems associated with the fact that the samples were electrically insulating. No significant difference was found in the measured beam current when the copper heat shield on the cryostat cold finger was rotated into the beam rather than the sapphire sample.

Several irradiations were also carried out using the Harwell 5MV Van de Graaff accelerator. This is a vertically mounted machine which accelerates the ions downwards and then bends their path with a large magnet to deliver them along a horizontal beam line. An unfortunate limitation of this machine which was not originally anticipated is that although it is intrinsically capable of producing, for example, several MeV krypton or xenon ions, the bending magnet is not sufficiently powerful to bend them through 90° along the horizontal beam line. A 15° beam line is available on the machine but this has a semi-permanent experimental rig attached and so could not be used for the present work. This accelerator was used to perform several neon and argon irradiations at energies higher than those used on the Danfysik accelerator and the results obtained provided a useful check on the dosimetry and general consistency of the main body of data.

§ 6.4 Experimental Procedure.

For a determination of the damage efficiency at a given temperature the sample was placed inside either the variable or constant temperature cryostat, cooled to the required temperature and an initial spectrum recorded over the range 900 to 190 nm. The cryostat was then transferred to the Van de Graaff electron accelerator and a short burst of electrons delivered to ionise impurities and existing colour centres as described in the previous chapter. It was generally found though that this had a negligible effect on the spectrum. Since the ion beams used were calculated to deposit most of their energy into ionisation in the target, the procedure used for the later experiments was to use a small ion dose to provide the initial ionisation and then use the spectrum recorded after this as the baseline. This had the advantage of avoiding the electron accelerator where the vacuum was somewhat poorer than the ion accelerator and occasionally caused thin hydrocarbon films to be deposited on the sample, especially for irradiations below room temperature. Optical spectra taken with the sample in this state would often show interference patterns, as discussed in section § 6.3. Another disadvantage with using the electron accelerator for this task is that the high intensity X-rays produced as the electrons are stopped in the target caused radiolysis to occur in the quartz windows of the cryostat and change their optical absorption. This problem

could be overcome by using sapphire windows but in view of these problems it was decided to forego the electron irradiation and use the ionisation from the ion beam as described. Tests were carried out to ensure that no differences were found between experiments which had used electrons and those which had used ions to provide the ionisation.

After the baseline spectrum had been recorded the cryostat could be transferred to the ion accelerator. Unfortunately the spectrophotometer could not be positioned around the cryostat as it sat on the accelerator and so it was necessary to move between the two, alternately irradiating and recording spectra. Transportation of the cryostat between these two machines was actually the most time consuming part of the experimental procedure since the accelerator vacuum had to be broken each time. During transportation the cryostat could not be pumped and the pressure would inevitably rise. This problem was most acute during 77 K irradiations, where water vapour could condense on the surface of the sample. For liquid helium temperature irradiations the cryostat dewar would effectively cryopump the internal volume and maintain the low pressure. The ion dose rate was not considered to be important for the low doses used and so varied considerably depending on the ion used. It was generally chosen to give a sufficiently long irradiation time to avoid errors in the current integrator. In all cases though the currents were sufficiently low to avoid significant beam heating.

§ 6.5 Results.

The number of oxygen vacancies created per incident ion was determined for H, D, He, B, N, Ne, Ar and Kr ions at both room temperature and 77 K. In order to use the minimum ion doses a degree of iteration was necessary. Thus one would first obtain a rough estimate of the efficiency and use this to select a more appropriate dose for a more careful experiment. For each ion the growth of the F and F^+ centres bands was monitored. In figs. 6.7 and 6.8 we present the results of room temperature proton and helium irradiations respectively, as examples of typical growth curves. The growth curves obtained at 77 K exhibited a curious phenomenon. It was invariably found that following irradiation at low temperature the

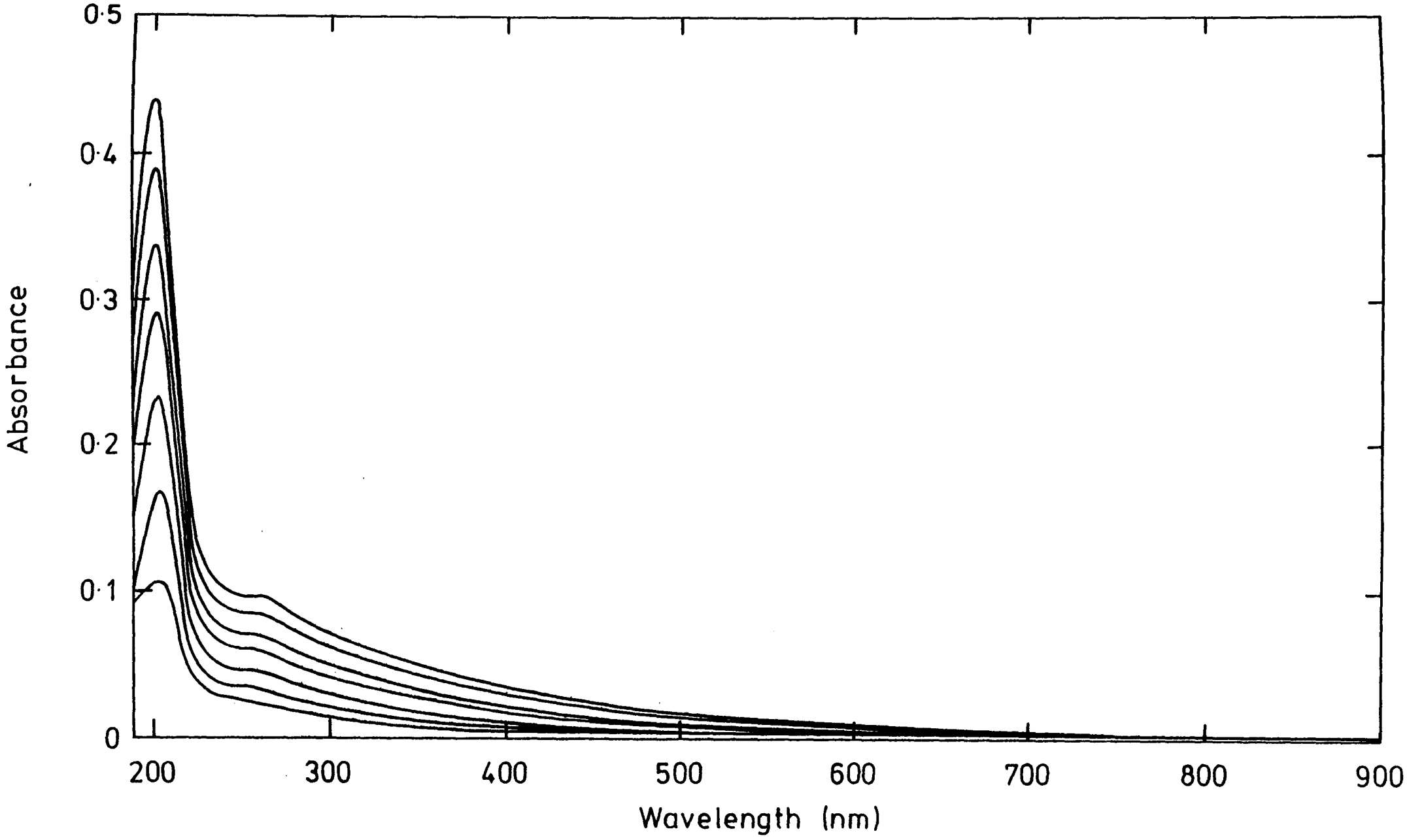


Fig. 6.7. Example of growth curves for proton irradiation.

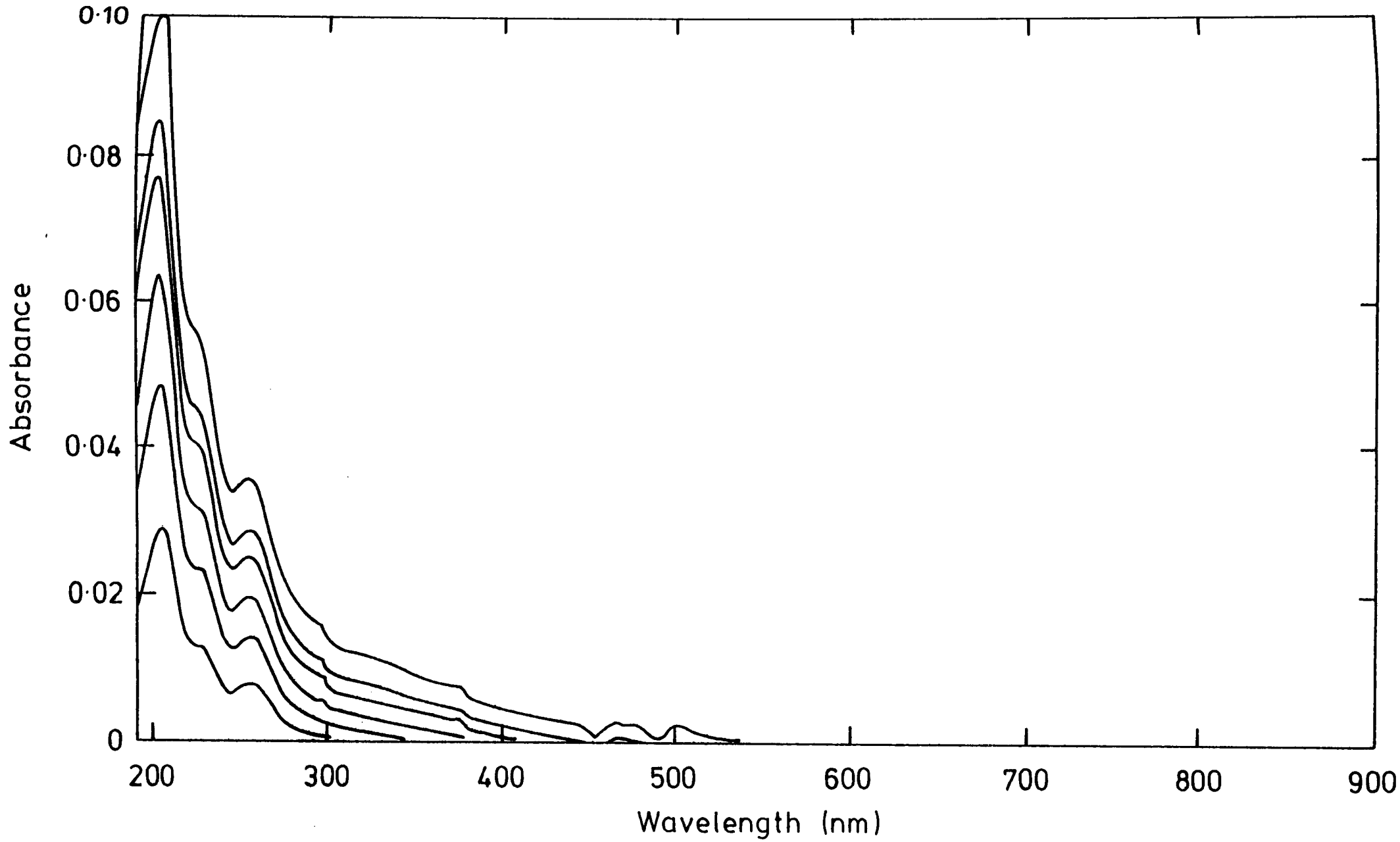


Fig. 6.8. Example of growth curves for He irradiation.

optical density of the sample decreased with decreasing wavelength across the spectral range from 900 to 190 nm, such that the difference spectra had negative absorbance values. The effect is small, but easily measurable and is illustrated in fig. 6.9 for a 400 keV Ar irradiation and in fig. 6.10 for a 100 keV He irradiation. The primary implication of this for the present investigation was that it introduced extra complications into the deconvolution of the spectra but from a broader viewpoint the effect itself is rather interesting. The large spectral range over which it occurs suggests that some bulk property is being affected rather than the properties of a localised centre. If the refractive index were to decrease following irradiation then the apparent absorption would decrease. We have tested the likelihood of this by assuming that the effect occurs as a result of a reduction in the reflection coefficient and then obtained the change in refractive index needed to cause a change of this magnitude. The wavelength dependent refractive index changes are shown in table 6.2 and have been calculated using the data in fig. 6.10. This shows that the required changes can be rather large, but are rather more credible at the longer wavelengths. This curious effect was not investigated to any large extent since it must be regarded as incidental to the main objectives of this study, but during the course of the low temperature experiments some further points were noted. The reduction in apparent absorption was progressive with dose but eventually saturated for all ions tested. Damaging a new piece of crystal, either by changing the ion energy or irradiating the opposite face caused a further reduction. It was also noted that greater reductions occurred for those ions where the ratio of electronic to nuclear stopping was highest, i.e. H and He. Some of these points may give indications of the cause of this effect but further experiments are clearly required.

The damage efficiency, defined here as

$$\zeta = \frac{\textit{measured no. oxygen vacancies per incident ion}}{\textit{calculated no. oxygen vacancies per incident ion}}, \tag{6.13}$$

was determined for the ions H, D, He, B, N, Ne, Ar and Kr, using eqn. (6.12) for both the F and F^+ centres. It was found that the measured number of oxygen vacancies per incident ion, ν_{meas}, decreased with increasing dose for all ions except H, which showed a constant value within experimental error. We have already indicated, in the introduction to this chapter, that

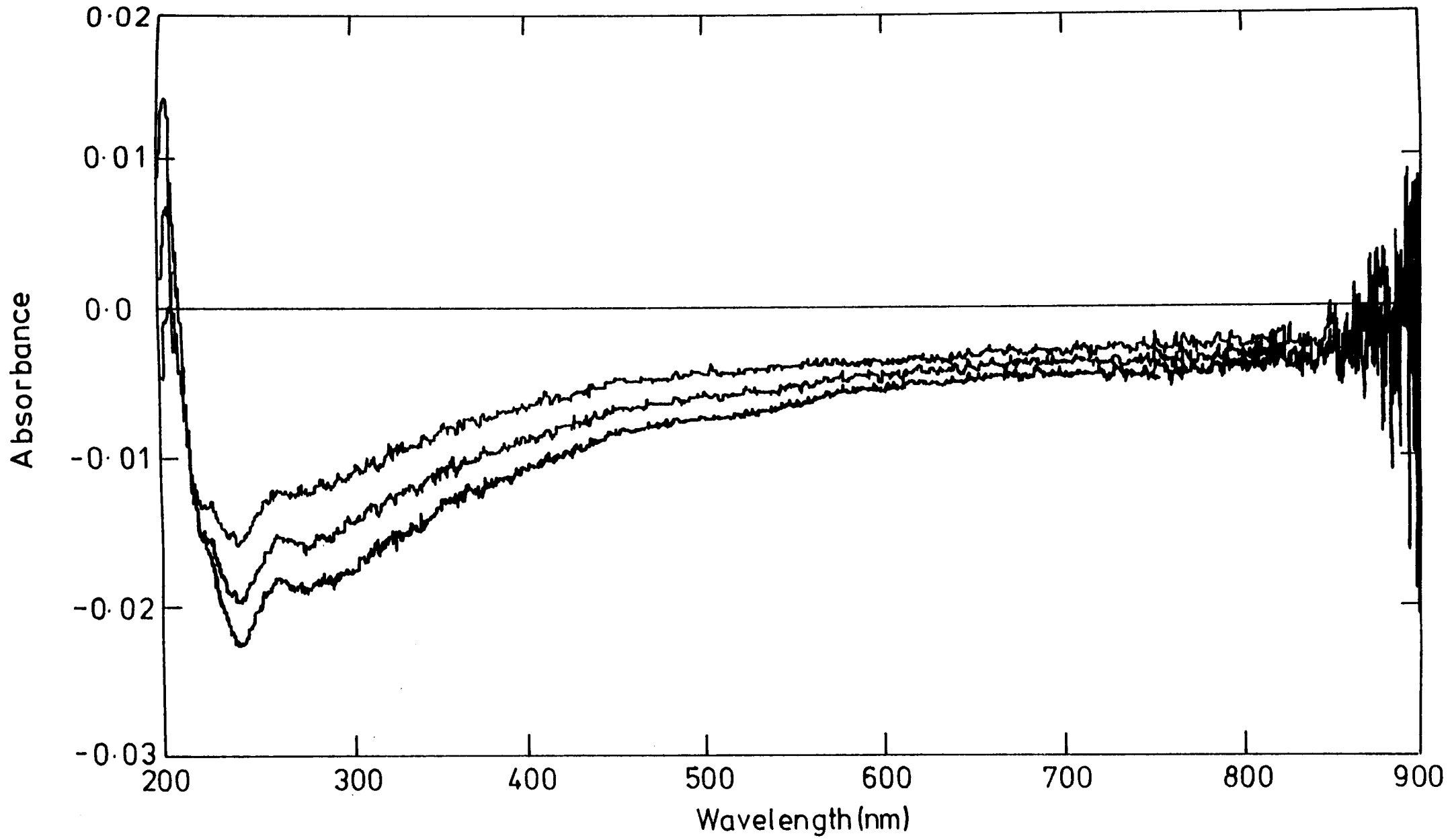


Fig. 6.9. Example of low temperature (77K) growth curve for Ar irradiation. The reduction in absorbance following low temperature ion irradiation is discussed in the text, § 6.5.

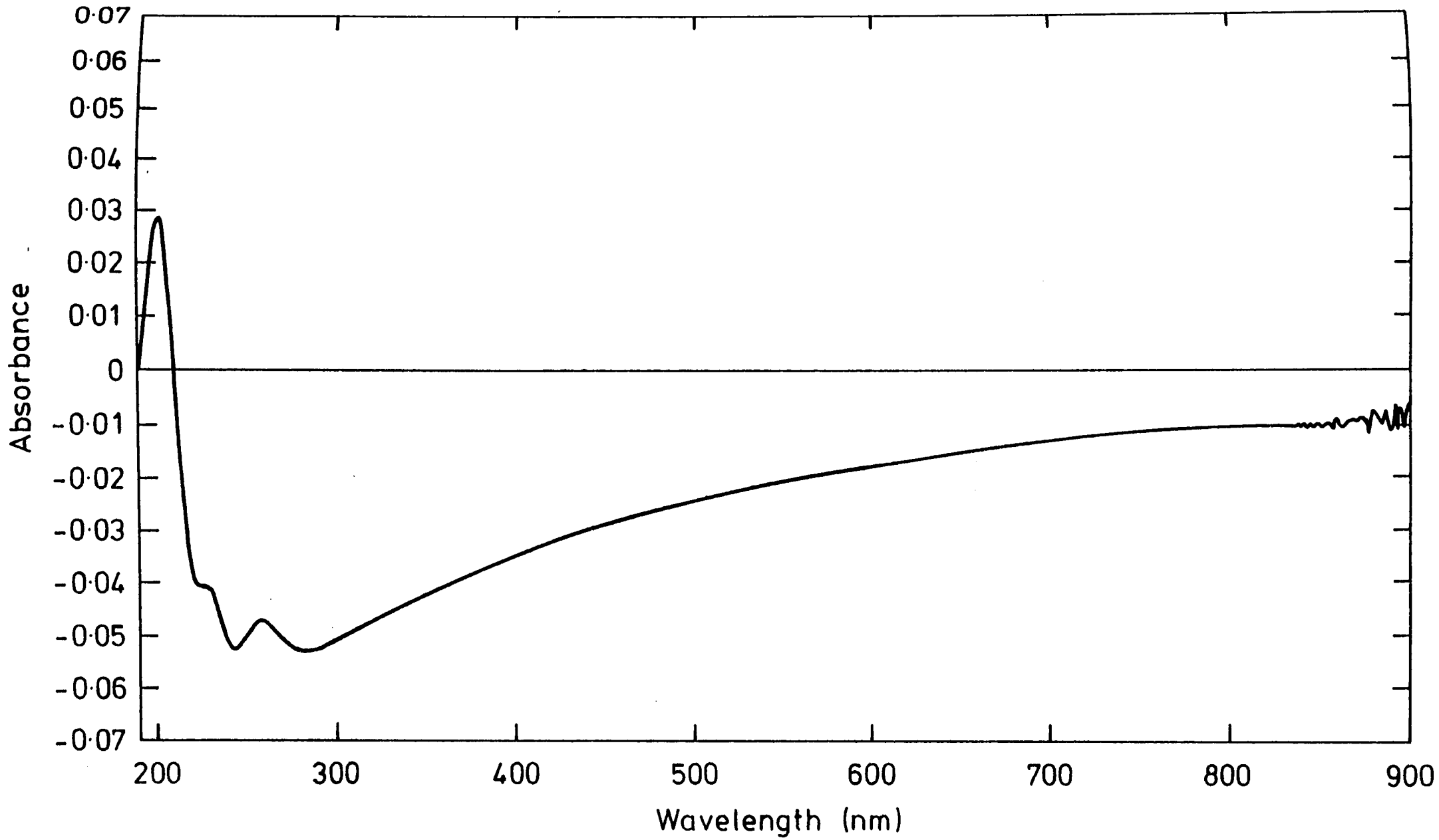


Fig. 6.10. Example of low temperature (77K) growth curve for He irradiation. The reduction in absorbance following low temperature ion irradiation is discussed in the text, § 6.5.

λ(nm)	n_1	n_2	R_2	Δn %
300	1.814	1.369	0.0243	25
400	1.787	1.515	0.0419	15
500	1.774	1.599	0.0531	10
600	1.768	1.652	0.0605	7
700	1.763	1.683	0.0648	5
800	1.760	1.708	0.0684	3
900	1.758	1.727	0.0711	2

Table 6.2. Refractive index changes required to cause observed low temperature reduction in apparent absorbance.

this phenomenon is probably related to the overlap of damaged regions. In the next chapter we shall present calculations which appear to confirm this. Here we simply note that a further degree of uncertainty is introduced into the determination of ζ. Figs. 6.11 to 6.15 show a representative selection of the growth of the F band absorbance with increasing ion dose. The curvature of these graphs is indicative of an apparent reduction in the damage efficiency. This is most clearly shown in figs. 6.16 to 6.20, where the F and F^+ centre growth curves have been used to determine the variation of ν_{meas} with dose for this same selection. In some cases, such as fig. 6.16, the curve was sufficiently regular to extrapolate back to zero dose. In other cases though, such as fig. 6.19, this was not possible. The procedure adopted in such cases was to use the first experimental point in the evaluation of ζ. Measurements were made over the greatest range of doses for a 400 keV Ne, room temperature irradiation. In this case values of ν_{meas} were determined over three orders of magnitude in dose. The results are shown in fig. 6.21 and show how the damage efficiency can fall dramatically for high doses. The final values of ζ are shown, together with relevant parameters such as ion energy and minimum dose, in table 6.3. These efficiencies are shown graphically in fig. 6.22 as a function of the ion masses. The error bars associated with the data are meant to indicate relative uncertainties within each data set (77 K and room temperature) but do not include systematic errors such as those associated with the oscillator strength. These relative errors include contributions from the dosimetry and those encountered in the curve fitting procedure described above. The latter of these introduces the greatest uncertainty, especially in the low temperature data set.

The most striking feature of fig. 6.22 is the large variation in ζ for the low mass ions. The low efficiency for He is especially significant since this has the lowest associated measurement error. In order to determine whether this is common to ionic insulators or just a property of sapphire, the efficiency was also measured in MgO for H and He at room temperature. The spectra are shown in figs. 6.23 and 6.24. It is very difficult to separate the F and F^+ bands in MgO since their peaks lie at 5.01 and 4.95 eV respectively <16>. This introduces a complication into the determination of the defect production since it is equally difficult to obtain separate estimates of the number of F and F^+ centres. We have evaluated the defect production in two different ways: first, by assuming that the band around 5 eV is

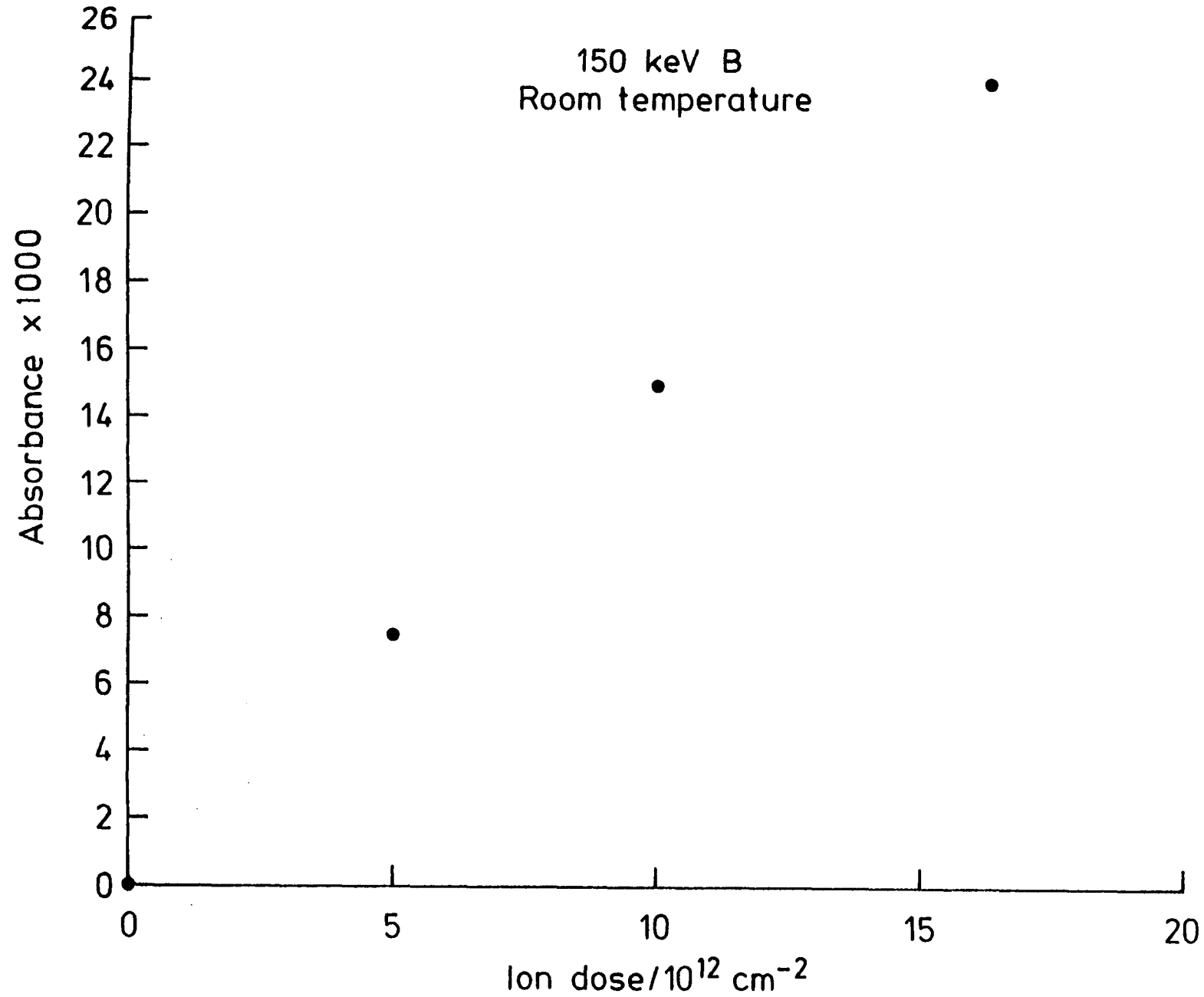


Fig. 6.11. Growth of the *F* band following 150 keV B irradiation at room temperature.

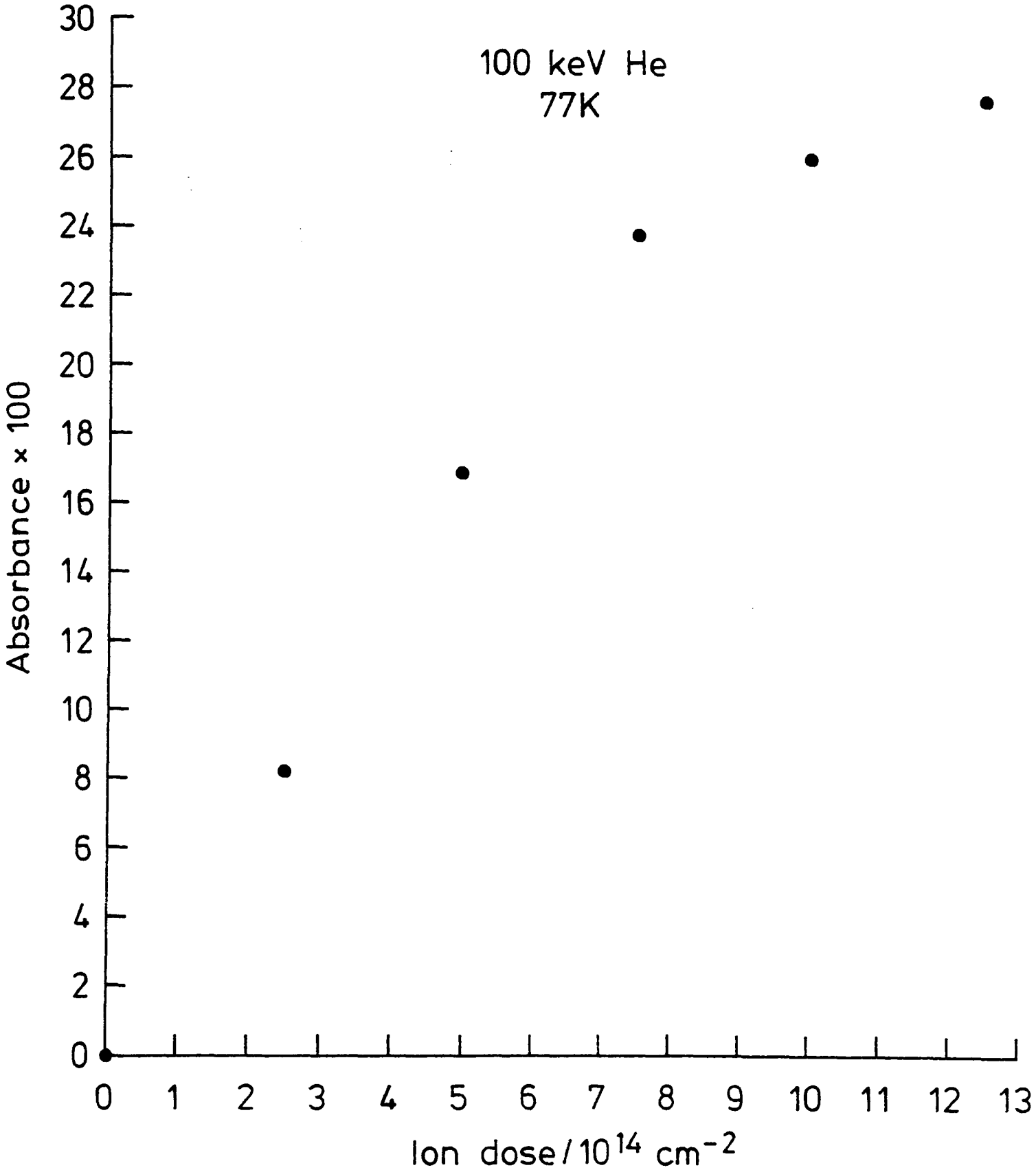


Fig. 6.12. Growth of the *F* band following 100 keV He irradiation at 77K.

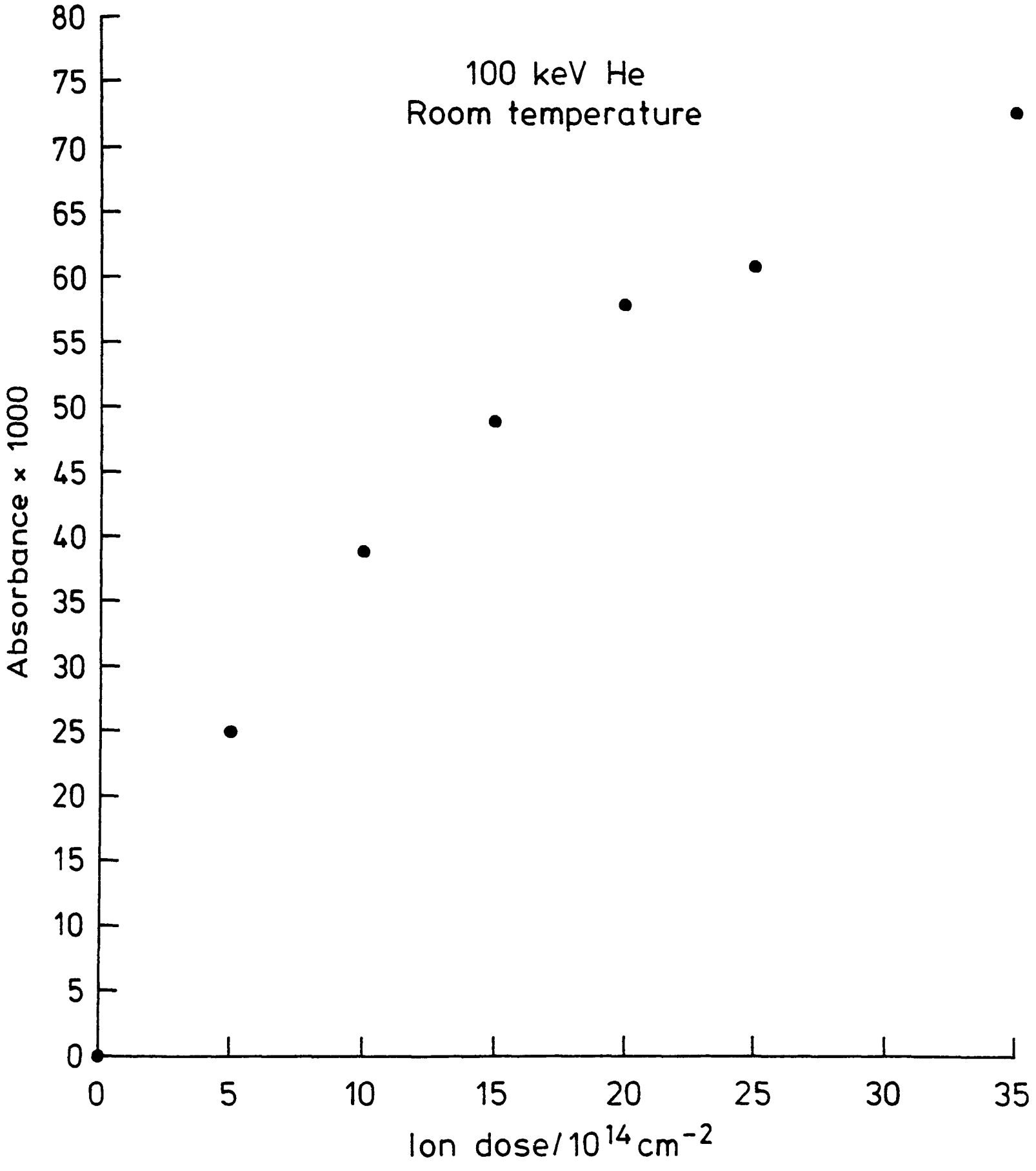


Fig. 6.13. Growth of the *F* band following 100 keV He irradiation at room temperature.

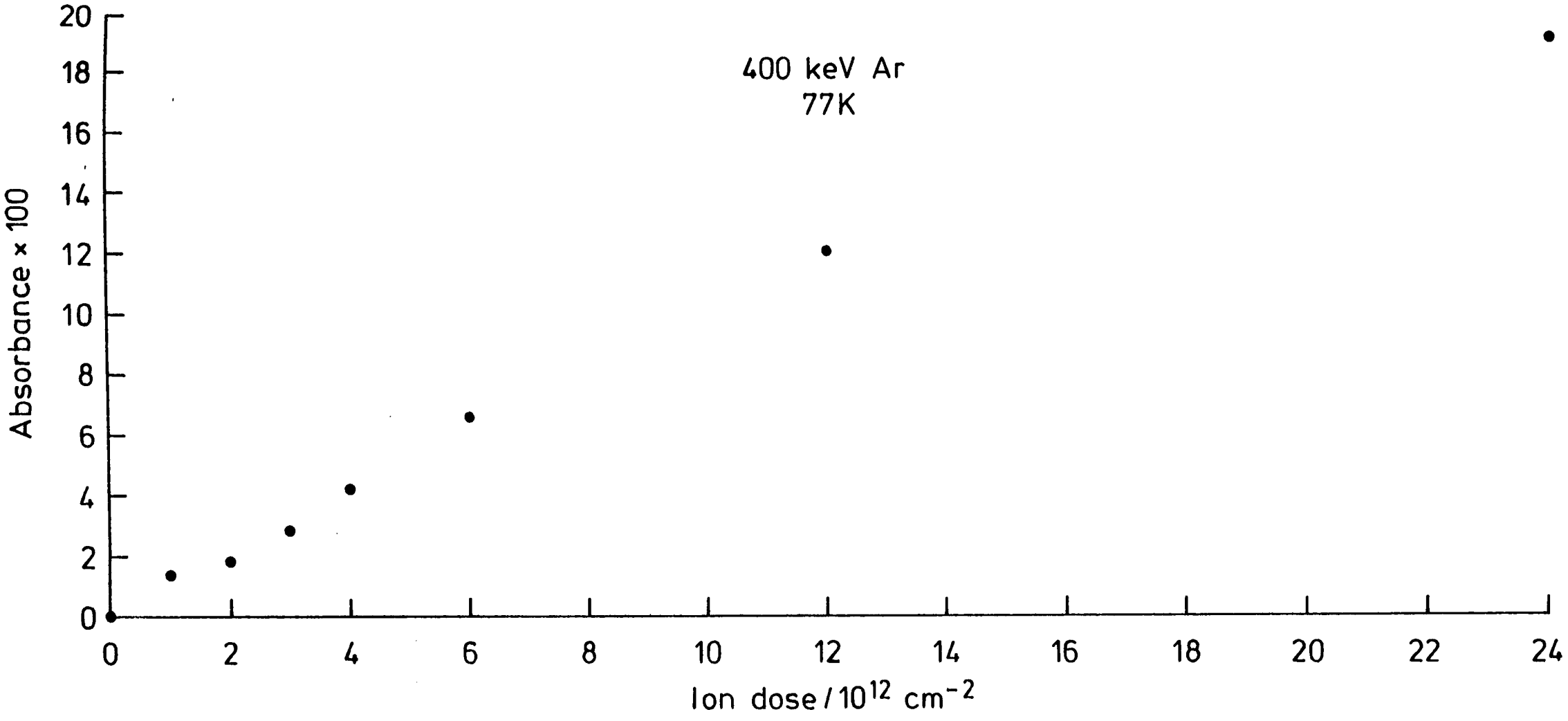


Fig. 6.14. Growth of the *F* band following 400 keV Ar irradiation at 77K.

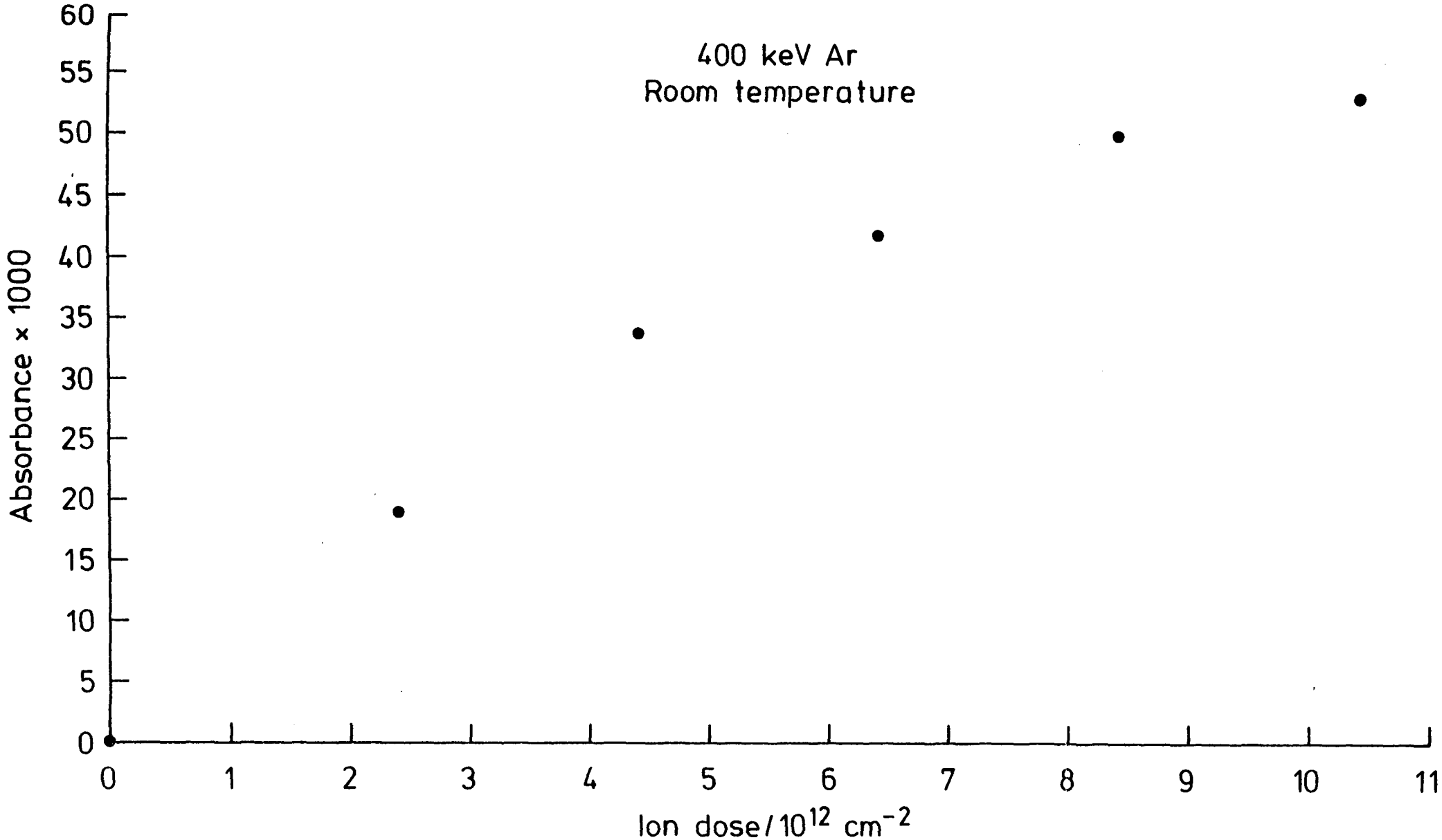


Fig. 6.15. Growth of the *F* band following 400 keV Ar irradiation at room temperature.

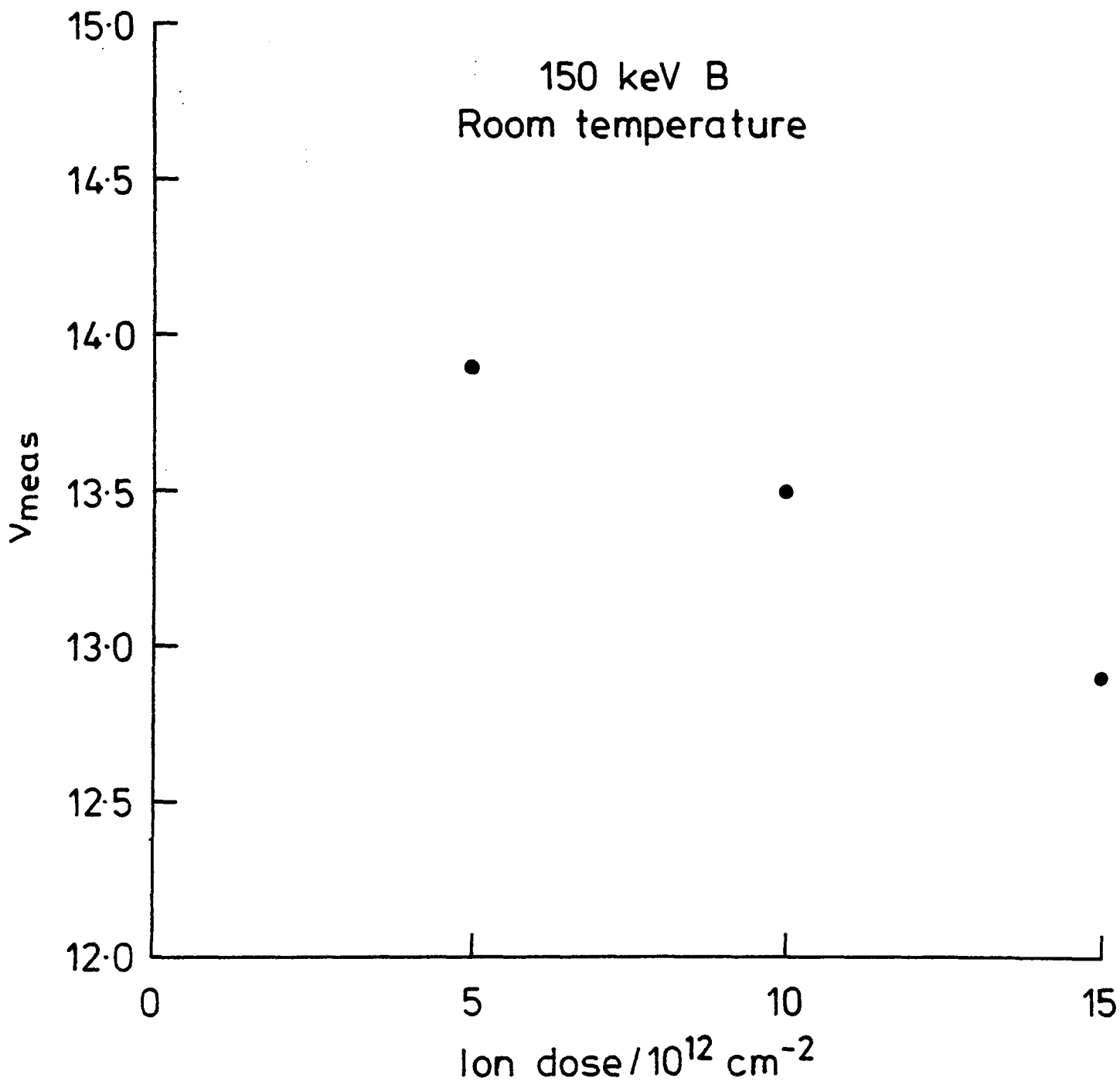


Fig. 6.16. Apparent number of oxygen vacancies produced per incident ion – 150 keV B, room temperature.

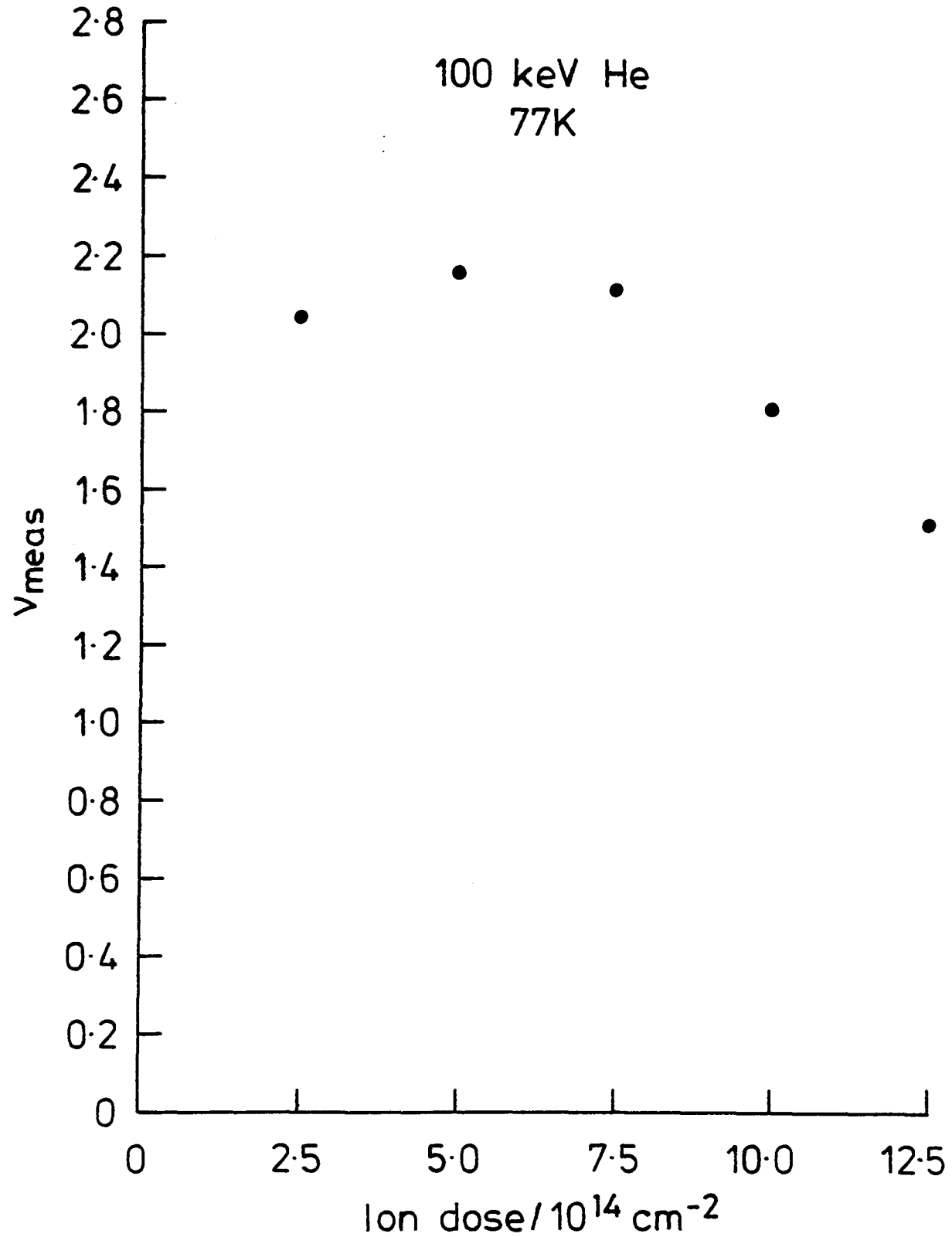


Fig. 6.17. Apparent number of oxygen vacancies produced per incident ion – 100 keV He, 77K.

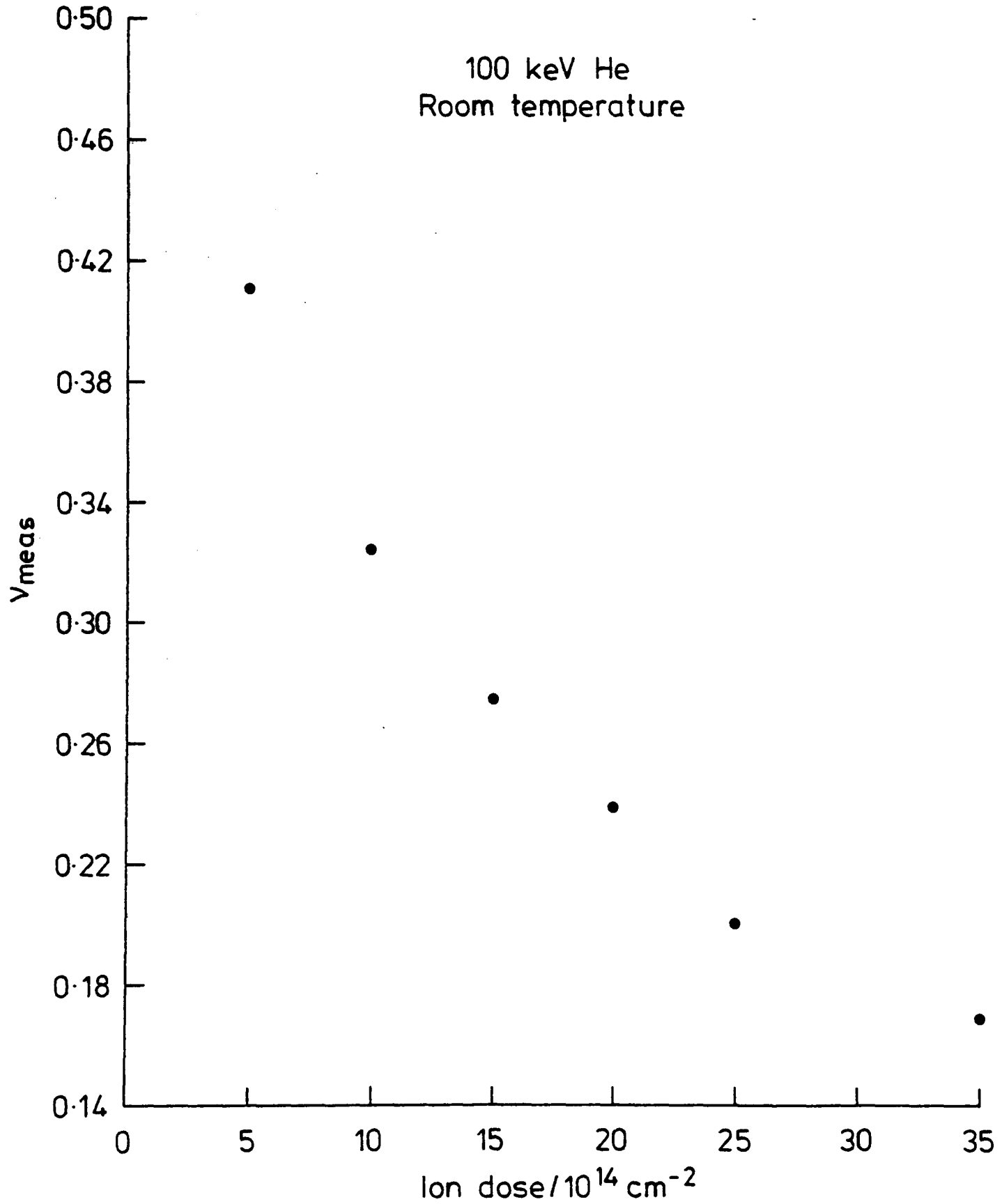


Fig. 6.18. Apparent number of oxygen vacancies produced per incident ion – 100 keV He, 77K.

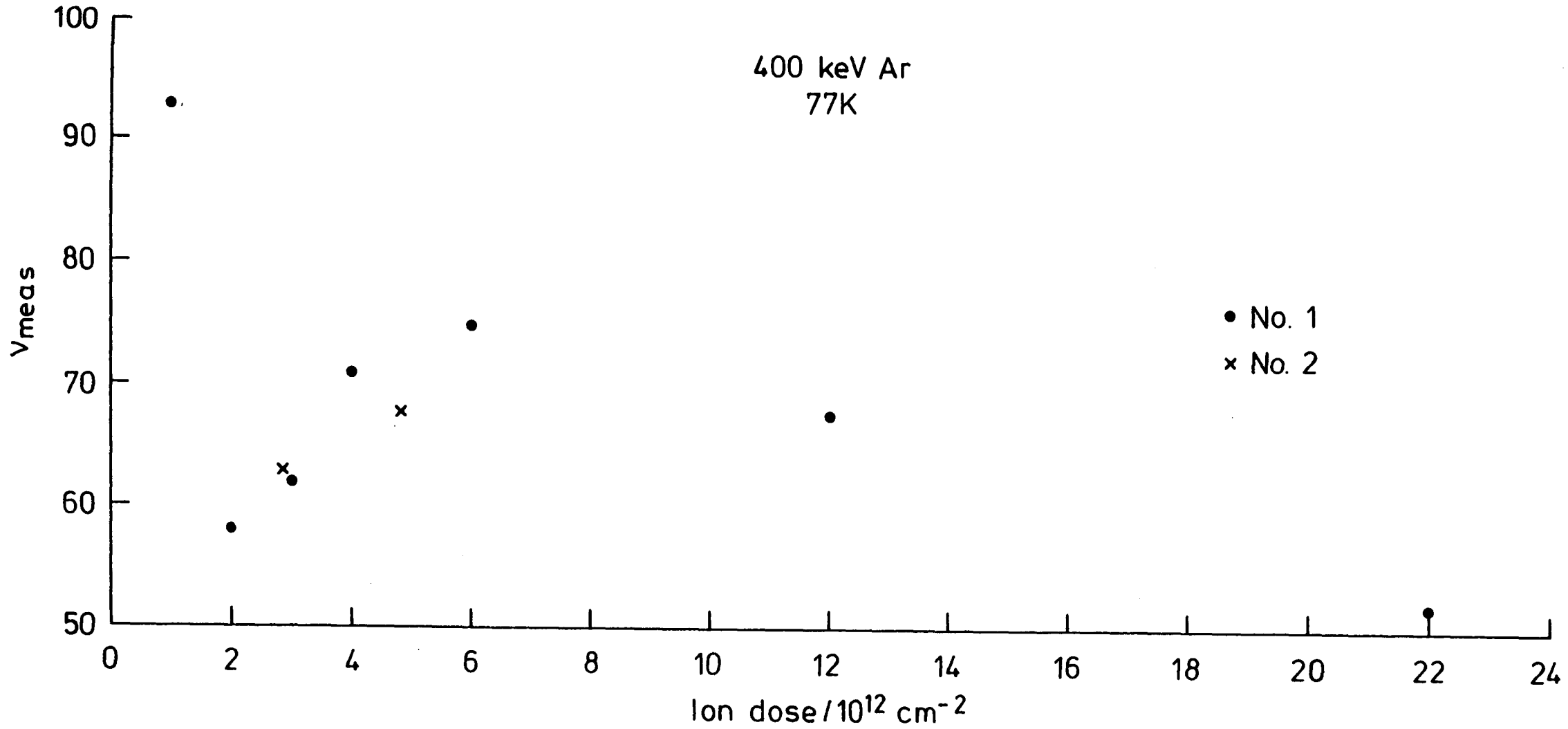


Fig. 6.19. Apparent number of oxygen vacancies produced per incident ion – 400 keV Ar, 77K.

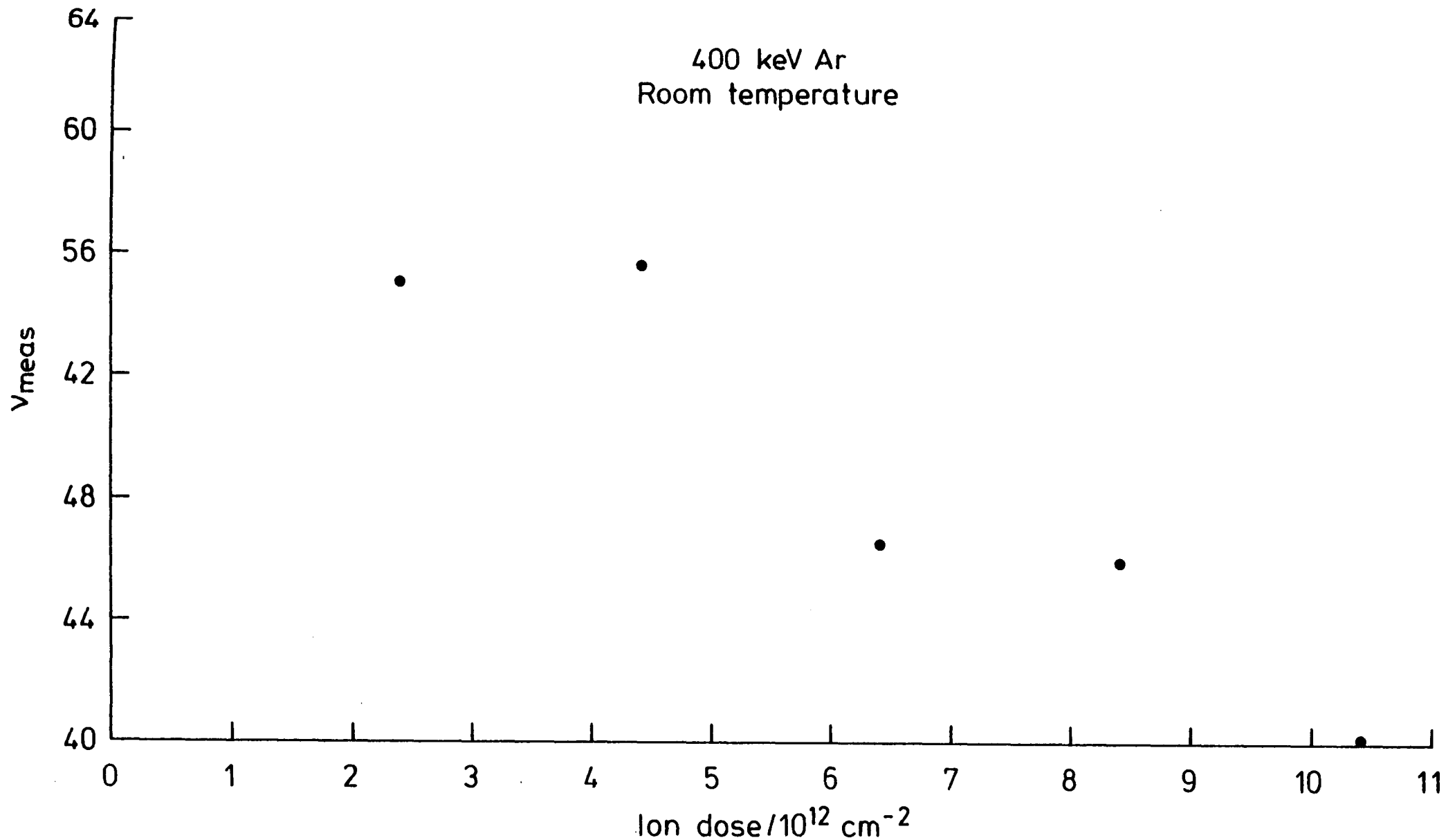


Fig. 6.20. Apparent number of oxygen vacancies produced per incident ion – 400 keV Ar, room temperature.

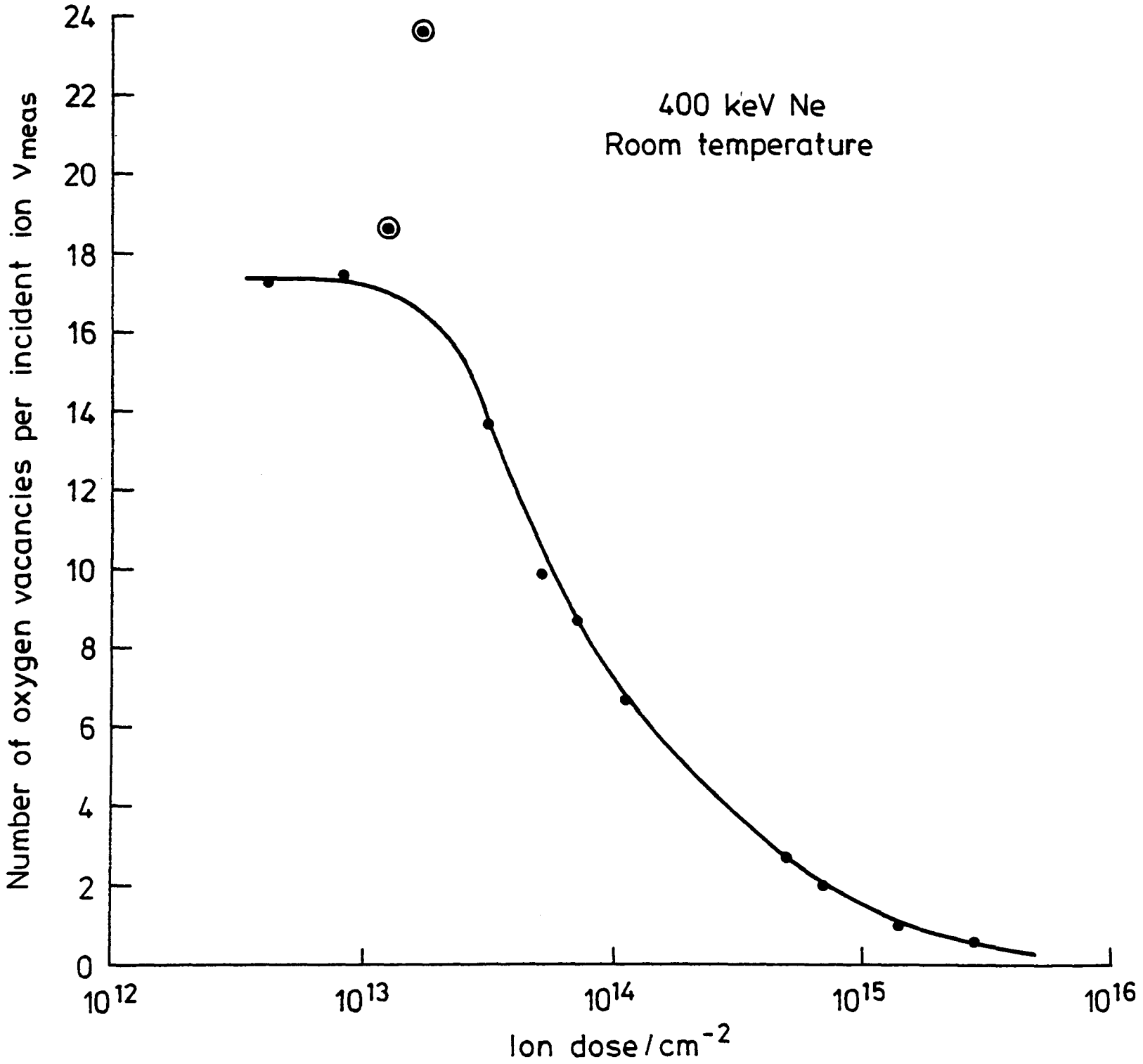


Fig. 6.21. Apparent number of oxygen vacancies produced per incident ion – 400 keV Ne, room temperature. This was the largest range of doses used. The circled points are taken from the same experiment but fall outside the main data trend.

Ion	Energy (keV)	Temp. (K)	Min. Dose (cm^{-2})	$\nu_{meas.}$	$\nu_{calc.}$	ξ
H	50	300	$1.8x10^{14}$	0.18	1.43	0.13
H	50	77	$4.0x10^{14}$	0.35	1.43	0.25
D	50	300	$1.0x10^{14}$	0.46	3.11	0.15
D	100	77	$1.0x10^{15}$	0.67	3.52	0.19
He	100	300	$5.0x10^{14}$	0.50	20.3	0.025
He	100	77	$2.5x10^{14}$	2.15	20.3	0.106
B	150	300	$5.0x10^{12}$	14.0	80.5	0.17
B	150	77	$2.0x10^{12}$	43	80.5	0.53
N	400	300	$5.0x10^{12}$	11.6	135	0.086
N	400	77	$1.0x10^{12}$	40	135	0.30
Ne	400	300	$4.0x10^{12}$	20	251	0.080
Ne	600	77	$2.8x10^{12}$	50	280	0.18
Ar	400	300	$1.0x10^{12}$	56	430	0.13
Ar	400	77	$1.0x10^{12}$	93	430	0.22
Kr	400	300	$1.2x10^{12}$	5.5	676	0.08
Kr	400	77	$5.0x10^{11}$	200	676	0.33

Table 6.3. Irradiation parameters and damage efficiency results.

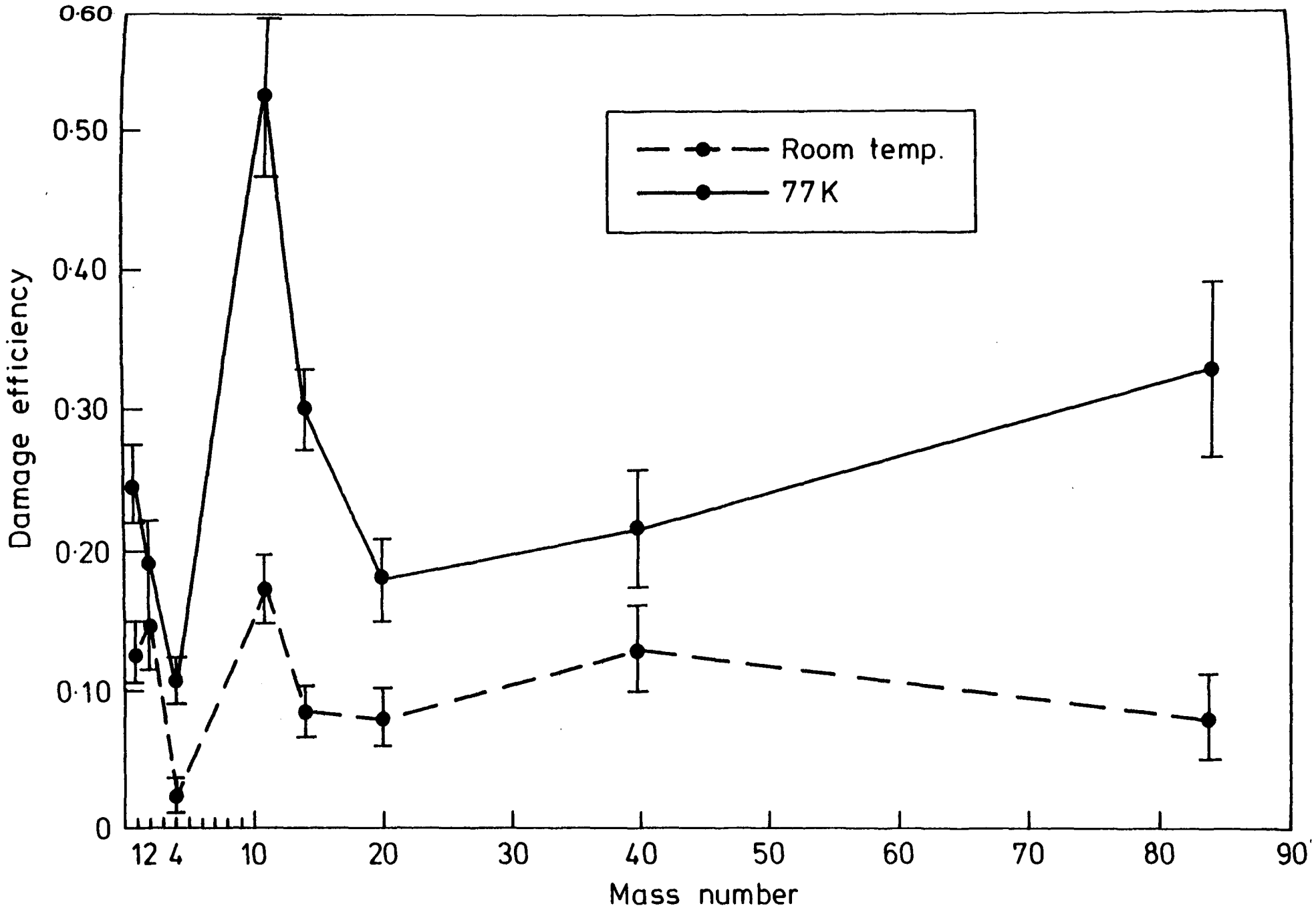


Fig. 6.22. The variation of damage efficiency with incident ion, at both room temperature and 77K.

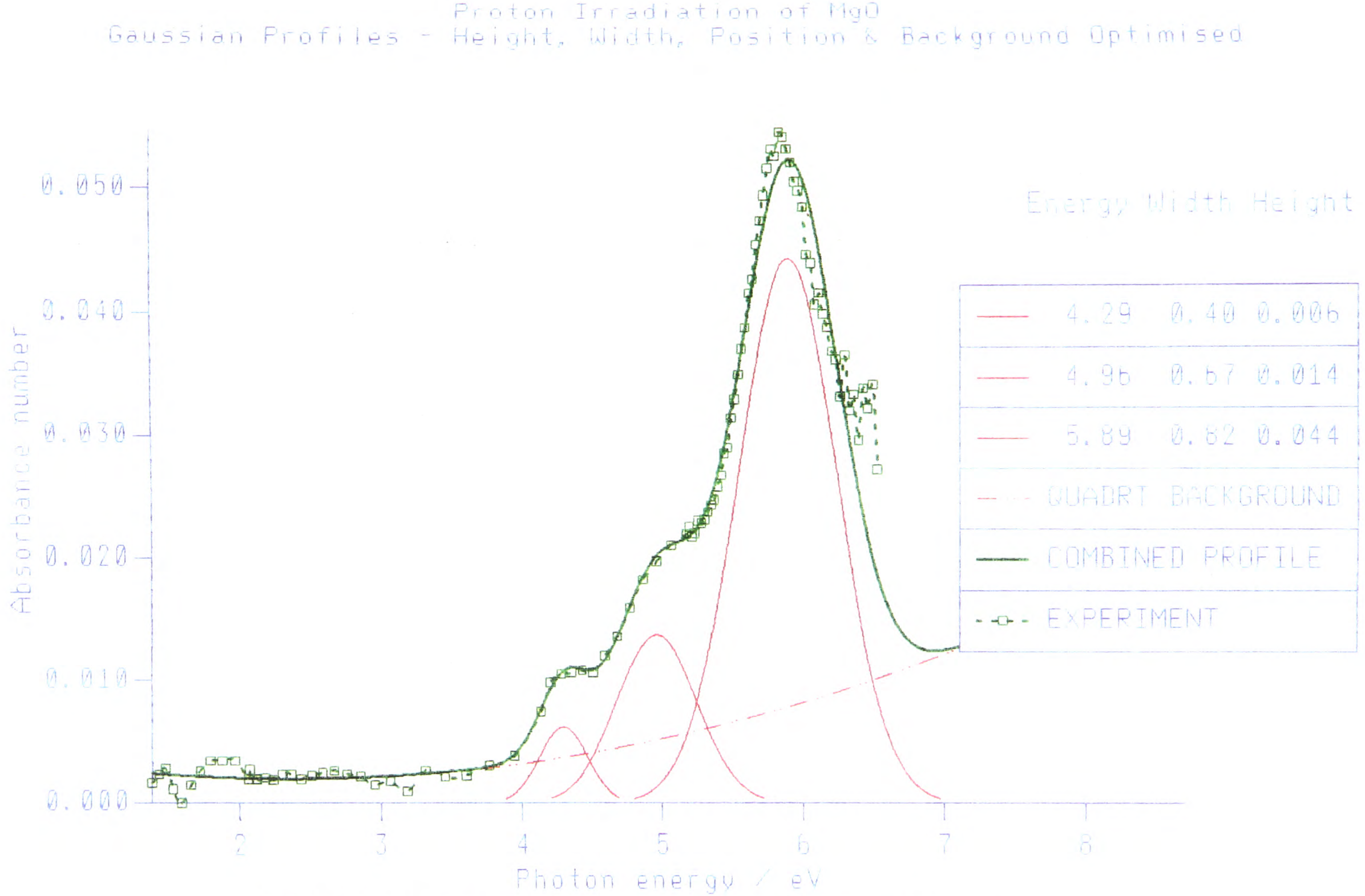


Fig. 6.23. Optical spectrum of 50 keV proton irradiated MgO. Dose of $2.0 \times 10^{14}\ cm^{-2}$.

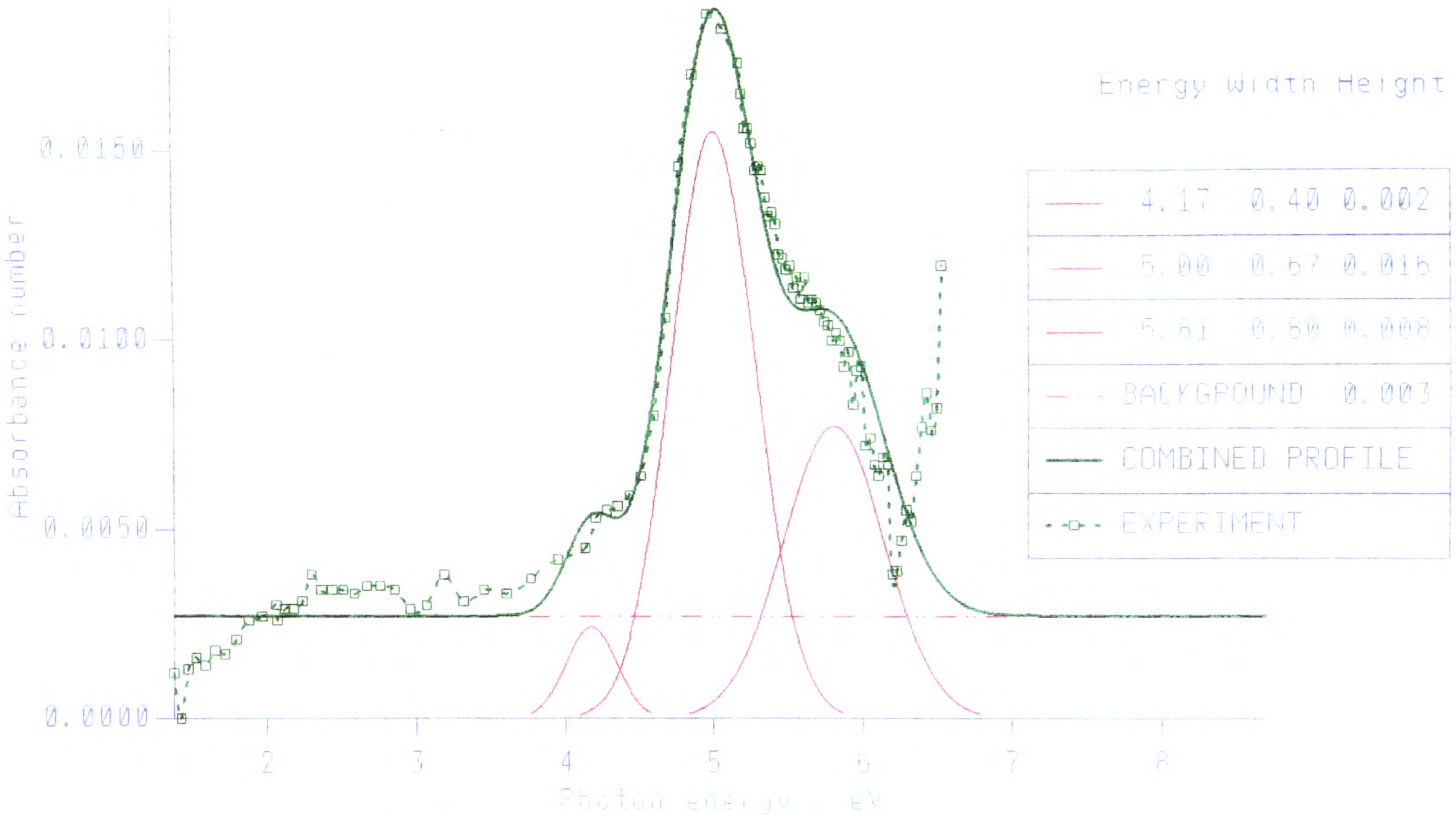


Fig. 6.24. Optical spectrum of 100 keV He irradiated MgO. Dose of $8.0 \times 10^{13}\ cm^{-2}$.

entirely due to the F centre and second, by assuming it is entirely due to the F^+ centre. In the first case the we find that the efficiency for protons is 0.35 and that for He is 0.07. In the second case we find values of 0.49 and 0.10 respectively for these two ions. In both cases then the ratio of efficiencies is about five. This agrees well with the results for sapphire where the same ratio is also around five. We shall now discuss these results in greater detail.

References

<1> A. Smakula, Z. Physik 59 , 603 (1930).

<2> P.W. Levy, Phys. Rev. 123 (4), 1226 (1961).

<3> B.D. Evans, J. Comas and P.R. Malmberg, Phys. Rev. B 6 (6), 2453 (1972).

<4> B.D. Evans, Phys. Rev. B 9 (12), 5222 (1974).

<5> G.W. Arnold, G.B. Krefft and C.B. Norris, Appl. Phys. Letts. 25 (10), 540 (1974).

<6> G.B. Krefft, Rad. Eff. 60 , 223 (1982).

<7> K. Atobe and M. Nakagawa, Cryst. Lattice Defects Amorphous Mater. 17 (1-2), 229 (1987).

<8> T.F. Luera, J. Appl. Phys. 51 (11), 5792 (1980).

<9> D.L. Dexter in ' Solid State Physics ', Vol. 6, Ed. F. Seitz and D. Turnbull, Academic Press (1958).

<10> V.N. Abramov, B.G. Ivanov, A.I. Kuznetsov, I.A. Meriloo and M.I. Musatov, Phys. Stat. Sol. (a) 48 , 287 (1978).

<11> R.H. Silsbee, Phys. Rev. 103 , 1675 (1956).

<12> K.H. Lee and J.H. Crawford, Phys. Rev. B19, 3217 (1979).

<13> T.J. Turner and J.H. Crawford, Phys. Rev. B13, 1735 (1976).

<14> B.D. Evans and M. Staplebroek, Phys. Rev. B, Vol.18, No. 12, 7089 (1978).

<15> S.Y. La, R.H. Bartram and R.T. Cox, J. Phys. Chem. Solids, 34 , 1079 (1973).

<16> B. Henderson and J.E. Wertz, 'Defects in the Alkaline Earth Oxides ', Taylor and Francis Ltd (1977).

Chapter 7

Discussion of Damage Efficiency

Introduction.

In this chapter we discuss the interpretation and implications of the damage efficiency trends observed in sapphire in the previous chapter. We shall discuss the absolute values, the temperature variation and also the variation of incident ion. With regard to this latter point, there are two important features to be noted in the measured damage efficiency curves shown in fig. 6.22: (i) the sharp differences in ζ for low mass ions, especially He, where the measurement error is smallest, and (ii) the relative constancy of ζ between light and heavy ions. Neither of these features is observed in metals. The first feature is quite unexpected on the basis of the modified Kinchin-Pease model of point defect production, described in chapter 2, and so initially we examine the irradiation details more closely to see if this feature could be a consequence of some unanticipated experimental artifact. This appears not to be the case and so we examine those aspects of the standard model which could possibly give rise to the observed efficiency variations. In particular, we examine the use of a universal differential scattering cross section. Turning to feature (ii) noted above, we discuss the concept of the displacement cascade in low Z materials, in an attempt to explain the difference in efficiency behaviour between aluminium and its oxide under heavy ion bombardment. Finally, some suggestions are made for characterising the displacement cascade which would enable one to correlate different irradiations in a more complete and meaningful way than at present.

§ 7.1 Magnitude of Measured Efficiencies and Temperature Variation.

If the theoretical estimates of point defect production presented in chapter 4 were in agreement with experiment then a graph such as fig. 6.22, showing the variation of efficiency, ζ, with incident ion mass would be a straight line parallel to the x-axis, corresponding to a constant efficiency. If the form of Smakula's equation presented in § 6.1, which relates the F and F^+ concentration to the parameters of the optical absorption bands, were also correct then the value of this constant efficiency would be unity. In fact the numerical values of certain parameters used in Smakula's equation, such as the oscillator strength, contain large uncertainties, as discussed in § 6.1. Other, possibly large, errors may be associated with the particular effective field approximation used and so the deviation from unity of the mean efficiency values is not really surprising. Actually, the efficiencies measured by other authors have been considerably lower than those found in the present investigation. For example, Evans *et. al.* <1> defined a quantity β whose reciprocal is equivalent to our damage efficiency and found $\beta^{-1} \sim 0.013$ for 3 MeV Ne bombardment of MgO. The dose used by these authors (1.2×10^{14} cm $^{-2}$) was much larger than those used here and is likely to have given significant overlapping of damaged regions. The effect of this on the measured efficiency is most dramatically demonstrated by fig. 6.21, which shows a much reduced value for such high doses.

Hughes <2> has presented theoretical and experimental estimates of point defect production on the anion sublattice for 400 keV and 3 MeV proton bombardment of MgO and CaO. The theoretical estimates were obtained using a Rutherford scattering cross section to describe the proton-pka interaction and the original Kinchin-Pease damage function was used to estimate secondary defect production. Both of these are good approximations for the case of proton irradiation. The first, because a proton must approach a target nucleus very closely in order transfer energies of the order of E_d and so screening is relatively unimportant. The second, because only low energy pka's are produced, for which the damage energy is very close to the total energy. These approximations are better for CaO than MgO, but in both cases will tend to give overestimates of defect production. Hughes' results for experimental and theoretical oxygen vacancy production have been combined to give a

damage efficiency and are shown in table 7.1. They are numerically low compared to the values found here for sapphire. The proton doses used by Hughes are about an order of magnitude greater than those used here and whilst his growth data does not show too much curvature it is possible that the lower efficiency values are due in part to these higher doses.

The difference in efficiency found between 77 K and room temperature in the present experiments can be attributed to differing amounts of recombination of close FP's following the initial displacement event. In experiments of this kind the number of observed FP's comprises the initial number of FP's created, minus those which undergo recombination during the subsequent lattice relaxation. The initial displacement events occur on a timescale of ~ $10^{-15}s$, which is much shorter than the period of a lattice vibration (~ $10^{-13}s$). The lattice is effectively stationary during the displacement event and so the number of atoms initially displaced must be quite insensitive to temperature. However on timescales greater than a lattice vibration, random thermal motion is able to influence defects and cause close vacancies and interstitials, interacting both electrostatically and by a strain field, to recombine. We are able to go further by considering the results of the annealing study reported in chapter 5 and using an argument due to Hughes <2>. This author measured the growth curve of oxygen colour centre production for proton irradiation of CaO at 15 K and found that, on warming the sample to 300 K, no centres were lost. Subsequent irradiation at this higher temperature continued to increase the colour centre concentration but the production rate was much reduced. Hughes invoked the concept of the recombination volume (the region beyond which an interstitial must move in order to avoid recombination with *its own* vacancy) and suggested that the higher production rate at low temperatures could result from one of two mechanisms:

(i) the recombination volume is larger at 300 K than low temperatures. In this case one would expect some annealing to occur on raising the temperature after the 15 K irradiation.

(ii) The recombination volume is independent of temperature, but at low temperatures more interstitials are able to escape from this region.

Hughes' results were consistent with the latter mechanism. This is also the case for sapphire. In chapter 5 we reported that, following irradiation at 13 K, no significant annealing of

MgO

E / MeV	T / K	ζ
0.4	15	0.071
0.4	77	0.043
0.4	300	0.029
3	15	0.095
3	77	0.062
3	300	0.055

CaO

E / MeV	T / K	ζ
0.4	15	0.048
0.4	77	0.038
0.4	300	0.021
3	15	0.12
3	77	0.08
3	300	0.052

Table 7.1. Damage efficiency results obtained by Hughes <2> for proton irradiation of alkaline earth oxides.

oxygen vacancies occurred. The higher damage efficiency noted for 77 K irradiations is then just a different way of stating that the defect production rate is higher at low temperatures and so we must also conclude that the second mechanism noted above is correct. Hughes speculates that the greater ease with which interstitials are able to escape from the recombination volume may be due to increased channelling at low temperatures. One would intuitively expect thermal vibrations to interfere with the channelled particle and indeed Lehmann and Leibfreid <3> have shown that the range of a channelled particle should decrease exponentially with increasing temperature according to the relation

$$R(T) = R_0 \exp(-2\overline{u^2}/a^2), \tag{7.1}$$

where R_0 corresponds to the range when thermal vibrations are neglected, $\overline{u^2}$ is the mean square thermal vibration amplitude and a is the screening length of the interatomic potential. However recent molecular dynamics simulations of radiation damage <4> have suggested that in certain materials channelling may in fact increase with increasing temperature. The reason appears to be that thermal expansion of the lattice opens up the channels and this compensates for the closing of the channels due to increased thermal vibrations. These particular simulations were conducted for copper but this effect will clearly depend on the details of the structure and expansion characteristics of each material and no general conclusions can be made. It is an area where molecular dynamics simulations of radiation damage in sapphire would be useful.

§ 7.2 Validity of Damage Efficiency Results.

We now turn our attention to the trends in damage efficiency with increasing ion mass and, as noted in the introduction, there are two noteworthy features: (i) the sharp differences for low mass ions and (ii) the absence of a low efficiency for high mass ions. The first of these is so curious that before we enter into a detailed discussion of it we wish to consider if it could simply be an artifact of the particular irradiation conditions. The first thing to consider is the possibility of the He ion interacting with the defects it produces. It is well known that in metals helium will occupy vacant lattice sites <5>. If this were also the case in

oxides then such sites would not produce the usual colour centres. However the calculated number of defects per incident ion is sufficiently high in the case of 100 keV He irradiation (see table 7.2) to make the loss of a single centre per incident ion negligible. Similarly, any chemical interaction between an implanted ion and the oxygen vacancies it produces is unable to affect more than a small fraction of the total number created. Therefore these implanted ion-vacancy interactions cannot explain the low efficiency found for He.

As we noted in the introduction to chapter 6, apparently low values of ζ can be found if the ion doses used are such that overlapping regions of damage are likely. In order to determine the degree of overlap in each of our irradiations we require an estimate of the dimensions of the damaged region. Reasonable estimates of cascade sizes in intermediate Z materials such as copper can be obtained by equating the cascade dimensions with the straggling parameters of the pka <6>. However in low Z materials this procedure is invalid, giving large overestimates. A more detailed approach is necessary and we have adopted the following model: (i) the potential for overlap is most acute in the region of the nuclear stopping power maximum so we first determine the incident ion energy E_m at which the energy transferred to pka's is a maximum. (ii) We then calculate the mean pka energy, $\overline{E}_{pka}$, when the incident ion has this energy E_m. (iii) With a coordinate system having the sample face in the x-y plane and the ion initially travelling in the z-direction, the transverse (x-y) straggling of pka's with energy $\overline{E}_{pka}$ is determined using the PRAL (Projected Range ALgorithm) code <7>, taking an average of the values for aluminium and oxygen pka's. This is used to obtain an areal projection in a transverse plane, A_p, of the damaged region. (iv) The projected area is then multiplied by the ion dose to give the mean number of *projected* overlapping damage regions, which we call f_p. This parameter is given in table 7.2 for each irradiation. Physically, f_p corresponds to the mean number of ions incident upon the area A_p. To determine the degree of damage overlap it is necessary to take into account the longitudinal straggling of the incident ion, since the damaged regions are not all produced in the same x-y plane. We do this as follows: we assume that the displacement cross section has a Gaussian distribution as a function of depth, with the peak displaced from the surface by an amount equal to the mean projected range and a standard deviation equal to the longitudinal

straggling of the incident ion, S_i. We then calculate the mean projected range, $\bar{r}_{pka}$, of pka's with energy $\bar{E}_{pka}$. This can be represented as a thin strip extending from the peak of the Gaussian distribution into the material (see fig.7.1). The fractional overlap in the z-direction, f_z, is given by the fractional area of this strip:

$$f_z = \frac{1}{S_i \sqrt{(2\pi)}} \int_0^{\bar{r}_{pka}} e^{-\frac{z^2}{2S_i^2}} \, dz \ , \tag{7.2}$$

where the origin is taken from the peak centre. The product $f_p f_z$, which we express as a percentage and denote f_{3D}, gives the degree of three dimensional overlap and is recorded in table 7.2 for all irradiations except those involving H and D, since only isolated FP's are produced for these ions. In all cases the overlap of damage regions is small, according to this model, although it is largest for the room temperature He irradiation, at about 3%. To estimate the influence this has on the damage efficiency we would need a model relating the degree of overlap to the amount of recombination. The extreme case corresponds to total recombination within the overlap region. This is clearly insufficient to account for the reduced efficiency found for He and we conclude that the measured drop in ζ for this ion is not produced by recombination as a result of damage overlap. The low values of overlap show that the measured efficiencies are indeed properties of a single ion. This again confirms the necessity of using low ion doses for experiments of this kind.

§ 7.3 Damage Efficiency Variations for Low Mass Ions.

On the basis of the above validation of the efficiency results it appears that the large efficiency variations found for low mass ions is a real effect. In fact the low efficiency of He compared to protons appears to have been found implicitly by other authors. In a study of radiation damage in sapphire, Luera *et. al.* <8> bombarded this material with H and He in a manner such that the calculated energy deposited into atomic processes at a given depth were nominally equal. The proton irradiation produced 6.8 times more *F* centres than He, in fair agreement with the ratio of 5.1 found in the present experiments. These authors interpreted

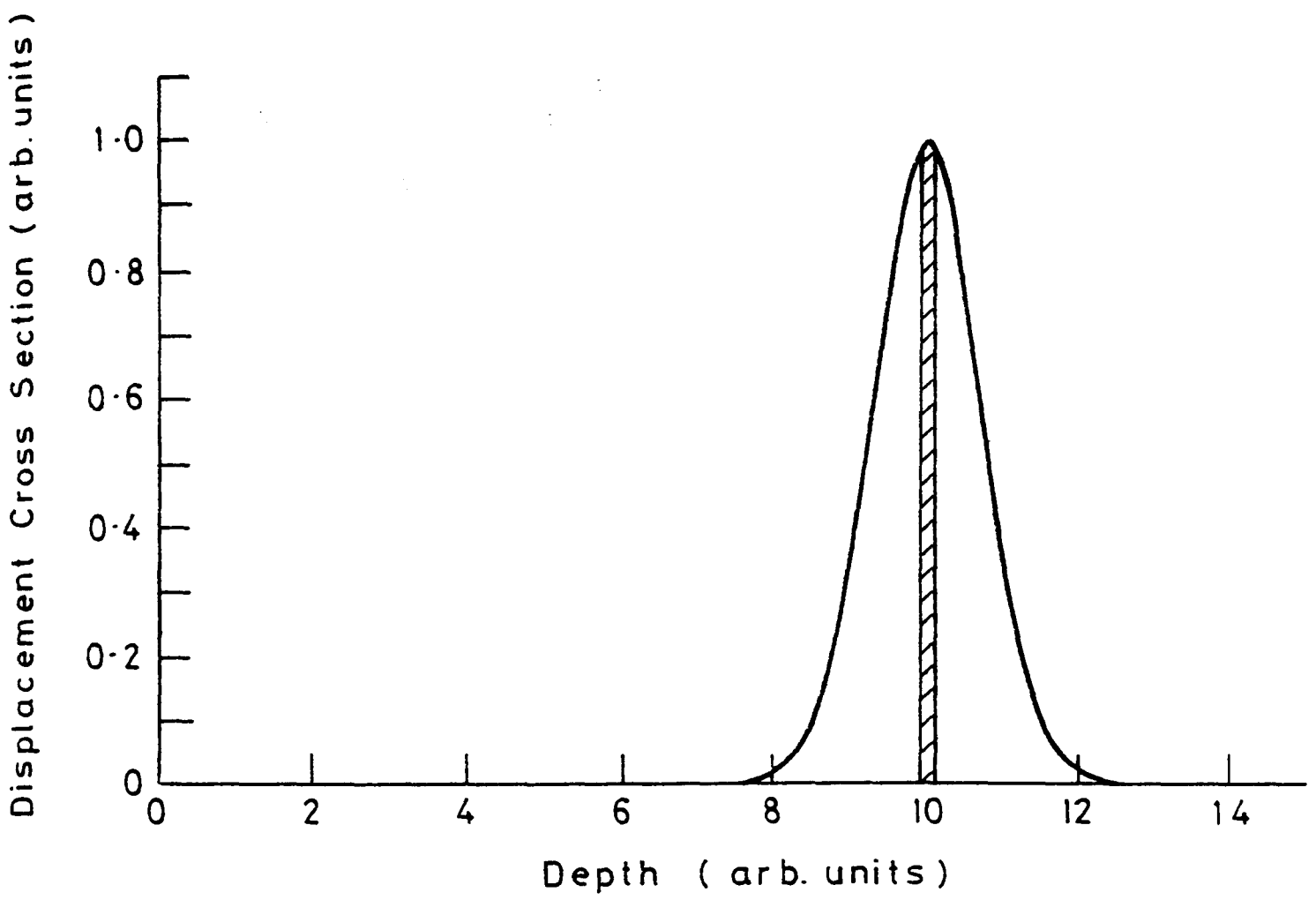


Fig. 7.1. A Gaussian displacement cross section is used to calculate the degree of damage overlap. The range of a pka is represented by the shaded strip. The fractional area of this strip gives the degree of overlap in the *z* direction.

Ion	Energy (keV)	Temp. (K)	Min. Dose (cm^{-2})	f_p	f_{3D}(%)	$\nu_{meas.}$	$\nu_{calc.}$	ξ
H	50	300	$1.8x10^{14}$	-	-	0.18	1.43	0.13
H	50	77	$4.0x10^{14}$	-	-	0.35	1.43	0.25
D	50	300	$1.0x10^{14}$	-	-	0.46	3.11	0.15
D	100	77	$1.0x10^{15}$	-	-	0.67	3.52	0.19
He	100	300	$5.0x10^{14}$	5.5	3.0	0.50	20.3	0.025
He	100	77	$2.5x10^{14}$	2.8	1.5	2.15	20.3	0.106
B	150	300	$5.0x10^{12}$	0.10	0.1	14.0	80.5	0.17
B	150	77	$2.0x10^{12}$	0.04	0.04	43	80.5	0.53
N	400	300	$5.0x10^{12}$	0.16	1.6	11.6	135	0.086
N	400	77	$1.0x10^{12}$	0.031	0.03	40	135	0.30
Ne	400	300	$4.0x10^{12}$	0.18	0.18	20	251	0.080
Ne	600	77	$2.8x10^{12}$	0.13	0.13	50	280	0.18
Ar	400	300	$1.0x10^{12}$	0.071	0.17	56	430	0.13
Ar	400	77	$1.0x10^{12}$	0.071	0.17	93	430	0.22
Kr	400	300	$1.2x10^{12}$	0.17	1.1	5.5	676	0.08
Kr	400	77	$5.0x10^{11}$	0.070	0.48	200	676	0.33

Table 7.2. Damage overlap parameters, f_p and f_{3D} for each irradiation.

this result as suggesting that the electronic excitation associated with light ions was responsible for *F* centre production. However this would be in direct contradiction to the large body of evidence, some of which was reviewed in chapter 3, which has shown that electronic excitation is not able to introduce new lattice defects into sapphire. We have certainly found no evidence for this in the experiments reported here and do not believe that the electronic excitation associated with light ion irradiation is responsible for FP production.

The above considerations suggest that the theoretical description of point defect production is incomplete. We can identify three different quantities which contribute to this description: the electronic stopping power, the nuclear stopping power and the differential cross section for energy transfer, $d\sigma/dT$. In § 4.3 we noted that the ZBL electronic stopping powers for He were the most accurate of all ions and agree well with many experimental results. It would require unrealistically large errors in the electronic stopping power for this to be responsible for the observed low damage efficiency of He. Similarly, the theoretical nuclear stopping power for He in the oxygen sublattice would have to be several times too large to account for this phenomenon. It is, in fact, rather difficult to measure the nuclear stopping power, $S_n(E)$, of low Z ions, since this component is very small compared to the electronic stopping for all but the lowest energies. In this sense, large errors in $S_n(E)$ are rather more credible than large errors in $S_e(E)$. However it is unlikely that the errors in $S_n(E)$ alone would be large enough to explain this result. Rather more likely is the possibility that the form of the differential cross section for energy transfer, $d\sigma/dT$, is incorrect. In the calculations presented in chapter 4 we employed the 'universal' ZBL version <9> of the scattering function $f(t^{1/2})$, which is derived from a universal nuclear stopping power curve, which is in turn derived from a universal potential. This procedure is possible since the differential scattering cross section and the nuclear stopping power are related by the expression

$$S_n(E) = N \int_0^{T_m} T \frac{d\sigma}{dT}\, dT \,. \tag{7.3}$$

This equation can be differentiated to give $d\sigma/dT$, as shown in chapter 4. Deriving a scattering function from the nuclear stopping power will ensure that the first moment of the energy transfer distribution, *i.e.* $S_n(E)$, is regenerated. However the higher moments may be in error. FP production is rather sensitive to these higher moments and would reflect any errors in them.

Universal potentials and scattering functions must, by their very nature, 'smooth out' the details of electronic shell structure and so it is not surprising to find some oscillations about a mean value. The phenomenon is well known in the case of the electronic stopping power, where the Z_1 oscillations, mentioned in chapter 2, are known to be a consequence of the detailed electronic configuration <10>. The variation of the electronic stopping cross section with incident ion, at a constant velocity, is shown in fig. 7.2. Given that these oscillations are due to the electronic shell structure one might also expect to see some non-uniform variation in the nuclear stopping power in the energy regime where screening of the target nucleus is significant. There are conflicting reports concerning the existence of Z_1 oscillations in the nuclear stopping power. Hogberg and Skoog <11> measured both the angular scattering half-width and the mean nuclear stopping cross section for small scattering angles, of particles transmitted through a thin carbon foil. The incident ion energies were in the range 32 to 56 keV and Z_1 ranged from 3 to 18. These authors found no oscillatory behaviour in any of the quantities measured. Geyer *et. al.* <12> chose to measure the stopping power of heavy ions (Z_1 ranging from 49 to 65) in hydrogen gas. They point out that measurements on solid targets are liable to a number of systematic errors which gaseous stopping media avoid. These authors *were* able to detect Z_1 oscillations in the nuclear stopping power, although the maximum amplitude was only 20% of the mean value. This is clearly a much smaller effect than the one found here in defect production. There are a number of possible explanations for this discrepancy. If an oscillation did exist in the nuclear stopping power of the incident ion one would expect this to be amplified for defect production since, the latter involves an integration over the whole path of the ion and the oscillation would be reinforced at each point. It must also be borne in mind that for light ions the nuclear stopping power is not a particularly good indicator of oscillations in the scattering cross section at large values of energy transfer T, since the dominant contribution to the integral in eqn.(7.3) comes from

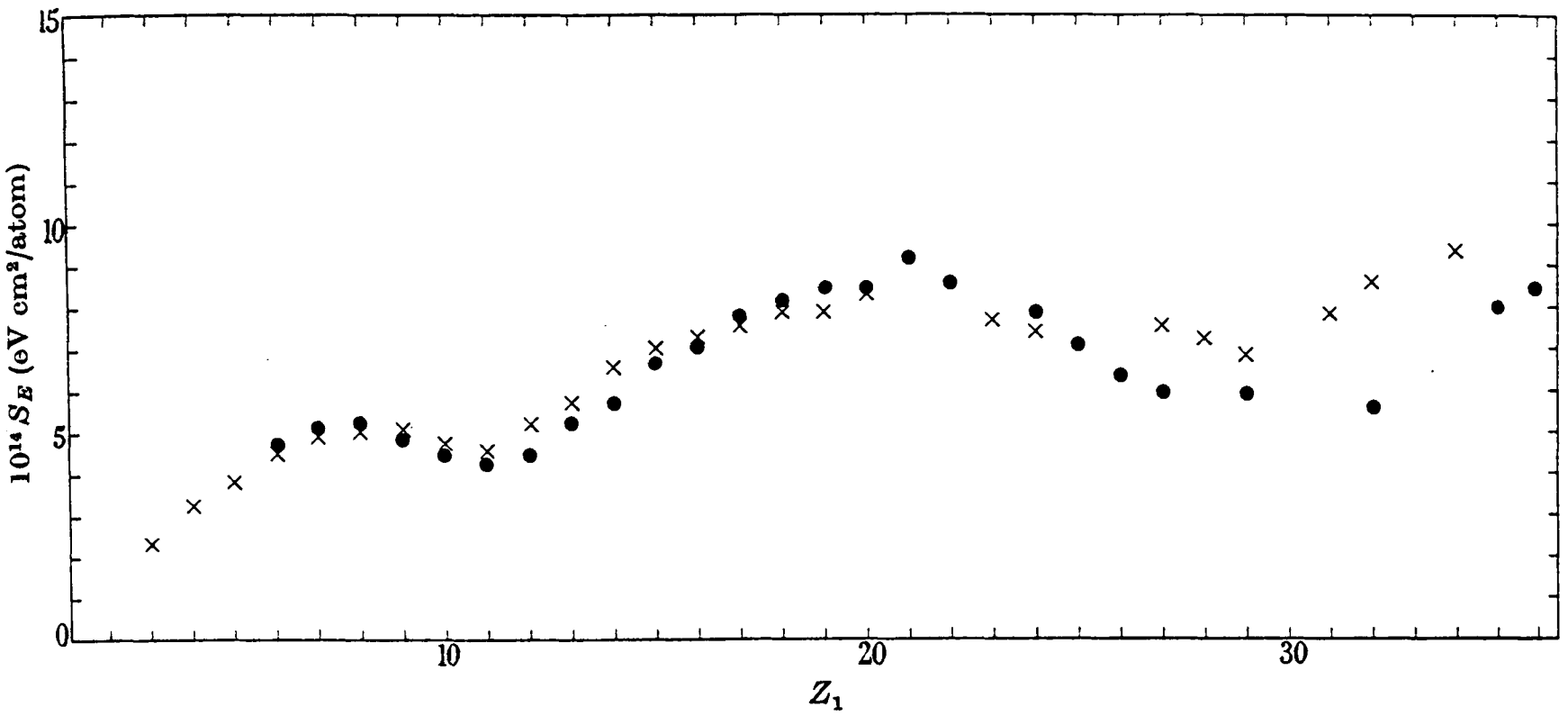


Fig. 7.2. Z_1 oscillations in the electronic stopping power. Experimental point are shown as dots and theoretical values as crosses. The target is amorphous carbon and the incident ion velocity is $1.38 \times 10^8\ cm\,s^{-1}$. Ref. <10>.

small values of T. Thus a small oscillation in the nuclear stopping power could be indicative of a much larger variation in the scattering cross section. In fact a non-universal Z_1 dependence *has* been found in the scattering cross section itself. Nelson <13> measured the backscattering parameters of various ions incident at constant velocity upon a gold target, as a function of channelling angle and found an oscillatory dependence, which is reproduced in fig. 7.3. This positive result of oscillatory behaviour is more significant for defect production than the evidence from the nuclear stopping power since backscattering events, like displacement events, involve the close approach of nuclei and so are sensitive to the form of the scattering function at large values of energy transfer. Cheshire and Poate <14> have theoretically analysed the effect of electronic shell structure on the interatomic potential between two colliding copper atoms. Their evaluation of the interatomic potential ignored electron kinetic energy, exchange, correlation, polarisation and solid state effects, and employed unperturbed Hartree-Fock wave functions. Despite these deficiencies they were able to qualitatively reproduce the oscillations found experimentally by Nelson.

If we wish to postulate that the sharp damage efficiency variations noted for low Z ions in sapphire are due to shell effects in the differential scattering cross section, then it is natural to ask why there appears to be no similar oscillations at higher values of Z_1. To be explicit, if He has a low damage efficiency then intuitively one might expect Ne, Ar and Kr to be similarly inefficient at producing damage, compared to their neighbours in the periodic table. Let us examine the nature of periodic interatomic interactions more closely. An interesting feature of both the electronic and nuclear Z_1 oscillations is that the periodicity is not simply related to the position of the element in the periodic table, as figs. 7.2 and 7.3 clearly show. So we have no reason to expect a simple periodicity with Z_1 in defect production. It is possible that the higher Z_1 ions also show periodic effects, but the following argument indicates why one would expect the amplitude to be reduced in comparison with low Z_1 ions. One would expect that of all the oxygen defects produced in a given irradiation, the fraction produced in ' incident ion-oxygen ion ' collisions (henceforth referred to as primary collisions) is greater for lower Z_1 ions. For the high Z_1 ions, most defects are produced by energetic target atom knock-ons. If, after normalisation with respect to a universal interaction, there does exist a Z_1 periodicity in the incident ion-target oxygen ion interaction, then this will show up most

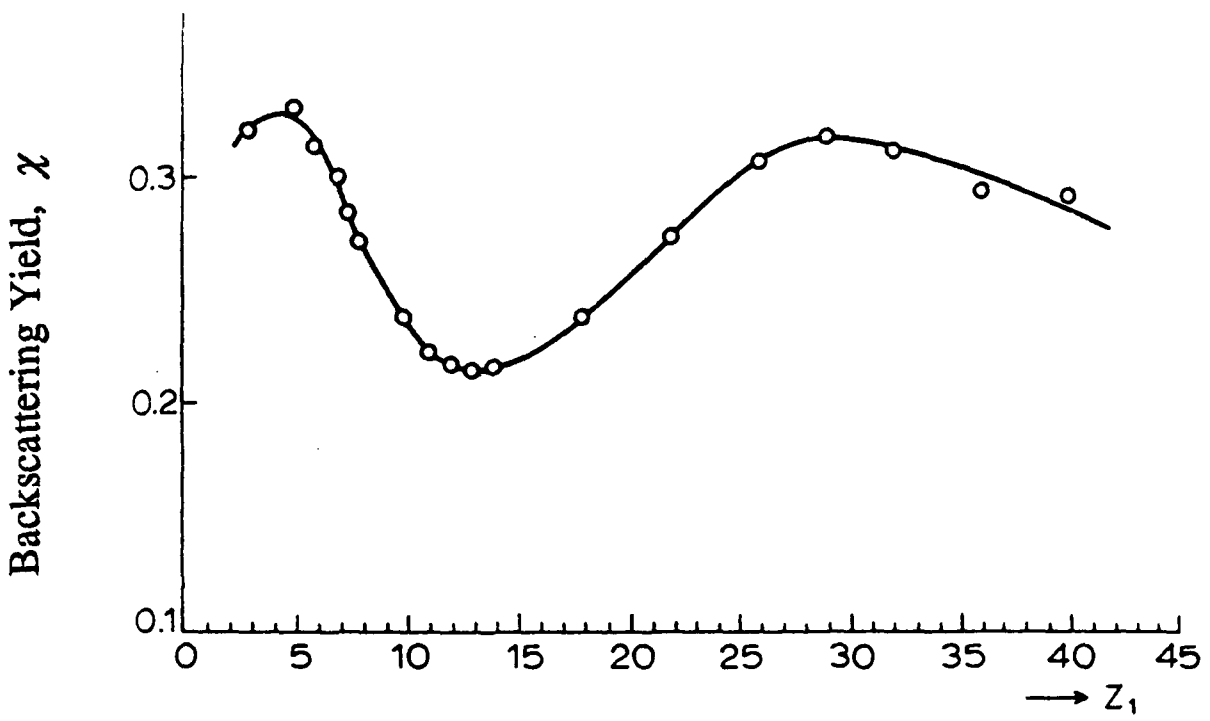


Fig. 7.3. Z_1 oscillations in the backscattering yield from a gold target. Ref. <13>.

strongly for the low Z_1 ions. We have calculated, on the basis of binary collision theory, the fraction of oxygen displacements created in primary collisions for each of the noble gas irradiations and find the following values, expressed as a percentage: He (39%), Ne (18%), Ar (14%) and Kr (11%). For equal amplitude Z_1 oscillations of the differential scattering cross section this would explain why the amplitude is quenched for the higher Z_1 ions.

A further question, of considerable importance, which must be addressed regarding this postulate is why there appears to be no evidence for similar oscillatory behaviour in metals. Although the valence electrons behave very differently in electrons and insulators, in both types of material the core electrons are largely unperturbed from their free atom states. Hence one expects the core electrons of an aluminium ion in aluminium metal to behave in much the same way as the core electrons of an aluminium ion in sapphire. It is, therefore, unlikely that the energetic scattering of an aluminium ion by an aluminium pka would differ very much in the two materials. How can we relate this observation to our postulate of Z_1 oscillations in sapphire? First we must note that our observations have been based solely on evidence from the oxygen sublattice and cation-cation collisions have only played an indirect role in producing the observed oxygen defects. However if a Z_1 oscillation in the scattering cross section *does* exist, it seems very unlikely that it should be limited to oxygen scattering. If there is some Z_2 dependence in this effect then one would expect at least one of the three metals Al, Ag, and Cu in which the Z_1 dependence of damage efficiency has been measured to exhibit some evidence for this. In fact Nelson's backscattering experiments <13> exhibiting oscillations were conducted on Au and and so the scattering effect is clearly confined to neither low Z materials nor insulators. It appears then that experimental evidence does exist for a Z_1 oscillation in the backscattering of ions in metals, but not in the damage production. One possible explanation for this is that oscillatory behaviour in the point defect production could be obscured by the presence of cascade effects, which are absent in sapphire as we shall discuss below. If the oscillations had a Z_2 dependence such that they became weaker for higher Z_2 materials, then cascade recombination effects might dominate the residual Frenkel pair production and any small variations in the initial production of pka's go unnoticed. These arguments are not particularly convincing though and this matter clearly requires further consideration.

Summary.

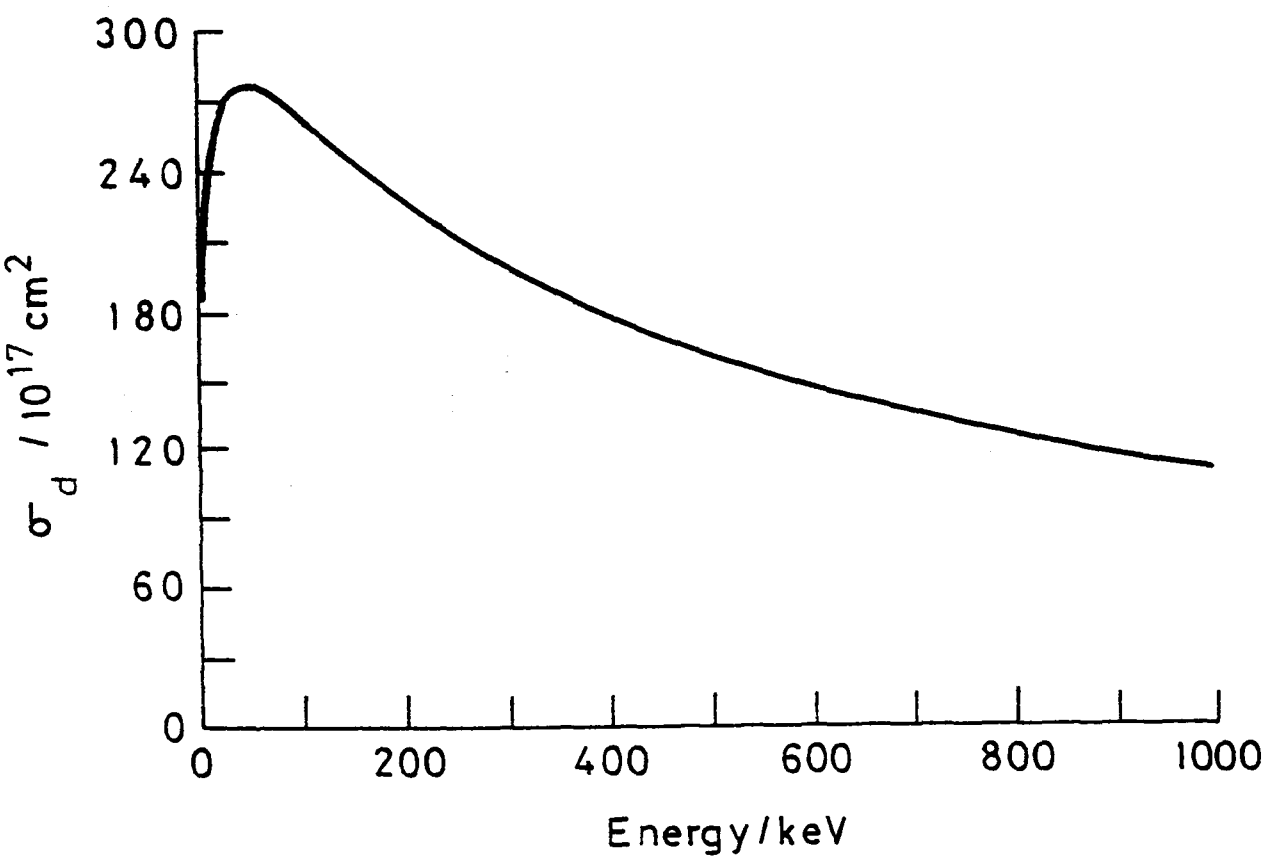
To summarise, we have shown that the measured efficiencies are properties of single ions and not a consequence of overlapping damage regions or some other experimental artifact. The existence was noted of sharp variations in the damage efficiency for low Z ions in sapphire and MgO and it was suggested that these may be related to Z_1 oscillations in the differential cross section for energy transfer. Similar backscattering experiments on sapphire to the ones performed by Nelson <13> would help in deciding the validity of the arguments put forward in favour of Z_1 oscillations. These experiments would have to be limited to the ions below oxygen in the periodic table, but it should be sufficient to study only H, He and B backscattering.

§ 7.4 Efficiency of High Mass Ions.

We now turn to the second important feature of fig. 6.22 noted in the introduction – the relatively constant mean value of ζ in sapphire for both light and heavy ions. The variation of efficiency ζ with incident ion mass found here for sapphire is in sharp contrast to that found in metals. There has been a much greater volume of work in this area for metals than insulators and, in general, good agreement has been found by a number of different workers. Some of the first conclusive experiments were performed by Averback *et. al.* <15>. These authors monitored the damage efficiency in copper and silver and found a uniform decrease with increasing incident ion mass. For example in Ag, ζ is around unity for protons, dropping to ~ 0.9 for He, ~ 0.7 for B and reaches an asymptotic minimum of ~ 0.4 with Ar. Further increase of the ion mass by self-ion irradiation caused no further reduction. It is now widely recognised that in metals this reduction in damage efficiency is a result of FP recombination within the displacement cascade <15, 16, 17>. Low mass ions, which produce mostly isolated FP's therefore have a high damage efficiency, whilst higher mass ions produce most of their FP's in cascades where recombination during the thermal spike results in a drop in efficiency. The saturation of the reduction in efficiency is usually explained by the onset of sub-cascade formation. This explanation of reduced damage efficiency clearly requires that

most of the FP's be produced in cascades where the energy density is high. It is perhaps surprising then that Averback *et. al* <18> have found a very similar trend in aluminium. In this low Z material the authors calculate that the cascade volume is two orders of magnitude larger than that in copper, for recoils of a similar energy, and hence has a correspondingly reduced energy density. However computer simulations of cascades using the MARLOWE code <19> showed that regions of relatively high defect density were still formed. In view of this the authors argued that the same mechanism for reducing ζ (i.e. recombination of FP's during the thermal spike) was just as effective in aluminium as in copper and silver.

The data for sapphire presented in chapter 6 show no such cascade effects and we must explain the different behaviour of aluminium and its oxide. First of all we examine the applicability of the cascade and thermal spike concepts to these two materials. A novel approach to this problem has been taken by Cheng <20>. Motivated by the obvious similarities between cascade structures and fractal patterns, this author used fractal concepts to deduce a simple criterion which states that thermal spikes, and hence cascades, will not form in elemental targets having $Z < 20$. However this appears to be in disagreement with the measurements of Averback *et. al.* <18> on aluminium. Here we take a more orthodox approach and attempt to gain some insight into the differences between aluminium and sapphire from binary collision theory. In fig. 7.4 we have plotted the total displacement cross section, σ_d, for pka's in iron as a function of energy. For clarity this is shown on both a linear and logarithmic energy scale. The maximum of this curve occurs at about 48 keV. In fig. 7.5 we have shown the corresponding curve for aluminium, which exhibits a maximum at 9.8 keV. Finally, in fig. 7.6 we have used the atomic properties of aluminium and oxygen in a suitably averaged manner to obtain the total cross section for displacement in sapphire. This curve reaches its maximum value at an energy of 5.4 keV. In all cases a displacement threshold energy of 30 eV was used. Different values of E_d change the absolute values of each curve but do not affect the position of the maximum. It is clear that the trend with decreasing Z is for the maximum to move to lower energies, which in turn means that the energy of the most energetic pka's in the region of the displacement cross section peak also falls to correspondingly lower energies. This is the basis for an atomistic explanation of the absence of cascade formation in low Z materials: when the point is reached where cascades



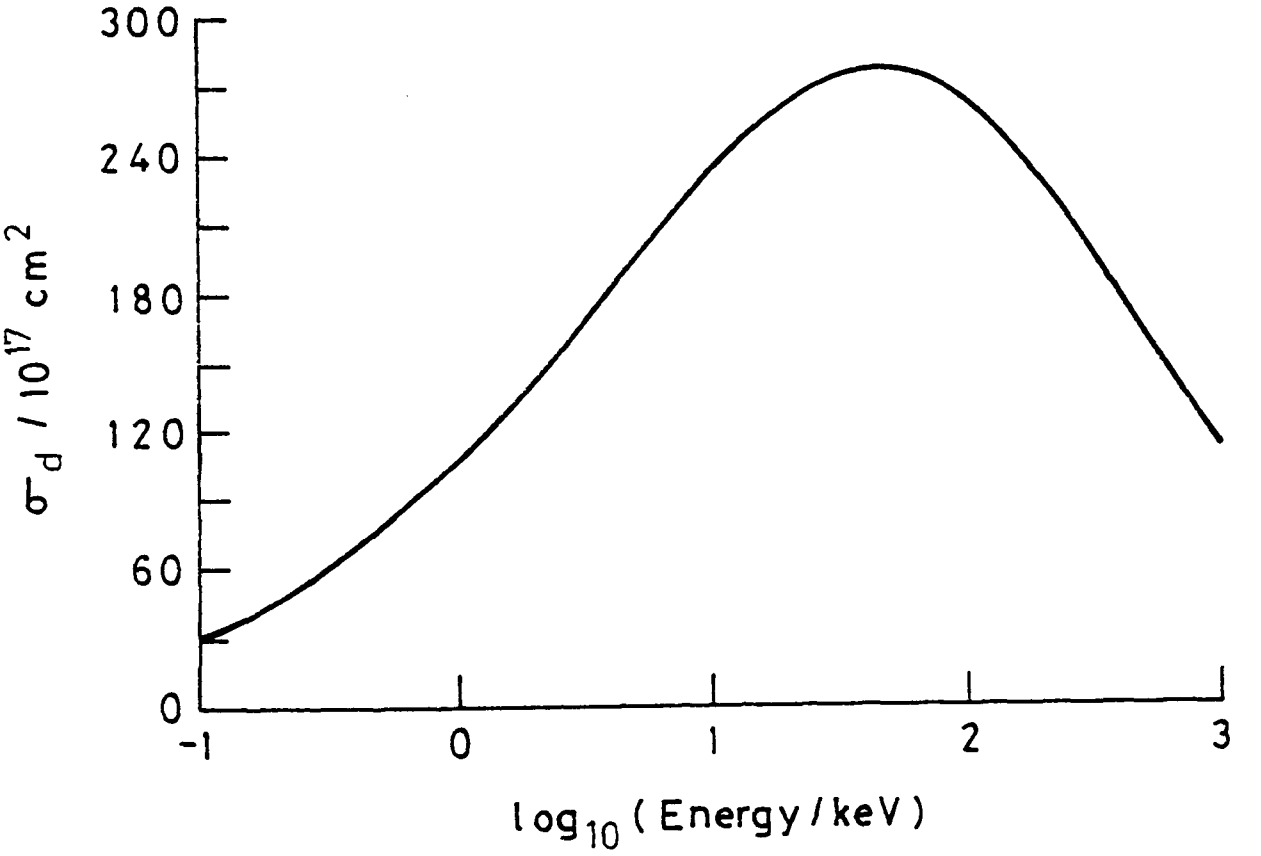
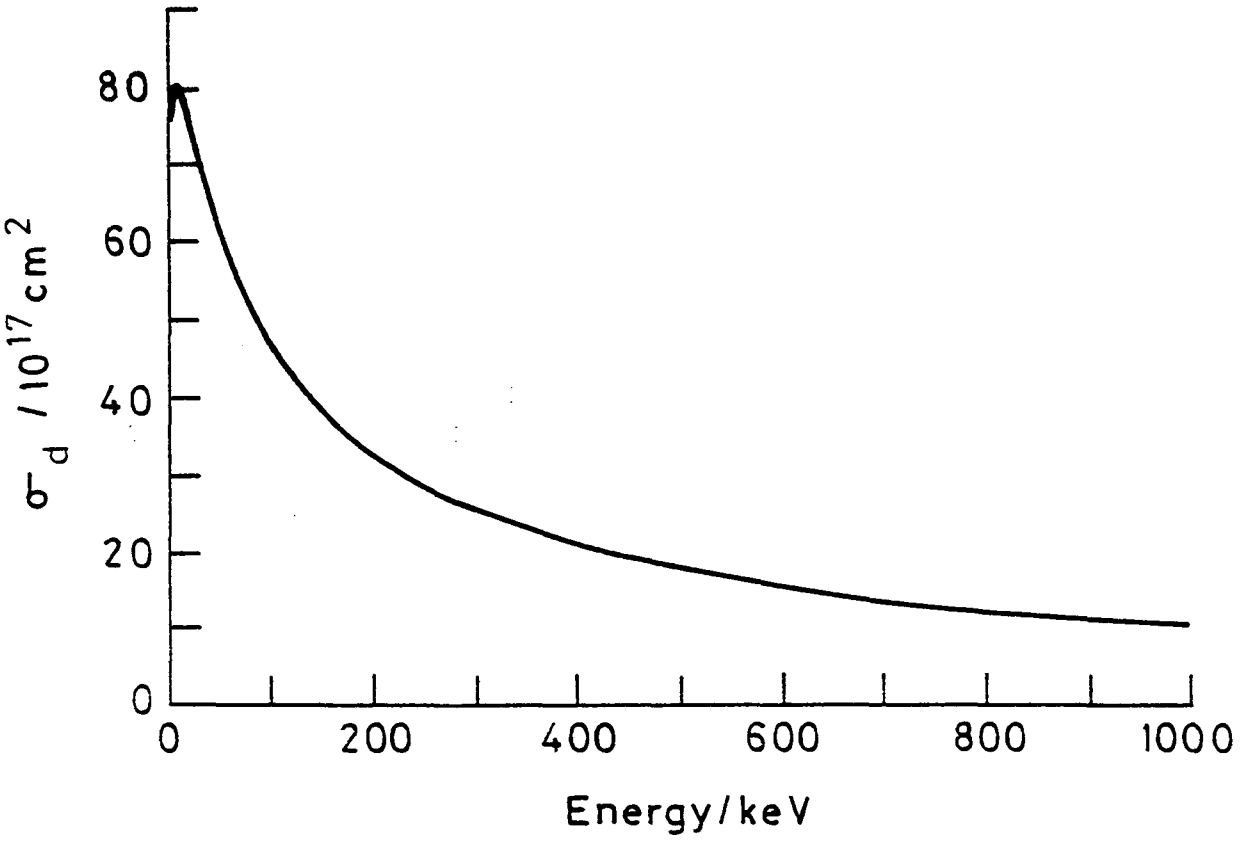


Fig. 7.4. Variation of the total displacement cross section with pka energy in Fe. Linear and logarithmic energy scales are shown for convenience.



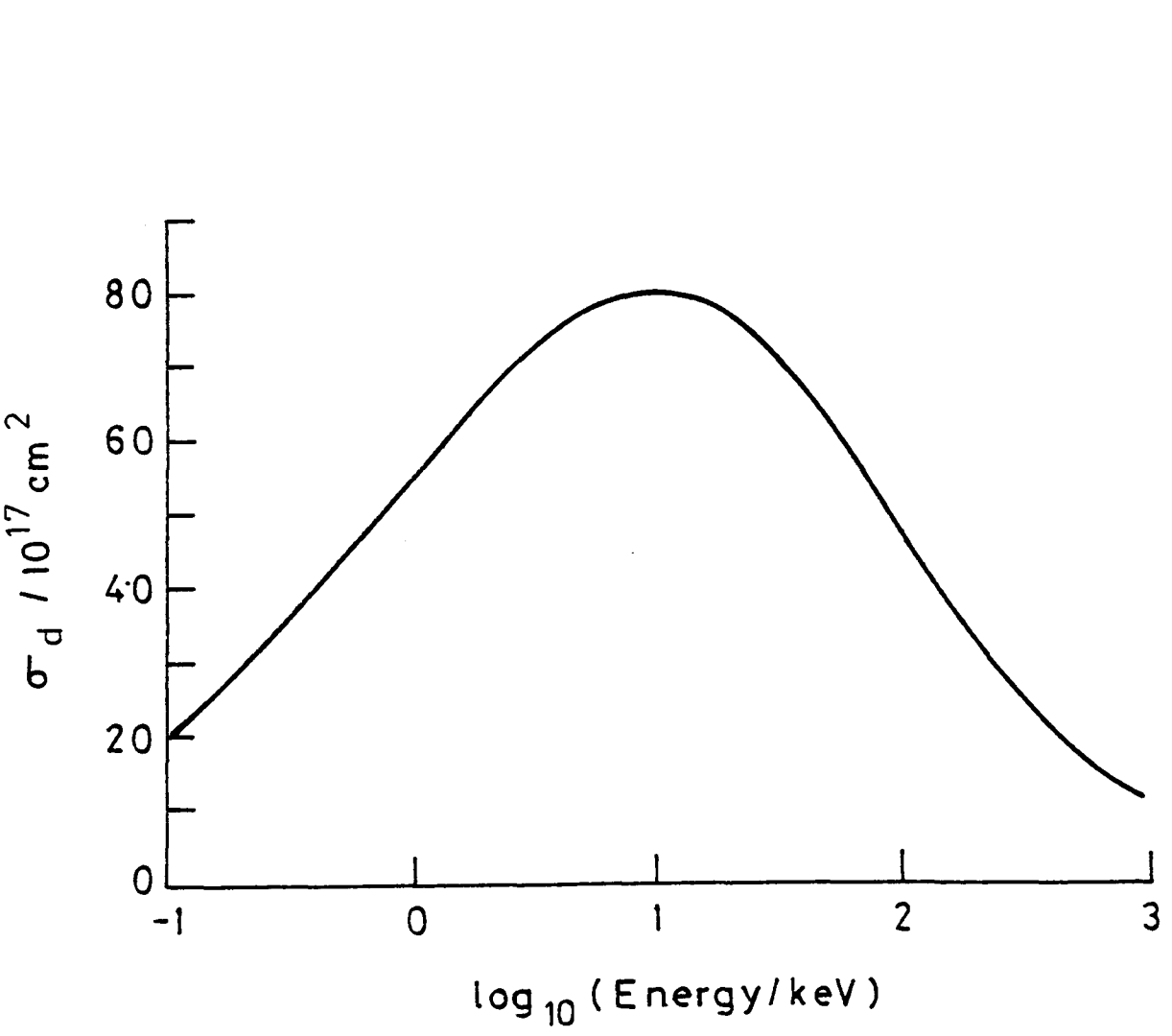
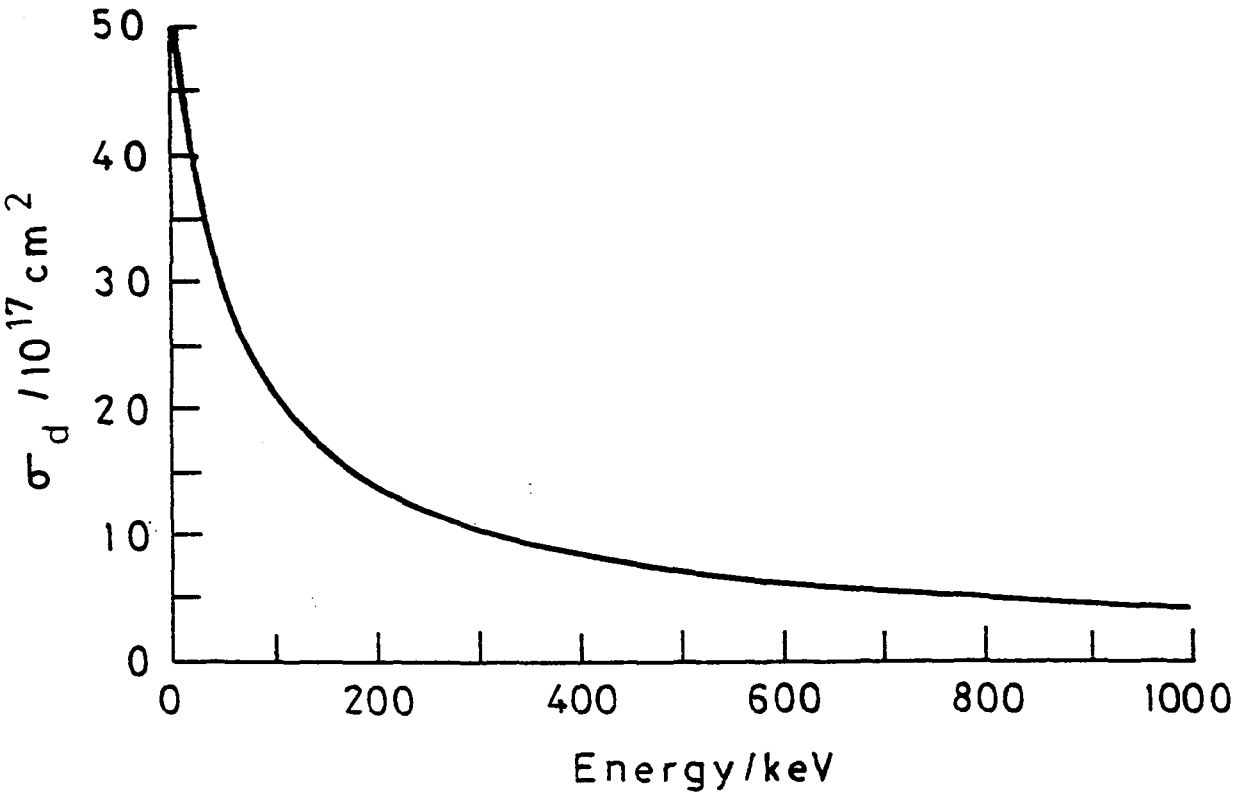


Fig. 7.5. Variation of the total displacement cross section with pka energy in Al. Linear and logarithmic energy scales are shown for convenience.



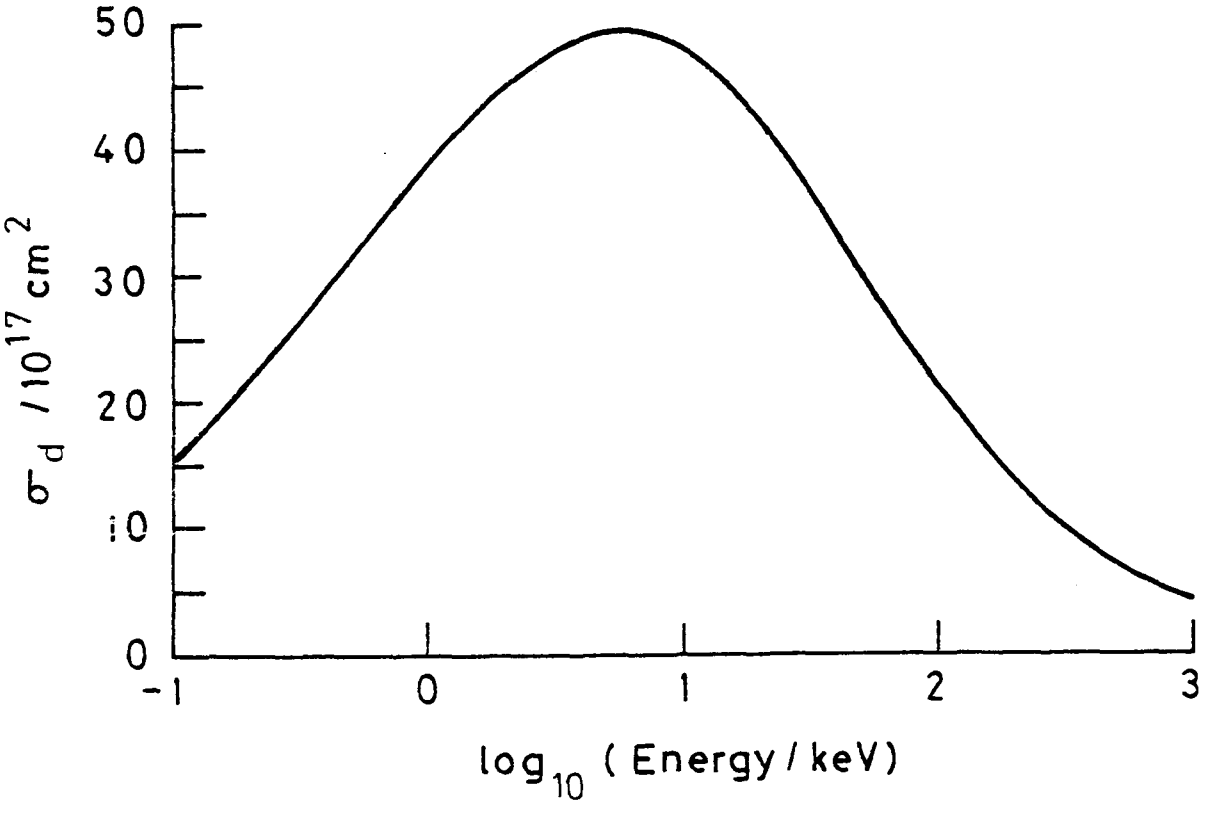


Fig. 7.6. Variation of the total displacement cross section with pka energy in sapphire. Suitable averages of oxygen and aluminium atomic properties were used. Linear and logarithmic energy scales are shown for convenience.

are *likely* to be formed, the pka's are not sufficiently energetic to produce the number of displacements required to cause a thermal spike. Regarding the important question of how many displacements are necessary to cause a thermal spike, binary collision theory remains silent.

This is as far as it is possible to go with binary collision theory towards explaining the difference in cascade behaviour between aluminium and sapphire. We have been able to show significant differences in the behaviour of aluminium and its oxide on the basis of simple atomic properties. However it is unlikely that the cascade behaviour of any material is determined solely by atomic properties. Since one expects the behaviour of a thermal spike to be dependent upon the thermal characteristics of the material, it is natural to invoke thermodynamic arguments to explain the difference in cascade behaviour between sapphire and aluminium. This approach has been taken by Cheng <20> and van Rossum and Cheng <21>, who have demonstrated the influence of the target heat of mixing and cohesive energy on the thermal spike. The difference in thermal properties of aluminium and its oxide is indicated by their widely differing melting temperatures. Aluminium has $T_m = 932\,K$ whilst sapphire has $T_m = 2300\,K$. On this basis one could expect large differences in the thermal spike behaviour of aluminium and sapphire, with corresponding differences in their damage efficiency trends. Thus sapphire would be much more stable with respect to thermal spikes than aluminium and be less likely to exhibit enhanced recombination in the cooling phase of the cascade.

Summary.

In conclusion, we can point to two factors which indicate why sapphire is much less likely than aluminium to show evidence of enhanced Frenkel pair recombination following heavy ion bombardment. The first is concerned with differences in the *formation* of cascades in the two materials and we have shown, using binary collision theory, that the energy at which the total cross section for displacement reaches a maximum in sapphire is approximately one half that of the corresponding quantity in aluminium, leading to lower cascade energies. The second is concerned with the *evolution* of the cascade and we have indicated how higher

thermal activation energies in sapphire could lead to greater stability against subsequent annealing of defects. These two facts taken together are believed to be responsible for the observed differences. The most profitable area for gaining further insight into this problem is probably with the use of molecular dynamics simulations. With this technique the dynamics of pka motion and cascade evolution can be followed in detail and comparisons between aluminium and sapphire could be made in a straightforward manner.

§ 7.5 Irradiation Characterisation and Damage Correlation.

As we discussed in chapter 1, one of the main reasons for studying point defect production in a laboratory is to enable us to understand and predict the behaviour of materials in a genuine radiation environment. In order to transfer our experimental results to a real situation it is necessary that we should be able to relate one set of radiation conditions to another in a meaningful way. It is impossible to find a single parameter which is able to characterise all the different aspects of a given irradiation. However one can find parameters which characterise the most relevant aspects in a given situation.

Characterisation of the PKA Spectrum.

From a technological point of view one of the most important areas in which to achieve reliable damage correlations is neutron irradiation of reactor materials. In this case we effectively have self-ion irradiation taking place and the only variation in the damage efficiency is due to cascade effects, as discussed in § 7.4. The problem arises when comparing irradiations where the neutron spectra differ, for these will also give rise to differing pka spectra and hence a different spectrum of damage efficiencies. In this case it is useful to have a single parameter which characterises the pka spectrum. Some authors (e.g. <15, 18, 22> choose a correlation parameter referred to as $T_{1/2}$, which is defined to be that pka kinetic energy such that one half of all the FP's created as a result of the irradiation are generated by pka's with an initial energy greater than $T_{1/2}$. For a monatomic target this parameter satisfies the equation

$$\frac{1}{2} N_d(E) = \int_{E_d}^{E} \left\{ \frac{N \int_{T_{1/2}}^{T_m^{ki}} \Psi(T)\, d\sigma_{ki}(E';T)}{S_t^{(k)}(E')} \right\} dE' , \qquad (7.4)$$

where $N_d(E)$ is the total number of defects created by an ion with energy E and the other symbols have their usual meanings. By corollary, it is also true that one half of all the FP's are generated by pka's with energy less than $T_{1/2}$. This parameter gives an indication of the 'hardness' of the pka spectrum, though it not unique since different combinations of incident ion mass and energy can give rise to the same $T_{1/2}$ values. In this application, the physical significance of this parameter is that high values of $T_{1/2}$ will correspond to low values of damage efficiency and vice versa. We have used suitably averaged parameters for sapphire in eqn. (7.4) to calculate the values of $T_{1/2}$ for each of the experiments performed in the present investigation. These are given in table 7.3.

The apparent absence of cascade effects in sapphire, discussed in § 7.4, has an interesting corollary. It would indicate that the damage efficiency is not sensitive to the pka spectrum. This has important implications for fusion technology, where sapphire or its polycrystalline form may be used as electrical insulators. Displacement damage is known to degrade the dielectric properties and attempts have been made to simulate the effects of high energy fusion neutrons with ion beams. The insensitivity of ζ to the pka spectrum makes such simulations more realistic. Sapphire has also found applications as a neutron dosimeter in fission reactors <23>. Again, the insensitivity of ζ to the pka spectrum would suggest that a constant efficiency can be used to match the measured optical absorption with calculated values and hence deduce an equivalent neutron dose which is insensitive to the particular neutron spectrum.

Displacement Damage Characterisation.

The most common way of characterising the degree of displacement damage suffered by a target in a given irradiation is to express the radiation dose in terms of the quantity *displacements per atom (dpa)*. This unit is defined such that if a target has been subjected to

Ion	Energy (keV)	Temp. (K)	$T_{1/2}$ (keV)	ξ
H	50	300	0.123	0.13
H	50	77	0.123	0.25
D	50	300	0.175	0.15
D	100	77	0.197	0.19
He	100	300	0.450	0.025
He	100	77	0.450	0.106
B	150	300	1.84	0.17
B	150	77	1.84	0.53
N	400	300	2.87	0.086
N	400	77	2.87	0.30
Ne	400	300	4.51	0.080
Ne	600	77	4.63	0.18
Ar	400	300	7.87	0.13
Ar	400	77	7.87	0.22
Kr	400	300	11.03	0.08
Kr	400	77	11.03	0.33

Table 7.3. Pka characterisation parameter, $T_{1/2}$, for each irradiation.

a dose of 1 *dpa* then, on average, every target atom will have been displaced from its lattice site one time. The number of displacements is invariably calculated with the standard, binary collision model in the modified Kinchin-Pease approximation discussed in § 2.3. But we have seen that this model is at variance with experimental results. If we consider the irradiation of different materials, such as oxides and metals, by any single ion, then we have shown that the damage efficiency can vary widely in the two cases. We have also shown that within a single material, sapphire, the damage efficiency can vary dramatically with the irradiating ion. This is simply another way of stating that the standard model of defect production gives inconsistent results.

In what sense can we still meaningfully use the *dpa* unit? It is important to realise that the concept of *dpa* is itself perfectly valid. Problems with comparisons only arise when we use inconsistent models to determine the number of displacements produced. Thus using the standard model to compare *dpa* values between proton irradiated Al and Ag would be quite acceptable, since in both cases the damage efficiency is around unity. But using the same method to compare proton damaged Al with krypton damaged Ag would lead to discrepancies, since the latter has a low damage efficiency. In sapphire it is clear that the use of a universal potential in evaluating displacement rates under He and B irradiation would also give inconsistent comparisons.

Clearly a more versatile model of defect production is needed, which is able to take all these differences into account. If our interpretation of the damage efficiency results of chapter 6 is correct then the way towards an improved displacement model in low Z insulators is straightforward in principle: it is necessary to obtain scattering cross sections which are Z_1 specific. The most reliable approach would be to perform *ab initio* self consistent field calculations of the interatomic potential as a function of the separation of two ions. This has already been done for a limited number of ions pairs <24>, but requires a great deal of effort. Similar calculations for a variety of Z_1 – target atom collisions would enable one to construct the required differential scattering cross sections. The use of these in future *dpa* calculations should give a much better correlation between irradiations.

Unfortunately the way forward in metals has become less clear, even in principle, due to

recent work which we shall discuss in chapter 8. Until comparatively recently a sensible scheme might have been as follows:

(i) recognise that the standard model fails in metals when most of the Frenkel pairs are produced in displacement cascades and the subsequent atomic motion leads to vacancy-interstitial recombination.

(ii) Perform molecular dynamics (MD) simulations of cascades in one metal (probably copper, since this metal has been studied most) to obtain the variation of damage efficiency, ζ, with pka energy.

(iii) Express the variation of ζ as a function of the energy per atom of the cascade (effectively the cascade temperature). The obvious physical basis of this approach is that the energy per atom (or cascade temperature) is crucial in determining the degree of motion of Frenkel pairs, and hence their recombination during the cascade cooling phase.

(iv) Normalise the cascade temperatures with respect to the melting temperature (or perhaps some other macroscopic thermodynamic property, such as the cohesive energy) of this metal in order to establish a *universal* damage efficiency curve.

(v) Modify future calculations of point defect production in different metals by a simple damage efficiency factor, $\zeta(T)$, which varies with the pka energy and is scaled by the melting temperature (or other thermodynamic property).

This type of approach has a number of points to commend it:

(a) the standard binary collision theory remains intact, apart from an additional modifying factor which only depends on the pka energy and is easily calculated. Standard computer codes for calculating displacement rates would, therefore, require only a simple modification.

(b) Thermodynamic properties of the target are taken into account by scaling the universal damage efficiency curve with respect to thermodynamic properties.

A major problem with this approach, which has only recently been addressed, is that the manner in which the target thermodynamic properties are introduced is incomplete. By simply scaling with respect to the melting temperature we neglect an important aspect of the

thermal evolution of the cascade – the role played by the electron gas in carrying heat away from the excited region. In the final chapter we discuss this problem.

References.

<1> B.D. Evans, J. Comas and P.R. Malmberg, Phys. Rev. B 6 (6), 2453 (1972).

<2> A.E. Hughes, J. De Physique, Colloque C9, 34 (11 – 12), 515 (1973).

<3> C. Lehmann and G. Leibfreid, J. Appl. Phys. 34 , 2821 (1963).

<4> Dr. A.J.E. Foreman, private communication.

<5> A. van Veen, Mat. Sci. Forum, 15 – 18 , 3 (1987).

<6> M.L. Jenkins and M. Wilkins, Phil. Mag. 34 (6), 1155 (1976).

<7> J.P. Biersack, Z. Phys. A – Atoms and Nuclei 305 , 95 (1982).

<8> T.F. Luera, J.A. Borders and G.W. Arnold in: Ion Implantation in Semiconductors, Ed F. Chernow, pub. Plenum, New York (1977).

<9> J.F. Zeigler, J.P. Biersack and U. Littmark, ' The Stopping and Range of Ions in Solids ' , Pergamon Press (1985).

<10> I.M. Cheshire, G. Dearneley and J.M. Poate, Proc. Roy. Soc. A. 311 , 47 (1969).

<11> G. Hogberg and R. Skoog, Rad. Eff. 13 (3 & 4), 197 (1972).

<12> E. Geyer, D. Reschke and K. Freitag, Nucl. Instr. Meths. in Phys. Res. B15 , 81 (1986).

<13> R.S. Nelson, Phys. Letts., 28A (10), 676 (1969).

<14> I.M. Cheshire and J.M. Poate in, ' Atomic Collision Phenomena in Solids ', Ed. D.W. Palmer, North-Holland (1970).

<15> R.S. Averback, R. Benedek and K.L. Merkle, Phys. Rev. B 18 (8), 4156 (1978).

<16> J.H. Kinney, M.W. Guinan and Z.A. Munir, J. Nucl. Mater. Vol. 122-123, 1028 (1984).

<17> K.L. Merkle, W.E. King, A.C. Bailey, K. Haga and M. Meshii, J. Nucl. Mater. Vol. 117, 4 (1983).

<18> R.S. Averback, R. Benedek, K.L. Merkle, J. Sprinkle and L.J. Thompson, J. Nucl. Mater. 113 , 211 (1983).

<19> M.T. Robinson and I.M. Torrens, Phys. Rev. B9, 5008 (1974).

<20> Y.T. Cheng, Mater. Sci. Rep 5 , 45 (1990).

<21> M. van Rossum and Y.T. Cheng, Defect and Diffusion Forum Vols. 57-58, 1 (1988).

<22> A. Iwase, S. Sasaki, T. Iwato and T. Nihira, J. Nucl. Mater. Vols. 133-134, 365 (1985).

<23> G.P. Pells, Radiat. Phys and Chem. 22 (6), 1053 (1983).

<24> N.H Sabelli, R. Benedek and T.L. Gilbert, Phys. Rev. A20 , 677 (1979).

Chapter 8

Thermal Excitation of Electrons in Energetic Displacement Cascades

Introduction.

In our discussion of the displacement cascade in chapter 2 we noted that three stages could be identified: the displacement phase, the relaxation phase and the cooling phase. At the beginning of the relaxation phase the cascade energy is almost entirely associated with the kinetic energy of the ion cores whilst at some later time during the cooling phase the cascade energy is being dissipated into the surrounding material via normal conduction processes involving electronic heat conduction. We have thus progressed from a state where the ion cores and electrons are 'unaware' of each other to a state where they are in mutual thermal equilibrium. There has clearly been some interaction between the two systems which we have neglected. Indeed in chapter 2 we pointed out that whilst standard models of the cascade take into account the target electrons during the displacement phase (via the damage energy formalism) they essentially ignore the electronic system thereafter. In this chapter we attempt to correct this neglect by developing a quantitative description of the electron-ion interaction which bridges the gap between the displacement and cooling phases. The theory described enables one to predict the relative strengths of the interaction in different metals and hence determine parameters relevant to the net production of point defects, such as the cooling rates within individual cascades. We begin with a discussion of the problems encountered when the bulk value of thermal conductivity is used to describe cascade cooling.

§ 8.1 Inapplicability of Bulk Thermal Conductivity.

A simple but reasonable model of a displacement cascade in an elemental metal such as copper treats the disordered region as a spherical volume. As we enter the relaxation phase and an equipartition of energy is achieved we will be able to associate a temperature with the ion cores in the region. Let us attempt to follow the dissipation of the cascade energy by solving the heat flow equations for a spherical region of initial temperature Θ and radius r_i. The subsequent temperature distribution is given by <1>

$$T(r,t) = \frac{2\Theta}{r}\sum_{n=1}^{\infty}\left\{\frac{a}{n^2\pi^2}\sin\left(\frac{n\pi r_i}{a}\right) - \frac{r_i}{n\pi}\cos\left(\frac{n\pi r_i}{a}\right)\right\} \times \sin\left(\frac{n\pi r}{a}\right) e^{-\Delta n^2\pi^2 t/a^2}, \quad (8.1)$$

where Δ is the thermal diffusivity and a is the radius of a surface held at ambient temperature, which we take as 300K. The value of Θ is related to the energy input Q and initial radius r_i as follows. Suppose each atom of the cascade has energy $3k\Theta$ (where k is Boltzmann's constant); the number of atoms involved is r^3/r_0^3, where r_0 is the radius of the Wigner-Seitz sphere. Hence by energy conservation

$$\Theta = \frac{r_0^3 Q}{3kr_i^3} \ . \quad (8.2)$$

The normal bulk value of thermal conductivity for copper is around 385 $W m^{-1} K^{-1}$. With the density taken as 8930 $kg\,m^{-3}$ and the specific heat capacity as 385 $J kg^{-1} K^{-1}$ the thermal diffusivity has the value 0.112 $(nm)^2 (fs)^{-1}$, expressed in more useful units. An estimate for r_i can be obtained from molecular dynamics (MD) studies of cascades in copper <2> to be about 2.5 nm for a 2 keV cascade. In fig. 8.1 we give solutions of eqn.(8.1) showing how the cascade temperature varies with both time and position, assuming the bulk value of Δ. Thirty terms in the Fourier summation were evaluated and the curves are taken at intervals of 5 fs. In fig. 8.2 we plot the temperature as a function of time at a point 1.5nm from the centre of the cascade (rather than at the origin, where the Gibbs' phenomenon has not been suppressed and causes error). We see clearly that the cascade is quenched after some tens of femtoseconds with the implication that atomic mobility is quenched equally fast.

What would be the implications if the cascade did indeed cool this quickly and atomic

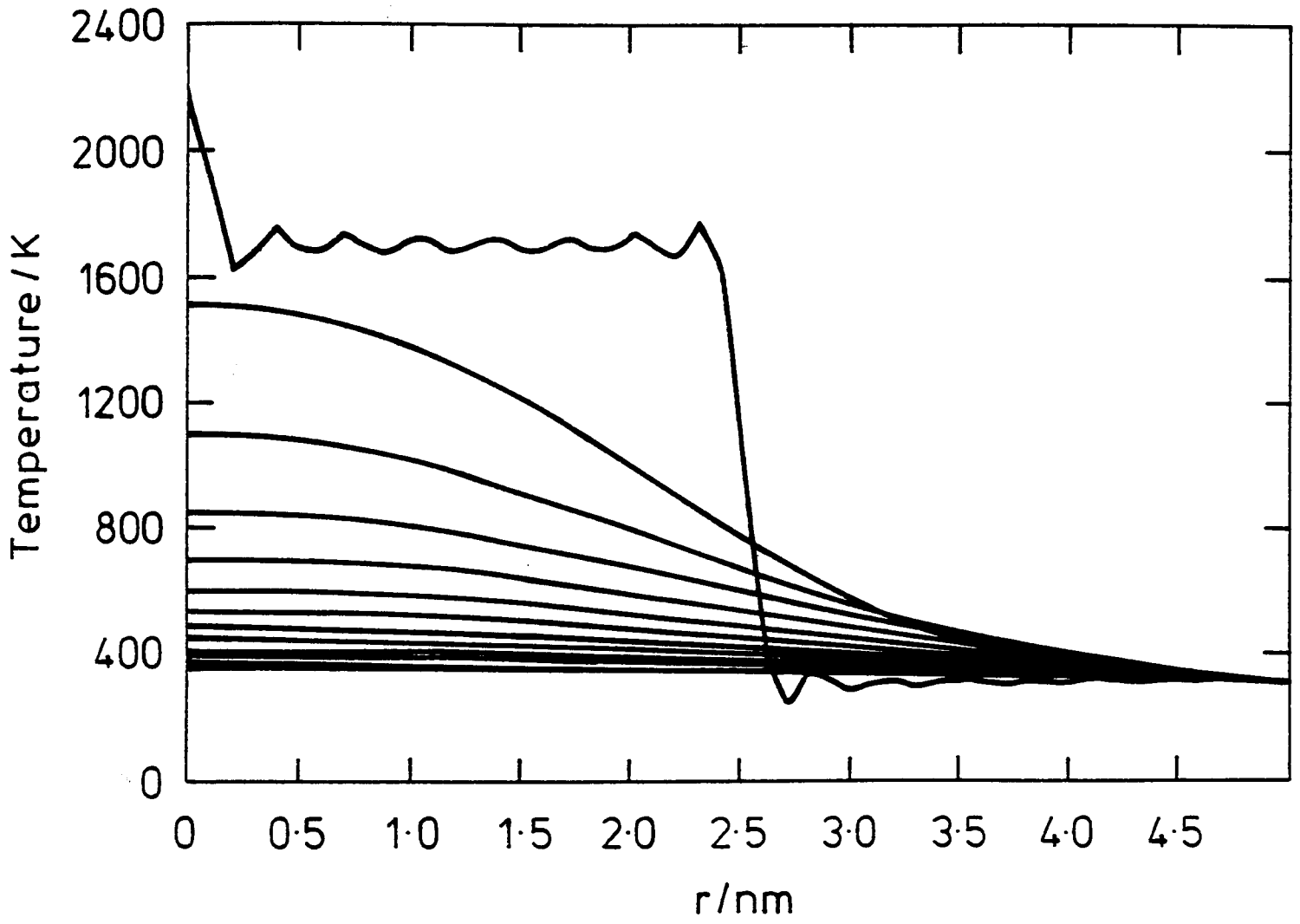


Fig. 8.1. Temperature variation at 5 fs intervals for a 2 keV cascade, according to eqn. (8.1). Use of the bulk value of thermal conductivity leads to rapid quenching of the cascade.

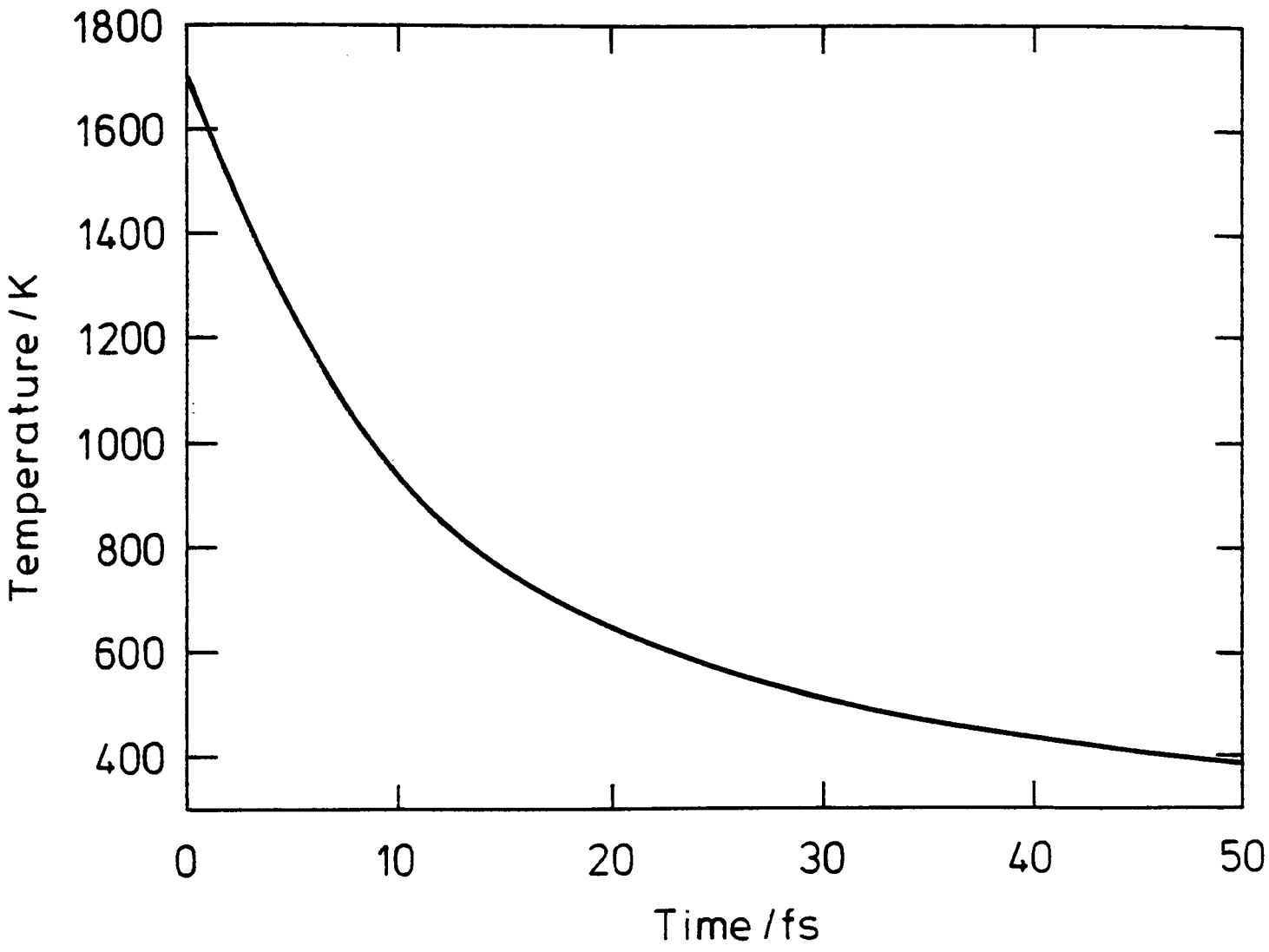


Fig. 8.2. Variation of the temperature within a 2 keV cascade as a function of time, assuming the bulk value of thermal conductivity.

motion was confined to the first few tens of femtoseconds? It is well known from irradiation studies in metals (*e.g.* ref. <3> and other references therein) that the point defects produced in displacement cascades in metals are able to collapse into dislocation loops and this obviously requires that the point defects are able to cluster after they have formed. Let us estimate the timescales required for such clustering by calculating the time taken for a vacancy to diffuse across the radius of a cascade in Cu. A value for the diffusion coefficient of vacancies in Cu used in the modelling of radiation effects in Cu with a considerable degree of success is <4>

$$D = 7.8 \times 10^{-5} \exp(-0.8\, eV/kT)\ m^2 s^{-1} \quad . \tag{8.3}$$

Then using the simple relationship

$$\delta \sim \sqrt{D\,t} \quad , \tag{8.4}$$

to give the approximate distance δ travelled in time t, we find that for a cascade temperature of 1700 K, $\delta \approx 5$ ps or for a temperature of 1000 K, $\delta \approx 200$ ps. These simple estimates are confirmed by the rather more elaborate molecular dynamics calculations of Protosov and Chudinov <5> who were attempting to simulate the formation of vacancy dislocation loops in Cu following irradiation. These authors removed energy from the cascade boundary to simulate heat conduction away from the cascade and found that clustering only occurred for a 'slowly' cooling cascade on a timescale of ~ 100 ps. Although the results of modelling point defect motion in the extreme conditions encountered in a cascade must be treated with some caution, the qualitative result is in no doubt: the defect clustering necessary to explain the existence of dislocation loops in metals requires timescales of at least some *picoseconds*.

§ 8.2 Role of the Electron Gas.

The above discussion shows that the use of the bulk value of the thermal conductivity, κ, in modelling cascade evolution leads to conclusions which differ from those obtained experimentally. Since the major contribution to κ in metals is electronic conduction (for example in copper at room temperature roughly 98% of heat is transported by electrons), we

must recognise that the electron gas is somehow prevented from strongly interacting with the cascade. The reason for this is not hard to find in fact. The spatial extent of the thermal spike is less than, or of the order of, the electron-phonon mean free path in the surrounding material and consequently there is very poor coupling between the two systems in the vicinity of the cascade. Under these conditions the participation of the electron gas in heat transfer from the region is severely limited and the resulting thermal conductivity is dramatically reduced. In this model the cascade region remains hot for a relatively long time, allowing a much greater degree of atomic motion. This qualitative description has been recognised for some time now (*e.g.* <6>) but the lack of a physical model of the energy transfer from the hot ions to the electron gas has prevented a quantitative treatment. Interest was renewed recently though with the paper of Flynn and Averback <7> which we now discuss.

§ 8.3 Model of Flynn and Averback.

Flynn and Averback (FA) describe a model of a spherical cascade with electrons diffusing randomly through the hot region and gathering energy $k\theta_D$ at each encounter with a phonon, where θ_D is the Debye temperature. Their analysis proceeds as follows. Eqn.(8.2) may be inverted to give the variation of the thermal spike radius with ion temperature (which we now write as T_i for later convenience) as

$$r = r_0\left(\frac{Q}{3kT_i}\right)^{1/3} \quad . \tag{8.5}$$

Thus for a given cascade energy Q, higher initial temperatures are attained if the energy is confined to a smaller radius. In the harmonic approximation the electron-phonon mean free path is inversely related to the local temperature. A useful way of writing this is

$$\lambda = r_0 T_0 / T_i \quad , \tag{8.6}$$

where r_0 is the radius of the Wigner-Seitz sphere and T_0 is the temperature at which λ reduces to the Wigner-Seitz radius. FA then consider the physical mechanism by which the

surrounding electron gas is able to achieve thermal equilibrium with the spike. They proceed to determine how much energy the electron will acquire as it traverses the spike. Simple statistical arguments show that if the electron is undergoing a random walk through a thermal spike of radius r, gaining energy $k\theta_D$ at each collision with phonons, then the total energy gained is just

$$\beta\left(\frac{r}{\lambda}\right)^2 k\,\theta_D\ , \tag{8.7}$$

where β is a constant of order unity. The FA criterion for whether the electron gas will interact strongly with the thermal spike is just that this should be sufficient to allow the electrons to reach the same temperature as the ions. A useful criterion can be established by combining eqns.(8.5), (8.6) and (8.7) to show that for thermal equilibrium to be attained the initial spike radius must be smaller than the critical value

$$r_c = \frac{r_0\,\theta_D\,Q}{3kT_0^2}\quad , \tag{8.8}$$

or alternatively, using eqn.(8.2), the initial cascade temperature must exceed the value

$$T_c = \frac{9k^2T_0^6}{\theta_D{}^3Q}\quad . \tag{8.9}$$

The important point to note in these equations is the *extreme* sensitivity shown to the parameter T_0. FA have deduced values of T_0 for Cu and Ni on the basis of electrical resistivity data and find the values 4.5×10^4 K and 1.5×10^4 K respectively. The critical temperature T_c is a factor of 3^6 higher for Cu than Ni and they conclude that the electronic system in Ni is able to achieve equilibrium throughout the thermal spike phase of the cascade whereas in Cu it may never equilibrate with the lattice during the lifetime of the spike.

The FA model gives a simple picture of the physical process by which the electron gas interacts, to a greater or lesser degree, with the thermal spike. This model has now been put on a firmer theoretical basis by Finnis, Agnew and Foreman <8> who have derived expressions for the flow of heat in both electronic and ionic systems in the form of two coupled partial differential equations for T_e and T_i, the local temperatures of electrons and ions. This work confirms the qualitative conclusions of FA and also brings out the important role played by γ_e, the coefficient of the electronic heat capacity, in determining the relative interaction strengths.

§ 8.4 Theory of Finnis et. al.

We assume that the electronic system can be described as a uniform perfect gas obeying Fermi-Dirac statistics and that the cascade is sufficiently hot that only phonons at the Debye frequency need be considered. We further assume the validity of the harmonic approximation, expressed by eqn.(8.6). T_e is the local electronic temperature and we assume that $kT_e N(E_f)$ electrons participate in scattering with phonons, where $N(E_f)$ is the density of states at the Fermi energy. τ is the mean free flight time for electron-phonon scattering, which we can replace by λ/v_f, where v_f is the Fermi velocity. We assume that energy $k\theta_D$ is exchanged in each collision to obtain an expression for the rate of transfer of energy from ions to electrons:

$$R_t = \frac{k^2\theta_D N(E_f) v_f T_i T_e}{r_0 T_0} \quad . \tag{8.10}$$

A net rate of energy transfer may be established by replacing T_i with $(T_i - T_e)$.

The standard expressions for the thermal conductivity and heat capacity of the electron gas <9> may be written in the form

$$\kappa = (\pi^2/9)\, k^2 T_e N(E_f) v_f \left(\frac{r_0 T_0}{T_i}\right) \tag{8.11}$$

$$C_e = (\pi^2/3)\, k^2 N(E_f) T_e \quad . \tag{8.12}$$

These expressions may be used in the energy balance equation for the electronic system,

$$C_e \frac{\partial T_e}{\partial t} = \kappa \nabla^2 T_e + R_t \quad , \tag{8.13}$$

to derive an expression for the changing electronic temperature:

$$\frac{\partial T_e}{\partial t} = \left(\frac{3\theta_D v_f}{\pi^2 r_0 T_0}\right)\left(\frac{T_i - T_e}{T_0}\right) + \frac{v_f r_0 T_0}{3T_i} \nabla^2 T_e \quad . \tag{8.14}$$

A similar expression may be obtained for the ionic system

$$\frac{\partial T_i}{\partial t} = \left(\frac{\kappa_i}{\sigma\rho}\right)\nabla^2 T_i - \left(\frac{3\theta_D v_f \gamma_e}{\pi^2 r_0 \sigma\rho}\right) T_e \left(\frac{T_i - T_e}{T_0}\right) \quad . \tag{8.15}$$

Here κ_i is the ionic thermal conductivity, σ is the specific heat capacity, ρ is the density and γ_e is the coefficient of the electronic heat capacity per unit volume.

The relationship of these formulae to the inequalities of FA may be noted if we consider characteristic timescales for the heating up and dissipation of energy in the electronic system. Returning to eqn.(8.14), let us rewrite this expression as

$$\frac{\partial T_e}{\partial t} = \frac{T_i - T_e}{\tau_h} + \frac{1}{\tau_c}(r^2 \nabla^2 T_e) , \tag{8.16}$$

where

$$\tau_h = \frac{\pi^2 r_0 T_0}{3\theta_D v_f} \quad \text{and} \quad \tau_c = \frac{3T_i r^2}{v_f r_0 T_0} \quad . \tag{8.17}$$

τ_h is a characteristic heating time and τ_c is a characteristic cooling time. The temperature of the cascade is related to the initial energy input Q and its radius r via eqn.(8.2), enabling us to write the following expression for τ_c:

$$\tau_c = \frac{Q r_0^2}{k v_f T_0 r} . \tag{8.18}$$

The factor r in the denominator explains why for large times (corresponding to large r) the electrons have no time to equilibrate with the hot lattice. In fact the critical radius for equilibration is when $\tau_h = \tau_c$. This equality recovers the FA expression for T_c (eqn. 8.9), with a slightly different numerical coefficient:

$$T_c = \frac{\pi^6}{81} \frac{k^2 T_0^6}{\theta_D^3 Q^2} \quad . \tag{8.19}$$

It is useful to consider a simplification of the above equations which occurs when we ignore phonon diffusion (which is much slower than diffusion in the electronic system) and assume T_e to be constant. Then eqn.(8.15) reduces to the following ordinary differential equation:

$$\frac{dT_i}{dt} = -\alpha(T_i - T_e)$$

where (8.20)

$$\alpha = \frac{3\theta_D \gamma_e T_e v_f}{\pi^2 r_0 \sigma \rho T_0} \quad .$$

In this approximation the time constant for the cooling of the lattice by electrons is given by $\tau = \alpha^{-1}$, implying that rapid quenching of cascades is favoured by small values of T_0 and large γ_e. Values of τ for Cu and Ni are 4.3ps and 0.12ps respectively, for an electron temperature of 300 K. The value for Ni is of the order of one lattice vibration and so clearly some caution is needed in the sense of which the term 'cooling' is applied. However this approach does enable one to predict, from elementary considerations, whether cascades in otherwise similar metals will have different cooling characteristics – it is only necessary to compare values of $T_0 / \gamma_e = \zeta$. Comparing Ni and Cu in this way we find a ζ ratio of around 30, suggesting that the cooling characteristics of cascades in these two materials should differ significantly, with Ni cooling faster than Cu. Evidence of a difference in cascade behaviour in these two otherwise very similar metals is indeed found experimentally. For example loop production is found to be much more efficient in Cu than Ni <10> and one also finds that the fraction of vacancies produced which are contained within loops is higher in Cu than Ni <11>. Both of these observations are consistent with the prediction of this model that cascades in Ni cool much faster than cascades in Cu.

§ 8.5 Numerical Solutions.

We must now investigate the *absolute* cooling rates of cascades in these two metals by finding numerical solutions of the coupled eqns.(8.14) and (8.15) using realistic cascade parameters. For numerical work the equations were put in dimensionless form by choosing the unit of length as r_0, time as $3r_0/v_f$ and temperature as $9\,\theta_D/\pi^2$. Then eqns.(8.14) and (8.15) take the following simple form:

$$\frac{\partial T_e}{\partial t} = \frac{T_0}{T_i} \nabla^2 T_e + \frac{T_i - T_e}{T_0} \qquad (8.21)$$

$$\frac{\partial T_i}{\partial t} = \left(\frac{3\kappa_i}{\sigma\rho r_0 v_f}\right)\nabla^2 T_i - \left(\frac{9\theta_D \gamma_e}{\pi^2 \sigma\rho}\right) T_e \left(\frac{T_i - T_e}{T_0}\right) \quad . \tag{8.22}$$

Discretised versions of the continuous equations were set up for a spherically symmetric cascade and solved using 'FACSIMILE' – a commercially available numerical package <12>. The initial temperature distribution was

$$T_i = \begin{cases} T_1, & 0<r<r_1 \\ T_{am}, & r_1<r<2r_1 \end{cases} \tag{8.23}$$

$$T_e = T_{am}, \quad 0<r<2r_1 \quad . \tag{8.24}$$

where T_1 is the initial cascade temperature, calculated from eqn.(8.2) and r_1 is the cascade radius. This was estimated from MD studies of a 2 keV cascade in Cu <2> to be about 2.5 nm. T_{am} denotes the ambient temperature, which was taken to be 300 K in all calculations. The boundary conditions imposed were (i) no heat flow at r = 0 and (ii) no temperature change in either system at $r=2r_1$. Care was taken that this second condition did not significantly influence the cascade region. The values of parameters used in the calculation for Cu and Ni are shown in table 8.1. Values of T_0 were taken from FA for consistency to be 4.5×10^4 K and 1.5×10^4 K for Cu and Ni respectively. The lattice thermal conductivity, κ_i, is difficult to measure because it is dominated by the electronic thermal conductivity in pure metals. A value of $1.0\,W m^{-1} K^{-1}$ was estimated from the aforementioned MD study of Cu and this value was also used for Ni. In practice these calculations are rather insensitive to the value of κ_i since this is so much smaller than the electronic thermal conductivity.

The results of these calculations are shown in fig. 8.3, where we plot the temperature at the centre of the cascade as a function of time on a logarithmic scale. It is clearly seen that the Ni cascade quenches much faster than that in Cu. In fig. 8.4 we show how the temperature at the centre of the 2 keV cascade in Cu changes with time when the electron-phonon interaction is both included and neglected. The effect clearly makes a significant difference in the cooling phase of the cascade. In fig. 8.5 we present a similar graph for a 5 keV cascade in Cu showing that the effect is more pronounced at higher energies. An initial cascade radius of 3.5 nm was used in this case. The Ni cooling curve for such a cascade shows the cascade

	Cu	Ni
v_f / ms^{-1}	$1.57x10^6$	$1.57x10^6$
Θ_D / K	343	440
r_o / nm	0.142	0.138
γ_e / $JK^{-2}\,m^{-3}$	104	1104
ρ / kgm^{-3}	8920	8900
σ / $JK^{-1}\,kg^{-1}$	385	460
T_o / K	$4.5x10^4$	$1.5x10^4$

Table 8.1. Parameters used in numerical solution of heat flow equations.

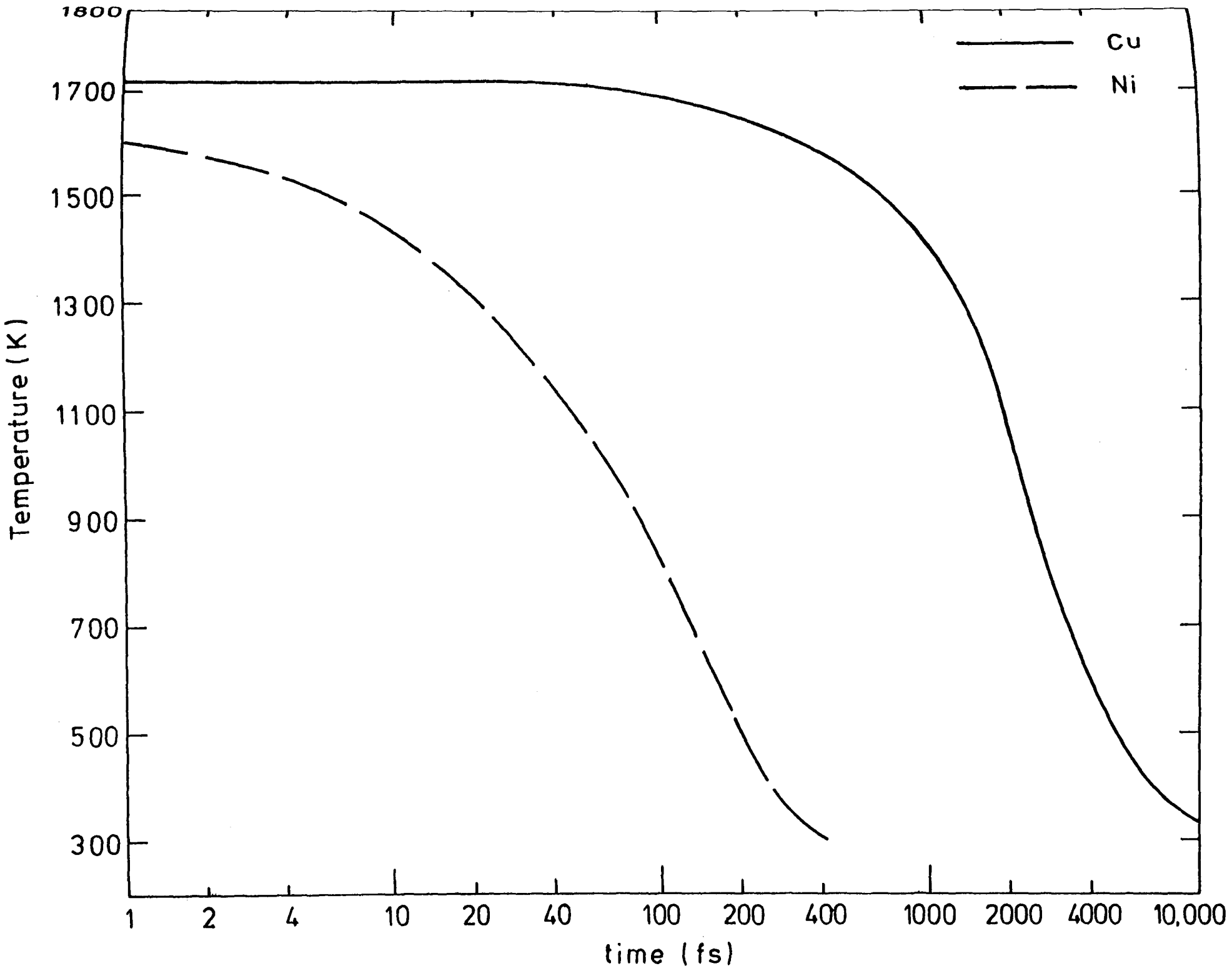


Fig. 8.3. Temperature variation at the centre of a 2 keV cascade in copper and nickel according to the theory of § 8.4. The stronger electron-phonon interaction in nickel causes much faster cooling than in copper.

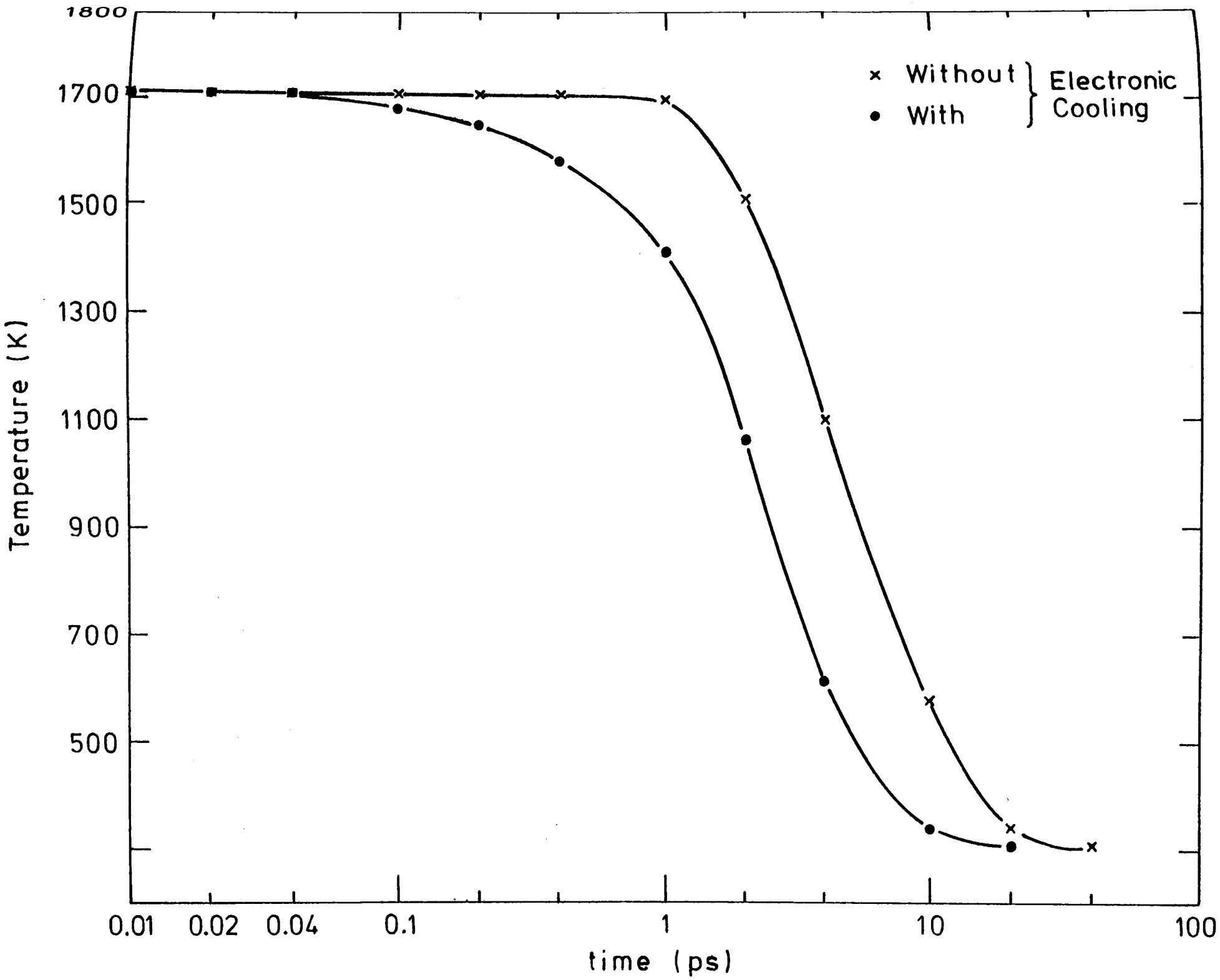


Fig. 8.4. Cooling rate of a 2 keV cascade in copper, calculated with and without electronic cooling.

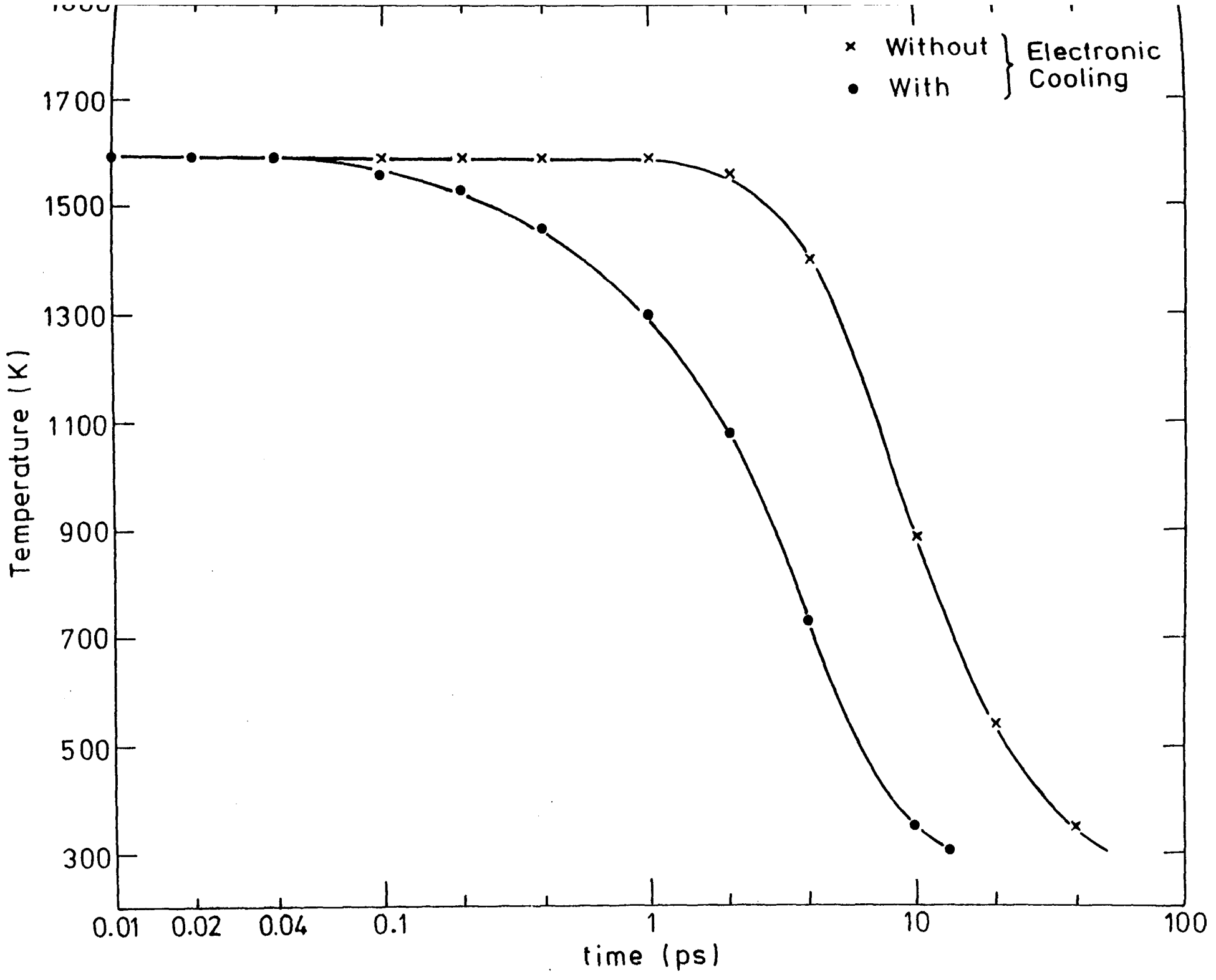


Fig. 8.5. Cooling rate of a 5 keV cascade in copper, calculated with and without electronic cooling.

cooling faster than the period of one lattice vibration. Although our thermal model of the interaction becomes unphysical at such rapid cooling rates the message is clearly that electronic conduction cannot be ignored.

The equations on which the preceding calculations are based indicate that heat flow from the cascade cannot be described by a simple thermal conductivity. A detailed description of the cascade evolution from the displacement phase to the cooling phase requires a molecular dynamics approach (see for example refs. <13,14,15>) and indeed MD studies of cascades in Cu are currently being carried out by several groups, but these do not take into account the potential cooling effect of electrons. In the standard MD approach no coupling of the ionic motion to the electron system is considered, hence the heat transfer rate is underestimated because it only includes the lattice thermal conductivity. The atoms are treated as rigid classical particles, interacting via simple pairwise or many-body potentials. The continuum calculations presented above allow us to assess the importance of terms omitted in conventional MD. On the basis of these results it appears that the low value of γ_e for Cu makes the importance of electronic heat conduction minimal in the cascade energy regime (up to about 5 keV) simulated to date in this metal. This is rather fortuitous since the situation is clearly different in Ni, where γ_e is some ten times greater and a standard MD calculation would significantly underestimate the heat conduction away from the cascade region. In order to obtain a picture at the atomistic level of the effect of electronic heat conduction away from the cascade region it is necessary to incorporate the above model into MD simulations. We now discuss how this may be achieved.

§ 8.6 Atomistic Simulation with MD.

Implementation of the above ideas into a MD code requires the definition of both ion and electron local temperatures. However in most cases where eqn.(8.20) is expected to remain a good approximation, T_e remains close to ambient temperature because the timescale for conduction through the electron gas is usually much shorter than the timescale for loss of energy of ions to electrons. In this case the equation of motion of the ions needs to be

modified to add the effect of the term introduced by eqn.(8.20). There are two straightforward ways to achieve this. One possibility is to scale all ionic velocities after each time step by an appropriate amount depending on the local temperatures. An alternative approach and the one adopted here is to apply a damping force $\mathbf{F}_i$ to each ion in the form

$$\mathbf{F}_i = -\mu \mathbf{v}_i \quad , \tag{8.25}$$

as has been suggested by other authors <16>. The rate of change of thermal energy is then

$$\mathbf{F}_i \cdot \mathbf{v}_i = -\mu \mathbf{v}_i \cdot \mathbf{v}_i \quad , \tag{8.26}$$

which we equate to $\frac{\partial}{\partial t}(3kT_i)$. Hence from eqn.(8.20) we have

$$-\mu \mathbf{v}_i \cdot \mathbf{v}_i = -3k\alpha(T_i - T_e) \quad . \tag{8.27}$$

Finally, using eqn.(8.27) and the following expression for T_i

$$T_i = \frac{m v_i^{\,2}}{3k} \quad , \tag{8.28}$$

where m is the ion mass, we may write the equation for μ as

$$\mu = \alpha m \left(\frac{T_i - T_e}{T_i} \right) \quad . \tag{8.29}$$

This equation presents a problem as $\mathbf{v}_i$ tends to zero (which will often be the case in a vibrating solid) because T_i will also go to zero, causing the expression for μ to become singular. To avoid this possibility we have introduced a smooth cut-off to μ at $T_e/20$ by re-writing eqn.(8.29) as

$$\mu = \alpha m \frac{T_i - T_e}{(T_i^{\,2} + (T_e/20)^{\,2})^{1/2}} \quad , \tag{8.30}$$

where the factor 1/20 has been chosen to be compatible with the time steps used in the MD code when atoms are thermally vibrating. In this way the value of μ becomes constant when an atom comes to rest. Test calculations with the atoms at the same temperature as the electrons show that the above cut-off has no appreciable effect on the vibrations of the atoms over the timescale of cascade calculations. It is found that vibrating atoms can sustain their temperature to better than 1K over times of the order of 10ps with this approximation. It has

also been verified that when the atom temperature is initially higher than that of the electrons then it will steadily fall towards the electron temperature with a time constant given by $\tau = \alpha^{-1}$, in good agreement with similar continuum calculations.

§ 8.7 Comparison with Other Work.

Caro and Victoria <16> have described a scheme to add a velocity dependent damping term to the ionic equation of motion to simulate the electron-ion interaction over the whole range of energies encountered in the cascade, from the collisional phase through to the thermal phase. An empirical interpolation scheme is proposed to smoothly connect the 'stopping power regime' and the 'thermal regime' of the electron-ion interaction by varying the coupling according to the local electronic density encountered by a moving ion. Detailed comparison with the present work is difficult since no relationship between the ion energy and the electronic density encountered is given in ref. <16>. However it is clear that the thermal model we have presented above will tend to underestimate the damping in the collisional phase in comparison. This should not be a serious error though, since most ion-ion collisions are glancing angle and, in terms of the description of Caro and Victoria, the electronic density encountered by the ions will not differ greatly from the equilibrium value. A comparison of the present model with ref. <16> can be obtained by noting that our product αm is the same as their damping parameter β at high temperatures. If we assume the electron density is given by the conduction electron density in Cu then we find $\beta = 2.7 \times 10^{-14}\ kg\, s^{-1}$ whilst $\alpha m = 2.4 \times 10^{-14}\ kg\, s^{-1}$, in satisfactory agreement.

The problem of the electron-ion interaction has been considered by Kaganov *et. al.* <17> who derived the following expression for α:

$$\alpha = \frac{\pi^2}{6} \frac{m_e s^2 n_0}{\tau \theta_D \sigma \rho} \quad , \tag{8.31}$$

where m_e is the electron mass, s is the speed of sound in the solid and n_0 is the number density of electrons. If we substitute expressions for the free electron density of states, Fermi energy and Debye wavelength <18> into our expression for α, eqn.(8.20), and also make the

assumption that $T_i \approx T_e$, we obtain a similar result but with the coefficient $\pi^2/6$ replaced by $108^{1/3}/Z^{2/3}$, where Z represents the number of free electrons per atom. The agreement between these two equations is satisfactory in the free electron approximation. However our expression clearly has the greater generality since it takes the band structure of the solid into account via the factor γ_e.

§ 8.8 MD Simulations.

The above formalism has been implemented in a recent version of the MD code MOLDY <19> and used to study the effects of electron-phonon coupling on displacement cascades in copper using a modified Ackland *et. al.* many-body potential between the atoms <20>. The original Ackland potential does not contain a short range repulsive core potential and as a result it allows Cu atoms to pass through one another at energies greater than around 60 eV. A short range Born-Mayer type potential has been incorporated in such a way that the fitted properties, such as single crystal elastic constants, cohesive energy, *etc.* are unaffected. The coefficients of the potential were adjusted to give the best fit to the measured threshold displacement energies for a range of crystallographic directions. The resulting fit is close to the well-known 'Gibson 2' repulsive potential commonly used in simplified cascade simulations. The atoms were thermally equilibrated at 100 K for around 10ps (~150 vibrations) before the cascade is initiated. We chose to simulate a 500 eV knock-on event in the <345> direction with the primary atom situated near the centre of the block. Four different levels of electron-phonon interaction were introduced, ranging from a zero interaction (as currently assumed in MD cascade simulations) to the strong interaction predicted for nickel. Periodic boundary conditions are employed in MOLDY which have the advantage that the cascade does not necessarily have to evolve in the centre of the block. The block size is chosen so that replacement collision sequences are contained within the block and do not overlap with one another through the faces as a consequence of the periodic boundary conditions. For the 500 eV cascades a block of 6912 Cu atoms ($12 \times 12 \times 12$ unit cells) was used. The computer generated pictures in fig. 8.6 show a three dimensional view of the cascade according to the criteria:

(i) atoms displaced by more than one quarter of a lattice constant from any lattice site are shown as solid squares

(ii) vacant lattice sites, defined as having no atom within one quarter of a lattice constant of the site, are shown as open squares.

It is a general feature of cascade simulations that very small changes in the initial conditions often produce large differences in the final defect configuration. Ideally one would average over many simulations to reduce statistical fluctuations before producing quantitative results <21>, however qualitative conclusions can be drawn from the results of just a few simulations and it is in this spirit that we present the following results.

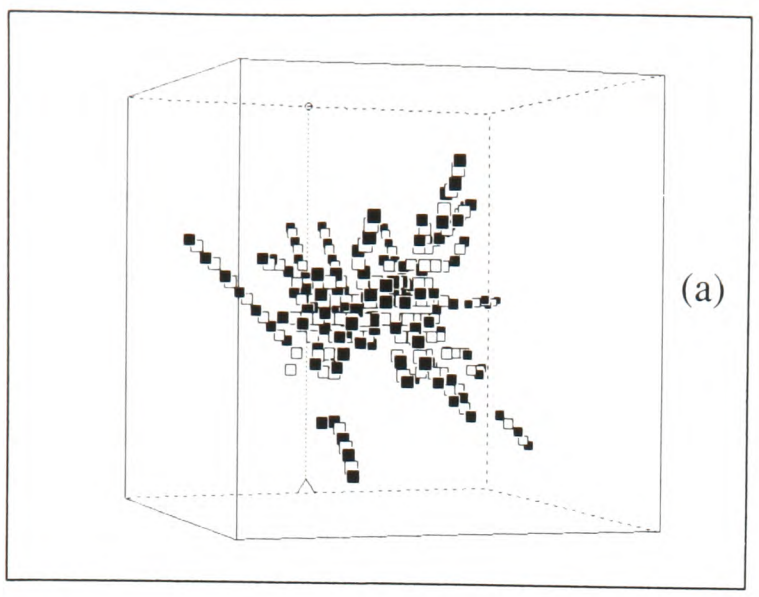
Results of MD Simulations.

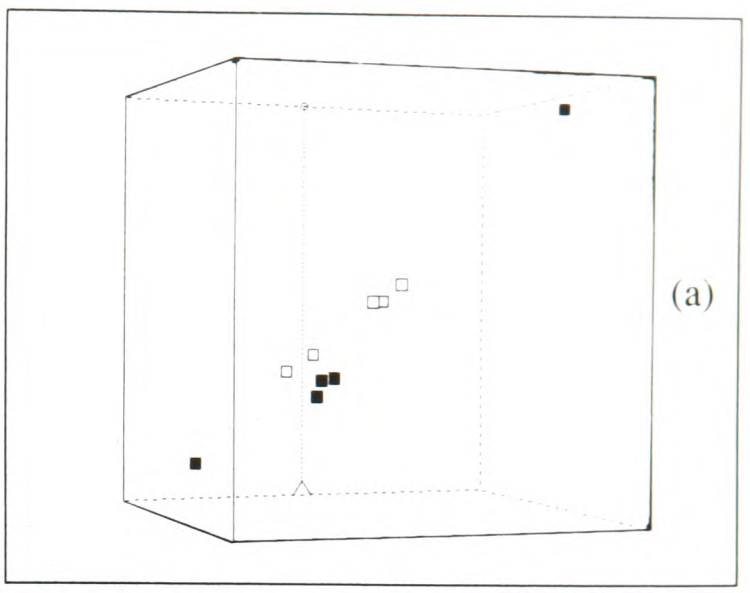
For an electron temperature of 100 K we find from eqn.(8.20) that the coupling constant for Cu is $\alpha m = 2.49 \times 10^{-14} kg\, s^{-1}$ whilst for Ni it is $7.98 \times 10^{-13}\, kg\, s^{-1}$, which is around a factor of 30 stronger. We have also made MD simulations for the intermediate value of $2.5 \times 10^{-13}\, kg\, s^{-1}$, corresponding to ten times that of Cu (or one-third that of Ni). In fig. 8.6 we present a comparison of the evolution of a 500 eV cascade in the <345> direction of a Cu lattice, with the above coupling constants. The atom vibrations had previously been equilibrated at a temperature of 100 K (corresponding to a classical kinetic energy of $(3/2)kT$), which is intended to simulate the residual thermal motion of the atoms at low temperature. The weak electron-phonon coupling in Cu has little effect on the peak disorder at 0.2 ps but reduces the final defect yield from five to four Frenkel pairs (FP). With the strong coupling to be expected in Ni the defect yield was reduced to only two FP. The cascade structure at 0.2ps shows that strong coupling appreciably retards the propagation of the replacement collision sequences, thus the overall effect is not dissimilar to a reduction in the cascade energy.

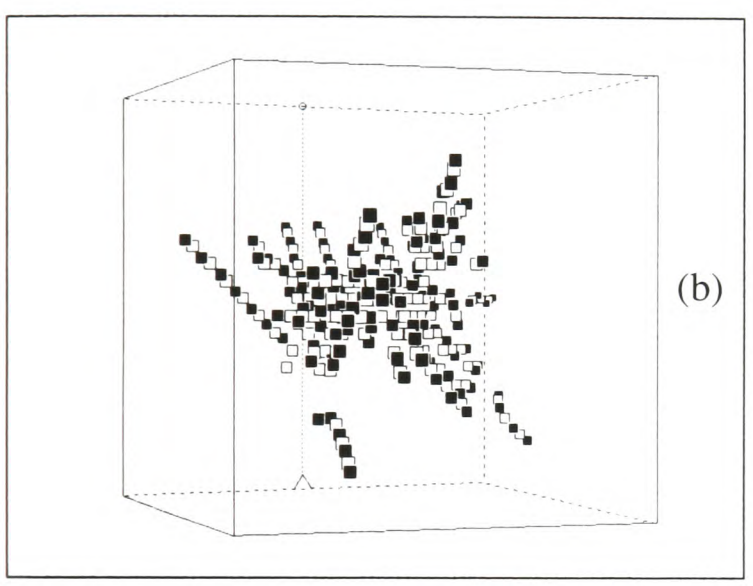
We have not observed any obvious quenching-in of defects during these and other similar cascade simulations which have been made in the energy range 250 eV to 1 keV, although this could well occur at energies above 1 keV, where a quasi-liquid zone is likely to be

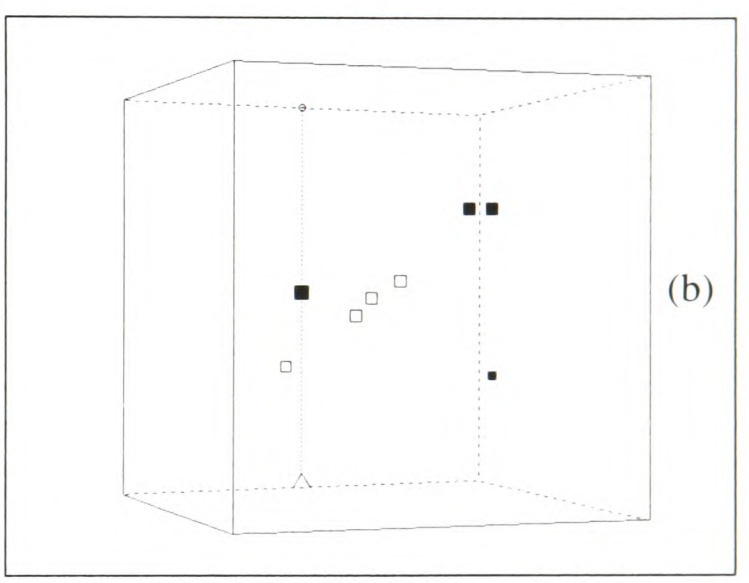
Fig. 8.6. The effect of different electron-phonon coupling strengths on the evolution of 500 eV cascade in copper. Interstitials are shown as full squares and vacancies as ope squares. The left-hand column shows the defect configuration 0.2ps after the primary ever whilst the right-hand column is after 7ps. The coupling strengths used are thos corresponding to (a) zero coupling, (b) copper, (c) ten times that of copper (or one third thi of nickel), (d) nickel.

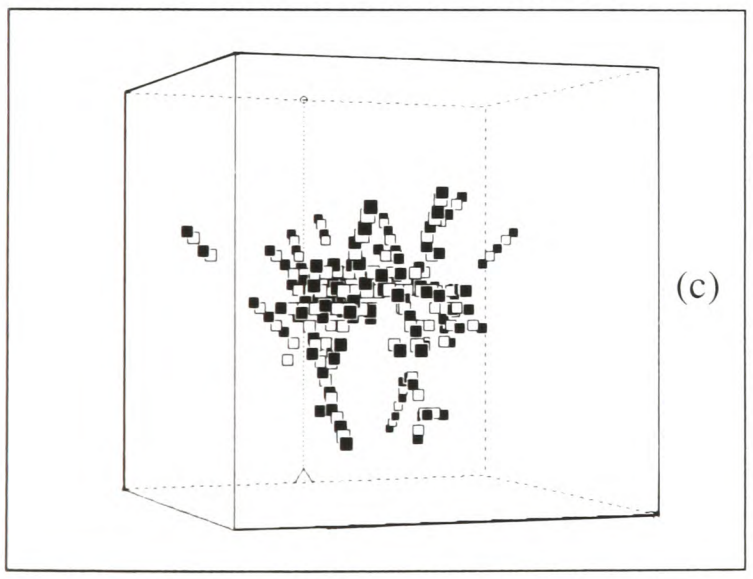
Fig. 8.6. The effect of different electron-phonon coupling strengths on the evolution of a 500 eV cascade in copper. Interstitials are shown as full squares and vacancies as open squares. The left-hand column shows the defect configuration 0.2ps after the primary event whilst the right-hand column is after 7ps. The coupling strengths used are those corresponding to (a) zero coupling, (b) copper, (c) ten times that of copper (or one third that of nickel), (d) nickel.

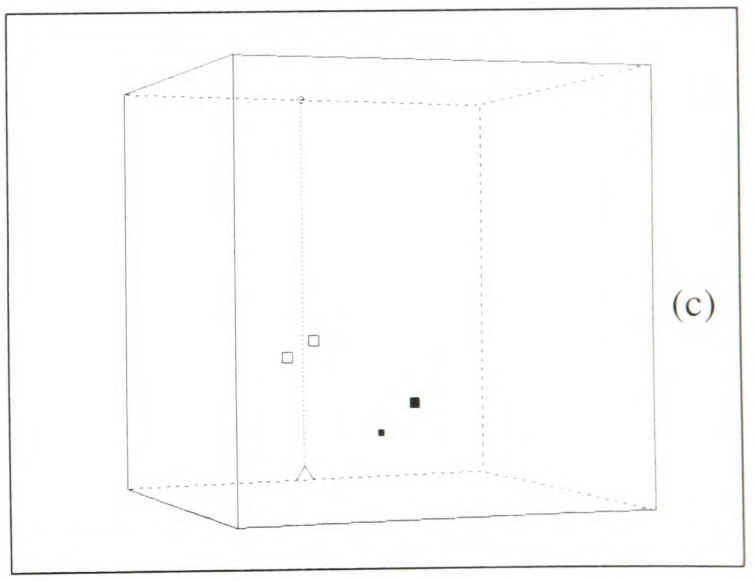

(a)

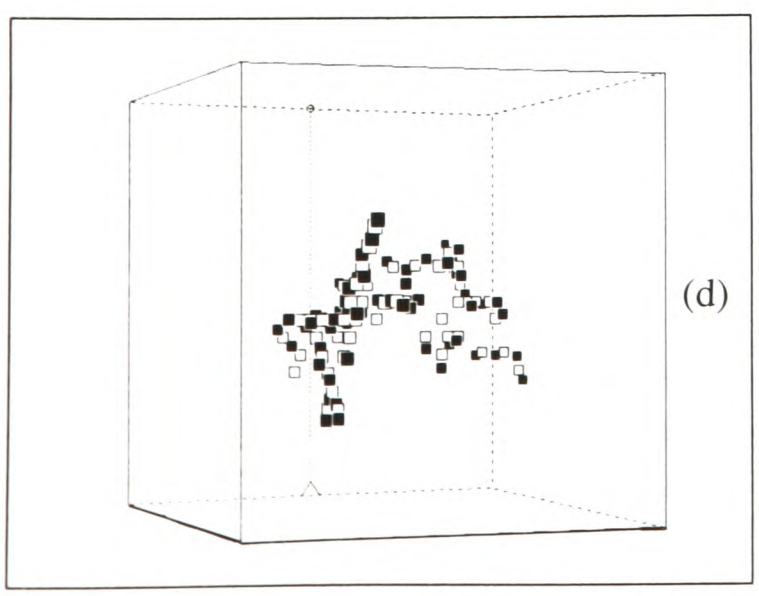

(a)

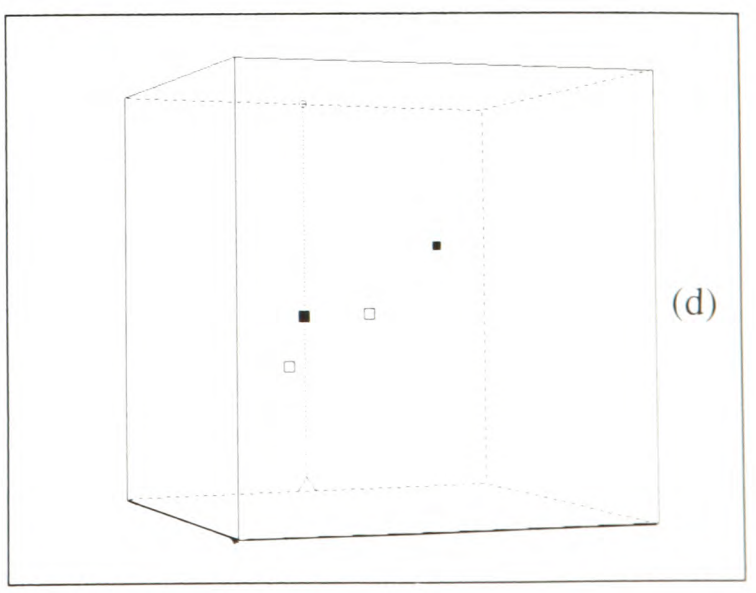

(b)


(b)


(c)


(c)


(d)


(d)

formed at the centre of the cascade. This formation of a liquid-like zone has been observed by other workers in 5 keV cascades <22>. The electron-phonon coupling would shorten the lifetime of such a zone, which might enhance the defect yield.

Having shown how the electron-ion interaction can cause two apparently very similar metals such as Cu and Ni to behave differently in their response to radiation it is natural to ask if there exist other pairs of metals which would show a similar difference. As we have shown in § 8.4, this involves a determination of the ζ ratio for the two metals, which in turn requires a knowledge of both γ_e and T_0. The former has been determined for many metals and simply involves measuring the low temperature specific heat capacity. The results of these measurements are widely available, *e.g.* <23>. We now present a simple method of determining T_0.

§ 8.9 Estimation of T_0.

From the Drude model of metals we can write the electrical resistivity as

$$\rho = \left(\frac{m^*}{n e^2}\right)\frac{1}{t}, \tag{8.32}$$

where m^* is the effective mass of the charge carriers, e is their charge and n their number density. In this model t is a mean free flight time between scattering events. In practice there are usually several different scattering mechanisms which contribute to t such as scattering from defects, impurities, and phonons. Each of these have an associated mean free flight time which contributes to the net value of t in eqn.(8.32). Thus we may write

$$\frac{1}{t} = \frac{1}{t_d} + \frac{1}{t_i} + \frac{1}{t_p} \quad , \tag{8.33}$$

to denote each of these scattering sources. Now t_p is related to the electron-phonon mean free path by

$$t_p = \lambda / v_f \quad , \tag{8.34}$$

and so we may use eqn.(8.6) to write

$$\frac{1}{t_p} = \frac{T v_f}{r_0 T_0} \quad . \tag{8.35}$$

We now make the assumption that scattering from defects and impurities is independent of temperature. This approximation is better for low temperatures where the mean phonon wavelength is large compared to the lattice constant but is quite reasonable even above the Debye temperature for most metals. We then differentiate eqn.(8.32) with respect to temperature and use eqn.(8.35) to obtain

$$\frac{d\rho}{dT} = \left(\frac{m^*}{ne^2}\right)\left(\frac{d}{dT}\ \frac{1}{t}\right) = \left(\frac{m^*}{ne^2}\right)\left(\frac{v_f}{r_0 T_0}\right) \quad . \tag{8.36}$$

This expression rearranges to give

$$T_0 = \left(\frac{m^* v_f}{n e^2 r_0}\right)\left(\frac{1}{d\rho/dT}\right) . \tag{8.37}$$

The effective electron mass m^* may be measured, for example, by cyclotron resonance experiments, n may be determined from measurements of the Hall coefficient, r_0 follows directly from the molar volume and values of the Fermi energy (and hence v_f) are known in many cases. $d\rho/dT$ should be evaluated above the Debye temperature of the material since phonons of the Debye frequency dominate the thermal spike.

This procedure allows one to estimate T_0 and together with γ_e one is then able to fully characterise the cascade cooling characteristics. If data on effective masses and Hall coefficients (to determine n) are not available it is still possible to compare the cooling characteristics of similar metals by comparing ratios of the quantity $\zeta = T_0 / \gamma_e$, since for similar metals the quantity

$$\left(\frac{m^* v_f}{n e^2 r_0}\right) \tag{8.38}$$

should not vary too widely. Thus we may write

$$\frac{(T_0)_1}{(T_0)_2} = \frac{(d\rho/dT)_2}{(d\rho/dT)_1} \quad . \tag{8.39}$$

The evaluation of this ratio only requires a knowledge of the variation of resistivity with temperature above θ_D.

A study of the properties of various metals has revealed several pairs which, on the basis of the above considerations, could be expected to show differences in their response to radiation at least *as* significant as those observed between Cu and Ni. Perhaps the most interesting combination is that of silver and palladium. These two metals have a ζ ratio of ~ 70 so one would expect a large difference in their cascade cooling behaviour. This system is especially interesting since they are neighbours in the periodic table and so other relevant radiation damage parameters, such as cascade size and damage distributions, could be expected to be very similar. Another interesting combination is found in the rare earth metals. These materials have never been studied in the context of radiation damage however they do possess some rather interesting properties. α – Pr has a very large value of $\gamma_e \sim 20\, mJ\, mol^{-1}\, K^{-2}$ whilst α – (Yb) has $\gamma_e \sim 3.3\, mJ\, mol^{-1}\, K^{-2}$. Using the above procedure for T_0 we find a ζ ratio of ~ 30, which is similar to that of Cu and Ni. Ion bombardment of these high-Z metals could be expected to give compact cascades with a small initial radius and hence large initial temperature. This would favour the enhancement of the electron-ion interaction and any differences in their behaviour would be accentuated. It is unfortunate that Yb and Pr are not closer in the periodic table but the other lanthanides have less attractive T_0 ratios.

§ 8.10 Summary.

We began this chapter by demonstrating the inapplicability of the normal value of thermal conductivity in the modelling of cascades in metals. We saw how this arose from the inability of the electron gas to participate in the conduction process and then discussed the physical model of Flynn and Averback which clearly illustrates the importance of cascade size in determining the level of electron-phonon interaction. This physical picture was then

placed on a more formal basis by deriving equations governing the thermal interaction of electrons and phonons in the cooling phase of energetic displacement cascades. We obtained numerical solutions of these equations for 2 keV cascades in both Ni and Cu and these calculations confirm that cascades in Ni should quench much faster than those in Cu – a result fully consistent with the experimentally observed differences in the response of these two metals to ion irradiation. This model of the electron-ion interaction in cascades demonstrates the importance of the ratio of two parameters in determining the efficiency of electronic cooling of the cascade region: T_0, the temperature at which the electron-phonon mean free path reduces to the radius of the Wigner-Seitz sphere and γ_e, the coefficient of the electronic heat capacity. These calculations also demonstrate quantitatively that current MD simulations of displacement cascades underestimate the rate of removal of energy from the cascade region during the cooling phase by neglecting the electron-phonon interaction. A method was described for incorporating this thermodynamic model into the MD code 'MOLDY' and a number of cascade simulations were performed using this approach. A surprising result of these simulations is that in materials where the electron-phonon interaction is stronger and heat transfer from the cascade region is enhanced during the cooling phase, defect production is actually inhibited, as atomic configurations which would result in high residual defect concentrations are less likely to develop. No quenching-in of defects was observed during the MD simulations, although with higher energy cascades it appears this is possible. We concluded with a discussion of a simple method showing how the theory developed earlier can be used to determine the cooling characteristics of cascades in a given metal and identified two systems which should behave differently in their response to ion irradiation according to the theory.

§ 8.11 Conclusions.

The main implication of this work for the topic of this thesis is that we can no longer hope to provide a universal description of point defect production in metals, in the sense that simple scaling rules based on atomic properties could be applied to go from one material to another. It is clearly necessary to also consider the properties of the electron gas in any future

model. The theory developed in this chapter goes some way towards providing a basis for an improved model of radiation damage in metals. The current trend in this area of research is, quite rightly, moving away from a binary collision description of displacement damage and towards a greater emphasis on MD studies. This does not mean that scattering theory is obsolete – as a practical means of describing radiation effects the standard binary collision theory is still by far the most convenient. It is also sufficiently versatile to incorporate any modifications suggested by MD in a phenomenological manner. Despite the successes of MD studies it is important to remember that current formulations certainly do not contain all of the physics required to describe high energy particle-solid interactions. The addition of an electron-ion interaction in the manner described in this chapter will hopefully serve to make the picture a little more complete. However the main importance of the model described here lies not just in the potential to perform more accurate MD simulations, but in the realisation that metals with a high value of ζ may have an intrinsic resistance to cascade radiation damage. The possibility exists therefore of 'tailoring' alloys with a high ζ which will have an increased lifetime when used in nuclear reactors.

References

<1> H.S. Carslaw and J.C. Jaeger, *Heat Conduction in Solids,* Oxford University Press. (1959).

<2> Dr. A.J.E. Foreman, private communication.

<3> C.A. English and M.L. Jenkins, Mater. Sci. Forum, Vols. 15-18, 1003 (1987).

<4> Dr. S.M. Murphy, private communication.

<5> V.I. Protosov and V.G. Chudinov, Rad. Eff. 66 , 1 (1982)

<6> K.B. Winterbon, Chalk River Nuclear Laboratories report AECL-8054, April 1983.

<7> C.P. Flynn and R.S. Averback, Phys. Rev. B 38 (10) , 7118 (1988).

<8> M.W. Finnis, P. Agnew and A.J.E. Foreman, Phys. Rev. B 44 , 567 (1991).

<9> J.M. Ziman, *Electrons and Phonons,* Oxford, Clarendon Press (1960).

<10> J.S. Vetrano, I.M. Robertson, R.S. Averback and M.A. Kirk, 15th Int. Symp. Rad. Dam. in Metals, ASTM, Nashville (1990).

<11> K. Smalinskas, I.M. Robertson, R.S. Averback and M.A. Kirk, 15th Int. Symp. Rad. Dam. in Metals, ASTM, Nashville (1990).

<12> A.R. Curtis and W.P. Sweetenham, Unclassified Harwell Report A.E.R.E R-12805 (1988).

<13> J.B. Gibson, A.N. Goland, M. Milgram and G.H. Vineyard, Phys. Rev. 120 (4), 1229 (1960).

<14> G.H. Vineyard, J.B. Gibson, A.N. Goland and M. Milgram, Bull. Am. Phys. Soc. 5 , 26 (1960).

<15> T. Diaz de la Rubia, R.S. Averback, R. Benedek and W.E. King, Phys. Rev. Letts, 59 (17), 1930 (1987).

<16> A. Caro and M. Victoria, Phys. Rev. A40 (5), 2287 (1989).

<17> M.I. Kaganov, I.M. Lifshitz and L.V. Tanatarov, Sov. Phys. JETP, 4 (2), 173 (1957).

<18> N.W. Ashcroft and N.D. Mermin, *Solid State Physics* , Saunders College Publishing (1988).

<19> M.W. Finnis, Unclassified Harwell Report, A.E.R.E. R 13182 (1988).

<20> G.J. Ackland, M.W. Finnis, G. Tichy and V. Vitek, Phil. Mag. 56 , 735 (1987).

<21> A.J.E. Foreman, W.J. Phythian and C.A. English, Unclassified 'AEA Technology' Report, AEA-TRS-2031, Jan. 1991.

<22> T. Diaz de la Rubia, R.S. Averback, H. Hsieh and R. Benedek, J. Mater. Res., 4 (3), 579 (1989).

<23> N.B.S. Monograph 21 , (1960).

Appendix 1

Numerical Integrations Involving the Divergent Thomas-Fermi Differential Cross Section

Many of the partial damage energy calculations presented in chapter 4 involve integrals of the type

$$\int_0^{T_m} \nu(T)\left(\frac{d\sigma}{dT}\right) dT \quad , \tag{A1.1}$$

where $(d\sigma/dT)$ is the differential scattering cross section. As we saw in § 2.1, an analytic expression for this can be derived from the Thomas-Fermi model of the atom. In the reduced units described in chapter 2, this cross section has the form

$$\frac{d\sigma}{dt} = \frac{-\pi a_{TF}{}^2}{2} \frac{f(t^{1/2})}{t^{3/2}} \quad , \tag{A1.2}$$

or in ordinary units it can be expressed as

$$\frac{d\sigma}{dT} = \frac{\gamma\alpha^{1/2}}{T^{3/2}} f\left[\left(\frac{T}{\alpha}\right)^{1/2}\right], \tag{A1.3}$$

where we have written

$$\gamma = \frac{-\pi a_{TF}{}^2}{2} \text{ and } \alpha = \frac{T_m}{\varepsilon} \quad .$$

These symbols are defined in § 2.1. The factor of $T^{3/2}$ in the denominator means that the differential scattering cross section is singular at the origin and so although the integral in eqn.(A1.1) may converge, any straightforward numerical integration which requires the

evaluation of the integrand at the origin will fail. The fact that the integral *does* converge means that in practice it is not necessary to take the lower integration limit as equal to zero, but only sufficiently small that no significant error is introduced. In this way a simple quadrature formula such as Simpson's rule can be used to produce a result but will be very inefficient. The reason is that in the vicinity of the singularity the integrand will have a rapidly varying curvature which is poorly represented by a polynomial (in the case of Simpson's rule, only a second degree polynomial, whose curvature is constant). It would be necessary to use a very small integration step size in this region to avoid excessive error. But further away from the origin, where the integrand is changing much less rapidly, one could easily use a much larger step size and still maintain the same level of accuracy, hence the integration will be inefficient. The standard technique in this situation is to re-write the integral in terms of the logarithm of the independent variable:

$$\int_0^{T_m} y(T)\, dT = \int_{\delta}^{\ln T_m} y(e^z).e^z\, dz \quad , \tag{A1.4}$$

where $z = \ln T$ and δ tends to zero. Evaluating the integral in this way, with a constant step size in $\ln(T)$, ensures that the step size is smaller near the origin, where the integrand is changing rapidly, but increases at points further out where only a larger step size is required to give the same level of accuracy. This results in a very worthwhile increase in efficiency and the integration times can be reduced by a factor of five or more over a linear integration for the same level accuracy. This technique has been used on all the integrals presented in this investigation which are singular at the origin. This includes the integrals over the McKinley-Feshbach cross section for relativistic electron scattering used in chapter 5, as well as those integrals over the Thomas-Fermi cross section.

Whilst the above technique improves the efficiency of such a numerical integration, the fact still remains that a polynomial gives a very poor representation of a quotient whose denominator is tending to zero. Another technique is available for analytically *removing* the singularity, leaving a rather more well-behaved function which can be efficiently numerically integrated. Suppose we have a function $\chi(t)$ which is singular at the origin. If we

can find another function $\Phi(t)$ which tends to infinity at the same rate but which can be analytically integrated, then we may write

$$\int_0^{T_m} \chi(t)\,dt = \int_0^{T_m} \Phi(t)\,dt + \int_0^{T_m} (\chi(t) - \Phi(t))\,dt \quad . \tag{A1.5}$$

The second integral now tends to zero at the origin, rather than infinity and a simple quadrature can be used. We shall illustrate the method for the integral in eqn.(A1.1) where $\nu(T)$ represents the damage energy. Let $\chi(T)$ represent the integrand in eqn.(A1.1). We have seen in chapter 4 that the damage energy can be represented in the form

$$\nu(T) = \frac{T}{1 + aT^{.15} + bT^{.75} + cT} \quad , \tag{A1.6}$$

where a,b, and c are constants. Near the origin this has the simpler form

$$\nu(T) = T - aT^{1.15} \quad . \tag{A1.7}$$

It can also be shown <1> that near the origin, the scattering function has the form (in the Thomas-Fermi approximation)

$$f(\zeta) = 1.43\,\zeta^{0.35} \quad , \tag{A1.8}$$

where we have written $\zeta = t^{1/2}$. Let us now construct a function $\Phi(T)$ from the behaviour of the integrand in eqn.(A1.1) for small values of its argument

$$\Phi(T) = 1.43\,\gamma\,\alpha^{0.325}\,(T^{-0.325} - aT^{-0.175}) \quad . \tag{A1.9}$$

This function will become a more faithful representation of the integrand in eqn.(A1.1) as we approach the origin and the difference $\chi(T) - \Phi(T)$ will tend to zero. The latter function can be analytically integrated to give

$$\int_0^{T_m} \Phi(T)\,dT = 1.43\,\gamma\,\alpha^{0.325}\left(\frac{T_m^{0.675}}{0.675} - \frac{aT_m^{0.825}}{0.825}\right) \quad . \tag{A1.10}$$

Substitution of eqns.(A1.9) and (A1.10) into eqn.(A1.5) then gives the required result. The reduction of the curvature in the integrand obtained by this technique allows a much larger

integration step size for a given level of accuracy. Maximum efficiency in the evaluation of such singular integrands can be obtained when this method of removing the singularity is used together with the first technique discussed.

Reference

<1> C.A. Coulter and D.M. Parkin, J. Nucl. Mater. 88 , 249 (1980).

Appendix 2

Units of Radiation

The many different ways in which radiation can interact with matter and cause observable changes has resulted in the development of a somewhat confusing system of units. In 1974 the International Commission on Radiological Units (ICRU) recommended the adoption of the International System (S.I.) of units in this field however many of the older units are still widely used. We give below both the S.I. unit relating to a particular effect and its older counterpart.

(i) The radioactive decay of atoms is measured in S.I. units of the Bequerel (Bq) which gives the number of disintegrations per second. This is rather a small unit and the older, more useful is the Curie (Ci), where

$$1 \text{ Ci} = 3.7 \times 10^{10} \text{ Bq} \ . \tag{A2.1}$$

(ii) The old unit of radiation exposure, applying only to X– and γ– rays, is the Roentgen (R). This is defined as the quantity of X– or γ– rays such that the sum of the electrical charges on all the ions of one sign produced in air when all the electrons liberated by the radiation are completely stopped in air, is 2.58×10^{-4} Coulombs per kg of air at standard temperature and pressure. This unit is numerically equal to one electrostatic unit (e.s.u.) of charge per 0.001293 g of air. No special name has been given to the S.I. form of this unit, thus

$$1 C kg^{-1} = 3876 R \ . \tag{A2.2}$$

(iii) To quantify the energy a given radiation deposits in unit mass of a target (the absorbed dose) the unit Gray (Gy) is used. This can be applied to all types of radiation and all

targets and is the special name given in this case to the S.I. unit Joules per kg. The deposited energy will depend on the characteristics of the target and so this should also be quoted. The older unit is the *rad* and the relationship between them is

$$1\,Gy = 100\,rad \quad . \tag{A2.3}$$

(iv) For the purposes of radiological protection a quantity known as the dose equivalent is defined which weights the absorbed dose on the basis of biological considerations. The special name for the S.I. unit $J\,kg^{-1}$ when applied to dose equivalents is the Sievert (Sv). The old unit is the *rem* and the relationship between them is

$$1 \text{ Sv } = 100 \text{ } rem \quad . \tag{A2.4}$$

(v) In the study of structural radiation damage it is necessary to define a unit which is able to quantify the number of lattice displacements produced in a given case. The most commonly used unit here is the 'displacement per atom' (*dpa*). This is defined such that if a target has been subjected to 1 *dpa* of radiation then, on average, every target atom will have been displaced from its lattice site one time.

Reference

B.A.J. Lister, E.M. Flew and D.J. McDowell, AERE – EMS Gen. 18 (1982).